Title

Solid State Electrochemical Sensors for Nitrogen Oxide (NOx) Detection in Lean Exhaust Gases

Permalink

https://escholarship.org/uc/item/7g8290w7

Author

Rheaume, Jonathan Michael

Publication Date

2010

Peer reviewed|Thesis/dissertation

Solid State Electrochemical Sensors for Nitrogen Oxide (NO$_x$) Detection in Lean Exhaust Gases

by

Jonathan Michael Rheaume

A report submitted in partial satisfaction of the

requirements for the degree of

Doctor of Philosophy

in

Engineering – Mechanical Engineering

in the

Graduate Division

of the

University of California, Berkeley

Committee in charge:
Professor Albert P. Pisano, Chair
Professor J. Karl Hedrick
Professor Seth Sanders

Spring 2010

**Solid State Electrochemical Sensors for Nitrogen Oxide (NO$_x$) Detection
in Lean Exhaust Gases**

©2010

Jonathan Michael Rheaume

Abstract

Solid State Electrochemical Sensors for Nitrogen Oxide (NO$_x$) Detection in Lean Exhaust Gases

by

Jonathan Michael Rheaume

Doctor of Philosophy in Mechanical Engineering

University of California, Berkeley

Professor Albert P. Pisano, Chair

Solid state electrochemical sensors that measure nitrogen oxides (NO$_x$) in lean exhaust have been investigated in order to help meet future on-board diagnostic (OBD) regulations for diesel vehicles. This impedancemetric detection technology consists of a planar, single cell sensor design with various sensing electrode materials and yttria-stabilized zirconia (YSZ) as the electrolyte. No reference to ambient air is required. An impedance analysis method yields a signal that is proportional to the analyte gas concentration at a specific frequency. These sensors function by detecting the change in impedance caused by electron exchange in the redox reactions of NO$_x$ gases at the sensing electrodes. From the impedance data, the resulting shift in phase angle ($\Delta\Theta$) is calculated, which can be calibrated to yield to the NO$_x$ concentration at low parts per million (ppm) levels.

The applicability of surface micromachining techniques to unfired ceramic sheets has been evaluated for the potential to reduce the size and mass of sensors. A reduction in size according to the principles of microsystems technologies (MST) is desired for faster light-off, lower temperature operation, decreased heater power, and a faster response leading to decreased emissions. Both wet and dry etching have been investigated. These techniques, however, were not effective at micromachining unfired ceramic sheets of partially stabilized zirconia.

Three varieties of impedance-based, lean NO$_x$ sensors have been fabricated manually, tested with both NO and NO$_2$ gases at concentrations typical of diesel exhaust, and analyzed under various conditions. All sensors consisted of a planar, single cell design. Sensing electrodes were either gold wire or prefired, gelcast lanthanum strontium manganate (LSM, La$_{0.85}$Sr$_{0.15}$MnO$_3$). The LSM sensors were mounted on dense substrates consisting either of alumina (Al$_2$O$_3$) or of partially stabilized zirconia (PSZ, ZrO$_2$ with Y$_2$O$_3$). Electrochemical impedance spectroscopy (EIS) techniques were used to interrogate the sensors. At low frequency (10 Hz), a signal was obtained proportional to low analyte gas concentration. The effects of temperature, total gas flow rate, and cross sensitivity to oxygen were examined for all sensors.

Sensors with gold wire electrodes showed higher sensitivity to NO$_x$ than gelcast LSM sensors. None of the impedancemetric sensors showed dependence on total gas flow rate within

the examined flow range of 100-500 sccm. They did exhibit, however, cross sensitivity to O_2, requiring P_{O_2} to be known in order to evaluate NO_x concentration.

In addition, a strong temperature dependence was observed for the sensors with gold wire electrodes. The phase angles correlated linearly with temperature at 10^5 Hz. Generally, lowering the sensing temperatures resulted in larger phase angle responses, possibly due to the slower kinetics of the oxygen reduction reaction at lower temperatures. The lowest temperature evaluated for sensors with gold wire electrodes, 600°C, exhibited the largest change in phase angle. Nevertheless, even the lowest operating temperature examined was several hundred degrees above the temperature of the exhaust in the designated location of the sensor, requiring the sensors described herein to be continuously heated by a separate power source.

At high frequency (10^5 Hz), a linear correlation between phase angle and temperature was observed between 600-700°C in the sensors with gold wire working electrodes. As a result, a stable sensor could be calibrated to serve as a thermometer.

Equivalent circuit modeling was performed for the sensors in order to better understand the processes underlying the sensing mechanism. Excellent agreement with gold sensor data was obtained with a R_0-(R_1C_1)-(R_2C_2) circuit. The subcircuit elements are associated with the following physical processes: (0) contact resistance, (1) charge transport through electrolyte bulk, and (2) adsorption and dissociation of O_2. NO_x exposure evoked changes in the parameter values of R_2 and C_2 only. Both varied linearly over the entire range of NO (0-100 ppm). This finding suggests that these parameters can be calibrated to determine NO concentration. The rate limiting step was likely a process with atomic oxygen such as dissociation or surface diffusion.

An equivalent circuit with an additional Cole element successfully modeled the output of the NO_x sensors with LSM electrodes: R_0-(R_1Q_1)-(R_2Q_2)-(R_3Q_3). The Cole element accounted for the additional time constant exhibited by the impedance spectra. The subcircuit elements were associated with similar physical processes as the sensors with gold wires except the additional circuit element (2) was attributed to an electrode-based conductivity process (through electrode bulk or interfacial conductivity).

Design of experiments techniques were applied to the NO_x sensors with gold wire electrodes. The optimum sensor design was achieved with a thicker electrolyte and was insensitive to the spacing between sensing electrodes. Within the design space investigated, the surface area of the electrode affected NO_2-sensing and specifically reduced surface area enhanced detection. Equivalent circuit modeling performed in conjunction with the optimization studies confirmed that R_1 in the model of the system with gold electrodes refers to bulk electrolyte resistance. Thicker porous electrolyte resulted in lower resistance, contrary to expectations, suggesting that the increased surface area is involved in the sensing mechanism.

Although the sensor results showed promise, the technology based on this material system faces several challenges prior to commercialization. Signal drift and poor manufacturability are interrelated problems. Signal drift results from microstructural changes (aging) in the electrolyte during exposure to high temperature gases. Elevating the sintering temperature to 1500°C as is standard practice in the manufacturing of oxygen sensors using high temperature cofired ceramic (HTCC) methods would mitigate aging by completing the microstructural phase transformation, however, this temperature would degrade the electrodes. Typically the electrodes and electrolyte are cofired in order to achieve good contact, but at 1500°C the gold electrodes would melt, and the LSM electrodes would form nonconductive zirconate phases. Microfabrication methods that

physically deposit the electrolyte might address the aging issue, but this approach would require significant cost reduction analysis and implementation in order to be successful in the marketplace.

In summary, this dissertation presents research that is novel in numerous respects. It relates the first publicly available study of surface micromachining techniques applied to unfired sheets of ceramic material. In addition, it contains the first ever published optimization study of impedance-type NO_x sensors; design of experiments techniques were applied to sensors with gold wire electrodes. Last of all, this treatise conveys the first ever analysis of gelcast LSM electrodes used in a NO_x sensor.

Dedication

I dedicate this dissertation to my wife, Jill.

Table of Contents

List of Figures

List of Tables

Acknowledgements

Table of Symbols and Abbreviations

α	Exponent of gas concentration used to determine rate-determining step
ALD	Atomic layer Deposition
APS	Ammonium persulfate (initiator)
C	Capacitor
CARB	California Air Resources Board
CNLS	Complex Nonlinear Least Squares Regression
CO	Carbon monoxide
CPE	Constant Phase Element
CTE	Coefficients of Thermal Expansion
$deNO_x$	NO_x removal
$deSO_x$	Desulfurization
DOC	Diesel Oxidation Catalyst
DPF	Diesel Particulate Filter
E_a	Activation Energy
ECU	Engine Control Unit
EGO	Exhaust Gas Oxygen sensor, a potentiometric (lambda) sensor
EGR	Exhaust Gas Recirculation
EIS	Electrochemical Impedance Spectroscopy
EPA	Environmental Protection Agency
$\varepsilon_{res}(\omega)$	Residual error
$\varepsilon_{fit}(\omega)$	Systematic error that due to inadequacies of the model,
$\varepsilon_{bias}(\omega)$	Systematic experimental bias error
$\varepsilon_{stoch}(\omega)$	Stochastic error
f_k	Frequency of kth data point, $f = \omega/2\Pi$
FTP	Federal Test Procedure
HC	Hydrocarbon
HD	Heavy Duty (OBD)
HMAM	Hydroxymethyl-acrylamide (monomer)
MBAM	N,N-methylene-bisacrylamide (cross linker)
HTCC	High Temperature Cofired Ceramic
i(t)	Current response to small signal alternating voltage
I	Maximum current response to applied sinusoidal voltage
IS	Impedance Spectroscopy
j	Imaginary number
k	Reaction rate
LTCC	Low Temperature Cofired Ceramic
λ	Fuel to air ratio
MST	Microsystems Technologies
n	Index of Voigt element in a Voigt circuit
n	Exponent of gas partial pressure used to determine rate-determining step
N	Nitrogen radical
N_{dat}	Number of data points

NO_x	Nitrogen oxides
O	Oxygen radical
$O^=$	Oxygen ion
O^{2-}	Oxygen ion
OBD	On-Board Diagnostics
OH	Hydroxyl radical
ω	Angular frequency
ϴ	Phase angle
|Δϴ|	Phase angle difference caused by analyte gas
$\vec{P}$	Parameter vector used in regression
PLD	Pulsed Laser Deposition
Po_2	Partial pressure of oxygen
ppm	Parts Per Million
PSZ	Partially Stabilized Zirconia
Q	Constant phase element
Q	Constant phase element parameter (usually related to double layer capacitance)
R	Ideal gas constant
R	Resistance
$S(\vec{P})$	Weighted sum of squares
SCR	Selective Catalytic Reduction
σ_i	Conductivity of circuit subelement i
$\sigma_{r,k}^2$	Real part of variance of experimental stochastic errors
$\sigma_{j,k}^2$	Imaginary part of variance of experimental stochastic errors
t	Time
T	Temperature
TDI	Turbocharged Direct Injection (Volkswagen diesel engine)
TEMED	Tetra-methyl-ethylene diamine (catalyst)
TPB	Triple Phase Boundary
TZP	Tetragonal Zirconia Polycrystals
UEGO	Universal Exhaust Gas Oxygen sensor, an amperometric sensor
v(t)	Small signal alternating excitation voltage
V	Excitation voltage amplitude
φ	Phase angle exponent
W	Warburg diffusion element
χ^2	Sum of squares – used in regression analysis to assess regression quality
YSZ	Yttria Stabilized Zirconia
Z	Impedance
|Z|	Impedance magnitude (modulus)
Z_{imag}	Imaginary component of impedance
Z_{real}	Real component of impedance
Z_0	Impedance parameter for Gerischer impedance
$Z_r(f_k)$	Real part of measured impedance at f_k
$Z_j(f_k)$	Imaginary part of measured impedance at f_k
$\hat{Z}_r(f_k\|\vec{P})$	Real part of calculated impedance at f_k

$\hat{Z}_j(f_k|\vec{P})$ Imaginary part of calculated impedance at f_k

$Z(\omega)$ Impedance value from experimental observation

$\hat{Z}(\omega)$ Impedance value from equivalent circuit modeling

CHAPTER 1: Introduction

Computer control of internal combustion engines has improved efficiency and reduced emissions to the benefit of the environment and public health. Regulations for emissions from diesel engines have recently tightened in the United States and Europe (US Tier 2, Euro 5).[1] A sensor that detects nitrogen oxide (NO_x) emissions can be used with an engine control unit (ECU) for closed loop feedback control.

This dissertation presents research that is novel in several significant respects. It presents the first publicly available study of surface micromachining techniques applied to unfired sheets of ceramic material. It documents the first ever optimization study of impedance-type NO_x sensors with gold wire electrodes using design of experiments techniques. Last of all, it relates the fabrication and analysis of the first ever gelcast LSM electrodes used in a NO_x sensor.

1.1 Overview

The goal of this research is to relate research findings on NO_x sensors that can be used in conjunction with an engine control unit of a vehicle to minimize NO_x emissions from diesel engines. Future emissions regulations for on-board diagnostics (OBD) require detection of NO_x on the order of parts per million, which is beyond the capability of NO_x sensors on the automobile market at present.[2] A NO_x sensor is intended to be located in the tailpipe of a diesel engine downstream of emissions abatement hardware, as shown in Figure 1. Its purpose is to monitor the NO_x mitigation system performance by detecting NO_x in exhaust gases that have
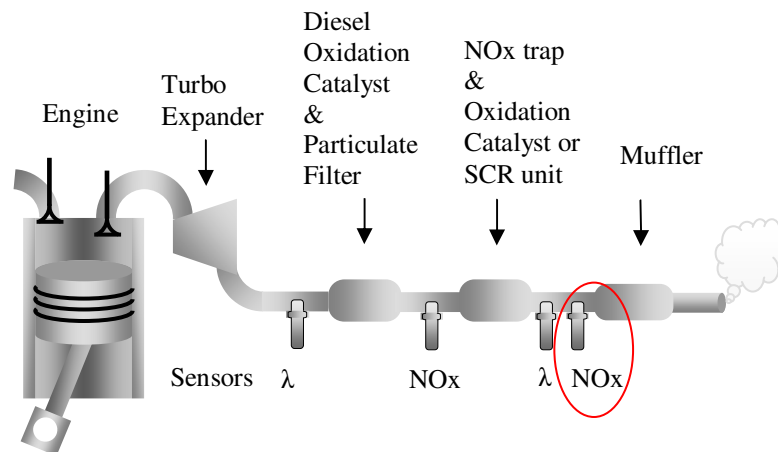
Figure 1. Location NO_x sensor in diesel exhaust pipe to monitor NOx abatement performance.

---

[1] Winston Harrington, "The Design of Effective Regulations of Transport", International Transport Forum, 2008-2, (Washington, DC, Jan. 2008), 14-16.

[2] California Air Resources Board, "Staff Report: Initial Statement of Reasons for Proposed Rulemaking -- Technical Status and Revisions to Malfunction and Diagnostic System Requirements for Heavy-Duty Engines (HD OBD) and Passenger Cars, Light-Duty Trucks, and Medium-Duty Vehicles and Engines (OBD II)", (Apr. 10, 2009), 21-25, (accessed Oct. 28, 2009), available from http://www.arb.ca.gov/regact/2009/hdobd09/obdisor.pdf .

slipped through the emissions abatement equipment. This sensor must be highly sensitive with a detection ability on the order of single ppm.

Single cell, impedance-based sensors with partially stabilized zirconia electrolytes have been investigated in a controlled setting. By applying an alternating current at a low frequency (10Hz or less), these sensors provide a signal that is proportional to the amount of NO_x present in a mixture of gases containing excess air.[3] NO_x undergoes redox reactions at the working electrode, which alters the impedance of the sensor in a predictable fashion. The output can be calibrated to yield NO_x concentration, which is linearly proportional to phase angle at low NO_x partial pressure.

Three types of impedance-based sensors have been fabricated and evaluated. The first type had working electrodes of gold wire. The second and third types had lanthanum strontium manganate (LSM) prepared by a gelcasting technique as their working electrodes. They were prepared on substrates of either dense alumina or partially stabilized zirconia that measured $1cm^2$. These sensors are depicted in Figure 2. The notation under each picture refers to sensor features as follows: Sensing electrode / Electrolyte / Counter electrode// Substrate

| Gold / YSZ / Pt // Al_2O_3 | LSM / PSZ / LSM // Al_2O_3 | LSM / PSZ / LSM // PSZ |
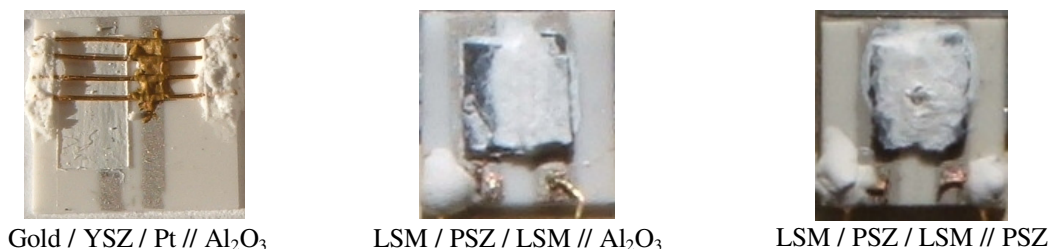
Figure 2. Photos of three types of impedance-based sensors evaluated.

The sensors were analyzed for their ability to detect NO_x species in simulated exhaust gas containing 10% O_2. Impedance spectroscopy was performed, and equivalent circuit-modeling provided insights into the sensing mechanism.

In addition, a study of the manufacture of sensors by applying micromachining methods to unfired ceramic sheet has been undertaken. Last of all, design of experiments methods have been applied to sensors with gold wire electrodes.

1.2 Motivation

Engines based on the Diesel Cycle have an attractive advantage over stoichiometric engines based on the Otto Cycle. Diesel engines boast higher fuel efficiency than gasoline engines due to the higher compression ratio. However, diesel engines emit more smog-causing nitrogen oxides than gasoline engines due to the ineffectiveness of three way catalysts at chemically reducing NO_x species in the presence of excess air. Exhaust gas cleanup technologies such as selective catalytic reduction (SCR) and NO_x traps can be used to mitigate NO_x emissions. These

---

[3] N. Miura, M. Nakatou, S. Zhuiykov, "Impedance-based total-NO_x sensor using stabilized zirconia and $ZnCr_2O_4$ sensing electrode operating at high temperature", <u>Electrochem Comm</u>, 4 , (2002), 284–287.

technologies lack an important component to monitor operation of the NO_x abatement systems: a low level NO_x sensor.[4]

The California Air Resources Board (CARB) specified on-board diagnostics features for vehicles sold in California starting in model year 1991 (OBD I), and tightened regulations in 1996 (OBD II). Vehicles sold in California must monitor every aspect of operation that could increase emissions and communicate a malfunction via a "check engine" warning light.[5] The United States Environmental Protection Agency (EPA) set similar requirements for vehicles nationwide in an amendment to the Clean Air Act of 1990 which was promulgated for 1996 model year light duty vehicles and trucks.[6]

In 2005, CARB adopted separate requirements for heavy duty (HD) vehicles, which are defined as having a gross weight over 14,000 pounds. The new regulations, HD OBD, were to apply to vehicles of the 2010 model year and beyond. HD OBD regulations specify a malfunction threshold for SCR units of 0.6 g/bhp-hr (or 60ppm) above the NO_x tailpipe standard for the 2010 model year. The initial threshold specification for malfunction was half this amount, but the requirement was relaxed because no commercially available NO_x sensor could detect NO_x to such low concentration levels.

According to automobile manufacturers, a brand new, state of the art NO_x sensor can measure with tolerance of ±6 ppm. Over time, the exhaust's harsh environment causes the tolerance to deteriorate to ±15 ppm, which is on the same order of magnitude as the permissible NO_x in the exhaust. Therefore, manufacturers maintain that a sensor with accuracy of ±5 ppm is necessary to meet the OBD requirements.

In addition, for HD diesel vehicles that are equipped with a NO_x adsorber (trap), CARB regulations require performance monitoring. Starting with the 2013 model year, when NO_x emissions exceed a threshold value of 0.2 g/bhp-hr (20 ppm), a malfunction is registered. This threshold NO_x emissions level is calculated over the federal test procedure (FTP) transient cycle.[2]

Martin *et al.* reported NOx sensing on the order of single ppm using a single cell device and an impedance-based measuring technique.[7] This technology shows promise in helping automobile manufacturers meet OBD regulations.

In summary, new OBD regulations are driving the need for a NO_x sensor that detects NO_x on the ppm level that has slipped through the NO_x abatement unit. CARB proposed a NO_x detection requirement that no sensor on the market could meet and was later forced to relax.[8] The body of knowledge on impedance-based sensors presented in this treatise may someday help CARB to meet OBD requirements.

---

[4] California Air Resources Board, "Final Statement of Reasons for Rulemaking, Including Summary of Comments and Agency Responses", Oct. 25, 2001, 61.

[5] California Air Resources Board, "On-Board Diagnostic II (OBD II) Systems - Fact Sheet / FAQs", (Sep. 28, 2009), (accessed Oct. 28, 2009), available from http://www.arb.ca.gov/msprog/obdprog/obdfaq.htm

[6] US Environmental Protection Agency Office of Transportation and Air Quality, "On-Board Diagnostics", (accessed May 05, 2010), available from http://www.epa.gov/obd/basic.htm.

[7] L. P. Martin, L. Y. Woo, R. S. Glass, "Impedancemetric NO_x sensing using YSZ electrolyte and YSZ/Cr_2O_3 composite electrodes", J Electrochem Soc, 154:3, (2007), J97-J104.

[8] California Air Resources Board, "Technical Status and Revisions to Malfunction and Diagnostic System Requirements for 2010 and Subsequent Model Year Heavy Duty Engines (HD OBD)", (Sep. 11, 2008), 16-18, (accessed Nov. 12, 2009), available from www.arb.ca.gov/msprog/obdprog/hdobd_wsreport.doc.

1.3 Summary of Findings

NO_x sensors have been fabricated and analyzed using EIS and equivalent circuit modeling techniques. This work yielded the following results:

- Flow rate does not affect sensor output within the range of 100-500 sccm.
- Sensors with gold electrodes sense better than those with LSM (larger phase angle shift).
- Cross sensitivity requires O_2 removal or compensation.
- Sensors are affected by NO_2, NO, and O_2 (in order of size of the response).
- The sensor consisting of LSM on a substrate of PSZ did not exhibit sensitivity to NO_2 and NO.
- Temperature affects the output of sensors.
- The sensors with gold wire working electrodes can be used to determine temperature. Phase angles correlated linearly with temperature at 10^5 Hz.
- Lowering the sensing temperatures generally resulted in larger phase angle responses.
- The resistance of the low frequency arc is proportional to P_{NO}.
- The surface area of the porous YSZ electrolyte layer affects sensing ability.

The equivalent circuit modeling was successful in helping to understand the various physicochemical processes involved in sensor operation. This knowledge is useful for sensor design.

1.4 Dissertation Organization

The layout of the thesis as follows: Chapter 2 introduces the problem statement. It provides background on lean engines and emissions control, especially emissions gas sensors. Chapter 3 reviews relevant literature and concepts in electrochemical impedance spectroscopy. Chapter 4 details the application of microfabrication methods to sheets of unfired ceramic material used in conventional oxygen and NO_x sensors. Chapter 5 describes the development of a NO_x sensor with gold electrodes, including equivalent circuit modeling. Chapter 6 explains similar work on a NO_x sensor with lanthanum strontium manganate (LSM) electrodes. Chapter 7 reviews design of experiments techniques and presents the results of a statistical optimization of a NO_x sensor with gold electrodes. Finally, Chapter 8 compares the gold wire and gelcast LSM sensors, discusses challenges with this technology and summarizes results and conclusions.

CHAPTER 2: Background

This chapter sets the stage for the work performed by providing information relevant to the sensor technology under development. It explains the motivation of this research effort and it frames the research in terms of the state of the art of technology.

2.1 Problem Statement

Recent geopolitical and economic events that have caused price shocks at the pump are causing consumers to pay more attention to passenger vehicle fuel economy. Diesel engines tend to get more miles per gallon than gasoline engines on account of an intrinsically higher efficiency due to their higher compression ratios. Unfortunately, diesels tend to emit more particulate matter and smog-forming nitrogen oxides than gasoline engines. New emissions reduction technologies that decrease particulates and NO_x have laid the foundation for a resurgence in the popularity of diesel engine passenger vehicles. Although it is possible to meet Tier 2 Bin 5 emissions standards in the US market without a NO_x sensor at this time,[9] future OBD requirements may necessitate a highly sensitive NO_x sensor in order to monitor NO_x cleanup hardware operation. The requirements call for a device that is more sensitive than any sensor that is currently available on the automotive market. An improved NO_x sensor with an accuracy of ±5 ppm is necessary to meet proposed requirements.[2]

A list of sensor requirements and attributes appears below.[10,11]

- Sensitive to NO_x concentrations less than 10 ppm
- Selective for NO_x in presence of oxygen and water vapor
- Speed: sub second detection
- Stable in harsh environment (robust to chemical attack, morphology changes, grain boundary growth, crystallographic phase changes)
- Simple design and control
- Accurate (±1%)[12]
- Repeatable and reproducible signal
- Electrolyte and electrodes free of cracks for good ionic conductivity
- Strength to handle mechanical shock (10 G) due to vehicle operation
- Withstand thermal shock (dT/dt > 100°C/s) and total $\Delta T=1000$°C
- Operation in wide temperature range exhaust (200 to 700°C) in ambient temperatures from -30 to 50°C)
- Longevity: 10,000 hours of operation
- Robust to thermal cycling (on/off and transients)
- Heater required to reach and maintain operating temperature

---

[9] Jens Hadler, Falko Rudolph, Richard Dorenkamp, Hartmut Stehr, Jürgen Hilzendeger, Sebastian Kranzusch, "Der neue 2,0-l-TDI-Motor von Volkswagen für niedrigste Abgasgrenzwerte – Teil 1", Motortechnische Zeitschrift, 69, (May, 2008), 386.

[10] J. Riegel, H. Neumann, H.-M. Wiedenmann, "Exhaust gas sensors for automotive emission control", Sol. Stat. Ion., 152–153, (2002), 788.

[11] Sheikh Akbar, Prabir Dutta, and Chonghoon Lee, "High-Temperature Ceramic Gas Sensors: A Review", Int. J. Appl. Ceram. Technol., 3:4 (2006), 305.

[12] Zhuiykov, Serge, Electrochemistry of Zirconia Gas Sensors, (New York: CRC Press, 2008), 228.

- Attains operating temperature in < 5 s (with built in heater)
- Low operating temperature to reduce parasitic load of heater
- Fabrication process suitable for mass production (tape-cast, co-fired laminated ceramic sheets)
- Low cost

A sensor for commercial production must meet these design requirements, in particular the sensitivity, longevity and robustness criteria.

2.2 NO_x Emissions

Nitrogen oxides take on many forms, as shown in Table 1. Of these, only NO and NO_2 occur naturally. The collective term "NO_x" refers to these two molecules. It can also refer to N_2O_4, which is the dimer form of NO_2.[13] NO_x occurs naturally from lightning, soil emissions, and forest fires.

Anthropogenic emissions of nitrogen oxides originate predominantly from combustion processes.[14] Automobile engines, gas turbines, industrial burners and boilers all generate nitrogen oxides.[15] Two species

Formula	Name
NO	Nitric oxide
NO_2	Nitrogen dioxide
N_2O	Nitrous oxide
NO_3	Nitrogen trioxide
N_2O_4	Nitrogen tetroxide
N_2O_3	Dinitrogen trioxide
N_2O_5	Dinitrogen pentoxide

Table 1. Nitrogen oxides.

constitute virtually all nitrogen oxide emissions: nitric oxide (NO) and nitrogen dioxide (NO_2).[14] These are the most important forms of nitrogen oxides for vehicle emissions. At T>600°C, NO_x in exhaust gases equilibrates so that the mixture consists primarily of NO >90%.[16] Whereas NO is present in the hundreds to thousands of parts per million (ppm), NO_2 comes out in tens of ppm.

One nitrogen oxide that is commonly associated with combustion does not occur as an emission: nitrous oxide (N_2O). It used as an oxidant in motor vehicle racing and in rocketry as well as in anesthesiology (laughing gas).

NO_x garners attention due to its role in atmospheric pollution according to the photochemical reaction:

$$NO + O_3 \overset{h\upsilon}{\leftrightarrow} NO_2 + O_2$$
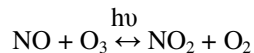
NO depletes ozone (O_3) and readily oxidizes to NO_2, a brown gas involved in smog formation. NO_2 causes adverse health effects such as respiratory difficulties.[13] In addition, NO_2 in the atmosphere is a precursor of nitric acid, which a cause of acid rain.[17]

The following sections deal with the formation of NO_x and the emissions regulations put in place to reduce NO_x emissions from vehicles.

---

[13] Jan Meulenbelt, "Nitrogen and Nitrogen Oxides", <u>Medicine</u>, 31:10, (Oct. 2003), 64.

[14] V. Vestreng, L. Ntziachristos, A. Semb, S. Reis, I. S. A. Isaksen, and L. Tarrason, "Evolution of NO_x emissions in Europe with focus on road transport control measures", <u>Atmos. Chem. Phys.</u>, 9, 1503–1520, (2009), 1503.

[15] Gary L. Borman and Kenneth W. Ragland, <u>Combustion Engineering</u>, (McGraw Hill: Boston, 1998), 608.

[16] Zhuiykov, 215.

[17] Borman, 125-6.

2.2.1 NO_x Formation

NO_x emissions are generated during combustion according to three primary mechanisms: thermal (Zeldovich), prompt (Fenimore), and fuel-bound. Other mechanisms exist, but these three are responsible for most anthropomorphic NO_x production. These mechanisms are discussed below.

Thermal (Zeldovich) NO_x

The Zeldovich mechanism for thermal NO formation consists of several reactions that occur at high temperature in the post flame zone, as shown below.[18]

(1) $N_2 + O \leftrightarrow NO + N$
(2) $N + O_2 \leftrightarrow NO + O$
(3) $N + OH \leftrightarrow NO + H$
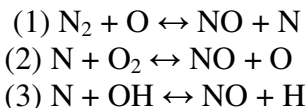
In reaction (1), an oxygen radical (O) attacks dinitrogen (N_2). It is the rate-determining step due to the high activation energy necessary to cleave the stable triple covalent bond in N_2. The nitrogen radical (N) then attacks other species in the subsequent steps, even regenerating the oxygen radical for step (1). Thermal NO_x production yields results in thousands of ppm of NO if unmitigated.

Prompt (Fenimore) NO_x

Fenimore prompt NO production occurs at the flame front during combustion (hence "prompt"). The mechanism occurs as follows:

$CH + N_2 \leftrightarrow HCN + N$
$CH_2 + N_2 \leftrightarrow HCN + NH$
$N + O_2 \leftrightarrow NO + O$
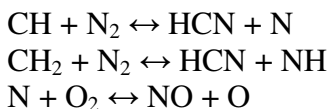
Similar to N, the species HCN and NH react with oxygen to form NO. The Fenimore prompt NO mechanism produces orders of magnitude less NO than the Zeldovich thermal NO mechanism. Typically only 40-60ppm form at the flame front.[19]

Fuel-Bound NO_x

Fuel-bound NO is produced from the naturally occurring, organic nitrogen compounds in the fuel. For example, crude oil contains about 0.1% nitrogen; coal contains approximately 1.5% nitrogen. During combustion, anywhere from 20-50% of fuel-bound nitrogen gets converted to NO.[20]

All of the reaction mechanisms thus far have dealt with NO production. NO_2 can be formed by the oxidation of NO. This reaction is extremely temperature-dependent. At higher temperatures (T > 600°C), NO_x in exhaust gases equilibrates so that the NO_x mixture consists primarily of NO > 90%.[16]

---

[18] Ibid., 126.
[19] Ibid., 131.
[20] Ibid., 133.

2.2.2 NO$_x$ Regulations

This section discusses NO$_x$ emissions standards for the US, Europe, and Japan. These standards are difficult to compare directly due to differences in the test cycles and definitions of pollutants, however, these standards are tending converge to ever lower values over time.[1]

In the US, the California Air Resources Board and the Environmental Protection Agency have enacted legislation for OBD of heavy vehicles.[2] The NO$_x$ requirements established for HD vehicles in the US have consistently led Europe and Japan, as shown in Figure 3.
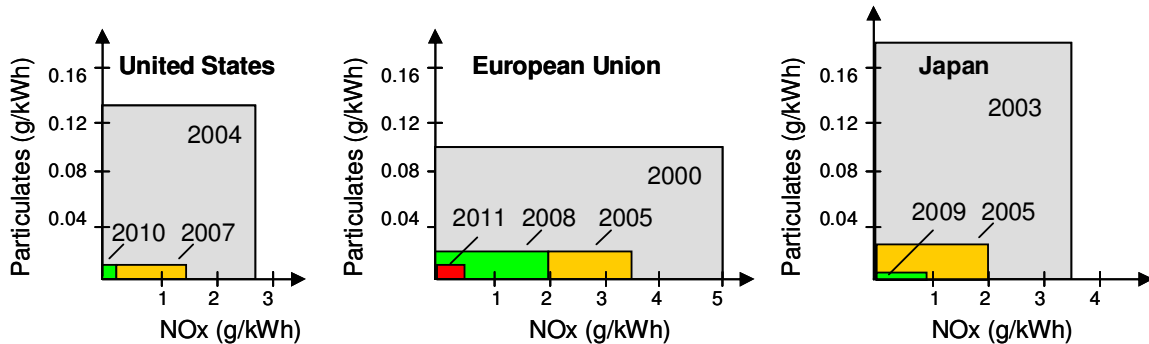
Figure 3. Exhaust regulations for trucks and busses in the US, EU, and Japan.[21]

2.3 Background on Lean Engines

This section introduces lean engines and control of their emissions. Lean refers to combustion with excess oxygen that is typical of gas turbines and diesel engines. They feature direct injection of fuel into a high pressure combustion chamber where the fuel undergoes the following steps: atomization, evaporation, and diffusion. An excess of air results in lower flame speed compared to stoichiometric engines, however, lean burn engines are more efficient due to the higher compression ratio and lower throttling losses. In the work that follows, the NO$_x$ sensors under development are envisioned for operation with diesel engines for automotive applications.

2.3.1 Diesel Engines

Due to their high efficiency and excellent fuel economy, diesel engines are the most widely used internal combustion engine in the world. They are found in passenger vehicles, heavy duty vehicles, agricultural and construction machinery, locomotives, ships, and stationary generator sets.[22] Diesel engines are characterized by the compression ignition of long chain hydrocarbon fuel that is mixed with excess air inside the engine.[23] Diesel engines are more efficient than stoichiometric engines on account of their higher compression ratio, which is possible because direct injection of the fuel precludes the problem of premature ignition (knocking) in

---

[21] NGK Insulators, Ltd., "Bringing the world's first high-precision NO$_x$ sensor to market", Press release, (Jun. 11, 2008), (accessed Nov. 3, 2009), available from http://www.ngk.co.jp/english/news/2008/0611.html

[22] Robert Bosch GmbH, <u>Diesel-Engine Management</u>, (United Kingdom: John Wiley & Sons, 2004), 10.

[23] <u>Ibid</u>., 16.

stoichiometric engines. In diesels, neither carburetors nor spark plugs are used; rather high pressure fuel injectors portion out fuel and glow plugs warm up engines during cold starts.[24]

Historically, diesel engines have had problems with soot formation and NO_x emissions.[25] Soot results from incomplete combustion caused by the heterogeneous, non-stoichiometric, diluted charge. Because the charge is not premixed like in stoichiometric engines, at high engine speeds soot forms when there is insufficient time for vaporization, diffusion, and combustion. To exacerbate the problem, dilution by excess air slows the diffusion flame speed. These factors combine to cause soot formation by incomplete combustion, which can be addressed by a particulate trap and a computer-controlled regeneration strategy.

Smog-forming NO_x emissions also tend to be problematic for diesel engines. Although diesels produce less NO_x because of lower flame temperatures caused by dilution in excess air, after treatment systems consisting of a three way catalytic converter are ineffective at converting NO_x in the presence of excess air.[26,27] Any reducing gases that could react with the NO_x tend to get oxidized by the overwhelming quantity of excess oxygen. NO_x cleanup technologies have been developed to address NO_x emissions, as explained in the next section.

Diesel engines face some additional challenges to adoption in the United States. One is the lack of widespread availability of diesel fuel at filling stations in the US. Another obstacle is the higher price of desulfurized diesel fuel compared to gasoline in the US market (which diesel engines' higher efficiency makes up for). Due to compression ignition, a stronger, more costly engine block is required. For cold starts, sometimes the glow plugs are insufficient and a block heater is necessary; diesel fuel can also form a viscous gel at low temperatures. Last of all, at lower engine speeds, even with sufficient time available for complete combustion, the diluted fuel has difficulties igniting, leading to high levels of HC emissions.[25] The next section explains how the problems associated with emissions from diesel engines are addressed.

2.3.2 Diesel Emissions Mitigation Strategies

The ever tightening statutory restrictions on motor vehicle emissions have resulted in pollution reduction strategies for diesel engines as summarized in Table 2 below.[28] In particular, particulates and NO_x are problematic in diesel engine exhaust.[29] The best mitigation strategy is of course to avoid generating undesired species in the first place, which is possible to some extent by clever design of engine hardware and control strategies. Nevertheless, back end systems (e.g. catalysts, absorbers) are necessary to clean up harmful pollutants that inevitably occur despite the preventive measures.

---

[24] Ibid., 15.
[25] Borman, 413.
[26] B. J. Cooper, "Challenges in Emission Control Catalysis for the Next Decade", Platinum Metals Rev., 38:l, (1994), 3.
[27] R. Burch, J.P. Breen, F.C. Meunier, "A review of the selective reduction of NO_x with hydrocarbons under lean-burn conditions with non-zeolitic oxide and platinum group metal catalysts", Appl Catal B Environ, 39 (2002), 284.
[28] Tim Johnson, "Review of diesel emissions and control", Int. J. Engine Res., (2009), 275-285.
[29] Robert Bosch GmbH, 448-9.

Strategy	Description
Engine design	Combustion chamber geometry, injector location, fuel pressure, control strategies
Exhaust Gas Recirculation (EGR)	Lower P_{O_2} of charge and combustion temperature by dilution with exhaust gases for lower NO_x formation
Selective Catalytic Reduction	NO_x reduction by urea/ammonia addition; requires refill
NO_x trap	NO_x adsorbs, forms nitrates; trap regenerated via rich combustion
Two-way catalyst	HC, CO conversion; not for NO_x
Diesel Oxidation Catalyst	HC, CO, and light particulate matter combustion
Particulate Filter	Soot capture; late fuel injection (rich) regenerates

Table 2. Diesel emissions control strategies.

NO_x Abatement

To avoid NO_x formation, lowering the flame temperature is effective because the Zeldovich mechanism by which most NO_x is formed is an exponential function of temperature.[30] One way to accomplish this is by retarding injection timing, however, this causes particulate emissions to rise in accordance with the particulate-NO_x tradeoff curve.[31,32] An additional strategy to lower flame temperature and thereby retard NO_x formation is exhaust gas recirculation (EGR). A portion of the depleted exhaust is routed from the exhaust manifold into the intake manifold. The recirculated gases consist mostly of nitrogen, carbon dioxide, and water vapor. They dilute the intake air resulting in lower combustion temperature. Water injection will also depress flame temperature, but this method is not practical in vehicles due to corrosion issues and the necessity to replenish the water. Emulsions of diesel fuel and water decrease both NO_x and soot, but this type of fuel is unstable and incompatible with modern fuel-injection systems.[33]

To deal with NO_x after it has been generated, it is not possible to oxidize NO_x using a three way catalytic converter as with gasoline engines. The presence of excess oxygen in diesel exhaust makes it difficult to reduce ppm quantities of NO, which is also an oxidant.

Selective Catalytic Reduction (SCR) is the most common NO_x cleanup method for both light duty and heavy duty vehicles.[34] It involves injecting a reducing agent such as urea to the exhaust upstream of a catalytic converter based on vanadia or zeolytes.[35] The urea forms ammonia which reacts with NO_x in the SCR unit to form nitrogen and water vapor.[36] Some ammonia slips through unreacted, necessitating an additional "slip" catalyst.[35]

As an alternative to SCR, NO_x can be adsorbed and reduced, using a NO_x trap (adsorber). It consists of three components. (1) A catalytic oxidation component converts $NO + \frac{1}{2}O_2 \rightarrow NO_2$. (2) The NO_2 adsorbs on the NO_x trap, which consists of an alkaline earth metal oxide such as

---

[30] Y. B. Zeldovich, "The Oxidation of Nitrogen in Combustion Explosions", Acta Physicochimica U.S.S.R., 21, (1946), 577-628.
[31] Borman, 415.
[32] Robert Bosch GmbH, 58.
[33] Ibid., 39.
[34] Johnson, (2009), 278.
[35] Tim Johnson, "Diesel Engine Emissions and Their Control", Platinum Metals Rev., 52:1, (2008), 28.
[36] Robert Bosch GmbH, 455.

BaO, and forms a nitrate: $NO_2 + BaO + \frac{1}{2}O_2 \rightarrow Ba(NO_3)_2$.[37] The nitrate can be regenerated by a rich excursion—by injecting fuel late in the power stroke to cause a rich pulse ($\lambda=0.95$) that clears the NO_x from the trap surface by oxidation.[38,39] Because they require fuel for regeneration, NO_x traps lower fuel economy.

Particulate Mitigation

For particulates, as with NO_x emissions, it is best to avoid generating them in the first place. Advancing the start of fuel injection decreases soot formation, but increases NO_x production.[32] Swirl chamber combustor designs contribute to more complete combustion by forcing turbulent mixing of diesel fuel and air.[40] Since combustion is never 100% complete, a diesel oxidation catalyst (DOC) located immediately downstream of the engine burns hydrocarbon (HC), carbon monoxide (CO), and some volatile particulate emissions, converting them to water vapor and carbon dioxide.[41] Otherwise particulates can trapped in a diesel particulate filter (DPF). The filter must be periodically regenerated, usually by a rich pulse of fuel late in the power stroke.[42]

Sulfur Removal

Sulfur is also a pollutant. In exhaust, it forms atmospheric pollution in the form of sulfurous oxides (SO_x) and mercaptans. In addition, sulfur in fuel can poison catalytic converters (most times irreversibly), thereby ruining it, leading to raised hydrocarbon and carbon monoxide emissions levels.[43,44] Sulfur also poisons NO_x traps. Not all sulfur is removed from diesel fuel in the refinery; sulfur deactivates NO_x traps when sulfates build up on the catalytic surfaces. The NO_x traps must be periodically desulfurized.

Regeneration of DPF and NO_x Trap

Periodic regeneration of the DPF and NO_x trap is required for pollution control. Both are regenerated with fuel. The regeneration process for the DPF and NO_x trap subjects them and the sensor downstream to thermal transients. Under normal operation, the NO_x trap operates at $T < 300°C$. The regeneration of the DPF causes exhaust temperature to attain $650°C$, which provides the enthalpy for removal of sulfur oxides ($deSO_x$) from the NO_x trap. This temperature would cause NO_x desorption, therefore NO_x trap regeneration is necessary prior to DPF regeneration.[45]

---

[37] Raj Rao Rajaram, Stephen Poulston, "NO_x-trap", US Patent 7287370, (filed Sep. 17, 2001).
[38] Robert Bosch GmbH, 62.
[39] Ibid., 454.
[40] Ibid., 33.
[41] Ibid., 452.
[42] Ibid., 62.
[43] Tai-Chiang Yu, Henry Shaw, "The effect of sulfur poisoning on methane oxidation over palladium supported on g-alumina catalysts", Appl Catal B Environ, 18, (1998), 105-114.
[44] Heidi Karjalainen, Ulla Lassi, Katariina Rahkamaa-Tolonen, Virpi Kroeger, Riitta L. Keiski, Thermodynamic equilibrium calculations of sulfur poisoning in Ce–O–S and La–O–S systems, Catal Today, 100, (2005), 291–295.
[45] Jens Hadler, Falko Rudolph, Richard Dorenkamp, Martina Kösters; Dieter Mannigel; Burkhard Veldten, "Der neue 2,0-l-TDI-Motor von Volkswagen für niedrigste Abgasgrenzwerte – Teil 2", Motortechnische Zeitschrift, 69, (June 2008), 536-7.

Regeneration Process	Temperature	Notes
Diesel Particle Filter	650°C	Provides enthalpy for NO_x trap desulfurization (deSO$_x$)
NO_x Trap deSO$_x$	620°C	Always follows DPF regeneration
NO_x Trap deNO$_x$	250°C - 450°C	Must be regenerated first to avoid desorption

A NO_x sensor located downstream of the NO_x trap should operate at a similar temperature as the NO_x trap (300°C), otherwise a parasitic heating load may be necessary.

Example of Diesel Exhaust Pollution Abatement System

Figure 4 shows the process flow and instrumentation layout of the 2009 Volkswagen 2.0 L TDI engine and exhaust gas cleanup system that meets US Tier 2 Bin 5 emissions requirements.
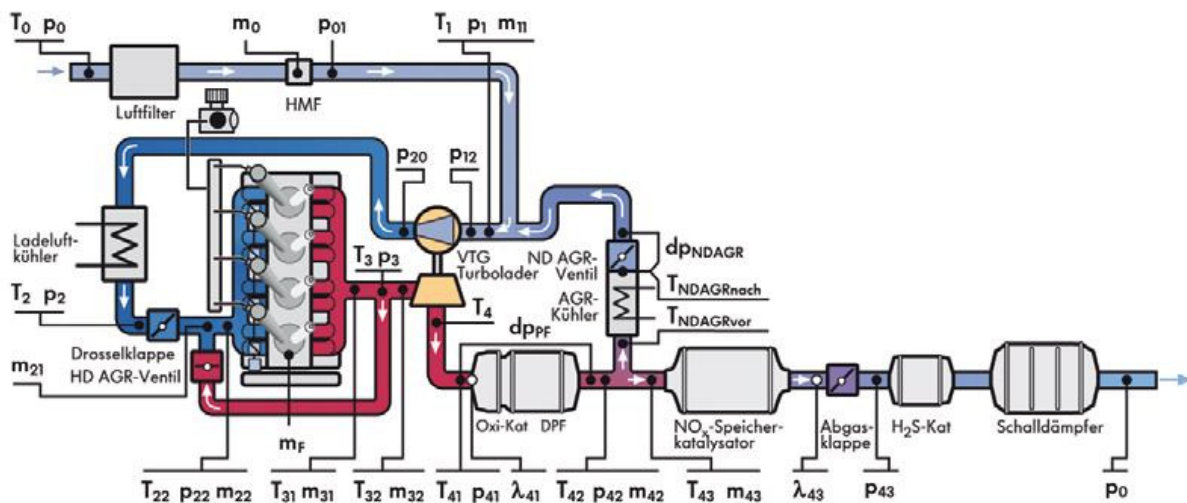
Figure 4. Volkswagen 2009 TDI instrumentation layout.[46]

This engine features two stages of EGR, individual cylinder pressure measurement, a DPF, and a NO_x trap. Instead of a NO_x sensor, an oxygen sensor (lambda "λ" sensor) in the exhaust determines the end of NO_x trap regeneration by detecting the rise of reductants from the fuel, which indicates the completion of the NO_x reduction process. Because the lambda sensor is cross sensitive and unreliable at the low temperature of NO_x regeneration (T < 450°C), software on the engine computer helps to predict the end of regeneration in parallel to the sensor. In the future, a NO_x sensor may be necessary in order to meet OBD requirements.

In summary, diesel emissions of soot and NO_x are addressed by particulate traps and NO_x cleanup systems that have become standard in all passenger diesel vehicles sold in the United States. Microprocessor-controlled fuel injection and exhaust cleanup make current diesel engines higher performing and less polluting than those of the 1970s and 1980s.

---

[46] Hadler, (May, 2008), 394.

2.4 State of the Art of Automotive Exhaust Gas Sensors

NO_x sensors are a specific type of electrochemical cell that is derived from oxygen sensor technology. An overview of the technology underpinning oxygen sensors and NO_x sensors follows.

2.4.1 Introduction to Electrochemical Cells

This section introduces electrochemical cells, including the various types of NO_x sensors. Explanations of how they operate are included, as well as a discussion of the standard electrode and electrolyte materials for exhaust gas sensors.

Batteries, electrolyzers, and gas sensors all consist of electrochemical cells. In electrochemical cells, redox reactions occur in which electron transfer takes place. The simplest electrochemical cells consist of two electrodes sandwiched around an electrolyte, as shown in Figure 5. Electrodes are the sites of chemical reactions involving electron transfer (loss or gain) with charged species (ions) that are transported by the electrolyte. The electrolyte must conduct ions well but electrons poorly. The electrodes are electrically linked externally via a wire or circuit in order to maintain charge conservation. Depending on the type of electrochemical cell, the external circuit could supply a voltage, measure current, or present a load.
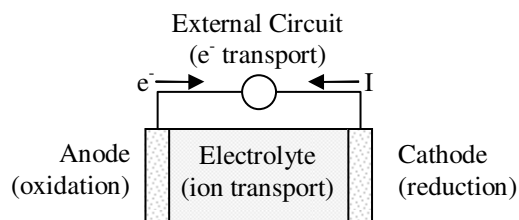
Figure 5. Components of general electrochemical cell.[47]

An anode is an electrode where an oxidation reaction (loss of electrons to circuit) occurs, whereas a cathode is where a reduction reaction (gain of electrons from circuit) takes place. The external circuit allows charge balance by electron transport to complement that the charge transport via ions in the electrolyte. External circuits can take many forms. In the case of a battery or fuel cell, one draws power from the external circuit. Alternately, by providing a voltage, one can make a sensor or an electrolyzer. By reading an open circuit voltage of the cell, one has a simple, potentiometric oxygen sensor.

Electrolyte: Zirconia Stabilized by Yttria

As noted above, an electrolyte readily conducts ions but not electrons. Electrolytes applicable for exhaust gas sensors typically consist primarily of an oxide of group IVB transition metals (e.g. ZrO_2, HfO_2, CeO_2) in a solid solution with group IIA alkaline earth metal oxide(s) (BeO, MgO, CaO, SrO, BaO) and/or with group IIIB rare earth metal oxide(s) (e.g. Sc_2O_3, Y_2O_3).[48]

---

[47] Jonathan Rheaume, "Simulation of In Situ Solid State Electrochemical Sensor for Improved Diagnostics and Control of Lean Engines", (Masters Thesis, University of California at Berkeley, 2008), 13.

[48] T. H. Etsell AND S. N. Flengas, "The Electrical Properties of Solid Oxide Electrolytes", Chem. Rev., 70, (1970), 339.

Both oxygen and NO_x sensors use a solid state electrolyte, yttria stabilized zirconia (YSZ).[11] In the 19th century, Walther Nernst discovered that doped zirconia conducts oxygen ions (O^{2-}) at high temperature as he searched for a better light bulb material.[49] This property was put to use in oxygen sensors as the electrolyte. This material has refractory properties that make it also useful for kiln furniture and for thermal barrier coatings for gas turbine blades. In both oxidizing and reducing conditions, YSZ is stable.[50] However, if not properly heat-treated, YSZ can undergo phase changes from one crystallographic state to another that causes changes in the ionic conductivity.

Imperfections in the zirconia lattice imbue YSZ with the property of oxygen ion conduction at elevated temperatures. Ionic conduction in bulk YSZ occurs at temperatures greater than 800ºC whereas for thin films conduction occurs at a lower temperatures depending on thickness of the film and composition of the electrolyte.[51] Zirconia is limited to operation below 1100°C due to partial electronic conductivity at this elevated temperature, which affects device output.[52]

Other solid oxide electrolytes have higher ionic conductivity than stabilized zirconia. Ceria-based electrolytes gadolinia doped ceria and samarium-neodymium doped ceria show an improvement in conductivity over stabilized zirconia. The bismuth oxide-based electrolytes (erbia stabilized bismuth oxide, and dysprosium-tungsten stabilized bismuth oxide) exceed the ionic conduction of zirconia by an order of magnitude or more. These electrolytes, however, degrade in environments of low oxygen partial pressure, making them unsuitable for use in exhaust gas sensors.[53] Stabilized zirconia is not the most conductive electrolytic material, but it is stable, relatively cheap and has acceptably low conductivity of electrons.

Structurally, stabilized zirconia consists overwhelmingly of zirconia (ZrO_2) –over 90 mol%– with the balance consisting of yttria (Y_2O_3). Sometimes SiO_2 is added (1%) to suppress grain boundary formation. These materials are the oxides of the metals zirconium, yttrium, and silicon. Zirconium and yttrium are in neighboring columns of the periodic chart. Their valences differ by one. Aliovalent yttrium (Y^{3+}) substitutes zirconium (Zr^{4+}) in the lattice. Since yttrium forms a different number of chemical bonds with neighboring oxygen atoms, vacancies (lattice defects) are introduced to the lattice in order to preserve electroneutrality. These vacancies are responsible for the oxygen ion (O^{2-}) transport from one vacancy to another.

Electrolytic ionic conductivity depends on temperature, composition (dopant concentration and distribution), microstructure (crystallographic phase) and density (porosity). Grain boundaries found at the interfaces of different phases exhibit vacancy depletion, retarding ion transfer. Micro cracks also increase resistance of the bulk material.[54] Porosity has a similar effect.

---

[49] Walther Nernst, "Über die Elektrolytische Leitung Fester Körper bei Sehr Hohen Temperaturen", Zeitschrift für Elektrochemie, 6, (1899), 41-43.

[50] X.J. Chen, K.A. Khor, S.H. Chan, L.G. Yu, "Influence of microstructure on the ionic conductivity of yttria-stabilized zirconia electrolyte", Mater Sci Eng, A335, (2002), 246–252.

[51] Selmar de Souza, Steven J. Visco, and Lutgard C. De Jonghe, "Reduced-Temperature Solid Oxide Fuel Cell Based on YSZ Thin-Film Electrolyte", J Electrochem Soc, 144:3, (March 1997), L35-L37.

[52] Zhuiykov, (2008), 136-7.

[53] Eric Wachsman and Subhash Singhal, "Solid Oxide Fuel Cell Commercialization, Research, and Challenges", Interface, (New Jersey: The Electrochemical Society, 18:3, Fall 2009), 41.

[54] D. Vladikova, G. Raikova, Z. Stoynov, J. A. Kilner and S. J. Skinner, "Electrical Properties in Yttria Stabilized Zirconia Investigated by Impedance Spectroscopy", Recent Progress and Future Perspectives in Infrared Microscopy and Spectroscopy with Advanced Light Sources, Triest, Italy, (Oct. 28-30, 2004), 1-3.

A high firing temperature during the sintering step increases both the density and the ionic conductivity.

Stabilized zirconia is an insulator due to its large band gap. At room temperature, its band gap is approximately 5 eV.[55] The band gap increases with decreasing grain size.[56] The band gap is also sensitive to the crystallographic phase.[57] The band gap of all phases of YSZ at room temperature is smaller than that of silicon oxide ($\approx$ 9eV)[58], the insulator material used in semiconductors. As temperature increases, though, the band gap of silicon oxide decreases such that YSZ's is larger. YSZ shows low electronic conductivity until approximately 1100°C.[52] This feature makes zirconia attractive for a high *k* dielectric material.

In addition to increasing ionic conductivity, yttria also serves to prevent crystallographic phase change of zirconia at high temperature and its accompanying change in volume. Hence yttria stabilizes the zirconia-based solid solution.

YSZ exists in three crystallographic phases: monoclinic, cubic, and tetragonal, as described below. In this treatise, YSZ refers to any combination of these polymorphs.

1) <u>Monoclinic</u> is the natural phase of pure zirconia at room temperature. This polymorph can be doped with up to 1.5 mol% Y_2O_3.[59] In a monoclinic crystal, two of the crystal axes are orthogonal, whereas the third is oblique. In this pure form, cracks form in zirconia upon heating to approximately 1200ºC on account of a microstructural phase change. The rearrangement of the lattice changes the density of the zirconia, introduces stresses, and induces crack formation.[60]

2) <u>Tetragonal</u> zirconia typically contains 2-6 mol% yttria content. It is sometimes referred to as TZP (tetragonal zirconia polycrystals).[61] It has higher oxygen ion conductivity at lower temperature than the cubic fluorite phase. Also, it shows high mechanical strength and toughness, and an ability to cope with thermal shock.[62] The stability of this phase in the presence of water vapor is a concern, though.[63]

[55] Shoji Kobayashi, Atsushi Yamasaki and Takeo Fujiwara, "Electronic Structure and Dielectric Properties of Cubic Zirconia" <u>Jpn. J. Appl. Phys.</u> 42, (Japan: Japan Society of Applied Physics, 2003), 6946.

[56] H.U. Anderson, W. Huebner, I.Kosacki, Z. Byars and B. Gorman, "Thin Film Structures and Low Temperature Electrodes for SOFC's", EPRI /GRI / DOE Fuel Cells Review Meeting, (Chicago, IL, Aug. 1999), 16, (accessed July 22, 2007), available from http://www.netl.doe.gov/publications/proceedings/99/99fuelcell/fc4-1.pdf.

[57] J. Nowotny, T. Bak, M. K. Nowotny and C. C. Sorrell, "Charge transfer at oxygen/zirconia interface at elevated temperatures Part 1: Basic properties and terms", <u>Adv. App. Cer.</u>, 104:4, (2005), 152.

[58] Philip Schneider, W. Beall Fowler, "Band Structure and Optical Properties of Silicon Dioxide", <u>Phys Rev Lett</u>, 36:8, (New York: American Physical Society, Feb. 23, 1976), 426.

[59] Nowotny, 148.

[60] Stanford Materials, "Applications and Preparations of Zirconia and Stabilized Zirconia Powders", (accessed Nov. 12, 2009), available from http://www.stanfordmaterials.com/zr.html.

[61] Evgenij Barsoukov, J. Ross Macdonald (eds.), <u>Impedance Spectroscopy: Theory, Experiment, and Applications</u>, 2nd edn., (John Wiley & Sons, Inc., New Jersey, 2005), 239.

[62] Masato Nakao, Harunobu Sato, Kiichi Kamimura, Yoshiharu Onuma, "Preparation and Property of Tetragonal Zirconia Thin Films for Oxygen Sensor", <u>Proceedings of the IEEE/CPMT International Electronics Manufacturing Technology (IEMT) Symposium 1995</u>, (Japan: IEMT Symposium, 1995), 162.

[63] William C. Maskell, "Progress in the development of zirconia gas sensors", <u>Sol. Stat. Ion.</u>, 134, (Amsterdam: Elsevier Science B.V., 2000), 43–50.

3) <u>Cubic fluorite</u> zirconia is the name given to fully stabilized zirconia with greater than 6-10 mol% yttria. Cubic zirconia does not change phase upon heating (hence it is called "stabilized"). Figure 6 illustrates the lattice structure including the defects (vacancies) responsible for ion transport. This phase is more shock resistant and ionically conductive than unstabilized (monoclinic) zirconia.[60,64]

These phases often coexist in solid state solutions. For example, partially stabilized zirconia (PSZ) is a mixture of phases that occurs at an intermediate dopant level of 6-10 mol% yttria. It consists of a cubic matrix that contains a finite dispersion of tetragonal and/or monoclinic precipitates. Under stress, the tetragonal precipitates transform to monoclinic and thereby retard crack propagation. As a result, this material is very tough. It is suitable for both electrolytic and structural applications.[61]
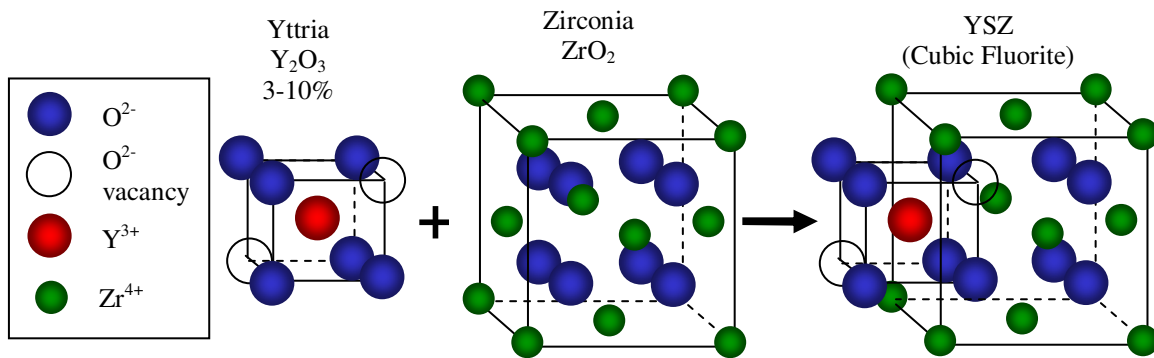
Figure 6. Crystalline structure of cubic fluorite phase of yttria stabilized zirconia.[65][66]

Some debate exists about the concentration of yttria that yields maximum ionic conductivity. Zhuiykov writes that fully stabilized zirconia's conductivity is substantially inferior to partially stabilized zirconia,[67] whereas Kharton *et al.* write that the maximum conductivity occurs for fully stabilized zirconia at the low stabilization limit, the minimum dopant concentration at which the electrolyte is fully stabilized.[68] It is possible that authors are comparing results that do not take into account the effects of thermal aging (discussed below), which shifts the peak conductivity from approximately 8 mol% to 10 mol% after exposure to high temperature (e.g. 30 days at 1000°C).[69]

Conductivity and mechanical strength must be balanced. For sensor applications, usually 4–5 mol% yttria is incorporated in the zirconia for desirable mechanical properties such as thermal shock resistance upon startup.[70]

---

[64] Zhuiykov, (2008), 136-7.
[65] Yttria Stabilized Zirconia graphic, (accessed Dec. 11, 2006), available from
    http://www.jaist.ac.jp/ms/labs/handoutai/horita-lab/YSZ/YSZ.files/image004.gif.
[66] Rheaume, 18.
[67] Zhuiykov, (2008), 137.
[68] V.V. Kharton, F.M.B. Marques and A. Atkinson, "Transport properties of solid oxide electrolyte ceramics: a brief review", <u>Sol. Stat. Ion.</u>, 174, (2004), 136.
[69] Zhuiykov, (2008), 15.
[70] Riegel, 785.

Electrolyte Aging

In solid state mixtures comprised of multiple polymorphs, protracted exposure to elevated temperature can induce a loss of ionic conductivity, resulting in signal drift. This phenomenon is known as aging. It occurs primarily due to the rearrangement of oxide ion vacancies around zirconia atoms. Aging results from the relaxation of lattice distortion.[71] During aging, the tetragonal precipitates transform to monoclinic, with a small increase in size.[72]

In addition, grain boundaries can decrease (or increase) conductivity in polycrystalline solid electrolytes over time. All three phases (m, t, and c) have different conductivities. Impedance analysis picks up these changes in microstructure.[72] The addition of Y_2O_3 can reduce the deterioration in conductivity,[73] but the amount must be carefully controlled. An optimum amount exists for desired properties beyond which conductivity decreases with the addition of Y_2O_3.[68]

In addition to the conductivity degradation of the electrolyte, aging adversely affects electrodes. Aging decreases the double layer capacity, the porosity, and catalytic activity. These factors result in a less electrochemically active surface, an increase in electrode impedance due to a reduction in the 3-phase contact regions, and an increase in the Warburg impedance (diffusion of analyte gas is hindered).[74,75]

Stability in a polyphase ceramic can be achieved by completing the phase transformations using protracted heat treatment (e.g. 20 h at 1400°C).[76]

Electrodes

In an electrochemical system, electrodes are the sites of chemical reactions at which electron exchange occur. Anodes are the site of an oxidation reaction where electrons are lost to an external circuit, whereas cathodes are where a reduction reaction in which electrons are gained from an external circuit takes place.

Sensing electrode material selection is empiric because reaction mechanisms are not well understood.[77] In the case of exhaust gas oxygen sensors, electrode materials are usually an alloy of platinum. Other noble metals such as gold and silver have been investigated, however, they cannot be cofired at high temperature and they undergo thermal aging (microstructural changes) that causes the signal to drift over time.[78] In addition, their coefficients of thermal expansion differ from YSZ. To address these issues, metal oxides are under investigation. Some metal oxides have a coefficient of thermal expansion that matches that of zirconia electrolyte (e.g. LSM: $La_{0.85}Sr_{0.15}MnO_3$).[79]

---

[71] Zhuiykov, (2008), 12.

[72] Barsoukov, 254.

[73] Zhuiykov, (2008), 137.

[74] Barsoukov, 294.

[75] Ibid., 514-5.

[76] Ibid., 255.

[77] Zhuiykov, (2008), 221.

[78] Cooper, 6.

[79] Fred van Heuveln, "Characterisation of Porous Cathodes for Application in Solid Oxide Fuel Cells", (Doctoral Dissertation, Technische Universiteit Twente, 1997), 23.

Table 3 below lists sensing electrode materials consisting of oxides used in mixed potential type NO_x sensors.[80] WO_3 shows sensitivity in the single ppm range. The last two entries have been investigated for amperometric sensors.[81] These electrode materials may be applicable for impedance-based NO_x sensors.

Oxide Sensing Electrode Material	Temperature Range (°C)	Measurement Concentration (ppm)
WO_3	450-700	5-200, 20-1000
$NiCr_2O_4$	550-650	15-500
$ZnCr_2O_4$	550-650	20-500
$ZnFe_2O_4$	550-750	20-500
ZnO	550-700	50-450
Cr_2O_3	500-600	100-800
Cr_2O_3 + oxidation catalyst	500-600	20-1000
NiO	700-900	50-400
$LaFeO_3$	450-700	20-1000
$La_{0.8}Sr_{0.2}FeO_3$	450-700	20-1000
$La_{0.85}Sr_{0.15}CrO_3/Pt$	600-700	20-1500
Tin-doped indium (ITO)	613	100-450
$La_{0.6}Sr_{0.4}Fe_{0.8}Co_{0.2}O_3$	500	100-600
$CuO + CuCr_2O_4$	518-659	10-500
$Sr_{0.6}La_{0.4}Mn_{0.8}Ni_{0.2}O_3$	500-700	500–5000
$La_{0.5}Sr_{0.5}MnO_3$ (LSM)	500-700	500–5000

Table 3. Sensing electrode materials used in NO_x sensors (consolidated).

The ceramic electrode materials LSM ($LaSrMnO_3$) and LSC ($LaSrCoO_3$) have been reported to be unstable in reducing gases.[82] LSCF ($LaSrCoFeO_3$), a mixed ionic and electronic conductor, is also unstable in rich environments.[83] A possible cause is that reducing gases consume oxygen from the ceramic lattice, causing them to undergo changes in morphology that are detrimental to the sensor life. Even when used with a lean engine, a NO_x sensor might see a rich environment during transients in engine operation.

In addition, materials containing lanthanum and strontium form insulating zirconate phases when cofired with YSZ at high temperature (typically above 1200°C). For example, in the case of LSM, two zirconates may be form: $La_2Zr_2O_7$ and $SrZrO_3$. These phases inhibit conductivity and thus degrade sensor performance. Processing conditions, precursor materials, firing

---

[80] Zhuiykov, (2008), 103.

[81] Atanu Dutta, and Tatsumi Ishihara, "Amperometric NO_x sensor based on oxygen pumping current by using LaGaO3-based solid electrolyte for monitoring exhaust gas", <u>Sensor Actuator B Chem: Chemical Proceedings of the Tenth International Meeting on Chemical Sensors</u>, (108 1-2 Japan July 22, 2005), 309-313.

[82] Meilin Liu, "Oxygen sensor and emission control system", US Patent 6440283, (filed Aug. 27, 2002).

[83] Michel Prestat, Jean-François Koenig, and Ludwig J. Gauckler, "Oxygen reduction at thin dense $La_{0.52}Sr_{0.48}Co_{0.18}Fe_{0.82}O_{3-\delta}$ electrodes Part I: Reaction model and faradaic impedance", <u>Journal of Electroceramics</u>, (Springer Netherlands, Mar. 14, 2007), 87.

temperature, and crystallographic phase are all under investigation. Escobeda *et al.* report low zirconate formation at temperatures up to 1300°C by controlling the oxidation state of manganese precursor.[84] The formation of zirconates must be suppressed up to 1500°C in order to enable mass manufacturing methods such as the cofiring of electrodes with unfired sheets of zirconia substrate.

Stress mitigation is a major challenge when combining disparate materials such as electrodes with an electrolyte of partially stabilized zirconia. Stresses arise due to coefficient of thermal expansion (CTE) mismatch during heat treatment (bakeout and co-sintering) and then again during device use.

Several approaches are available to reduce stresses generated by difference in CTEs of different materials:

- Use materials with similar CTEs
- Use zirconia in all components including the electrolyte, electrode material (cermet), and diffusion barrier in an effort to mitigate CTE mismatch
- Sandwich a material of intermediate CTE in between the electrode and electrolyte
- Etch trenches in the YSZ to contain and anchor the electrodes
- Match binder content of various device layers and cofire all layers together[85]

These measures must be addressed during the design stage in order for fabrication to be successful in creating a mechanically strong and robust device.

2.4.2 Oxygen Sensors

NO_x sensors are derived from oxygen sensor technology. This section provides a brief overview of the types of oxygen sensors commonly used for exhaust gas monitoring. Several excellent reviews of automotive oxygen sensor operation have been written by Kumar[86], Ivers-Tiffée[87], Riegel[88], Lee[89], Ramamoorthy[90], Mukundan[91], Moos[92], and Park[93]. In addition, a detailed summary of oxygen sensors can be found in the literature.[94]

---

[84] Claudia Alicia Cortés-Escobedo, Juan Muñoz-Saldaña, Ana María Boların-Miró, Félix Sánchez-de Jesús, "Determination of strontium and lanthanum zirconates in YPSZ–LSM mixtures for SOFC", J Power Sourc, 180, (2008), 209–214.

[85] Paul Nahass, Richard L. Pober, Wendell E. Rhine,William L. Robbins, and H. Kent Bowen, "Prediction and Explanation of Aging Shrinkage in Tape-Cast Ceramic Green Sheets", J Am Ceram Soc, 75:9, (1992), 2373.

[86] R.V. Kumar, "Some Innovative Technologies using Solid Electrolytes in Measuring Gas Compositions", Ionics, 3, (1997), 161-169.

[87] E. Ivers-Tiffée, K.H. Härdtl, W. Menesklou, J. Riegel, "Principles of solid state oxygen sensors for lean combustion gas control", Electrochim. Acta, 47, (2001), 807–814.

[88] Riegel, 785.

[89] Jong-Heun Lee, "Review on zirconia air-fuel ratio sensors for automotive applications", Journal of Materials Science, 38, (2003), 4247 – 4257.

[90] R. Ramamoorthy, P. K. Dutta, S. A. Akbar, "Oxygen sensors: Materials, methods, designs and applications", J. Mats. Sci., (2003), 4274.

[91] Rangachary Mukundan and Fernando Garzon, "Electrochemical Sensors for Energy and Transportation", Interface, (The Electrochemical Society, Summer 2004), 30-35.

[92] Ralf Moos, "A Brief Overview on Automotive Exhaust Gas Sensors Based on Electroceramics", Int. J. Appl. Ceram. Technology, 2:5, (2005), 401–413.

The first oxygen sensor was developed by Leland Clark *et al.* for use with blood; this type of sensor can also be used with many other liquids.[95] Oxygen sensors for automotive purposes are comprised of ceramics that operate at elevated temperature in vehicle exhaust. Automobiles use oxygen sensors in order to monitor and control the fuel to air ratio for the following purposes: improve fuel economy, reduce harmful exhaust emissions, prevent premature catalytic converter damage, and improve engine performance problems by eliminating surging and hesitating. This section provides a brief introduction to the various types of oxygen sensors.

Automotive oxygen sensors are generally classified by the type of electrical measurement performed, whether it be 1) voltage (potentiometric), 2) current (amperometric), or 3) resistance (resistive). Oxygen sensors are found in the exhaust usually upstream and downstream of the catalytic converter. They are exposed to exhaust gases of relatively constant temperature and pressure compared to in the engine. For gasoline engines, the partial pressure of oxygen (P_{O_2}) is also relatively constant with minor fluctuations about the stoichiometric value. In diesels, the fuel to air ratio varies widely. Oxygen sensors in modern vehicles come equipped with heaters that allow the sensor to attain the necessary operating temperature in seconds.

Potentiometric

The first, most popular type of oxygen sensor used in vehicle control is the potentiometric variety. This type of sensor provides a binary output that is a high or low voltage corresponding to rich or lean with a steep transition between them at the stoichiometric value. Due to the steepness of the slope of the output curve in transition region, no information is available on how rich or how lean a mixture is, making them unsuitable for use in engines that are always lean such as diesels and HCCI.

Potentiometric sensors consist of a Nernst cell: YSZ sandwiched between two electrodes. They function because YSZ conducts oxygen ions (O^{2-}) naturally from high to low P_{O_2}. Reference air outside the exhaust pipe provides high P_{O_2} air (cathode), where electron depletion results as anions are formed. The YSZ transports the charge in ionic form through the electrolyte. Inside the tailpipe where P_{O_2} is low (anode), oxygen evolves from the ions resulting in electrons being deposited. This charge difference between the surfaces exposed to differing oxygen levels is expressed as a voltage.

Amperometric

The second type of oxygen sensor, the amperometric variety, has steadily gained in popularity because the output current yields the partial pressure of oxygen in the analyte gas, allowing them to be used with both Otto and Diesel cycle engines. They output a current limited by mass transport (arrival rate of oxygen) that can be calibrated to determine the precise air to fuel ratio in both rich and lean environments. As is the case with potentiometric sensors, amperometric sensors require an external reference to ambient air. These types of sensors have more complex designs and control circuits than other types. An amperometric oxygen sensor

[93] C.O. Park, J.W. Fergus, N. Miura, Jinsu Park, Angi Choi, "Solid-state electrochemical gas sensors", Ionics, 15, (2009), 261-284.

[94] Jonathan Rheaume, "Simulation of In Situ Solid State Electrochemical Sensor for Improved Diagnostics and Control of Lean Engines", (Masters Thesis, University of California at Berkeley, 2008).

[95] L C. Clark, Jr., R. Wolf, D. Granger and Z. Taylor, "Continuous recording of blood oxygen tensions by polarography", Journal of. Applied Physiology, 6:3, (1953), 189-193.

works by applying a voltage to electrodes connected by YSZ. Oxygen ions get pumped from one electrode to another. The current that results is proportional to the arrival rate of oxygen if the sensor has been designed to be diffusion limited, the temperature is known, and the pressure is constant.[66]

Resistive

Resistive sensors are the third and final type of conventional oxygen sensor. They are made of oxygen-sensitive materials whose resistance changes in the presence of oxygen. The materials are metal oxides whose lattice releases oxygen in rich conditions, causing a valence state shift (change in conductivity). The opposite process occurs in lean conditions. Their major advantage is that they do not require an oxygen reference source. Resistive sensors have been used with both Otto and Diesel engines. A drawback exists, however: the repeated intercalation and expulsion of oxygen from the lattice changes the material's morphology over time causing signal drift and mechanically weakening the material. As a result, this type of oxygen sensor has seen the least deployment in automobiles.

Table 4 below lists the various types of conventional oxygen sensors as well as their advantages and disadvantages.

Type	Advantages	Disadvantages
Potentiometric $E=f(\Delta P_{O_2})$	-Reliable -Established	-Requires reference to ambient O_2 (penetration) -Binary operation (cannot determine exact P_{O_2}) -Use with Otto cycle engines only
Amperometric I varies with P_{O_2}	-Determines precise P_{O_2} in both lean and rich -Applicable to all engines	-Complex design and control circuit -Requires reference to ambient O_2 (penetration)
Resistive ρ varies with P_{O_2}	-Simple operation -No reference to ambient O_2 required	-Mechanically unstable after cycling -Cross-sensitive to water vapor -Signal drift over time

Table 4. Comparison of oxygen sensor types.

2.4.3 NO$_x$ Sensors

On diesel vehicles, a NO$_x$ sensor is intended to be located in the exhaust pipe downstream of the NO$_x$ mitigation unit in order to monitor its performance. The heat of exhaust gases will help the electrolyte attain activation energy for ionic conduction. In addition, the oxidation catalyst upstream should convert most hydrocarbons and carbon monoxide that may invoke a response due to cross sensitivity of the sensor.

For OBD of SCR catalyst efficiency, a NO$_x$ detection tolerance of ±10 ppm is desired[96] down to detection limit of 20 ppm.[97] The "Smart NO$_x$ Sensor" developed jointly by NGK Insulators,

---

[96] Bundesministerium fuer Verkehr, Bau, und Stadtentwicklung, "German proposal Regulation [EC] 692/2008 Annex XVI, Section 6", European Commission Motor Vehicle Emissions Group, (99th Meeting, Feb. 23, 2009), 2.

[97] Qingwen Song, George Zhu, "Model-Based, Closed-Loop Control of Urea SCR Exhaust Aftertreatment System for Diesel Engine", SAE 2002-01-0287, (March 2002).

Ltd. and Continental AG (formerly Siemens VDO Automotive Corp.) claims 10 ppm tolerance and 1 s response time.[21] The lower limit of the detection range is not clear; neither are the effects of aging on tolerance. This sensor represents the latest state of the art in automotive NO_x sensors. It consists of multiple electrochemical cells with an amperometric sensing cell, as described below.

The technology underpinning this sensor as well as an overview of the various types of NO_x sensors follows. Reviews of NO_x sensors have been written by Menil,[98] Miura,[99] and Fergus.[100] The main types of NO_x sensors are mixed potential and amperometric. Both types use a zirconia-based electrolyte, as do oxygen sensors, which make them somewhat sensitive to oxygen as well.[101] Other types of gas sensors exist such as the Taguchi sensor, a semiconducting metal oxide whose electrical properties change in the presence of analyte gases.[102] However, this type of sensor is not seen to be as promising as mixed potential sensors or amperometric sensors due to cross sensitivity to other gases.

Mixed Potential NO_x Sensors

Mixed potential sensors have a working electrode where both reduction and oxidation reactions can occur simultaneously, resulting in a non-Nerstian, mixed potential. On account of their inherently simple, single cell design, mixed potential NO_x sensors are a rich source of inquiry.[103,104,105,106,107,108] Typically these sensors consist of an electrolyte in contact with two electrodes of different composition. Their design is similar to potentiometric oxygen sensors (Nernst cell). In mixed potential sensors, the working electrode is exposed to exhaust gases, whereas the reference electrode may be exposed to the working gas or to atmospheric air. A potential difference results from asymmetric electrodes due to their dissimilar catalytic activities,

[98] Francis Menil, Veronique Coillard, Claude Lucat, "Critical review of nitrogen monoxide sensors for exhaust gases of lean burn engines", Sensor Actuator B Chem, 67, (2000), 1–23.

[99] N. Miura, M. Nakatou, S. Zhuiykov, "Development of NO_x sensing devices based on YSZ and oxide electrode aiming for monitoring car exhausts", Ceramics International, 30, (2004), 1135–1139.

[100] Jeffrey W. Fergus, "Materials for high temperature electrochemical NO_x gas sensors", Sensor Actuator B Chem, 121, (2007), 652–663.

[101] N. Docquier, S. Candel, "Combustion control and sensors: a review", Progress in Energy and Combustion Science, 28:2, (2002), 132.

[102] N. Taguchi, "Gas-Detecting Device", U.S. Patent 3,631,436, (1971).

[103] Jinsu Park, B.Y. Yoon, C.O. Park, Won-Jun Lee, C.B. Lee, "Sensing behavior and mechanism of mixed potential NO_x sensors using NiO, NiO(+YSZ) and CuO oxide electrodes", Sensor Actuator B Chem, 135, (2009), 516.

[104] Norio Miura, Geyu Lu, Noboru Yamazoe, "High-temperature potentiometric / amperometric NO_x sensors combining stabilized zirconia with mixed-metal oxide electrode", Sensor Actuator B Chem, 52, (1998), 169–178.

[105] N. Miura, Y. Yan, G. Lu and N. Yamazoe, "Sensing characteristics and mechanism of hydrogen sulfide sensor using stabilized zirconia and oxide electrode", Sensor Actuator B Chem, 34, (1996), 367–372.

[106] Takashi Ono, Masaharu Hasei, Akira Kunimoto, Toshiro Yamamoto, Akira Noda, "Performance of the NO_x sensor based on mixed potential for automobiles in exhaust gases", JSAE Review, 22, (2001), 49-55.

[107] Serge Zhuiykov, Takashi Nakano, Akira Kunimoto, Noboru Yamazoe, Norio Miura, "Potentiometric NO_x sensor based on stabilized zirconia and $NiCr_2O_4$ sensing electrode operating at high temperatures", Electrochem Comm, 3, (2001), 97-101.

[108] S. Käding, S. Jakobs, and U. Guth, "YSZ-Cells for Potentiometric Nitric Oxide Sensors", Ionics, 9, (2003), 151-154.

disparate gas adsorption and different electrochemical reactions.[109] Typically these types of sensors operate in the range of 500-600°C.[110]

When exhaust gases contain both oxygen and oxidizable species such as NO or HCs, then both reduction and oxidation reactions can take place at the working electrode without direct exchange of charge between the chemical species.[111] In this situation, the potential that establishes itself under open circuit conditions results from both reduction and oxidation reactions. Since these reactions tend to influence the potential in opposite ways, the result is a "mixed" potential. The potential is established by the fastest reaction.[112] At the mixed potential, the current caused by multiple electrochemical reactions is equal to zero.[113] This mixed potential is non-Nernstian because the output of the device differs from the predictions of the Nernst Equation.[114]

Electrode materials for mixed potential sensors are chosen so that sorption processes are the rate-limiting step. Detailed mechanisms are not well understood. Electrodes usually consist of semiconducting oxides such as $LaMnO_3$ or alloys of noble metals.[114,115]

These sensors are strongly cross sensitive to several species (CO, HC, O_2).[110] In addition, NO and NO_2 generate electromagnetic forces (EMF) of opposite sign, which tend to cancel each other out and reduce the signal's magnitude. To address these drawbacks, a sensing strategy has been developed for mixed potential sensors:

1. Oxidize all HC and CO by a noble metal catalyst upstream of sensing electrode.
2. Equilibrate the NO_x mixture using the noble metal catalyst.
3. Convert all NO to NO_2 electrochemically using a NO conversion electrode (Pt-Rh).
4. Detect NO_2 using an oxide sensing electrode.[116]

Additional strategies have been developed to address cross sensitivity. The selectivity for a single NO_x species can be enhanced or suppressed by polarizing the sensing electrode. This allows control of selectivity to NO vs. NO_2.[117] Operating temperature can also be adjusted to minimize cross sensitivity; if the temperature is below 600°C, then cross sensitivity to O_2 is lessened due to poor kinetics.[111]

Assuming an output signal can be obtained for a specific gas, the signal is difficult to interpret.[110] In addition, with this technology, it is difficult to detect total NO_x concentrations less than 100 ppm.[121] For these reasons, mixed potential sensors have not found widespread commercial use in automobile exhaust gas monitoring.

[109] Jiho Yoo, Suman Chatterjee, and Eric D. Wachsman, "Sensing properties and selectivities of a WO_3/YSZ/Pt potentiometric NO_x sensor", <u>Sensor Actuator B Chem: Chemical</u>, 122:2, (2007), 644.
[110] Docquier, 135.
[111] Zhuiykov, (2008) 99.
[112] <u>Ibid.</u>, (2008), 100.
[113] Mark Orazem, Bernard Tribollet, <u>Electrochemical Impedance Spectroscopy</u>, John Wiley & Sons, Inc., New Jersey, (2008), 77.
[114] Docquier, 134.
[115] Zhuiykov, (2008), 101.
[116] <u>Ibid.</u>, (2008), 101-2.
[117] Zhuiykov, (2008), 110-111.

Amperometric NO$_x$ Sensors

NO$_x$ sensors that utilize amperometric detection techniques consist of an array of two or three electrochemical cells in adjacent chambers.[118,119] The first chamber removes excess O$_2$ from the exhaust gases whereas the second cell detects NO$_x$ species (Figure 7). Diffusion through multi-chambered sensors tend to be result in slower operation, however, this type of sensor detects NO$_x$ at lower concentrations than any other commercially available.[21]

When exhaust gases flow into the first chamber, the first cell electrochemically pumps O$_2$ out of the plenum. So that it does not interfere with the NO$_x$ measurement. This cell electrochemically reduces the O$_2$ and removes it by pumping O$^=$ ions out. This occurs by applying a bias of approximately -200 mV to -400 mV.[120, 121]

A negative bias is necessary to supply the O$_2$ with electrons so that they reduce to form ions. The current is proportional to O$_2$ concentration and is diffusion-limited.

Remaining gases diffuse into an adjacent chamber, where a reduction catalyst causes the NO to decompose into N$_2$ and O$_2$. A bias of -400 mV applied to the electrode of the sensing cell causes the O$_2$ to dissociate, and then get removed by electrochemical pumping.[120] This diffusion-limited current is proportional to the amount of oxygen that arrives at the electrode from the dissociated NO$_x$.[122] An additional electrochemical cell, a Nernstian lambda gauge (potentiometric oxygen sensor), may also be present to assist the control of the NO sensing cell. A Nernstian cell requires reference atmospheric air (not shown in Figure 7.)
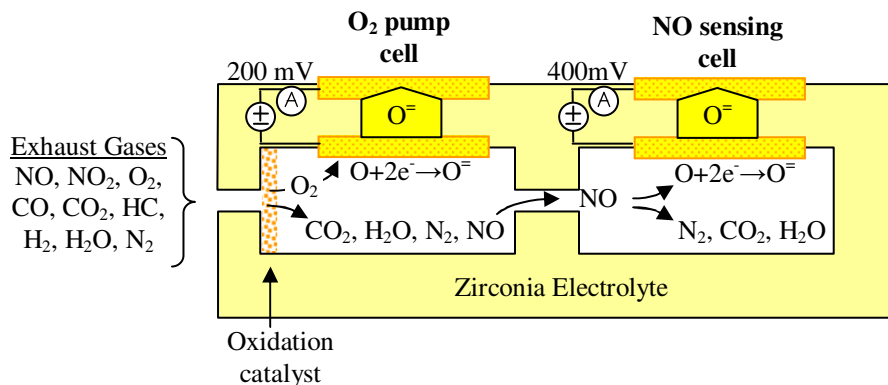
Figure 7. Amperometric NO$_x$ sensor operation.

In the case of the commercially available "Smart NO$_x$ Sensor" developed by NGK Insulators, Ltd. and Continental AG, an oxidation catalyst oxidizes any HC and CO in the sample of exhaust so that it does not affect the NO$_x$ sensing. Also, NO$_2$ is converted to NO.[21] It is desirable to convert all NO$_2$ to NO prior to the NO$_x$ sensing cell in order to obtain an accurate reading of NO$_x$

[118] Makoto Noda, Nobuhide Kato, Hiroshi Kurachi, "Electrochemical NO$_x$ sensor", U.S. Patent 4,770,760, (1988).

[119] Eleftherios Logothetis, Richard Soltis, "Method for determining relative amount of oxygen containing gas in a gas mixture", U.S. Patent 5145566, (1992).

[120] Docquier, 136.

[121] E. Magori, G. Reinhardt, M. Fleischer, R. Mayer, H. Meixner, "Thick film device for the detection of NO and oxygen in exhaust gases", Sensor Actuator B Chem, 95, (2003), 162–169.

[122] Taro Uedaa, Takayuki Naganoa, Hajime Okawaa and Seiji Takahashi, "Zirconia-based amperometric sensor using La–Sr-based perovskite-type oxide sensing electrode for detection of NO$_2$", Electrochem Comm, 11, (2009), 1654–1656.

concentration. The pumping current results from oxygen from the decomposition of NO_x. This current is dependent on the oxygen in the NO_x species, and if not converted to NO, the NO_2 would be double counted.[120] It is possible to convert NO_2 to NO by a rhodium catalyst,[118] or by raising the temperature. At high temperature, thermal equilibrium favors NO.[16]

It is possible to use multiple cell designs with other types of NO_x sensors such as mixed potential, which are also affected by the presence of O_2.[120]

Table 5 lists the main types of NO_x sensors as well as their advantages and disadvantages.

Type	Advantages	Disadvantages
Mixed Potential	- Simple design	- Cross sensitive to HC, CO, O_2 - NO and NO_2 evoke opposite responses - Difficult to interpret signal
Amperometric	- Accurate to ±10 ppm	-Complex design and control circuit - Speed -Requires reference to ambient O_2 (penetration)

Table 5. Comparison of NO_x sensor types.

The operation of conventional exhaust gas sensors has been reviewed. The next chapter covers background information necessary for comprehension of the operation of impedance-based NO_x sensors.

CHAPTER 3: Introduction to Electrochemical Impedance Spectroscopy

Electrochemical measurements generally have the goal of analyzing an interface or estimating a parameter.[123] Electrochemical impedance spectroscopy (EIS) is a tool that enables both tasks to be performed. Steady state measurements cannot notice RC time constants typical in electrochemistry.[124] By using small amplitude sine-wave perturbation, linearity in electrochemical systems can be assumed, allowing frequency analysis of a transfer function such as impedance. Analysis of impedance allows characterization of grain boundary resistance, mass transport rates and chemical reaction rates.[125]

In the latter half of the 19th century, Oliver Heaviside coined the words inductance, capacitance, and impedance, and laid a mathematical foundation for circuit analysis. Walther Nernst built upon his work and became the father of EIS by applying the Wheatstone bridge to measure the dielectric constants of aqueous electrolytes in 1894.[126] Later in 1969, James Bauerle first applied IS techniques to solid electrolytes; his consisted of YSZ.[127]

Impedance data can be represented as impedance or as admittance, which is the inverse of impedance. Admittance is used to examine high frequency behavior found in solid state systems, whereas impedance emphasizes low frequency phenomena such as mass transfer and electrode reaction kinetics.[128] Since gas sensors rely on these low frequency polarizations, in this work, impedance is used in stead of admittance.

3.1 Fundamental Concepts

This section introduces impedance, its analysis, and its representation on Nyquist and Bode plots, the traditional representations of impedance data.[129]

3.1.1 Impedance (Z), Phase Angle (Θ), and Modulus (|Z|)

Impedance is simply the ratio of small signal voltage to current. Impedance can have both complex and real components. One obtains the impedance of a system in the following fashion:

- apply a small signal alternating voltage $v(t) = V\sin(\omega t)$
- measure the current response $i(t) = I\sin(\omega t + \Theta)$, and
- calculate the impedance $Z(\omega) = v(t) / i(t)$.

Impedance is a frequency-dependent transfer function consisting of the ratio of potential over current.[130] The phase angle, Θ, quantifies lag or lead of $i(t)$ with respect to $v(t)$. Figure 8 illustrates these fundamental concepts.

---

[123] Orazem, 265.

[124] Ibid., 109.

[125] Ibid., 265.

[126] Ibid., xxv.

[127] James Bauerle, "Study of solid electrolyte polarization by a complex admittance method", J Phys Chem Solid, 30, 1969, 2657-2670.

[128] Orazem, 309.

[129] Ibid., xxix.

[130] Ibid., 109.

Impedance consists of real and imaginary components represented by Z_{real} and Z_{imag}, respectively, in the following expression for impedance: $Z(\omega) = Z_{real} + jZ_{imag}$. In this work, the electrical engineering convention is used for complex numbers. In specific, $j = \sqrt{-1}$ in order to avoid confusion with current, i(t).[131]
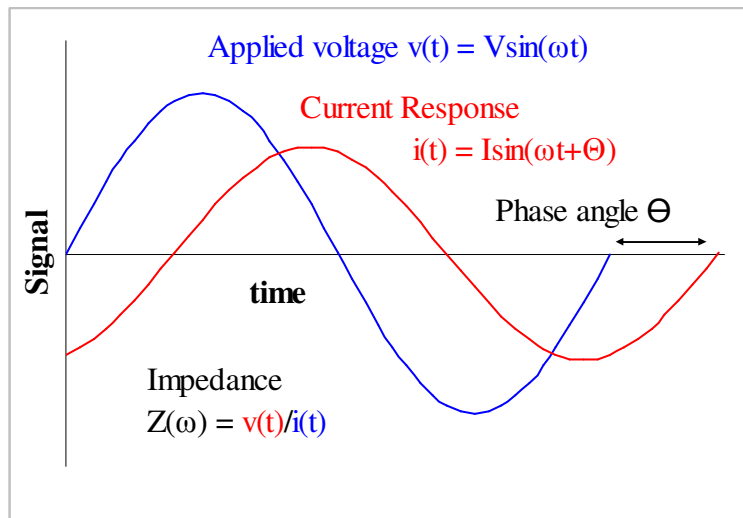
Figure 8. Impedance - fundamental concepts.

Impedance can be used to detect gases; some gases participate in redox reactions whose electron exchange alters complex resistance (impedance).

On the complex plane, impedance can be represented at each frequency by a vector whose magnitude, the modulus, is the length of the vector as defined by the Pythagoras relation: $|Z| = [(Z_{Real})^2 + (Z_{imag})^2]^{1/2}$.[132] The angle that the vector makes with the abscissa is the phase angle, Θ. This quantity also represents the lag or lead of the response current at a specific frequency, as defined above. By trigonometry, the phase angle is defined on the complex plane as follows: $\Theta = \tan^{-1}(Z_{imag} / Z_{Real})$. The phase angle is very sensitive to system parameters, whereas the modulus is much less sensitive to system parameters.[133] For this reason, the phase angle is used in this work to measure sensitivity.

When the input voltage and output current are in phase, the phase angle is zero, and there is no imaginary component of impedance.[134] In this case, the impedance consists of resistance only; it aligns with the real axis.

3.1.2 EIS Method

Electrochemical impedance spectroscopy involves examining the measured impedance at several frequencies. EIS is performed as follows:

- Apply alternating bias v(t) to system.
- Sweep frequency (approximate range 1 MHz to 1Hz, 10 pts/decade).

[131] Ibid., 5.
[132] Barsoukov, 478.
[133] Orazem, 315-6.
[134] Ibid., 67.

- Measure current i(t) at each frequency.
- Calculate impedance at each frequency.
- Evaluate the impedance data.

The evaluation of the impedance data depends on the ultimate objective. Equivalent circuit analysis helps with the understanding of physicochemical processes of the sensor. It is also possible to extract NO_x concentration from impedance data by calculating either the modulus or the phase angle difference at a specific frequency upon the introduction of NO_x. Over a specified range in concentration, the change in modulus ($\Delta|Z| = Z_2 - Z_1$) is directly proportional to NO_x concentration (e.g. 50-400 ppm).[135] The same is true for the change in phase angle $|\Delta\theta| = |\theta_2 - \theta_1|$ (e.g. 8-50 ppm).[136]

3.1.3 Nyquist Plot

A Nyquist plot presents impedance data on the complex impedance plane. For this reason, it is sometimes called a Complex Impedance Plane plot. Another name is a Cole-Cole plot.

On a Nyquist plot, it is customary to plot impedance as $-Z_{imag}$ vs. Z_{real} (with the ordinate values mirrored about the abscissa) because IS rarely involves inductance and usually involves capacitance.[137] A Nyquist plot presents data as a locus of points, where each point represents a different measurement at a particular frequency. Frequency is not explicitly shown on a Nyquist plot, but it is shown in a Bode plot. A Nyquist plot appears in Figure 9.
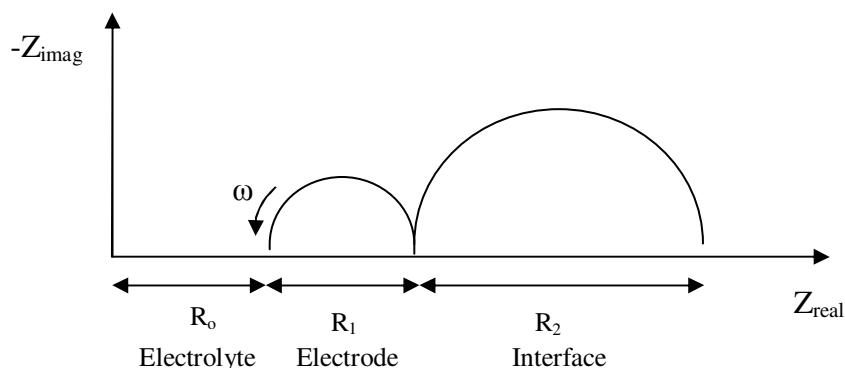
Figure 9. Nyquist plot of a typical impedance spectrum from a zirconia system.

The number of arcs is related to the number of relaxation processes, where a relaxation is a frequency-dependent response to an input such as a sinusoidal voltage signal. Most crystalline solid electrolytes exhibit a three arc response that corresponds to various physical processes.[138] Zirconia-based systems usually exhibit two or three arcs.[139] Sometimes the third arc is too small to be readily visible. Alternately, the appearance of arcs is sometimes temperature dependent;

---

[135] Miura, (2002), 284-287.
[136] Martin, J Electrochem Soc, (2007), J97-J104.
[137] Barsoukov, 15.
[138] Ibid., 246.
[139] Ibid., 293.

additional arcs may appear as the temperature decreases.[140] It is also possible for arcs to overlap, making it difficult to recognize the number of relaxation processes.

The shape of the impedance spectrum yields information about the system. For example, in Figure 9, a typical impedance spectrum from a zirconia-based system displays displaced arcs along the real axis. The arcs are displaced an amount equal to the bulk electrolyte resistance, which is typically visible at high frequency. The two arcs represent physicochemical phenomena. Common interpretations of the arcs follow: the first arc represents interfacial processes such as charge transfer at grain boundaries or at the triple phase boundary, whereas the second arc (at low frequencies) represents electrode processes such as diffusion or electrochemical reactions. The diameter of an arc represents the resistance involved with the process.

The low frequency arc may exhibit distortion depending on electrode material and preparation. At T=500°, the resistance of the low frequency arc is determined by the resistance of the oxygen reduction reaction: $\frac{1}{2}O_{2(gas)}+2e^-_{(electrode)} \rightarrow O^=_{(electrolyte)}$.[141]

As frequency approaches infinity, the electrolytic resistance represents the asymptotic limit of the real component of impedance. As frequency approaches 0 Hz (DC), the impedance approaches a real value that represents the sum of the resistances associated with physiochemical phenomena.[142]

3.1.4 Bode Plots

Bode plots show impedance-related data explicitly as a function of frequency, as seen in Figure 10. An advantage of the Bode representation over the Nyquist format is that frequency is seen more clearly.[143] The Bode representation consists of two semilog plots that show modulus, |Z|, or phase angle, Θ, versus the logarithm of frequency, log(f). This data was recorded with a zirconia-based sensor with gold wire electrodes operating at 650°C exposed to various concentrations of O_2 with balance N_2.

On Bode plots, frequency is plotted logarithmically in order to facilitate examination the responses over a wide range of frequencies, including at low frequencies. Figure 10 indicates that for gas analysis, the low frequency range is where the effects changing gas composition are visible.[144]

Bode plots are useful for identifying the frequency range in which a sensor detects gases. For example, Figure 10 shows that the phase angle and modulus vary with O_2 concentration at low frequencies. Bode plots are also helpful when comparing actual impedance data to modeling results.

---

[140] Barsoukov, 261-2.
[141] Ibid., 292-3.
[142] Orazem, 312.
[143] Ibid., 315-6.
[144] Ibid., 314.
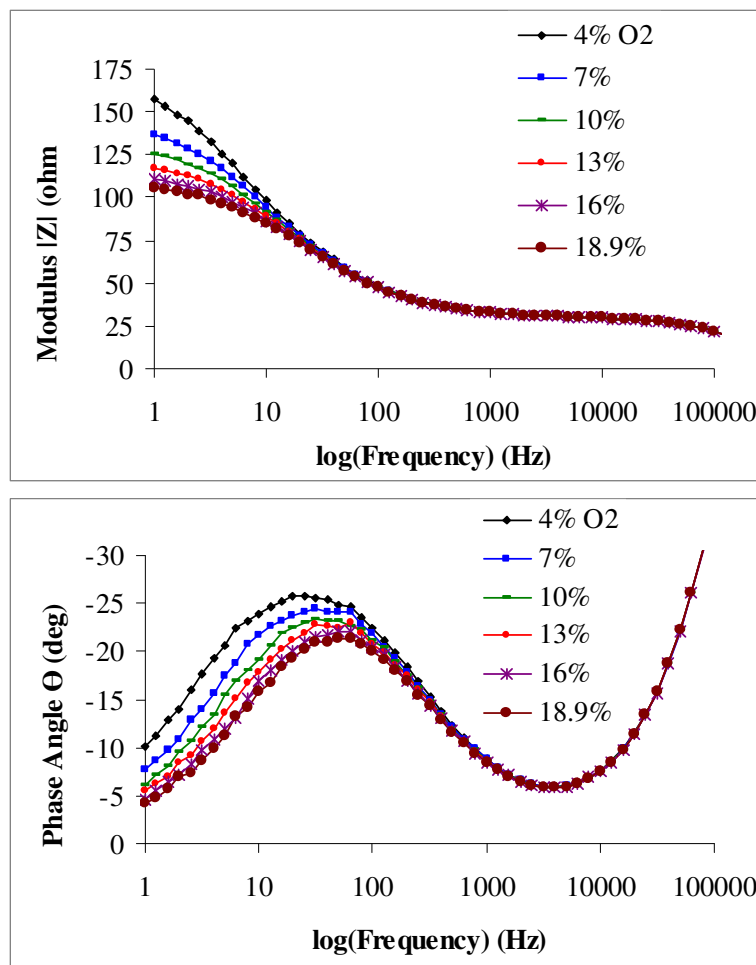
Figure 10. Bode plots for varying O$_2$ concentration.

3.1.4 Impedance Spectrum Analysis

A Nyquist plot of impedance data recorded from a sensor with YSZ electrolyte and gold working electrodes exposed to 10% O$_2$ at 650°C appears in Figure 11 below. The dominant features include two arcs labeled "high frequency" and "low frequency". Six decades of frequencies are indicated. The modulus and phase angle at 10Hz appear on the plot.

The two arcs are offset from the imaginary axis. This offset commonly represents resistance of the electrolyte. The arcs indicate that multiple processes with different time constants occur.[145] The high frequency arc results from processes in the electrolyte or electrode bulk (conductivity), whereas the low frequency arc result from processes at the electrode-electrolyte interface (double layer, charge transfer) or at electrode surface (mass transport, sorption, electrochemical reactions).

The shape of the arcs reveals information about sensor processes. In Figure 11, the high frequency arc forms a nearly perfect semicircle. This indicates that the impedance results from a

---

[145] Ibid., 313.

30

single activation energy controlled relaxation process such as ion transport.[141][146] The width of an arc indicates the resistance associated with a physicochemical process.
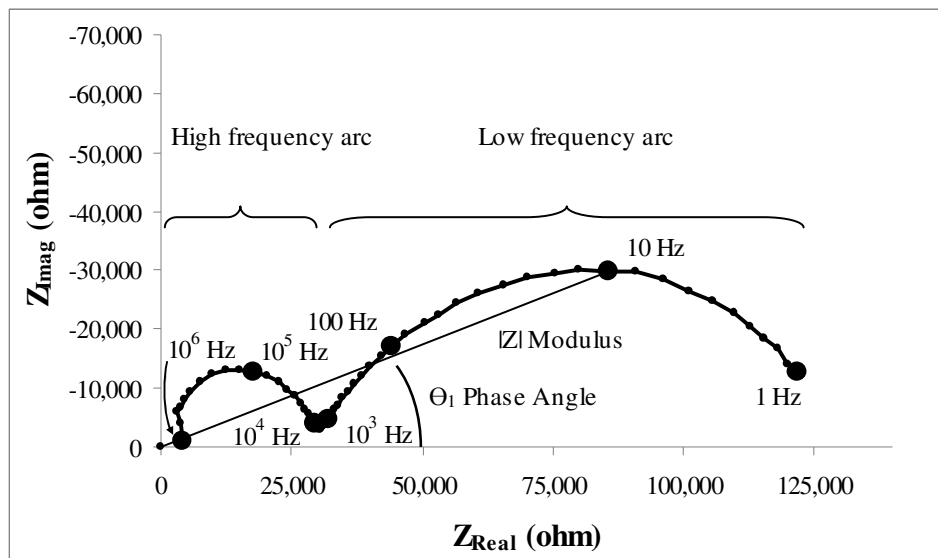
Figure 11. Impedance spectrum for zirconia-based sensor.

An oblong arc may obscure two overlapping arcs, as shown in Figure 12. On a Nyquist plot, overlapping arcs result from physical processes with similar characteristic time constants. The overlap can make it difficult to resolve relaxations.[147] Polishing the electrolyte before applying the electrodes can improve the resolution.[148]
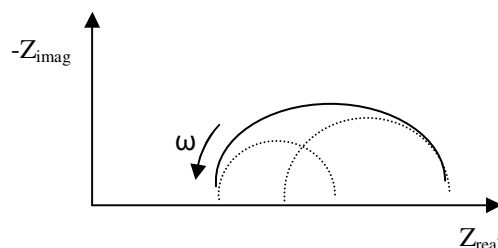
Figure 12. Overlapping arcs may appear as one arc on a Nyquist plot.

3.2 Equivalent Circuit Analysis

The impedance response from an electrochemical system can be modeled by equivalent electrical circuits. Models generally attempt to predict or explain an impedance response; they are either forward looking or retrospective. Process models predict the response of a system,

---

[146] Ibid., 313.
[147] Barsoukov, 263.
[148] Ibid., 234.

whereas measurement models serve to mimic impedance data and to explain processes.[149] This work focuses on measurement models.

Equivalent circuit analysis consists of identifying a circuit whose output matches experimental data using regression analysis, and correlating physical properties of the system to individual circuit elements. One disadvantage of EIS is the ambiguity in interpretation. Multiple circuit arrangements with an equal number of time constants can yield an identical impedance response over a range of frequencies.[150] An equivalent circuit with 3 or more circuit elements can be rearranged to yield the same exact impedance response.[151] As a result, additional observations are required for validation of a model.[152] High resolution transmission electron microscopy (TEM) is a valuable complement to EIS techniques. It allows physical confirmation of equivalent circuits.[153]

3.2.1 Circuit Elements

This section introduces the components that comprise equivalent circuits. When properly arranged, these circuit elements mimic the impedance response of a solid state gas sensor. The common circuit elements are introduced first, followed by the non ideal ones and combinations of elements.

Ideal Circuit Elements (R, C, L)

Behavior of the electrolyte, electrodes, interfaces, and gas diffusion, can be modeled using ideal circuit elements such as resistors (R), inductors (L), and capacitors (C). Equivalent circuit elements usually represent ideal lumped capacity properties.[154] Some exceptions exist such as constant phase elements (Q) and Warburg diffusion elements (W), as discussed in the next section.
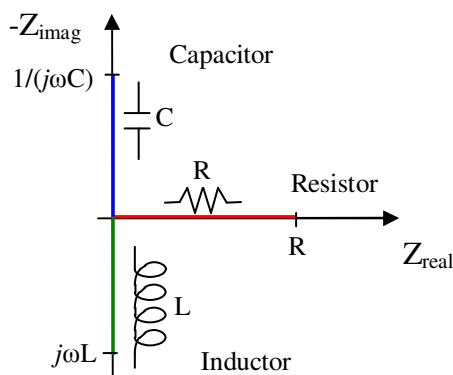
Figure 13. Ideal circuit elements on a Nyquist plot.

[149] Pankaj Agarwal, Mark E. Orazem, Luis H. Garcia-Rubio, "Measurement Models for Electrochemical Impedance Spectroscopy I. Demonstration of Applicability", J Electrochem Soc, 139:7, (1992), 1918.
[150] Orazem, 69.
[151] Barsoukov, 11.
[152] Orazem, 70.
[153] Barsoukov, 243.
[154] Ibid., 11.
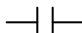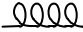
On a Nyquist plot, resistors, capacitors, and inductors have an impedance response that coordinate with the axes, as shown in Figure 13. By definition, a resistor is a device in which voltage and current are in phase, meaning the phase angle is zero ($\Theta = 0°$). Since the impedance of a resistor lies along the real axis, resistance can be read directly from this axis. For a capacitor, voltage lags current by 90° ($\Theta = -90°$); a pure capacitor results in impedance along the negative imaginary axis (which is upward on a Nyquist plot). Conversely, for an inductor, voltage leads current by 90° (phase angle $\Theta = +90°$). An inductance results in impedance along the imaginary axis in the positive direction. Since the impedance due to both capacitance and inductance result as a product of an imaginary number, neither can be directly read from the Nyquist plot.

Table 6 summarizes common ideal circuit elements used in equivalent circuit analysis, provides their impedance, and comments on their physical representation.

Symbol	Element	Icon	Impedance (Z)	Physical Significance
R	Resistor	—⋀⋀—	$Z = R + 0j$	Resistance of electrolyte, charge transfer, and reactions
C	Capacitor	—⊣⊢—	$Z = 0 + 1/(j\omega C)$	Double layer of charge
L	Inductor	⎯⎯⎯	$Z = 0 + j\omega L$	Stray inductance from leads

Table 6. Common equivalent circuit elements.

Resistance arises from several sources: ion transport in bulk electrolyte,[155] charge transfer across grain boundaries, and reactions at electrodes. Capacitance represents a double layer at an interface (such as an electrode in contact with electrolyte),[156] or the surface capacitance of a film.[157] Inductors are rarely seen in electrochemical sensors.[158] When an inductance exists, it is often attributed to the leads and cables used to interrogate the electrochemical cell.[159]

The familiar lumped property elements resistors, capacitors, and inductors all show behavior that ideally is independent of frequency.[160] In practice, however, the behavior of circuit elements is ideal only in a finite frequency range. Outside of this range, the impedance response strays from ideal, which necessitates the introduction of "distributed", or non-ideal, circuit elements.[161]

Constant Phase Element (Q)

A constant phase element (CPE) is a generalized circuit element that can be made to represent resistors, capacitors, inductors, and everything in between. CPEs are useful with the modeling of equivalent circuits. A CPE shows a constant phase angle (constant lag or lead between input voltage and response current) over a range of frequency. Resistors, capacitors, and inductors are all specific types of constant phase elements.[162] On a complex impedance plane, the impedance output from resistors, capacitors, and inductors align with axes ideally; a CPE is a

[155] Orazem, 86.
[156] Bauerle, 2657.
[157] Orazem, 312.
[158] Barsoukov, 15.
[159] J. L. Hertz, A. Rothschild and H. L. Tuller, "Highly Enhanced Electrochemical Performance of Silicon-Free Platinum – Yttria Stabilized Zirconia Interfaces", J. Electroceramics, 22, (2009), 428-435.
[160] A. J. Bard, L. R. Faulkner, Electrochemical Methods Fundamentals and Applications, (John Wiley & Sons, Inc., New York, 1980), 323.
[161] Barsoukov, 83.
[162] Orazem, 68.

mathematical tool that can be made to represent these same loci of points in addition to representing all similarly shaped loci of points in between (i.e. loci that do not align with axes).

A CPE-like response appears in most data involving electrolytes over a finite frequency.[163] Physical interpretation of CPEs, however, can be elusive.[164] One interpretation of a CPE is a non-ideal capacitor, which is apparent by examining the formula for impedance of a CPE: $Z = 1/[(j\omega)^{\varphi}Q]$, where Q is a CPE parameter. When the phase angle exponent takes on a value $0<\varphi<1$, then Q is related to double layer capacitance.[165] When $\varphi = 1$, a CPE is a capacitor; its impedance is identical to that of a capacitor: $Z = 1/(j\omega C)$. Neither the phase angle, Θ, nor the phase angle exponent (φ), nor the CPE coefficient (T) depend on frequency.[166]

On a Nyquist plot, a single CPE has an impedance response of a straight line that makes an angle equal to $\varphi*(-90)°$ with the abscissa, where φ is the phase angle exponent.[167] (The angle that the CPE forms with the real axis is negative due to the inversion of the imaginary axis.) When $\varphi = 1$, the phase angle is -90° and the CPE overlaps the ordinate, which is exactly the same as a capacitor.
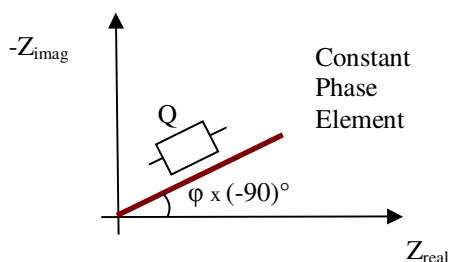
Figure 14. Constant phase element on a Nyquist plot.

A similar argument can be made for a CPE representing a non-ideal inductor when $-1<\varphi<0$. When $\varphi = -1$, the CPE is an inductor: $Z = 1/[(j\omega)^{-1}T] = j\omega/T$, so $L = 1/T$. In this case, on a Nyquist plot the CPE aligns with the Z_{imag} axis like a pure inductor. The same is true for a resistor, for which $\varphi = 0$. For the case of a resistor, $Z = 1/T = R$ (real component only).[168] Although mathematically the CPE could represent a range of types of non-ideal circuit elements, in the case of electrochemical sensors, a CPE usually approximates a capacitor on account of the geometry of sensors.

The cause of non-ideal capacitive behavior is time-constant dispersion resulting from distributed physical properties. For example, a distribution of relaxation times can be caused by inhomogeneities in an electrode-material system or by nonuniform diffusion.[169] Electrode surfaces are generally not uniform. Surface heterogeneities in the form of grain boundaries, crystal faces, and surface roughness cause the reactivity and electrical properties to vary, resulting in not a single time constant, but rather a distribution of time constants.[170] This

---

[163] Barsoukov, 87.

[164] Ibid., 13.

[165] Ibid., 495.

[166] Orazem, 234.

[167] Robert Rodgers, "The Constant Phase Element (CPE)", (accessed Oct. 30, 2009), available from http://www.consultrsr.com/resources/eis/cpe1.htm

[168] Orazem, 236.

[169] Barsoukov, 87.

[170] Orazem, 233-4.

behavior can also arise from non-uniform mass transfer, non-uniform current distributions, and electrode porosity.[171] Varying oxide composition results in heterogeneous properties that can cause time-constant dispersion.[172]

On circuit diagrams, a CPE typically has the symbol "Q". In equivalent circuit modeling, CPEs are often used in conjunction with a resistor as a part of a Cole-Cole circuit element, as explained below.

Warburg Element (W)

The Warburg impedance (W) represents "diffusion resistance" at low frequencies.[173] The infinite length Warburg impedance was the first distributed element introduced in electrochemistry. The impedance is obtained from the solution of Fick's second law of diffusion, however, real physical situations involve finite diffusion lengths. A more general solution was therefore obtained, with the infinite solution being a specific case.[174] The general Warburg impedance equals: $Z = \sigma/\omega^{1/2} - j\sigma/\omega^{1/2}$, where σ is the Warburg parameter. It depends on several factors including diffusivity, concentration, and temperature. The Warburg impedance is a CPE for which $\varphi = 0.5$, resulting in a phase angle of -45°. As a result, the real and imaginary components of impedance are equivalent at all frequencies.
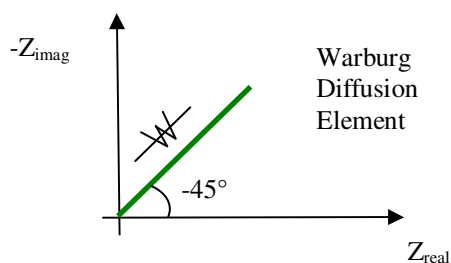
Figure 15. Warburg element on a Nyquist plot.

On a Nyquist plot, a Warburg element makes a line at a 45° angle with respect to either axis. At high frequency, the Warburg impedance tends to zero because frequency appears in the denominator of both the real and imaginary terms.[175] When combined with other circuit elements, a Warburg impedance may result in depressing the center point of an arc below the real axis.[176] A similar result may happen with all CPEs, as discussed in the following sections.

Gerischer Element (G)

A Gerischer element (G) describes impedance of a species that participates in a chemical reaction in the bulk and undergoes diffusion. It is observed in solid electrolytes with mixed conduction (ionic and electronic).[177] Its impedance response on a Nyquist plot appears as a skewed arc. The Gerischer impedance is given by $Z = Z_0/(k + j\omega)^{1/2}$ where Z_0 is an impedance

---

[171] Ibid., 236.
[172] Ibid., 260.
[173] Barsoukov, 528.
[174] Ibid., 84.
[175] Bard, 328-9.
[176] Barsoukov, 292-3.
[177] B.A. Boukamp and H.J.M. Bouwmeester, "Interpretation of the Gerischer impedance in solid state ionics", Sol. Stat. Ion., 157, (2003), 29-33.

parameter and k is the rate of the chemical reaction. This equation is derived from Fick's Second Law by including a reaction term.[178] The Gerischer impedance is a special circumstance of the fractal Gerischer element in which the exponent in the denominator can take on a range of values due to non ideal behavior of real systems.
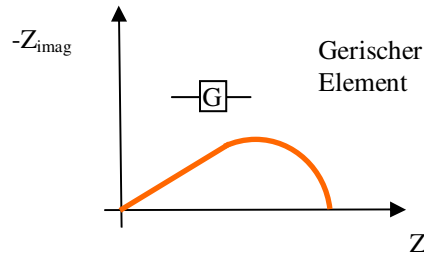
Figure 16. Gerischer element on a Nyquist plot.

Voigt Element (RC)

A Voigt element consists of a resistor (R) and a capacitor (C) in parallel.[179] This combination of circuit elements can be used to model an interface such as grain boundaries within electrolyte or YSZ-electrode contact. The R represents charge transfer resistance across the interface in the simple case of a single reaction on a uniform electrode.[180] The C represents the capacitance of a double layer of charges.
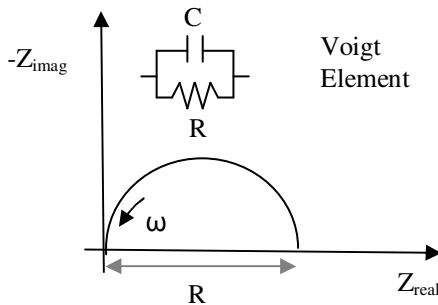
Figure 17. A Voigt element (RC) forms a semicircle on a Nyquist plot.

On a Nyquist plot, a Voigt element appears as a semicircular arc, as shown in Figure 17. The diameter of arc is characterized by R, whereas the height of the arc is determined by C. The value for R can be read directly from the Nyquist plot. The impedance of the arc is calculated according to standard procedure for parallel circuit elements: by adding the inverses of the individual elements and taking the inverse of the sum of elements. The impedance of a Voigt element is a function of frequency, capacitance, and resistance: $Z = (j\omega C + 1/R)^{-1}$. The phase angle takes on a value between that of the RC elements $-90° < \Theta < 0°$). The characteristic time constant, τ, equals the product of the resistance and capacitance: $\tau = R \times C$. It appears to occur at the maximum point of the arc on the Nyquist plot. (In reality, τ occurs at the minimum point, the

---

[178] B.A. Boukamp, "Electrochemical impedance spectroscopy in solid state ionics: recent advances", <u>Sol. Stat. Ion.</u>, 169, (2004), 65-73.
[179] Agarwal, 1918.
[180] Orazem, 155.

most negative, because on a Nyquist plot, the complex axis is reversed.) The characteristic time-constant corresponds to the frequency according to the following relations: $\tau = 1/\omega = 1/(2\Pi f)$.[181]

For single crystal YSZ, no grain boundaries exist, so no arc associated with this interface is visible. Similarly, when the highly conductive t-phase is dispersed along the grain boundary, it short-circuits the grain boundary impedance, and no arc for grain boundaries is visible on a Nyquist plot.[182]

Voigt elements can also be used to model inductive loops by assigning negative values to resistance and capacitance in an element.[183] Both must be negative for the time constant to be positive.

Cole-Cole Circuit Element (RQ)

A Cole-Cole element consists of a resistor (R) in parallel with a CPE (Q). Sometimes it is referred to as simply a Cole element, whereas Barsoukov and Macdonald refer to this element as a "ZARC".[184] This circuit combination results in a depressed arc on a Nyquist plot, as shown in Figure 18.[185] The CPE adjusts the center point of the arc relative to real axis. The width of the depressed arc is still R, however, for a Cole element R does not align with the Z_{real} axis.

A Cole-Cole element can be used to model grain boundaries that display a distribution of time constants.[186] It could also represent interfacial or electrode surface processes such as sorption or an electrochemical reaction.
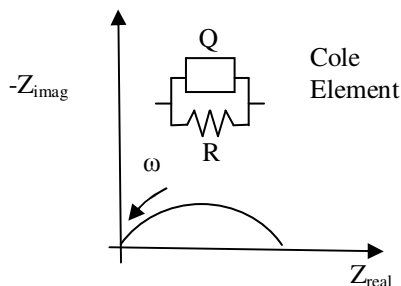
Figure 18. A Cole element (RQ) forms a depressed semicircle on a Nyquist plot.

Table 7 summarizes distributed some of the circuit elements used in equivalent circuit analysis, shows their physical representation, and provides their impedance. Although CPEs can behave as myriad circuit elements, in the context of circuit modeling of sensors, they usually represent distributed double layer capacitance. The most time-sensitive impedance elements are double layer capacitance, Warburg (diffusion) impedance, and charge transfer resistance.[187]

---

[181] <u>Ibid.</u>, 70.
[182] Barsoukov, 246.
[183] Orazem, 421.
[184] Barsoukov, 89.
[185] <u>Ibid.</u>, 89.
[186] <u>Ibid.</u>, 72.
[187] <u>Ibid.</u>, 514-5.
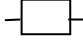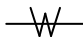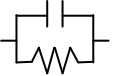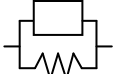
Symbol	Element	Icon	Impedance (Z)	Physical Processes
Q	Constant Phase		$Z = 1/[(j\omega)^{\varphi}Q]$, $-1 < \varphi < 1$	Capacitance $\varphi = 1$ Resistance $\varphi = 0$ Inductance $\varphi = -1$
W	Warburg		$Z = \sigma/\omega^{1/2} - j\sigma/\omega^{1/2}$	Semi infinite linear diffusion (to electrode)
G	Gerischer	G	$Z = Z_0/(k + j\omega)^{1/2}$	Reaction and diffusion in mixed conductor
(RC)	Voigt		$Z = (j\omega C + 1/R)^{-1}$	Interfacial charge transfer
(RQ)	Cole		$Z = [(j\omega)^{\varphi}Q + 1/R]^{-1}$, $0 < \varphi < 1$	Electrode reactions, grain boundary charge transfer

Table 7. Summary of distributed circuit elements.

3.2.2 Equivalent Circuits

Circuit elements can be combined into circuits that mimic the impedance response of an electrochemical system. The layout of the circuit yields information about the sequence of processes. Series connections represent sequential steps, whereas elements in parallel indicate simultaneous processes.[188]

As mentioned previously, several different combinations of circuit elements can achieve the same impedance response, so some insight into the physical system is necessary in order to appropriately model the system.

A very versatile, convenient, and generalized measurement equivalent circuit model is the Voigt circuit (shown in Figure 19). Agarwal *et al.* used Voigt circuits to model five different processes including hydrogen evolution, corrosion of carbon steel in salt water, corrosion of iron sulfuric acid, corrosion of a model pit electrode in salt water, and, corrosion of a painted metal.[189] It consists of a resistor in series with a variable number of Voigt elements: $R_0 + (R_1C_1) + ... + (R_nC_n)$. In many electrochemical systems, R_0 represents electrolyte resistance; C_1 corresponds to double layer capacitance; and R_1 indicates charge transfer or polarization resistance.
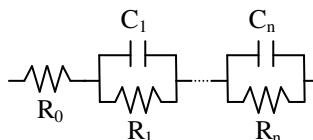
Figure 19. Voigt equivalent circuit.

A Nyquist plot with *n* arcs can be represented by a Voigt equivalent circuit with *n* Voigt elements. According to Miura *et al.*, the resistor R_0 represents the resistance of the electrolyte.

---

[188] Ibid., 512.
[189] Agarwal, 1919.

The Voigt elements (RC) represent the electrode bulk (R_1C_1) and the interface of the electrolyte and electrode (R_2C_2).[190]

In Figure 20, a typical Nyquist plot for an impedance-based sensor is shown with its corresponding Voigt equivalent circuit. Each element represents a physical or chemical process. The 2 arcs are represented by 2 Voigt elements with a unique time constant.
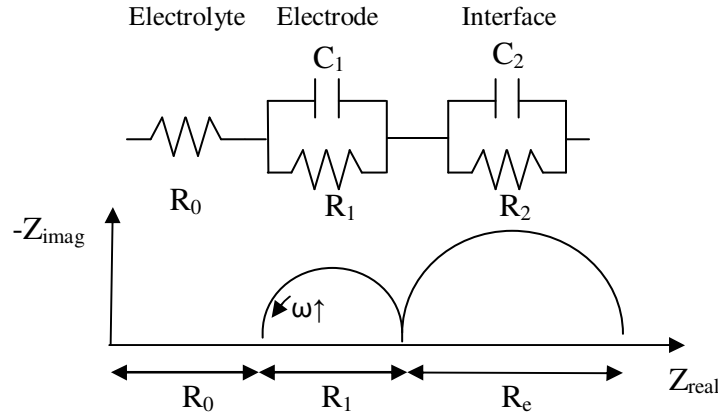
Figure 20. Nyquist plot and corresponding Voigt equivalent circuit (n=2).

The impedance of a Voigt circuit is given by the following:[191] $Z = R_o + \sum_{k=1}^{n} \dfrac{R_k}{(1 + j\omega C_k)}$, where the summation terms represents the individual Voigt elements.

In the cases when frequency approaches extreme values, the modulus of impedance is merely a resistance. As frequency approaches infinity, the impedance of a Voigt equivalent circuit approaches R_0. Conversely, as frequency approaches 0 Hz (direct current), the impedance approaches the sum of all resistance values in the equivalent circuit.

Most equivalent circuit models for systems with solid state electrolytes use a Voigt equivalent circuit—sometimes with modifications. For example, a CPE sometimes replaces a capacitor; the CPE can be conceptualized as a capacitors with distributed properties. Equivalent circuits based on the Voigt model will be discussed in more detail for sensors below in the literature review section. Voigt equivalent circuits are used for more than sensors: Barfod *et al.* modified a Voigt circuit to model a solid oxide fuel cell by replacing the capacitors with CPEs.[192]

To examine the validity of an equivalent circuit, one uses nonlinear regression techniques as explained below.

[190] Norio Miura, Mitsunobu Nakatou, Serge Zhuiykov, "Impedancemetric gas sensor based on zirconia solid electrolyte and oxide sensing electrode for detecting total NO_x at high temperature", <u>Sensor Actuator B Chem</u>, 93, (2003), 221–228.

[191] Pavan K. Shukla, Mark E. Orazem, Oscar D. Crisalle, "Validation of the measurement model concept for error structure identification", <u>Electrochim. Acta</u>, 49, (2004), 2881.

[192] R. Barfod, A. Hagen, S. Ramousse, P. V. Hendriksen, and M. Mogensen, "Break Down of Losses in Thin Electrolyte SOFCs", <u>Fuel Cells 06</u>, 2, (2006), 143.

Complex Nonlinear Least Squares (CNLS) Regression

Macdonald and Boukamp developed nonlinear complex regression techniques in the 1970s and 80s to perform equivalent electrical circuit modeling.[193] They based their work on the Kramers-Kronig relations, which constrain both the real and imaginary parts of measured impedance spectrum. Impedance is a strong function of frequency, so weighing strategies were developed by Macdonald.[194] The regression procedure involves simultaneous minimization of both the real and imaginary components of impedance with parameter values that minimize the objective function below.[195]

$$S(\vec{P}) = \sum_{k=1}^{N_{dat}} \frac{\left(Z_r(f_k) - \hat{Z}_r(f_k|\vec{P})\right)^2}{\sigma_{r,k}^2} + \sum_{k=1}^{N_{dat}} \frac{\left(Z_j(f_k) - \hat{Z}_j(f_k|\vec{P})\right)^2}{\sigma_{j,k}^2}$$

where

$S(\vec{P})$ = weighted sum of squares

$\vec{P}$ = parameter vector used in regression

N_{dat} = number of data points

$Z_r(f_k)$ and $Z_j(f_k)$ = real and imaginary parts of measured impedance at frequency f_k

$\hat{Z}_r(f_k|\vec{P})$ and $\hat{Z}_j(f_k|\vec{P})$ = real and imaginary parts of calculated impedance at f_k

$\sigma_{r,k}^2$, $\sigma_{j,k}^2$ = real and imaginary parts of variance of experimental stochastic errors

χ^2 = sum of squares used in regression analysis, used to assess quality of regression

Solving the objective function is usually handled by software. Seed values must be provided as initial estimates for parameters. Physical insight may provide good guidelines for selection.[196] The software then iterates through a range of parameter values in order to minimize the objective function, which treats the real and imaginary components separately, and adds together the sum of the square of the residuals of both components.[197] The quality of the regression depends on the accuracy of the seed values. Sometimes the model will identify a local minimum. Therefore it is good practice to test the model with several seed values, each time assessing the goodness of fit of the model, as explained below.

Assessment of Regression Quality

A good equivalent circuit model yields impedance values that match experimental observations. By subtracting the impedance values obtained by modeling from those measured by experiment, one obtains residuals for each frequency: $\varepsilon_{res}(\omega)$. The residuals consist of error contributions from several sources, including systematic inadequacies of the model (ε_{fit}), systematic experimental bias error (ε_{bias}), and the stochastic error (ε_{stoch}) that is expected to equal zero at any given frequency:

$$\varepsilon_{res}(\omega) = Z(\omega) - \hat{Z}(\omega) = \varepsilon_{fit}(\omega) + \varepsilon_{bias}(\omega) + \varepsilon_{stoch}(\omega).$$

---

[193] Orazem, xxvi.
[194] Ibid., 363.
[195] Ibid., 364-5.
[196] Ibid., 380.
[197] Ibid., 400.

Here, $Z(\omega)$ and $\hat{Z}(\omega)$ represent the impedance values observed and modeled, respectively, at a particular frequency.[198] A plot of the residuals versus frequency should not exhibit any organized patterns.

The best model has the lowest sum of the squares of residuals. Hence the goal of CNLS is to minimize the sum of squares of the residuals, and one chooses the equivalent circuit with minimum sum of squares $S(\vec{P})$.

The chi squared statistic, χ^2, is often used as a figure of merit for regression quality. The χ^2 statistic calculates the sum of the squares of the residuals.[199] It becomes smaller as the differences between observed and modeled values approach zero.[200] The best model has the lowest value of the χ^2 statistic. For a good fit, $\chi^2_{min} = \upsilon \pm (2\upsilon)^{\frac{1}{2}}$ where υ is degrees of freedom.[201] Fit quality can easily be seen on plots of residual errors.[202] These plots are also valuable for recognizing patterns in the residuals that may be due to stochastic, systematic, or bias errors.

A weighting strategy can be employed to emphasize data in particular ranges of frequency. For example, the low frequency impedance data is particularly important for gas sensing. The selection of an appropriate weighting strategy is important for data interpretation.[203]

3.3 Sensing of NO_x Concentration by Impedance

The presence of NO_x reversibly alters the impedance of some electrochemical systems at low frequencies ($f < 100$ Hz) in a repeatable fashion that can be correlated to concentration. This principle underlies impedance-based gas sensors. This type of sensor is the least developed of all types of NO_x sensors.[204] It has shown promise to detect NO_x at lower ppm than is possible using conventional sensors.[205,206] In addition, reference to external air is not necessary. As a result, impedance-based NO_x sensors may help diesel vehicles meet future OBD requirements.

3.3.1 Principle of Operation

Miura *et al.* originally proposed a novel, YSZ-based sensor in 2002 that relates gas composition to an impedance signal. In specific, the sensor detects total NO_x concentration (both NO and NO_2) down to 50 ppm between 600°C to 700°C using a complex impedance signal. Sensitivity was measured by the difference in the magnitude of the impedance signal (modulus) measured in air and in analyte gas at 0.1 Hz. The change in modulus, ΔZ, was approximately linear with NO_x concentration from 50 to 400 ppm. Sensing behavior is attributed to changes of resistance at the interface between the YSZ electrolyte and the oxide electrode; in specific, gas adsorption and electrochemical reactions affect this resistance.[207]

---

[198] Shukla, 2882.
[199] Orazem, 369.
[200] Ibid., 385.
[201] Ibid., 382.
[202] Ibid., 402.
[203] Ibid., 407.
[204] Fergus, 659.
[205] Martin, J Electrochem Soc, (2007), J97-J104.
[206] Fergus, 659.
[207] Miura, (2002), 284–287.

A coauthor of Miura's seminal paper wrote that the sensing mechanism of impedance-based sensors is poorly understood.[208] While the exact mechanism may not be clear, it is evident that in the low frequency range, specific physical processes impact the impedance spectrum.

In Figure 21, some processes that affect impedance are shown with a symmetric, single cell sensor with a zirconia-based electrolyte. First, gases diffuse to the electrode surfaces, where they absorb and dissociate. Then surface diffusion occurs, followed by charge transfer (redox reactions) at the electrode-electrolyte interface. Then ion transport through the electrolyte occurs with charge transfer across grain boundaries. At various frequencies, some of the processes may contribute to the impedance response, depending on the physical characteristics of the electrochemical cell.
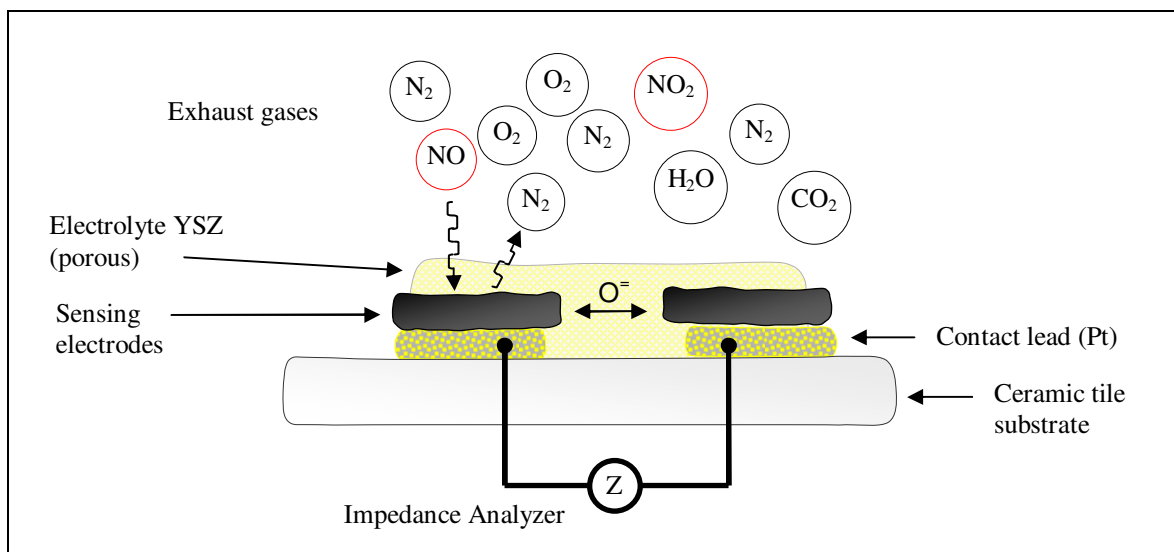
Figure 21. NO$_x$ sensing mechanism.

At particular frequencies, some processes contribute to impedance more than others. These processes appear in the impedance spectrum. Figure 22 shows a Nyquist plot recorded from a sensor with YSZ electrolyte and gold working electrodes exposed to two gases at 650°C: (1) 10% O$_2$ in N$_2$ and (2) 10% O$_2$ in N$_2$ with 100 ppm NO. A Nyquist plot shows the resistive and capacitive contributions of impedance, but it does not explicitly show frequencies, so the six decades of frequencies are indicated in the plot. Two impedance arcs labeled "high frequency" and "low frequency" resulted with both gases. The high frequency arc (approximately $f > 10^4$ Hz) provides information on kinetically controlled phenomena. Regardless of the gas, the high frequency arc remains invariant for a given temperature. The low frequency arc (approximately $f < 10^4$ Hz) is sensitive to mass transfer events; it varies in the presence of various gas species.[209]

The phase angles at 10 Hz are labeled in Figure 22. The effect of 100 ppm NO is to shift the low frequency arc inwards. Both the modulus, |Z|, and phase angle, Θ, change as a result. The modulus represents the length of the vector from the origin to an impedance measurement at a specific frequency (10 Hz). The phase angle is the arctangent of the ratio of the capacitive

[208] Zhuiykov, (2008), 128.
[209] Bard, 352.

contribution of the impedance to the resistive component at a specific frequency. The changes in modulus.[207] and phase angle[210] are linear over a specific range of gas concentration at a given frequency. The phase is more sensitive to changes in gas concentration than the modulus, so it is used for the detection of gases. [211] A NO_x sensor needs only to interrogate one frequency typically in the low frequency range ($f < 100$ Hz).[212] This frequency is selected as a compromise between speed of response, which favors higher frequencies, and sensitivity, which favors lower frequencies.
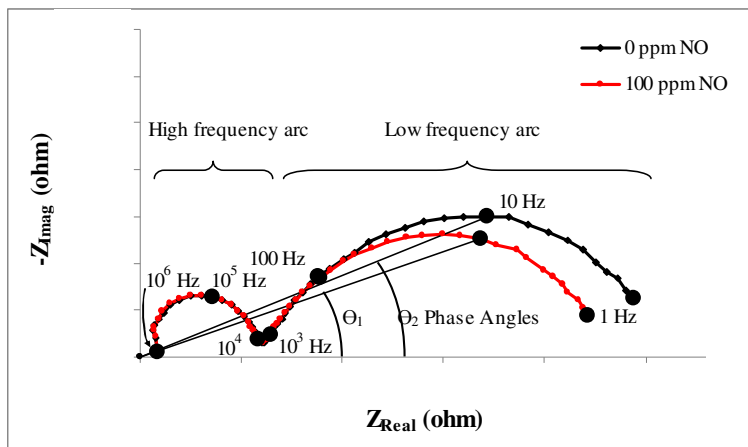
Figure 22. NO causes inward shift of low frequency arc on Nyquist plot.

For a sensor application, the shape of the low frequency impedance spectrum must change selectively in the presence of a specific gas.

3.3.2 Review of Literature on Impedance-Based Sensing

For almost two decades, the concept of sensing species by monitoring impedance has been known. An early application of this technique involved monitoring blood glucose levels using a vascular prosthesis.[213] Guttiérez *et al.* investigated tin oxide (SnO_2) and noticed changes in the impedance spectra dependent on the surrounding gas atmosphere, whether it be humidified air, dry air, or blends of air and CO. They used a Voigt equivalent circuit to model their system.[214] Oelgeklaus and Baltruschat proposed a hydrocarbon sensor with Pt electrodes and a sulfuric acid electrolyte. By continuously monitoring the impedance of their wet cell at a low frequency (10 Hz), they determined changes in capacitance of the electrode surface indicating the presence of hydrocarbon adsorbates. [215] A follow up paper by the same group reported a method to periodically strip the adsorbate from the surface to enable continuous monitoring of hydrocarbons. They also suggested a correction for O_2 cross sensitivity. They found a linear

---

[210] Martin, J Electrochem Soc, (2007), J97-J104.

[211] Orazem, 315-316.

[212] Zhuiykov, (2008), 127.

[213] W. Preidel, I. von Lucadou, W. Lager, L. Ruprecht, S. Saeger, "Glucose Measurements by Electrocatalytic Sensor in the Extracorporeal Blood Circulation of a Sheep", Sensor Actuator B Chem, 2, (1990), 257-263.

[214] J. Gutiérrez, L. Arés, M.C. Horillo, I. Sayago, J. Agapito, L. López, "Use of Complex Impedance Spectroscopy in Chemical Sensor Characterization", Sensor Actuator B Chem, 4, (1991), 359-363.

[215] R. Oelgeklaus, H. Baltruschat, "Detection of hydrocarbons in air by adsorption on Pt-electrodes using continuous impedance measurements", Sensor Actuator B Chem, 42, (1997), 31-37.

dependence of the sensor signal on concentration. The sensor struggled to distinguish between hydrocarbon species.[216]

The application of impedance techniques to sensors with an electrolyte of YSZ is particularly relevant to this work. Yoon *et al.* examined the affect of NO_2 on impedance spectra. They remarked that the low frequency resistance associated with the electrode/electrolyte interface depended on NO_2 content at levels of 100ppm.[217] A handful of research groups located around the globe have built upon this finding with their YSZ-based sensors.

Norio Miura of the Advanced Science and Technology Center for Cooperative Research at Kyushu University in Fukuoka, Japan and his research group wrote the first paper that proposed impedance-based sensing by calibrating a modulus shift to NO_x concentration.[207] They also wrote several follow up papers on sensing NO_x, steam, and propene, as explained below.

The group of Robert Glass of Lawrence Livermore National Laboratory in Livermore, CA has published several papers on the impedance-metric detection of NO_x using sensors with YSZ. In contrast to most of the impedance-sensing community, this group measures sensitivity by the change in phase angle due to the presence of analyte gases. They claim detection of the lowest concentration of NO_x yet recorded with an impedance-based sensor (8 ppm).[218]

Bilge Saruhan-Brings of the Institute of Materials Research at the German Aerospace Centre (DLR), in Cologne, Germany has investigated impedance-based sensors with YSZ for NO_x detection. This group has published multiple papers and developed an extensive equivalent circuit model, as discussed below.

A handful of groups have written individual papers of note on impedance-sensing. Nianqiang Wu *et al.* presented a novel interpretation of the equivalent circuit model elements in a CO sensor that uses a YSZ electrolyte.[219] The group of Daisuke Koba of Kyushu Institute of Technology in Fukoka, Japan wrote the only paper to date on a NO_x impedance sensor that uses a non zirconia electrolyte.[220] These papers are described in detail below. In the following sections, papers on impedance-based sensing are grouped by the type of gas.

Nitrogen Oxides (NO_x)

Since the seminal paper[207], Miura *et al.* proposed an equivalent circuit model for the NO_x sensor with a $ZnCr_2O_4$ sensing electrode in a follow-up publication. Their circuit consists of a Voigt circuit with two Voigt elements: R_0-(R_1C_1)-(R_2C_2). In their model, the lone resistor, R_0, represents YSZ bulk resistance; the first Voigt element (R_1C_1) represents the resistance and capacitance of the bulk of the oxide electrode; finally, the second Voigt element (R_2C_2) represents the resistance and capacitance of the interface between the YSZ and the oxide

[216] S. Ernst, R. Herber, E. Slavcheva, I. Vogel, and H. Baltruschat, "Continuous Detection of Volatile Aromatic, Unsaturated or Halogenated Hydrocarbons in Air by Adsorption on Pt-Electrodes and Subsequent Oxidative Desorption", Electroanalysis, 13:14, (2001), 1191-1197.

[217] Jong Won Yoon, Maria Luisa Grilli, Elisabetta Di Bartolomeo, Riccardo Polini and Enrico Traversa, "The NO_2 response of solid electrolyte sensors made using nano-sized $LaFeO_3$ electrodes", Sensor Actuator B Chem:, 76, (2001), 483-488.

[218] Martin, J Electrochem Soc, (2007), J97-J104.

[219] Nianqiang Wu, Zheng Chen, Jianhui Xu, Minking Chyu, Scott X. Maob, "Impedance-metric Pt/YSZ/Au–Ga_2O_3 sensor", Sensor Actuator B Chem, 110, (2005), 49–53.

[220] Youichi Shimizu, Satoko Takase, Daisuke Koba,"A NO_x Sensor Based on Solid-Electrolyte Impedance Transducer", Adv Mater Res, 47-50, (2008), 479-482.

electrode where adsorption and reactions occur. Only the resistance of the interface changed in the presence of NO_x. It was suggested that this resistance or even the entire real component of impedance could be used to determine NO_x concentration at low frequency, however, the measurement should be taken by measuring complex impedance and by calculating the real component of resistance. [221]

Miura then experimented with the thickness of $ZnCr_2O_4$ sensing electrodes in an impedance-based NO_x sensor. A platinum layer over the electrodes oxidized reducing gases that are known to evoke a cross sensitive response (CO, H_2, CH_4 and C_3H_8) at 700°C. At high temperature, thick electrodes (39μ) provide a large catalytic area for non-equilibrium mixtures of NO and NO_2 to equilibrate. An equilibrium NO_x mixture at 700°C consists of 95 vol.% NO and 5 vol.% NO_2. Because NO_2 is mostly reduced to NO during equilibration, the impedance-based sensor shows essentially the same response to NO as to NO_2 at high temperature.[222]

From the Lawrence Livermore National Lab group, Martin *et al.* applied a NO_x sensing technique using impedance to a planar sensor with YSZ electrolyte and identical metal-oxide composite electrodes consisting of Cr_2O_3 and YSZ (10:90% weight ratio). The NO_x sensitivity was measured by the shift in phase angle at 10 Hz. The shift was linear with concentration between 8-50 ppm. The response to both NO and NO_2 was similar. Since the NO_x sensor is cross sensitive to O_2, a compensation method was proposed. They suggest that the simultaneous measurement of NO_x and O_2 can occur at different frequencies because the impedance response at f > 100 Hz was negligible for NO_x but still significant for O_2. The slow response of this sensor to O_2, however, may make this chemistry of this sensor impractical.[223]

Subsequently Martin *et al.* developed an equivalent circuit model. Instead of the standard Voigt model, this group's model includes a fractal Gerischer element, which is used to model the diffusion of reacting gases. Their model consists of a resistor in series with the fractal Gerischer element in series with a Cole element: R_0-fG-(R_2Q). The Cole element models the low frequency behavior. The most significant parameter changes due to NO_x exposure occur in this subcircuit element. This element corresponds to physical processes that occur at the electrode surface and at the interface of the electrode and electrolyte. They further broke down the resistance of the Cole element into contributions from reactions that occur at the triple phase boundary (interface) that involve O_2, NO_x, and the solid, ionic form of oxygen (O^{2-}):

$$R_2 = \left[\frac{1}{R_{O2}} + \frac{1}{R_{NOx}} \right]^{-1}$$

For an electrode to sense NO_x, the values of R_{O2} and R_{NOx} must be within two orders of magnitude of each other. They confirmed this statement by adding a porous gold layer or a dense Pt plate to their electrodes; these actions both had the effect of increasing the electrode surface area for which O_2 and NO_x compete. The result was a decrease in R_{O2} to such an extent that the presence of NO_x no longer could be detected. R_{NOx} was much greater than R_{O2}; since R_{NOx}

[221] Miura, (2003), 221–228.
[222] Norio Miura, Tatsuya Koga, Mitsunobu Nakatou, Perumal Elumalai, Masaharu Hasei, "Electrochemical NO_x sensors based on stabilized zirconia: comparison of sensing performances of mixed-potential-type and impedancemetric NO_x sensors", <u>J Electroceram</u>, 17, (2006), 979–986.
[223] L. Peter Martin, Leta Y. Woo, and Robert S. Glass, "Impedancemetric Technique for NO_x Sensing Using a YSZ-Based Electrochemical Cell", <u>Mater Res Soc Symp Proc</u>, 972, (2007).

appears in the denominator, it did not contribute to the R of the Cole element. Martin *et al.* also provided a justification for their use of change in phase angle, $\Delta\Theta$, instead of change in modulus, $|Z|$, as the proxy for selectivity. The phase angle shift persists to higher frequency in the presence of NO_x than does the modulus change. Increasing the frequency at which a sensor operates is desirable for a faster response. Since the sensor responds to both oxygen and NO_x at 10 Hz, but at 1 kHz the sensor responds only to O_2, compensation for O_2 was carried out at 1 kHz by measuring impedance. Phase angle varies linearly with O_2 concentration over the examined range of 2–18.9 % at both frequencies, so phase angles can be calibrated to determine O_2 concentration at 1 kHz. Then the contribution of O_2 can be subtracted from the impedance at 10 Hz in order to determine NO_x concentration. Lastly, some signal drift was detected that may have been due to aging.[224]

A coauthor of Martin, Murray, investigated NO_x sensors consisting of $LaCr_{0.95}Mg_{0.05}O_3$ on fully stabilized YSZ. Phase angles were correlated to NO_x concentration to serve as the measurement of sensitivity. An analysis of the effect of both O_2 and temperature on sensitivity led her to conclude that monitoring these variables would be necessary for accurate sensing. The signal from sensors was found to drift over several days of operation due to material instability. In addition, long response times were required with these sensors.[225]

Yet an other coauthor of Martin, Woo, investigated planar, YSZ-based NO_x sensors with dense gold electrodes. A porous layer of electrolyte was present between the electrodes and the dense electrolyte. This layer enabled enhanced NO_x sensing, but the mechanism was not understood. A simplified equivalent circuit analysis was performed in which the low frequency arc that is sensitive to NO_x was modeled by a resistor in series with a Cole element: R_0-(R_1Q). Adsorption was suggested as the rate-limiting step.[226]

In a follow up paper, Woo *et al.* expatiated upon possible mechanisms for the NO_x response of the symmetrical gold/YSZ sensor. The resistor in the Cole element of the simplified equivalent circuit followed a power law with respect to the analyte gases: $R_1 \alpha [gas]^\alpha$. The determination of the exponent, α, suggested adsorption might be the sensing mechanism. In addition, the activation energies obtained from Arrhenius plots of R_1 tended to support adsorption. Competition for adsorption sites may have been the rate-limiting step.[227]

In a subsequent publication, Woo *et al.* applied EIS techniques to NO sensors with gold, platinum, or silver electrodes on a mixture of solid and porous YSZ electrolyte. Only gold showed sensing activity as long as the electrode was dense; porous gold was insensitive. Sensors that detected NO featured larger impedance values than those that did not; this suggested that a dearth of electrochemical reaction sites may play a role in NO-sensing. An equivalent circuit model was used to investigate the low frequency arc of NO impedance spectra. It was similar to a Voigt circuit but with the capacitors replaced by CPEs: R_0-(R_1Q_1)-(R_2Q_2). Two Cole elements

[224] Martin, <u>J Electrochem Soc</u>, (2007), J97-J104.

[225] E. Perry Murray, R.F. Novak, D.J. Kubinski, R.E. Soltis, J.H. Visser, L.Y. Woo, L.P. Martin, and R.S. Glass, "Investigating The Stability And Accuracy Of The Phase Response For NO_x Sensing 5% Mg-Modified $LaCrO_3$ Electrodes", <u>ECS Transactions</u>, 6:20, (The Electrochemical Society, 2008), 43-62.

[226] Leta Y. Woo, L. Peter Martin, Robert S. Glass, and Raymond J. Gorte, "Impedance Analysis of Electrochemical NO_x Sensor Using a Au/Yttria-Stabilized Zirconia (YSZ)/Au cell", <u>Mater Res Soc Symp Proc</u>, 972, (2007).

[227] L. Y. Woo, L. P., Martin, R. S. Glass and R. J. Gorte, "Impedance Characterization of a Model Au/Yttria-Stabilized Zirconia/Au Electrochemical Cell in Varying Oxygen and NO_x Concentrations", <u>J Electrochem Soc</u>, 154:4, (2007), J129-J135.

were required to model one low frequency arc, implying that two physicochemical processes with similar time constants were taking place. Woo suggested that the rate-determining step for NO-sensing may depend on O_2 reactions that take place away from the triple-phase boundary. Although the exact mechanism was not determined, adsorption and diffusion of O_2 were offered as possible rate-limiting steps for the detection of NO.[228]

Woo *et al.* announced that two impedance-type sensors detect changes in NO_x concentrations of 5 ppm. Building on previous work in which the best electrodes are poor O_2 catalysts, prototype sensors were made with electrodes of either dense gold or dense lanthanum strontium manganate (LSM), an n-type semiconducting oxide. Both sensor types had porous YSZ electrolyte. The sensor with gold electrodes showed better stability than the type with ones of LSM. A thicker porous YSZ electrolyte (150 μm vs. 75 μm) in the sensors with gold electrodes resulted in a larger response for NO_2 than for NO sensitivity. The thinner porous electrolyte layer was preferred for total NO_x sensing (equivalent response to both NO and NO_2).[229]

At the German Aerospace Research Centre, Stranzenbach *et al.* fabricated planar, impedance-based NO_x sensors by sputtering sensing electrodes of the spinel $NiCr_2O_4$ on both fully stabilized YSZ and PSZ electrolyte. They measured sensitivity by the change in magnitude of the impedance, ΔZ, on the addition of a sample gas. From 200-1000 ppm, ΔZ varied linearly with NO concentration at 0.1 Hz. The impedance values and their associated magnitudes for the FSZ electrolyte were found to be much higher than those for PSZ. They analyzed the sensors for cross sensitivity to various gases including O_2, CH_4, CO, and CO_2. They found that CO_2 does not affect sensing performance for either electrolyte. Since CH_4 and CO are oxidized to CO_2 in lean atmospheres, the sensor does not detect them either. Furthermore, no cross sensitivity to NO_2 was found because at high temperature (620°C), the NO_2 converts to NO at the electrodes due to thermodynamic equilibrium. They also identified an equivalent circuit model similar to a Voigt circuit with n = 4, except in the last two elements, the capacitors are replaced with a CPE and a Warburg element respectively: R_0-(R_1C_1)-(R_2C_2)-(R_3Q)-(R_4W). They found that changes in NO concentration affect these last two elements of the equivalent circuit. The second to last element, a Cole element, consists of a resistor and CPE in parallel. It represents changes in the double layer between the electrode and electrolyte which may be due to the reaction of NO over the catalytic sensing electrode. The last element, a resistor in parallel with a Warburg impedance, represents a diffusion process, but did not conclusively specify the diffusion of which species.[230]

Stranzenbach and Saruhan continued their work on impedancemetric NO_x sensors by examining NiO as the sensing electrode on YSZ and PSZ electrolytes. This sensor showed

---

[228] Leta Y. Woo, L. Peter Martin, Robert S. Glass, Wensheng Wang, Sukwon Jung, Raymond J. Gorte, Erica P. Murray, Robert F. Novak, and Jaco H. Visser, "Effect of Electrode Composition and Microstructure on Impedancemetric Nitric Oxide Sensors Based on YSZ Electrolyte", J Electrochem Soc, 155:1, (2008), J32-J40.

[229] L. Y. Woo, R. S. Glass, R. F. Novak, and J. H. Visser, "Impedancemetric NO_x Sensing Based On Porous Yttria-Stabilized Zirconia (YSZ) Electrolyte: Effect of Electrode Materials on Total-NO_x Sensing and Stability", 215th ECS Meeting, Abstract 1503, (2009).

[230] M. Stranzenbach, E. Gramckow, B. Saruhan, "Planar, impedance-metric NO_x-sensor with spinel-type SE for high temperature applications, Sensor Actuator B Chem, 127, (2007), 224–230.

excellent selectivity for NO in both reducing and oxidizing conditions with low cross-sensitivity to O_2 and other combustible gases.[231]

In a subsequent paper, Stranzenbach and Saruhan performed EIS on NO_x sensors with sputtered NiO or $NiCr_2O_4$ sensing electrodes on pre-aged electrolytes of fully stabilized YSZ and PSZ deposited by EBPVD.[232] They used the same equivalent circuit as in their previous work.[233] The resistor of the Cole element represents the "reaction-resistance" for adsorption, dissociation, and electrochemical reactions. It is an indicator of the oxygen sensitivity of the sensor. They also provided further discussion of the equivalent circuit and its relationship to the sensing mechanism.

Wu *et al.* examined an electrochemical CO sensor with an electrode of Au-doped Ga_2O_3 and an electrolyte of YSZ. They chose Au-Ga_2O_3 sensing electrode material because CO chemisorbs strongly on it. The change in modulus at 0.1 Hz, was used for sensitivity measurements. An equivalent circuit was proposed: R_0-(R_1C_1)-(R_2Q) where R_0 represents contact resistance, the Voigt element (R_1C_1) represents the YSZ bulk, and the Cole element (R_2Q) represents the interface between the electrode and the electrolyte. In virtually all other papers in the literature, R_0 is associated with the bulk electrolyte; here it is the Ohmic resistance of the electric connection. The value for C_2 was on the same order of magnitude as that for bulk YSZ found in a previous study, so the second element was identified as the bulk electrolyte. Neither R_0, R_1, nor C_1 changes with CO concentration. Rather the interfacial parameters R_2 and Q that represent the triple phase boundary respond to changes in CO concentration, where Q accounts for the non-ideal behavior of the double layer, and R_2 represents charge transfer. This conclusion agrees with the work of Miura's group. Interfacial impedance depends on the electrolyte and the sensing electrode materials; any change in either could affect the impedance.[234]

Shimizu *et al.* is the only group to use an electrolyte other than zirconia for an impedance-based NO_x sensor. They investigated a lithium solid electrolyte $Li_{1.5}Al_{0.5}Ti_{1.5}(PO_4)_3$ for use in NO_x sensors. This electrolyte operates at a lower temperature (400 - 500ºC) than zirconia electrolytes. They examined several different types of oxide electrodes including some perovskites and semiconductors. Sensors were interrogated over a frequency range of 50 Hz to 5 MHz; for most sensors, they investigated the response ΔZ at 1 kHz or at 10 kHz, which is 2-3 orders of magnitude higher than usual. In specific, they were interested in the change of R and C at a specific frequency due to the exposure of NO_x. They attributed R and C to the interface of the electrode and electrolyte.[235]

Water Vapor

Miura's group applied the impedance-based sensing technique that they pioneered to sense water vapor (steam) at high temperature. Several different single oxide sensing electrodes were evaluated with stabilized zirconia electrolyte. The maximum sensitivity was found using

[231] M. Stranzenbach and B. Saruhan, "Planar, impedance-metric NO_x-sensor with NiO SE for high temperature applications", <u>Transducers and Eurosensors '07</u>, The 14th International Conference on Solid-State Sensors, Actuators and Microsystems, (Lyon, France, June 10-14, 2007), 983-986.

[232] M. Stranzenbach, B. Saruhan, "Equivalent circuit analysis on NO_x impedance-metric gas sensors", <u>Sensor Actuator B Chem</u>, 137, (2009), 154–163.

[233] Stranzenbach, Gramckow, Saruhan (2007), 228.

[234] Wu, 49–53.

[235] Shimizu, 479-482.

electrodes of In_2O_3 operating at 900°C. Sensitivity was measured by the change in the magnitude of the impedance, ΔZ, at 1 Hz. The impedance change was linear over several orders of magnitude of H_2O concentration (70–30,000 ppm). The sensitivity is due to a change in impedance; in specific, the resistance of the electrode reaction at the interface of the oxide electrode and YSZ electrolyte decreases with increasing concentration of water vapor in the gas. Response times were measured in single seconds.[236]

Hydrocarbons

Miura and his group found that the In_2O_3/YSZ impedancemetric sensor is cross sensitive to hydrocarbons in dry gas at 900°C. They speculated that the sensing electrode serves as a catalyst for the oxidation of hydrocarbons that react to form CO_2 and $H_2O_{(v)}$. Detection of the hydrocarbon occurred indirectly; the water vapor from the combustion of the hydrocarbon was detected by the In_2O_3/YSZ sensor. Once again, the change in modulus, ΔZ, was used as the metric for sensitivity. The sensitivity, as measured by the change in impedance due to the analyte gas, is attributed to the change in resistance of the electrode reaction at the interface of the electrode of In_2O_3 and the electrolyte of YSZ.[237]

Miura's group developed a sensor that can selectively detect propene (C_3H_6) in a humidified gas stream (1 vol.% H_2O) at 600°C by first oxidizing reducing species and by applying a bias of +50 mV to the sensing electrode versus the Pt counter electrode. A sensing electrode of ZnO on YSZ shows negligible cross sensitivity to CH_4, where sensitivity is measured as the change in modulus upon exposure to a gas. Platinum (1.5 wt.%) was added to the sensing electrode in order to improve its catalytic activity for oxidation, resulting in the ability to detect propene even in the presence of CO, NO, NO_2, H_2, CH_4, CO_2, H_2O and O_2. The sensing ability is attributed to the change in the resistance of electrochemical reaction taking place at the interface between the electrode and electrolyte, however, the exact sensing mechanism is poorly understood.[238]

A follow up paper by Miura and colleagues reported that their propene sensor with a ZnO sensing electrode and YSZ electrolyte detected the specific hydrocarbon at extremely low concentrations (0.05 – 0.8 ppm). Sensitivity was defined by the change in modulus; it varied linearly with propene concentration and was only insignificantly affected by $H_2O_{(v)}$, NO_2, NO, H_2, CO and CH_4. In this study, an applied potential to the sensing electrode did not greatly affect sensitivity. The effect of propene on impedance is attributed to the change in resistance of the charge transfer reaction that occurs at the interface of the oxide electrode and YSZ electrolyte.[239] This statement differs from earlier reports from this group that attributed the change in resistance to adsorption and electrode reactions.[207, 240, 241, 242, 243]

[236] Mitsunobu Nakatou, Norio Miura, "Impedancemetric sensor based on YSZ and In_2O_3 for detection of low concentrations of water vapor at high temperature", <u>Electrochem Comm</u>, 6, (2004), 995–998.

[237] Mitsunobu Nakatou, Norio Miura, "Detection of combustible hydrogen-containing gases by using impedancemetric zirconia-based water-vapor sensor", <u>Sol. Stat. Ion.</u>, 176, (2005), 2411–2415.

[238] Mitsunobu Nakatou, Norio Miura, "Detection of propene by using new-type impedancemetric zirconia-based sensor attached with oxide sensing-electrode", <u>Sensor Actuator B Chem</u>, 120, (2006), 57–62.

[239] Ryotaro Wama, Masahiro Utiyama, Vladimir V. Plashnitsa, Norio Miura, "Highly sensitive impedance-based propene sensor using stabilized zirconia and zinc oxide sensing-electrode", <u>Electrochem Comm</u>, 9, (2007), 2774–2777.

[240] Miura, (2003), 221–228.

[241] Nakatou, (2004), 997.

[242] Nakatou, (2005), 2413.

Summary of Impedance-Based Gas Sensing

Several books contain reviews of impedance-based sensors. These reviews have generally been written by Zhuiykov[244,245] or Miura,[246] who were coauthors on the seminal paper that related NO_x concentration to changes in modulus.[207] These reviews generally frame impedance-type sensors in the larger context of solid state sensors including potentiometric, mixed potential and amperometric varieties.

To summarize, impedance-based gas sensors are less developed than amperometric or mixed potential types.[247] Most research papers on gas-sensing by impedance involve YSZ electrolyte and either noble metal or oxide electrodes. Typically a Voigt equivalent circuit model (sometimes with minor variations) is used to replicate impedance behavior. The influence of the analyte gas is seen at low frequency ($f \leq 100$ Hz) and usually attributed to the interface of the electrode and the electrolyte. Most research groups use the change in modulus at a specific frequency (typically $f \leq 10$ Hz) as the metric for sensitivity. Some groups report an equivalent response to NO and NO_2 alike allowing total NO_x sensing at a specified temperature. It is unclear whether the equivocal sensitivity is due to the detection capability of the sensor or due to the natural thermal equilibrium shift of NO_2 to NO. At T > 600°C, NO_x in exhaust gases equilibrates so that the mixture consists primarily of NO > 90%.[248]

Some drawbacks exist with impedance-based sensors. Selectivity remains a challenge. Long term stability of these sensors is lacking. They are still more complex and expensive than potentiometric ones, especially their electronics and signal processing equipment. The sensing mechanism is poorly understood.[249] As a result, impedancemetric sensors are not commercially available.

---

[243] Nakatou, (2006), 57-62.

[244] S. Zhuiykov, and N. Miura, "Solid-state electrochemical gas sensors for emission control", in Materials for Energy Conversion Devices", eds C. C. Sorrell, J. Nowotny, and S. Sugihara, (Cambridge: Woodhead Publishing, 2005), 303-335.

[245] Zhuiykov, (2008), 119-128.

[246] N. Miura, P. Elumalai, V. V. Plashnitsa, T. Ueda, R. Wama, M. Utiyama, "Solid State Gas Sensing", Chapter 5 in Solid State Electrochemical Gas Sensing, E. Comini, G. Faglia, G. Sberveglieri (eds.), (New York: Springer, 2009), 200-203.

[247] Fergus, (2007), 659.

[248] Zhuiykov, (2008), 215.

[249] Ibid., 127-8.

CHAPTER 4: Surface Micromachining of Unfired Ceramic Sheets

Conventional surface micromachining techniques including photolithography and both wet and dry etching have been directly applied to an unfired sheet of yttria-stabilized zirconia ceramic material. Unfired ceramic samples were reversibly bonded to silicon wafers in order to perform photolithography. A line-width feature size of 8 µm has been obtained using thin film photoresist. Thick film photoresist exhibited a coverage gradient after being spun on. Chemical etching was successfully performed isotropically with concentrated hydrofluoric acid. A dry thick film resist applied by lamination provided coverage during plasma etching. Neither an oxygen plasma nor a mixture and sulfur hexafluoride and oxygen plasma proved successful. Embossing was performed on the meso-scale with feature shrinkage of approximately 45% after sintering.

4.1 Introduction

Since the inception of the tape-casting process in 1961,[250] unfired ceramic tapes and sheets are common starting materials for electrochemical gas sensors and for high temperature electronic devices. The application of microfabrication techniques to unfired ceramic sheets according to the principles of microsystems technologies (MST) holds potential for the mass production of microscale fuel cells for power production and the manufacturing of solid state sensors for exhaust gas analysis.[251] The shorter diffusion path of these devices is expected to lower their operating temperature and in the case of sensors, improve the response time. Further applications in semiconductor device packaging may be possible.

Unfired ceramic sheets consist primarily of ceramic particles which make up approximately 80-90% of the weight of the sheet and roughly 50% by volume. The balance of the sheet consists of the following organic materials: binder, plasticizer, dispersant, and deflocculant.[252] The organics allow the ceramic powders to dissolve in a slurry for tape-casting and they imbue desirable mechanical properties to the sheet for subsequent processing.

Literature on microfabrication techniques [253], [254] is abundant, especially on silicon processing.[255,256] Papers that deal with microfabrication techniques applied to unfired (green) ceramic sheets generally deal with the formation of vias for multilayered cofired ceramics using

---

[250] J. L. Park, Jr, "Manufacture of Ceramics", U.S. Patent 2,966,719, (1961).

[251] David L. Wilcox, Sr., Jeremy W. Burdon, Rajnish Changrani, Chia-Fu Chou, Steve Dai, Ramesh Koripella, Manny Oliver, Daniel Sadler, Paul von Allmen, and Frederic Zenhausern, "Add Ceramic 'MEMS' to the Pallet of MicroSystems Technologies", Mater Res Soc Symp Proc, 687, (2002).

[252] Kug Sun Hong, "Synthesis of Particle Dispersion", in Somasundaran, P. (ed)., Encyclopedia of Surface and Colloid Science vol. 8., 2nd edn., (CRC Press, Boca Raton, 2006), 6216.

[253] Marc J. Madou, Fundamentals of Microfabrication: The Science of Miniaturization, 2nd edn., CRC Press, Boca Raton, (2002).

[254] Richard C. Jaeger, Introduction to Microelectronic Fabrication: Volume 5 Of Modular Series On Solid State Devices, 2nd edn., (Prentice Hall, Upper Saddle River, NJ, (2002).

[255] Robert N. Noyce, "Semiconductor device-and-lead structure", US Patent 2981877, (1961).

[256] Gordon Moore, "Cramming More Components onto Integrated Circuits", Proc. of IEEE, 86:1, (Jan. 1998).

a laser[257] or an electron beam.[258] A solvent jet process has also been demonstrated for this purpose.[259] Additional technologies have been developed to form unfired ceramic sheets including micro extrusion,[260] micro casting of slurry on photoresist,[261] stereolithographic printing,[262] micro injection molding[263,264] and micro embossing[265,266] One particularly innovative approach involved the use of photo-polymerizable binders mixed with ceramic particles to directly shape the bulk of an unfired ceramic film.[267]

Photolithography[268] and etching[269] have been applied to fired and polished ceramic material to pattern thin films.[270] These techniques have also been applied to partially sintered low temperature cofired ceramic (LTCC),[271] however, the application of these techniques to unfired high temperature cofired ceramic (HTCC) sheet is generally lacking from the literature. An investigation of photolithography and etching on HTCC green sheet forms the basis of this inquiry. Etching is thought to occur by chemical attack of the organic content in the unfired sheet and not the ceramic particles, which are very stable. In addition, an investigation of meso-scale embossing of unfired ceramic sheet has been undertaken. Meso-scale features measure greater than 10 μm.[272]

[257] Kamran Imen and Susan D. Allen, "Pulse CO Laser Drilling of Green Alumina Ceramic", IEEE Transactions on Advanced Packaging, 20:4, (Nov. 1999).

[258] You-Wen Yau, Michael A. Booke, and Nirmal S. Sandhu, Joseph J. Fulton, "Microelectronics Packaging Processing Using Focused High Power Electron Beams", Electronic Components and Technology Conference, 1991, Proceedings, 41st, (1991), 636-638.

[259] M.R. Gongora-Rubio, P. Espinoza-Vallejos, L. Sola-Laguna, J.J. Santiago-Avilés, "Overview of low temperature co-fired ceramics tape technology for meso-system technology (MsST)", Sensor Actuator Phys, 89, (2001), 227.

[260] Charles van Hoy, Andrew Barda, and Michelle Griffith, and John W. Halloran "Microfabrication of Ceramics by Co-extrusion", J. Am. Ceram. Soc., 81:1, (1998), 152–58.

[261] Wilcox, David L., Jeremy W. Burdon, "Methods for manufacturing patterned ceramic green-sheets and multilayered ceramic packages", US Patent 20020174935, (2002).

[262] X. Zhang, X.N. Jiang, and C. Sun, "Micro-stereolithography of polymeric and ceramic microstructures", Sensor Actuator Phys, 77, (1999), 149–156.

[263] S. Petronis, K. L. Eckert, J. Gold, and E. Wintermantel, "Microstructuring ceramic scaffolds for hepatocyte cell culture", Journal of Materials Science: Materials in Medicine, 12, (2001), 523-528.

[264] Volker Piotter, Thomas Gietzelt, and Lothar Merz, "Micro powder-injection moulding of metals and ceramics", Sadhana, 28:1&2, (Feb/Apr 2003), 299–306.

[265] R. Knitter, E. Günther, C. Odemer, and U. Maciejewski, "Ceramic microstructures and potential applications", Microsystem Technologies 2, Springer-Verlag, (1996), 135-138.

[266] Xuechuan Shan, S. H. Ling, H. P. Maw, C. W. Lu and Y. C. Lam, "Micro Embossing of Ceramic Green Substrates for Micro Devices", DTIP'08 Proceedings Symposium on Design, Test, Integration and Packaging of MEMS/MOEMS, (Nice, France, 2008).

[267] H. D. Lee, R. L . Pober, P. D. Calvert, and H. K. Bowen, "Photopolymerizable binders for ceramics", Journal of Materials Science Letters, 5, Chapman and Hall Ltd, (1986), 81-83.

[268] Harry J. Levinson, Principles of Lithography, 2nd edn., SPIE Press, (2005).

[269] K.R. Williams, R.S. Muller, "Etch rates for micromachining processing", Journal of Microelectromechanical Systems, (Dec. 1996), 5:4, 256-269.

[270] Wayne S. Young, Sarah H. Knickerbocker, "Chapter 9 Multilayer Ceramic Technology", Buchanan, Relva C. (ed), Ceramic Materials for Electronics – Processing, Properties, and Applications, 2nd edn., (Marcel Dekker Inc., New York, 1992), 517.

[271] Gongora-Rubio, 222-241.

[272] Ibid., 222.

Other microfabrication processes such as ion implantation,[273] thin film deposition[274] and chemical mechanical polishing[275] have generally not been investigated for unfired ceramic material in the literature. Ion implantation applies to electronic semiconducting materials, but many common ceramics such as alumina and yttria-stabilized zirconia are not semiconducting. Thin film deposition on unfired ceramic is impractical due to shrinkage during the firing step leading to delamination. The chemistry of chemical mechanical polishing is different for unfired ceramics than for silicon systems. For these reasons, these microfabrication techniques are not addressed here.

In the following, findings on the application of selected microfabrication methods directly to unfired ceramic material are reported, including reversible bonding, photolithography, both wet and dry etching, and meso-embossing. This fundamental work may be applied towards device fabrication. Unfired ceramic samples were mounted on 4" wafers using reversible bonding techniques. The wafers and samples were fed into coating tracks that dispense photoresist. The samples were subsequently exposed using contact photolithography, followed by development, etching, and photoresist removal. Either chemical or plasma etching were performed. Lastly, a study of meso-embossing was carried out.

4.2 Experimental

A ceramic sheet was obtained that was fabricated by a tape casting procedure. The unfired sheet consisted in majority of zirconia powder partially stabilized by 8 percent yttria by weight (MEL Chemicals), less than 1 % alumina by weight (AL-160SG, Showa Denko), polyvinyl butyral binder (Butvar B-98, Solutia Inc.), and ethanol and xylenes. The addition of Al_2O_3 reduces the grain boundary resistance by scavenging SiO_2 and forming mullite ($Al_6Si_2O_{13}$) upon sintering, which migrates into grain interiors where they have small influence on conductivity.[276] A proprietary combination of binders and dispersants were also used. The organic content including solvents comprised circa 35% of the weight of the feedstock materials for the green ceramic sheet. When dry, the green sheet measured 230 μm thick. Circles of unfired ceramic material were punched using cork borers of several different diameters of approximately 1 cm.

4.2.1 Reversible Bonding

In order to utilize microfabrication tools, the unfired ceramic samples were affixed to 4" silicon "handle" wafers using the following bonding agents: thermal release tape, photoresist, thermally conductive paste, or organic solvents. In addition, some investigations were performed with Aquabond™, a thermally activated adhesive.

First the wafers were cleaned of organics by immersion in a heated sulfuric acid and hydrogen peroxide (piranha) bath for ten minutes, rinsed in deionized water, and dried. The native oxide layer was not removed. Then adhesives were applied as described below.

---

[273] E. Rimini, <u>Ion Implantation: Basics to Device Fabrication</u>, (Springer, New York, 1995).

[274] Donald Leonard Smith, "Thin-film Deposition: Principles and Practice", (McGraw-Hill Professional, New York, 1995).

[275] Michael R. Oliver, <u>Chemical-Mechanical Planarization of Semiconductor Materials</u>, (Springer, New York, 2004).

[276] Barsoukov, 241.

Thermal Release Tape

Revalpha® double-sided 150ºC thermal release tape (3195H, Nitto Denko) was adhered to the green sheet. A cork borer was used to cut out samples of approximately 1 cm diameter. The samples were then affixed to a 4" silicon wafer.

Photoresist as Binder

Unfired ceramic samples were coated with hexamethyldisilane (HMDS, 98%, Alfa Aesar) in a vacuum oven in order to promote adhesion of the g-line positive photoresist (OCG 825, Olin Microelectronic Materials) that was subsequently applied as a binding agent. An SVG 4" coating track spun photoresist at 2200 RPM resulting in a 2 µm film. No softbake was employed. The ceramic samples were placed on the surface and pressed into place with wafer tweezers or a glass slide. The wafer and the attached green ceramic sample were placed in a vacuum oven at 120°C and pumped down to 6 mTorr to remove bubbles and to harden the photoresist.

Thermally Conductive Paste

Cool-Grease™ (CGR7016, AI Technology, Inc.) was applied sparingly to green sheet samples and placed on a wafer preheated at 50°C for 2 minutes. The sample was pressed in place using a glass slide, followed by 10 min on a hotplate at 50°C. Excess grease was dabbed away using a swab.

Organic Solvents

Two drops each of acetone, methanol, and ethanol were applied to a 4" wafer. An unfired ceramic sample was immediately placed on top of the area wetted by solvent. The solvent was allowed to dry for 10 min then driven off by placing the wafer and samples on a hotplate at 90° for 5 min. The experiment was later repeated for methanol at a temperature of 60°C.

Aquabond™

Aquabond 65™, a thermoplastic adhesive, was heated according to the manufacturer's instructions and used to secure unfired ceramic samples to a 4" wafer.

4.2.2 Photolithography

In order to pattern surface features such as trenches or electrodes, photolithographic methods were employed. Three photoresists were investigated: thin film, thick film, and dry thick film. A Karl Suss MA6 mask aligner equipped with a mercury bulb was used for exposure.

Thin Film Photoresist

G-line positive photoresist (OCG 825) was spun onto an unfired green sheet at 5000 RPM without any previous HMDS surface treatment. After softbake on a hotplate at 95°C for 60s, contact photolithography was performed for 6.5 s at 20 mW/cm^2 peak intensity. No post exposure bake step was carried out. The photoresist step height on the unfired ceramic was measured was measured with a stylus profilometer (Alpha-Step IQ). Development proceeded by immersion in OCG 934 developer for 30 s with intermittent agitation followed by rinsing in deionized water. The sample was not hardbaked.

Thick Film Photoresist

Thick film photoresists were investigated because of their utility as a mask during protracted period of etching. SPR-220 photoresist (Shipley Microelectronics) was spun onto a ceramic by a

coating track (SVG 8626) at 1800 RPM and softbaked at 115ºC on a hotplate for 5 minutes. The resulting photoresist film measured approximately 10 µm in diameter, but coverage was uneven. In addition, bubbles were readily visible in the photoresist (Figure 23 below).
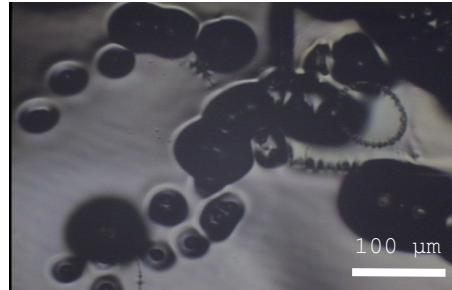
Figure 23. Bubbles in SPR-220 photoresist on surface of unfired ceramic sample.

The bubbles and uneven coverage prompted further experimentation. It was hypothesized that surface roughness affected the wetting of the green samples, which led to problems with coverage. Surface roughness is characterized by the amplitude parameter, R_a, which is the arithmetic average of absolute values of surface heights a surface measured by a stylus profilometer.

$$R_a = \frac{1}{n}\sum_{i=1}^{n}|y_i|$$

To reduce bubble formation, vacuum treatment and surface smoothing were employed. Vacuum treatment consisted of placing unfired ceramic samples coated with resist in a vacuum chamber under 3 mTorr vacuum for 15 min in an effort to rid the samples of bubbles.

Surface smoothing involved several methods that aimed to reduce the surface roughness of the surface of the unfired ceramic sheet: (1) pressing in an uniaxial press, (2) inducing reflow of organics by heating the green sheet, (3) smoothing surface by chemically inducing reflow using a solvent, and (4) depositing an intermediate layer of thin film photoresist. These methods are described below. The surface roughness was measured after each treatment with a stylus profilometer.

(1) Uniaxial press: Samples were pressed uniaxially for 30 s at 6,000 lbf.
(2) Reflow by heating: Samples that received thermal treatment were placed in a furnace at various temperatures (70°C, 90°C, 120°C, 150°C, 170°C, and 190°C) for 15 minutes followed by an equal amount of time for cooling.
(3) Reflow by solvent: One drop of methanol was added to the surface, allowed to dry in air for 5 min, dried at 70°C for an additional 5 min, and re-measured using the stylus profilometer. Once again, the average surface height parameter, R_a, was calculated to determine surface roughness. The surface roughness parameters of the three trials were averaged.
(4) Intermediate photoresist layer: A film was spun on at high speed (5,000 rpm) to fill in surface irregularities for the subsequent application of thick film photoresist. Two types of photoresist were investigated: OCG 825 g-line thin film photoresist and SPR-220 thick film resist.

The samples with the intermediate layer of thin film resist were subsequently coated with thick film photoresist. Contact lithography was performed on them with a Karl Suss photolithography tool for 15 s at 20 mW/cm^2 peak intensity. Following a hold time of 30 min

and a post exposure bake at 115ºC hotplate for 6.5 min, development took place in a tank using LDD-26W developer (Rohm-Haas) followed by rinsing in deionized water.

Dry Thick Film Photoresist

DuPont Riston® dry film negative photoresist FX930 measuring 30 µm in thickness was applied to the sample mounted on the handle wafer according to the manufacturer's instructions.[277] Contact photolithography was performed by exposing for 6.0 s at peak intensity of 20 mW/cm^2. The photoresist was developed in a 1% solution of potassium carbonate (anhydrous, 99%, Alfa Aesar) for 3 min.

4.2.3 Etching

Both wet chemical etching with hydrofluoric acid and dry plasma etching with oxygen and sodium fluoride were investigated.

Wet Chemical Etching

An etching solution consisting of CMOS grade hydrofluoric acid (HF, 49%, J.T. Baker) was used to etch an unfired ceramic sample that was reversibly bonded to a wafer by photoresist (OCG 825). Photoresist height and trench depth were measured with a stylus profilometer.

Dry Plasma Etching

Unfired ceramic samples were investigated in either an oxygen plasma or in a sulfur hexafluoride plasma using a Plasma-Therm PK-12 reactive ion etching apparatus. For the oxygen plasma, the oxygen flow was 50 sccm, power was 200 W, and duration was 6 min. The etching was interrupted to characterize the samples at 2 minute intervals. The sulfur hexafluoride plasma contained 10% oxygen; the conditions were 60 sccm of SF_6, 6 sccm of O_2 at 200 W power for 5 min.

4.2.4 Embossing

Unfired ceramic samples of PSZ were embossed with wires of the following nominal diameter 25, 50, 57, 60, 100, and 127 µm. Each wire was pressed into its own sample of unfired ceramic sheet. The sheets measured approximately 1 cm in diameter and were double thickness to avoid slicing through the sheet with the wire. Samples of individual sheet thickness were bonded together with a drop of ethanol. After drying, samples were pressed together for thirty seconds at three metric tons. Mylar sheets were inserted between the press and the samples to avoid sticking. Following pressing, the samples were sintered by firing to 1500°C for 5 hours using a low initial thermal ramp rate to drive off organic species.

4.3 Results and Discussion

Upon identification of appropriate temporary bonding agents to affix the unfired ceramic sheet substrates to the silicon wafer, further investigations of photolithography, embossing, and etching were possible.

---

[277] Dupont product literature, "DuPont™ Riston® Special FX900 Series Data Sheet and Processing Information", (accessed on Dec. 9, 2009), available from
http://www2.dupont.com/Imaging_Materials/en_US/assets/downloads/datasheets/fx900series.pdf.

4.3.1 Reversible Bonding

Unfired ceramic sheets were reversibly bonded onto handle wafers. This was performed successfully with photoresist, methanol, and Aquabond 65™ as described below.

Thermal Release Tape

Revalpha® Thermal Release tape was difficult and time consuming to cut. Removal of the transparent plastic backing film was not trivial. Although the tape generally adhered well to the silicon wafer substrate, the tape provided poor adhesion with the unfired ceramic due to the high surface roughness of the sample. The samples regularly detached during processing steps, making this method inappropriate for use. The tape itself, however, was easy to remove from the silicon wafers using a hotplate.

Photoresist as Binder

G-line photoresist (2 μm film) is easy to apply using the coating tracks. Photoresist provides better adhesion than thermal tape, although it can be somewhat difficult to remove using photoresist stripper. The long soak time in the strip bath tends to swell and soften the unfired sheet, distorting features.

Thermally Conductive Paste

Cool-Grease™ paste provides a weak, temporary bond that allows sliding of samples if provoked. The bond was not strong enough to fix a sample of unfired ceramic of 1 cm in diameter spinning at 5,000 rpm. The paste flowed out onto the wafer from under the unfired ceramic sample during thermal processing steps. In summary, this material did not meet processing requirements.

Organic Solvents

One drop of methanol sufficed to reversibly bond the sample to a silicon wafer. After applying the methanol, the drive out of the methanol performed at 90°C resulted in bulging of the surface of the sample due to solvent boiling. By driving out the methanol at a temperature below the boiling temperature of the solvent (T≤65°C for methanol), bulging did not occur. The unfired ceramic sample was removed from the wafer with a razor blade with care not to damage the sample. The other solvents that were tried did not yield satisfactory results; acetone evaporated too quickly to work with, and isopropanol did not cause sufficient adhesion.

Aquabond™

The Aquabond 65™ successfully fixed ceramic samples to a silicon wafer immersed in 49% HF for 20 minutes. It was not used with plasma etching because wafers in this tool sometimes reach a temperature at which the adhesive melts and flows

4.3.2 Photolithography

Three photoresists were tested for surface-patterning using standard UV-lithography.

Thin Film Photoresist

Good line definition was easily obtained using the OCG 825 thin film photoresist, as shown in Figure 24. A minimum feature size of 8 μm was obtained. The surface contours of the photoresist are readily visible. Conditions that usually yield a 1.3 μm film of photoresist when

spun on a silicon wafer resulted in an approximately 2.5 µm step height on the unfired ceramic sample.
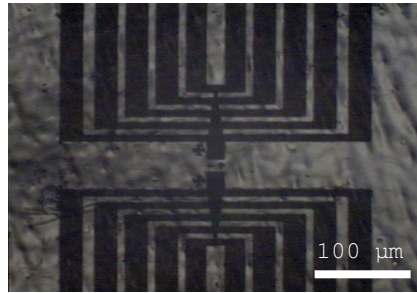
Figure 24. Pattern in g-line photoresist on unfired ceramic.

Although this photoresist exhibited the best pattern transfer ability, the thin film was not well suited for deep etching (several microns deep).

Thick Film Photoresist

The Shipley SPR-220 thick film photoresist provided numerous challenges with the unfired ceramic sheet. Although the thick film photoresist coats a smooth silicon wafer evenly and without bubbles, on the green sheet, it spun on unevenly and formed bubbles. The vacuum treatment failed to remove bubbles (Figure 25). In fact, outgassing appears to have created more bubbles.

Before   After
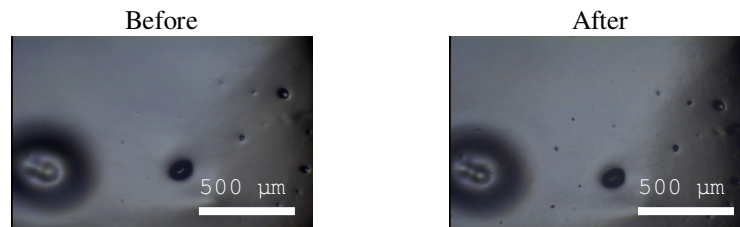
Figure 25. Effect of vacuum treatment on Shipley 220 photoresist.

Coverage problems were hypothesized to result from the surface roughness of the green sheet which negatively affects wetting of photoresist. Analogously, a water droplet does not wet a leaf on account of the epicuticular cilia of varying length that impart roughness.[278]

In these experiments with photoresist on the surface of unfired ceramic, surface roughness is indicated by the arithmetic average of the surface profile as expressed by the parameter, R_a. An unfired ceramic sheet typically has R_a of approximately 0.4 µm on its smooth side compared to an R_a of approximately 0.6 µm on the rough side. This difference arises due to the tape casting process; the rough side is exposed to a doctor blade. The smooth side with the lower R_a was typically used in experiments. For comparison, a silicon wafer and its native oxide layer has R_a of approximately 0.01 µm.

To reduce the roughness, the following methods were employed: (1) uniaxial press, (2) reflow by heating, (3) reflow by solvent, and (4) intermediate layer of thin film photoresist.

---

[278] Lu-quan Ren, Shu-jie Wang, Xi-mei Tian, Zhi-wu Han, Lin-na Yan, Zhao-mei Qiu, "Non-Smooth Morphologies of Typica1 Plant Leaf Surfaces and Their Anti-Adhesion Effects", Journal of Bionic Engineering, 4, (2007), 33-40.

All methods succeeded in reducing the surface roughness, but only the last treatment succeeded in reducing photoresist bubble formation. Table 8 presents the results of the various treatments.

Smoothing Treatment	Before R_a (µm)	After R_a (µm)	Decrease %
(1) Uniaxial press	0.437	0.338	23
(2) Heating reflow	0.316	0.312	1
(3) Solvent (methanol)	0.610	0.293	52
(4) Intermediate g-line photoresist layer	0.391	0.296	24

Table 8. Surface roughness before and after smoothing treatments.

The pretreatment methods that resulted in the smoothest samples did not resolve the coverage issues. These different smoothing treatment results are discussed in more detail below.

(1) Uniaxial press: The pressing technique resulted in a large decrease in the roughness of surface height, but bubbles persisted when the SPR-220 photoresist was spun on.

(2) Reflow by heating: The samples that received thermal treatment did not show significant variation in surface roughness (Figure 26). The change in the surface was small between 70° and 190˚C. The small increase in surface roughness at 120°C is attributed to the outgassing of organic species from the unfired ceramic sheet. This effect was not aberrant; rather it was repeated with the identical result. As the temperature increased from 150°C to 190°C, a minor decrease in the surface roughness was apparent. During the heat treatment, the ceramic samples experienced a weight loss of 9.8%, which is attributed to the loss of organic species.
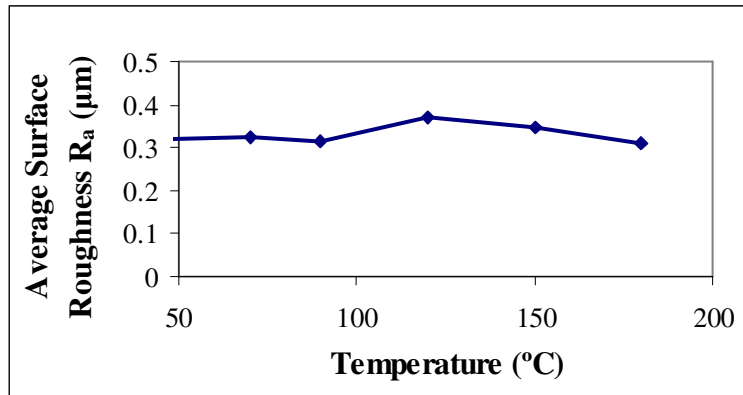
Figure 26. Average surface roughness as a function of temperature.

(3) Reflow by solvent: Treatment with methanol showed a reduction in surface roughness, but bubbles still persisted in thick film photoresist after spin-on. A reduction in surface roughness can be attributed to the dissolution of organic binders and plasticizers by the solvent, causing a localized rearrangement of species resulting in a smooth surface.

(4) Intermediate layer: Two different photoresists were spun on at 5,000 RPM. The g-line photoresist used as a smoothing agent succeeded in reducing the surface roughness considerably. No bubble formation was observed. For these samples, SPR-220 thick film photoresist was subsequently spun on for the purpose of photolithographic pattern transfer. Figure 27 shows the handle wafer with the unfired ceramic samples coated with an

intermediate layer of thin film photoresist and a layer of thick film photoresist. Clearly the coverage gradient problem persisted, as seen in Figure 28, which depicts a close up image of the rightmost sample in Figure 27. A buildup of photoresist is clearly visible on the side that faces the outer edge of the wafer. A similar result was observed for all samples. This unequal coverage occurs during the spin-on process.
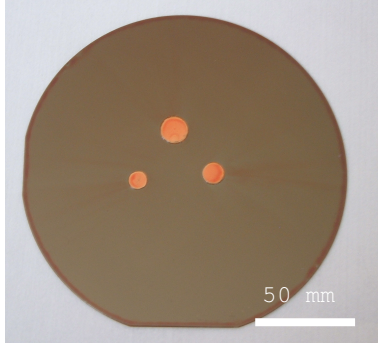
Figure 27. Four inch wafer with unfired ceramic samples coated with thick film photoresist.
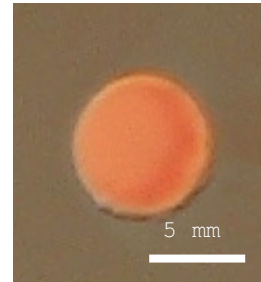
Figure 28. Close-up of unfired ceramic sample with coverage gradient.

Figure 29 shows the coverage gradient of the SPR-220 thick film photoresist as measured by a stylus profilometer. An edge bead is clearly visible at both extremities.
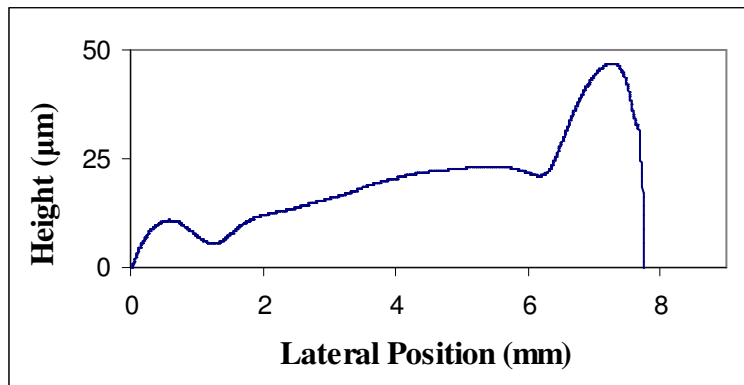
Figure 29. Coverage gradient of thick film photoresist on unfired ceramic sample.

When used as an intermediate smoothing layer, the SPR-220 thick film photoresist that was spun on at 5,000 RPM succeeded in eradicating bubbles, but despite the application at high angular velocity, the surface coverage gradient problem persisted. The thin film resist functioned better in this capacity.

Despite solving the bubble-formation problem with an intermediate smoothing layer of thin film photoresist, the SPR-220 thick film resist did not cover the surface of the unfired ceramic sheet evenly. Nevertheless, photolithography with this photoresist on unfired ceramic sheet was possible.

Other smoothing methods succeeded in lowering the average surface roughness (R_a) more as seen in Table 8, yet only the samples treated with an intermediate photoresist layer avoided bubble formation. These results suggest that surface roughness is not the primary factor that determines bubble formation in thick film photoresist.

Dry Thick Film Photoresist

DuPont Riston® dry film photoresist (FX930) obviated the issues with radial coverage gradient experienced with the wet thick film resist. It coated evenly and without bubbles. The manufacturer suggests that the minimum feature size is about half the thickness of the film (15 μm).[279] The minimum feature size is therefore smaller than what is possible using screen printing (approximately 50 μm with a film of circa 20 μm in height).[280]

Figure 30 depicts two images of square features patterned in dry film photoresist using the same mask. The image on the left is on a bare silicon wafer substrate; on the right, the film was applied to an unfired ceramic sheet. These experiments involved feature sizes well above the lower limitations stated by the manufacturer. With the unfired ceramic sheet, pattern distortion sometimes occurred. Despite wedge error compensation, sometimes the substrate was not perfectly parallel to the mask, resulting in regions of the wafer where the samples were outside the depth of focus of the photolithography tool. Some samples had images that were acceptable to proceed with etching.
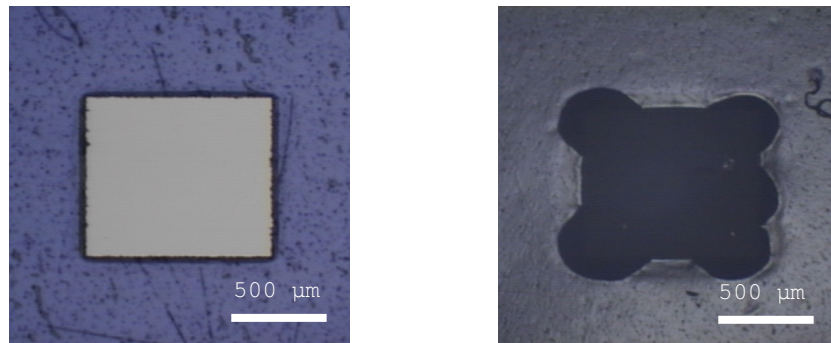
Figure 30. Images of dry thick film photoresist patterned on unfired ceramic sheet.

Gongora-Rubio *et al.* performed photolithographic patterning of partially sintered low temperature cofired ceramic (LTCC) using laminated dry photoresist film (Riston®). Their features measured in the tens and hundreds of microns.[281] Their experiences and ours confirm the resolution capabilities of the dry thick film photoresist in accordance with the manufacturer's product literature.[282]

4.3.3 Etching

G-line photoresist exhibited the best pattern transfer ability, but thick film photoresists are preferred for deep etching. Although photolithography with the thick film photoresist SPR-220 suffered from uneven coverage, it was used for some etching investigations. Dry thick film photoresist was also investigated.

---

[279] Dupont product literature, 3.
[280] Daniel C. Hughes, Steven E. Ernster, "Screen Printed Feature Size Capabilities", <u>Ceramic interconnect technology: the next generation</u>, IMAPS conference on ceramic interconnect technology, (Denver, CO, Apr. 7-9 2003), 58.
[281] Gongora-Rubio, 229.
[282] Dupont product literature, 3.

Wet Chemical Etching

The hydrofluoric acid etched the SPR-220 photoresist isotropically, as expected. Figure 31 shows the progression of etch depth with time. In this diagram, the vertical position "0" represents the surface of the unfired sheet. The isotropic nature of the etching process is evident from the diagram. Over time, the sample begun to delaminate from the wafer, causing the sample to curl. Photoresist was used as the bonding agent.
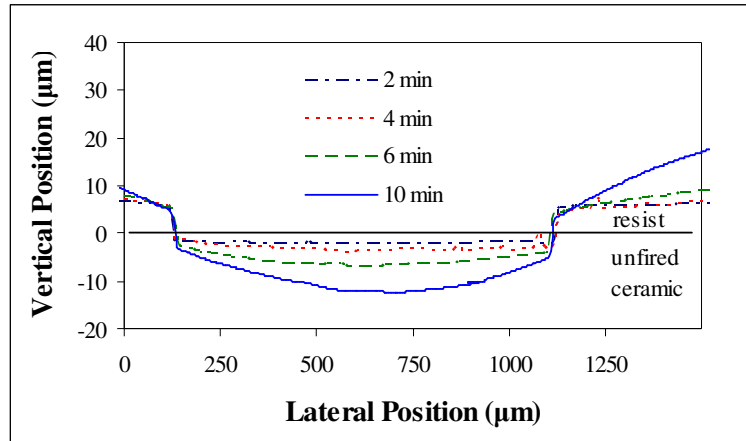
Figure 31. HF etching of unfired ceramic.

A plot of the log of etch depth versus time is shown in Figure 32. The etching process appears to follow a power law. An excellent fit for the trend line that fits this etching curve was obtained with $R^2 > 0.99$.
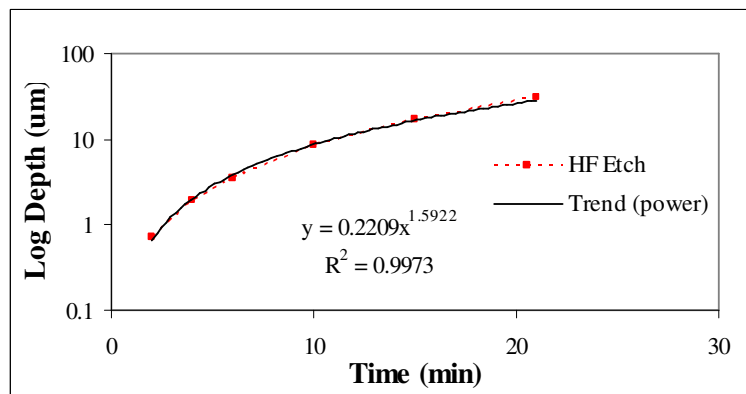
Figure 32. Semi log plot of HF etching over time.

Gongora-Rubio *et al.* discuss HF-etching of partially sintered low temperature cofired ceramic (LTCC). They first partially sintered the ceramic tape before pattern transfer in order to enable etching of the glass component using HF. LTCC contains higher glass content than HTCC which HF chemically attacks. They also reported exfoliation of the surfaces of the sheet. No exfoliation was observed in these experiments; rather exposure to HF caused the unfired green sheet to soften.[283]

---

[283] Gongora-Rubio, 229.

In a bath of 49% HF, the bulk of the dry film resist Riston[®] FX930 disintegrated, however, at the point where the resist contacted the wafer, a film of resist remained. Espinoza and Santiago reported HF-etching resistance for several hours of a similar product, Riston® 9015.[284]

Dry Plasma Etching

Neither the oxygen plasma nor the sulfur hexafluoride plasma succeeded in producing detectible etching of the unfired ceramic sheet. The lack of etching was initially attributed to reflow of the organic materials (binder and plasticizer). An investigation of reflow, however, concluded that no reflow was observed below 190°C, as discussed above. An alternative hypothesis is that ceramic particles insulate the underlying unfired ceramic sample from etching. The plasmas made the unfired ceramic samples dry and brittle.

The dry thick film photoresist Riston FX930 proved to be an acceptable photoresist for plasma etching. Although it degraded somewhat during etching, during the time interval that the etching was performed, it did not etch all the way through. Figure 33 depicts the result of O_2 plasma etching an unfired ceramic patterned with dry thick film photoresist. It shows the profile of a ceramic green sheet at several intervals during the O_2 plasma etching process. No etching of the unfired ceramic was detected. It is possible that the ceramic powders near the surface shielded the sample from chemical attack.
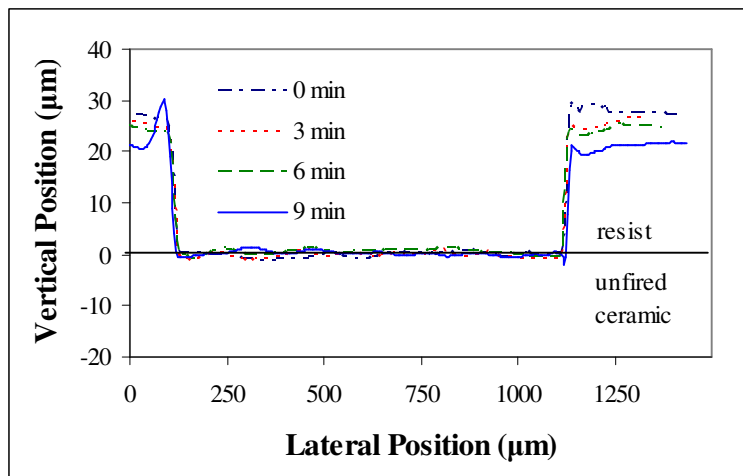
Figure 33. O_2 plasma – no etching of unfired ceramic observed.

Although plasma etching failed to affect the unfired ceramic material, the process of stripping the photoresist had a pronounced effect on surface roughness. Figure 34 shows that the surface of the green sheet developed considerable roughness during the strip. Prior to the resist removal step, R_a equaled approximately 0.250 μm, whereas afterwards the value was over 10 μm, an increase of almost two orders of magnitude. The surface was no longer smooth, and any micron-scale features in the green sheet would have been degraded.

[284] Patricio Espinoza-Vallejos and Jorge Santiago-Avilés, "Photolithographic Feature Fabrication in LTCC", The International Journal of Microcircuits and Electronic Packaging, 23:3, (2000), 288.
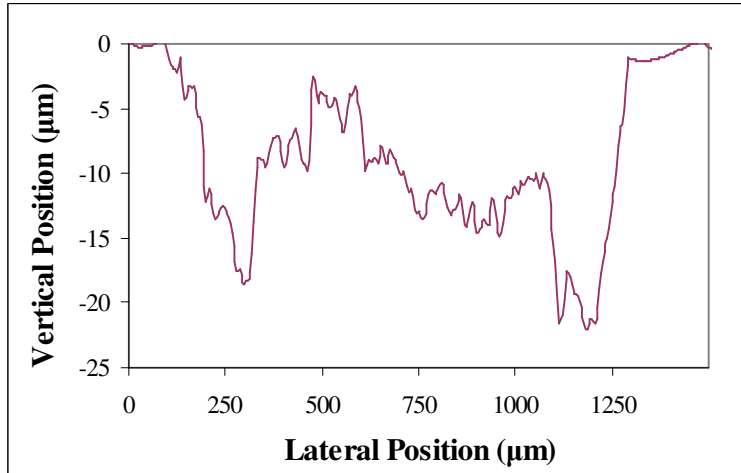
Figure 34. Roughness changed during photoresist strip after unsuccessful plasma etching.

The results of plasma-etching with SF_6 appear in Figure 35. Similar to the experiments with O_2 plasma, no etching of the unfired ceramic sheet was observed. In addition, the photoresist strip step after etching also changed the surface roughness drastically (not shown).
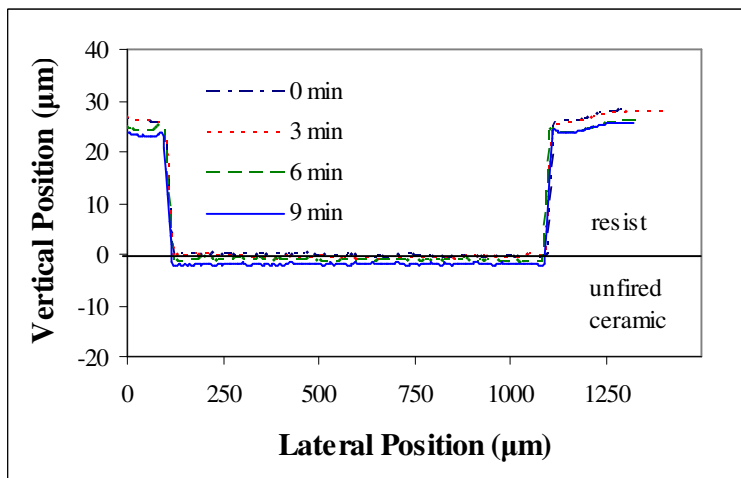
Figure 35. SF$_6$ plasma - no etching of green sheet observed.

In summary, plasma-etching was not successful with green sheet.

4.3.4 Embossing

Embossed wire patterns formed vias and ducts in the ceramic material. These shapes could serve as gas flow channels. Results from the meso-scale embossing study are presented in Table 9. A reduction in feature size greater than 40% was observed after the sintering process.

64

Sample	Nominal Wire Diameter (μm)	Average Trench Depth after Sintering (μm)	Reduction in Size after Sintering
1	25	11	56%
2	50	29	42%
3	57	32	44%
4	60	33	45%
5	100	61	40%
6	127	72	43%

Table 9. Meso-scale embossing of unfired ceramic sheet.

Shan *et al.* used hot embossing techniques to make channels 25-100 μm wide in unfired ceramic sheet. They reported reduction in depth of 20-22% after firing.[285]

4.4 Conclusions

Surface machining processes were attempted on an unfired ceramic sheet of yttria-stabilized zirconia. Photoresist, methanol, and Aquabond™ were identified as adequate bonding agents to attach samples to handle wafers, but removal sometimes resulted in the distortion of features. For photoresists, no one photoresist worked ideally under all conditions. Thin film OCG-825 had the best pattern transfer of all on unfired ceramic sheet. Thick film photoresist SPR-220 exhibited a coverage gradient on unfired ceramic sheet despite spinning at high angular velocity and surface smoothing treatments. Dry photoresist film held up well during plasma etching, but the removal process drastically altered the sheet roughness. Chemical etching with HF was more effective on unfired ceramic sheet than plasma etching. HF etched unfired ceramic sheet isotropically, but the photoresist removal step distorted features. Plasma etching was unsuccessful. Wire-embossing was carried out successfully with feature shrinkage above 40%. These findings may apply to a variety of unfired ceramic sheets, even ones of different ceramic composition, as long as the organic contents are similar.

In summary, processing unfired ceramic sheet using micromachining methods presented several difficulties. These results encourage future work on unfired substrates using thick film methods and on pre-sintered substrates using thin film technologies.

---

[285] Xuechuan Shan, H. P. Maw, R. T. Tjeung, S. H. Ling, C. W. Lu, R. Jachowicz, "Microstructure formation on low temperature co-fired ceramic green substrates using micro embossing", <u>Microsyst Technol</u>, 14, (2008), 1409.

CHAPTER 5: NO$_x$ Sensor with Gold Wire Working Electrodes

NO$_x$ sensors were fabricated with gold wire electrodes and examined using impedance spectroscopy techniques. The impedance signal is invariant to total flow rate. A linear relationship exists between the shift in phase angle and quantity of NO at concentrations between 25 to 100 ppm. Sensitivity to NO$_x$ species is larger than to O$_2$ by several orders of magnitude. A larger response for NO$_2$ compared to NO was found at 650°C. At 1 kHz, phase angle were dependent on both NO and O$_2$ concentrations, preventing the self correction for O$_2$ concentration. The largest phase angle shift due to NO$_x$ was found at 600°C, the lowest temperature investigated. At 10^5 Hz, phase angles correlated linearly to temperature, independent of gas species. An equivalent circuit model was identified with a good fit to the data: R$_0$-(R$_1$C$_1$)-(R$_2$Q$_2$). In this model, the lone resistor, R$_0$, represents YSZ bulk resistance; the first Voigt element (R$_1$C$_1$) represents the electrode bulk properties, and the Cole element (R$_2$Q$_2$) represents the electrode-electrolyte interface. Exposure to NO$_x$ affects the parameters of the Cole element. R$_2$ varied linearly with NO content from 1-100 ppm. R$_2$ is suggested as an indicator of NO$_x$ species.

5.1 Introduction

Diesel engines emit more particulates than gasoline engines due to the non-stoichiometric nature of combustion in diesel engines. The non pre-mixed nature of diesel combustion inevitably results in pockets of lean and rich gases that contribute to incomplete combustion. In addition, flame velocities are slower in non-stoichiometric conditions; as a result, not all fuel reacts and some is expelled in the exhaust.

Diesels also emit more NO$_x$ than gasoline engines because reducing the NO is difficult in the presence of excess air. A sensor can be used to monitor the NO$_x$ cleanup unit of a diesel vehicle in order to abate emissions from lean engines by providing a signal to the engine control unit. Commercial NO$_x$ sensors for diesel exhaust analysis consist of multiple electrochemical cells in series: the first amperometric cell removes O$_2$ so that a subsequent one can detect NO$_x$ concentration by dissociating the NO$_x$ and measuring the pumping current as oxygen from the NO$_x$ is expelled.[286]

Impedancemetric gas sensors for NO$_x$ detection are less developed than amperometric or mixed potential types.[287] They usually have an electrolyte of YSZ and electrodes of either noble metal or metal oxide. Certain gases influence the impedance at low frequencies (f $\leq$ 100 Hz).

Miura *et al.* proposed the first single cell impedancemetric NO$_x$ sensor with YSZ electrolyte. It had a solid oxide sensing electrode. They linearly related total NO$_x$ concentration (both NO and NO$_2$) to changes in modulus, ΔZ, at 0.1 from 50 to 400 ppm.[207] They proposed an equivalent circuit model.[288] Electrode thickness and coatings equilibrated reactive species resulting in a nearly equivalent response to NO as to NO$_2$.[289] Miura's group also investigated sensors with In$_2$O$_3$ electrodes to detect water vapor (steam) in which the change in modulus of

[286] Marek, 502-504.
[287] Fergus, (2007), 659.
[288] Miura, (2003), 221–228.
[289] Miura, (2006), 979–986.

was linear over several orders of magnitude of H_2O concentration (70–30,000 ppm).[290] This sensor also detected hydrocarbons in dry gas indirectly by sensing the water vapor generated by their oxidation at the electrodes.[291] An improved sensor selectively detected propene (C_3H_6) in a humidified gas stream using a sensing electrode of ZnO and Pt with limited cross sensitivity.[292] It detected propene at extremely low concentrations: 0.05 – 0.8 ppm.[293]

Other research groups have investigated impedancemetric sensors as well. Martin *et al.* made NO_x sensors with composite electrodes of Cr_2O_3 and YSZ. This group measured NO_x sensitivity by the shift in phase angle, which was linear for NO_x concentration between 8-50 ppm. A compensation method for cross sensitivity to O_2 was proposed.[294] This compensation method was further explored in a subsequent publication that involved an equivalent circuit analysis and an in depth examination of the resistance of the Cole element in their equivalent circuit.[295] Martin found some drift in his signal, as did a coauthor, Murray, in investigations of NO_x sensors of $LaCr_{0.95}Mg_{0.05}O_3$ on fully stabilized YSZ. Cross sensitivity to O_2 would require monitoring O_2 for accurate sensing.[296] Martin's colleague, Woo, investigated planar, YSZ-based NO_x sensors with dense gold electrodes and porous electrolyte. The porosity of the YSZ enabled enhanced NO_x sensing that was attributed to improved adsorption rates as the rate-limiting step.[297] In a follow up paper, Woo found further evidence that suggested adsorption as the sensing mechanism and in specific, competition for adsorption sites.[298] Woo *et al.* further suggested that a dearth of electrochemical reaction sites on electrodes may play a role in NO-sensing on gold electrodes.[299] Woo *et al.* offered that good NO_x sensing electrodes should be poor O_2 catalysts (gold). In addition, electrolyte thickness played a role: thinner electrodes were preferred for total NO_x sensing (equivalent response to both NO and NO_2).[300]

Stranzenbach *et al.* investigated planar, impedance-based NO_x sensors with sputtered $NiCr_2O_4$ sensing electrodes on both fully stabilized YSZ and PSZ electrolyte. They found a linear change in modulus over NO concentration of 200-1000 ppm. By performing equivalent circuit modeling, they proposed that the electrode reaction and diffusion were responsible for NO_x sensing.[301] Stranzenbach and Saruhan also examined NiO as the sensing electrode; it demonstrated excellent selectivity for NO.[302] Their equivalent circuit fit sensors with NiO and $NiCr_2O_4$ electrodes.[303]

Wu *et al.* examined an electrochemical CO sensor with an electrode of Au-doped Ga_2O_3 and an electrolyte of YSZ.[304] Shimizu *et al.* investigated a lithium solid electrolyte $Li_{1.5}Al_{0.5}Ti_{1.5}(PO_4)_3$ for use in NO_x sensors. This electrolyte operates at a lower temperature

[290] Nakatou, (2004), 995–998.
[291] Nakatou, (2005), 2411–2415.
[292] Nakatou, (2006), 57–62.
[293] Wama, (2007), 2774–2777.
[294] Martin, <u>Mater Res Soc Symp Proc</u>, (2007).
[295] Martin, <u>J Electrochem Soc</u>, (2007), J97-J104.
[296] Murray, (2007), J97-J104.
[297] Woo, <u>Mater Res Soc Symp Proc</u>, (2007).
[298] Woo, <u>J Electrochem Soc</u>, (2007), J129-J135.
[299] Woo, (2008), J32-J40.
[300] Woo, (2009).
[301] Stranzenbach, Gramckow, Saruhan, (2007), 224–230.
[302] Stranzenbach and Saruhan, (2007), 983-986.
[303] Stranzenbach, (2009), 154–163.
[304] Wu, 49–53.

(400-500ºC) than zirconia electrolytes. They examined several different types of oxide electrodes including some perovskites and semiconductors.[305]

Some drawbacks exist with impedance-based sensors. Selectivity remains a challenge. Long term stability of these sensors is lacking. They are still more complex and expensive than potentiometric ones, especially their electronics and signal processing equipment. The sensing mechanism is poorly understood. [306] As a result, impedancemetric sensors are not yet commercially available.

Nevertheless, impedancemetric NO_x sensors have shown improved sensitivity over commercially available amperometric sensors, [307] which do not detect NO_x at low enough concentration to meet stringent future HD OBD regulations according to vehicle manufacturers.[308] In addition, impedancemetric NO_x sensors have an advantage over the mixed potential variety: both NO and NO_2 cause a shift in signal in the same direction using impedance-based techniques, which is contrary to the mixed potential sensors whose output EMF is negative with NO and positive with NO_2.[309] As a result, these responses interfere with one another and hinder accurate NO_x detection.

To perform an impedance measurement on an electrochemical cell, an alternating voltage is applied at a specific frequency, and the resulting current signal is recorded. Impedance is calculated as the ratio of small signal voltage over current. By sweeping a range of frequencies and plotting the impedances on a Nyquist plot, the capacitive arcs that result reveal information about the sensor. Upon exposure to an electrochemically reactive gas, the magnitude of the impedance changes, as does the phase angle. The modulus is less sensitive than the phase angle.[310, 311]

Electrodes and operating temperatures can be tailored to make a sensor selective to desired species. Platinum generally does not make a good electrode material for NO_x detection because a low frequency arc is not resolved with this material. [312, 313] In order for an impedancemetric sensor to function, a low frequency process associated with a time-constant relaxation must occur.

The electrochemical system of gold electrodes and yttria-stabilized zirconia (YSZ) electrolyte has been investigated in the literature. In particular, the O_2 exchange reaction has

[305] Youichi Shimizu, Satoko Takase, Daisuke Koba,"A NO_x Sensor Based on Solid-Electrolyte Impedance Transducer", <u>Adv Mater Res</u>, 47-50, (2008), 479-482.
[306] Zhuiykov, (2008), 127-8.
[307] Martin, (2007), J97-J104.
[308] California Air Resources Board, "Technical Status and Revisions to Malfunction and Diagnostic System Requirements for 2010 and Subsequent Model Year Heavy Duty Engines (HD OBD)", (Sep. 11, 2008), 16.
[309] Norio Miura, Perumal Elumalai, Vladimir Plashnitsa, Taro Ueda, Ryotaro Wama, and Masahiro Utiyama, "Solid-State Eectrochemical Gas Sensing", in <u>Solid State Gas Sensing</u>, E. Comini, G. Faglia, G. Sberveglieri (eds.), Springer, New York, (2009), 201.
[310] Orazem, 315-6.
[311] Martin, (2007), J97-J104.
[312] Barsoukov, 235.
[313] Woo, <u>J Electrochem Soc</u>, (2008), J32-J40.

been modeled[314] and the impedance has been measured as a function of temperature, partial pressure of O_2, and overpotential.[315]

The NO_x sensors under investigation consist of a similar system but NO_x was used as the analyte gas. Working electrode were composed of a dense gold coated with porous electrolyte. The electrodes contact a porous, fully stabilized electrolyte layer. The counter electrode consists of porous platinum. These elements are stacked vertically on a tile of dense alumina (Figure 36). Leads of porous platinum provide conduction paths to the edge of the tile, where they connect with gold wires to interrogate the cell (not shown).
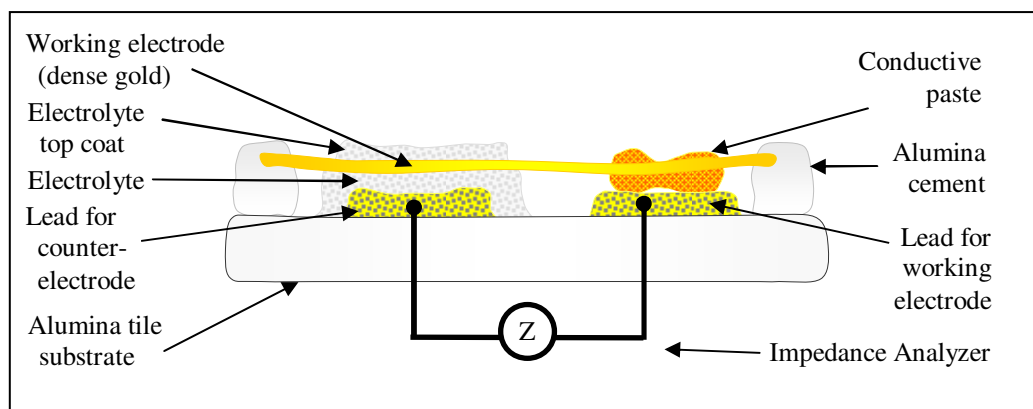
Figure 36. Schematic cross section of a NO_x sensor with gold wire electrodes (not to scale).

Operation of the sensor proceeds as follows: gaseous species such as NO, NO_2, and O_2 diffuse through the porous electrolyte topcoat. This layer increases the interface between the electrode and electrolyte, enhancing the detection of NO_x species. The gas species to be detected react electrochemically. The attendant transfer of electrons alters the conductivity between the leads, which is detected by an impedance measurement.

This investigation has the specific objectives of exploring the performance of impedance-based sensors with gold electrodes, including:

- effect of flow rate on phase angle

- relationship between NO_x concentration and phase angle below 100 ppm

- relative effect of O_2, NO, and NO_2 concentrations

- detection of O_2 and NO_x simultaneously

- effect of temperature on device performance

- equivalent circuit modeling

In the following pages, the results of the explorations into these areas are reported.

---

[314] B.A. van Hassel, B.A. Boukamp and A.J. Burggraaf, "Electrode polarization at the Au, $O_{2(g)}$/yttria stabilized zirconia interface. Part I: Theoretical considerations of reaction model", <u>Solid State Ionics</u>, 48, (1991), 139-154.

[315] B.A. van Hassel, B.A. Boukamp and A.J. Burggraaf, "Electrode polarization at the Au, $O_{2(g)}$/yttria stabilized zirconia interface. Part II: Electrochemical measurements and analysis", <u>Solid State Ionics</u>, 48, (1991), 155-171.

5.2 Experimental

Sensors were constructed on 1 cm^2 dense alumina substrates by painting leads of platinum ink (Engelhard 6082) in parallel stripes 1 mm wide and 1 mm apart and fired at 1200°C for 2 hours in air inside a Thermolyne muffle furnace. A low thermal ramp rate was followed early in the firing cycle to accommodate the burnout of organic species. Subsequently, an electrolyte layer of zirconia fully stabilized by yttria was applied as a slurry on top of one platinum stripe (counter electrode) and allowed to dry. On top of the electrolyte, gold wires measuring 10 mm in length were placed and attached to the other platinum lead using gold/palladium conductive paste (Engelhard A3770), thereby forming the working electrode. The sensing wires were anchored to the alumina tile with alumina cement (Aremco Resbond 920). Figure 37 depicts overhead view of a typical sensor at this stage of fabrication (prior to the application of the electrolyte top coat and gold interrogation leads).
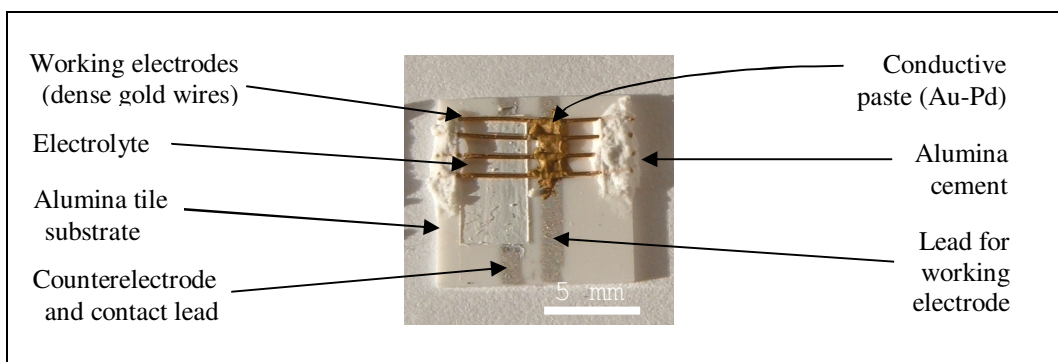
Figure 37. Top view of gold wire NO$_x$ sensor (top coat of porous YSZ not shown).

The sensing wires were further coated with three coats of electrolytic slurry. In order to provide a means to interrogate the sensors, gold wires were attached to the platinum leads using the gold/palladium paste. These wires were also anchored to the substrate using alumina cement. The sensors were allowed to dry and then fired at 1000°C for 2 hours, once again taking care to ramp the temperature gradually to burn out organic species.

The sensors were attached to gold lead wires and loaded into a quartz tube for analysis . using electrochemical impedance spectroscopy (EIS). Figure 38 depicts the experimental setup schematically.
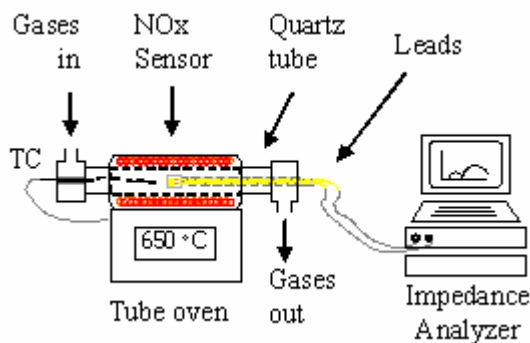
Figure 38. Experimental setup: NO$_x$ sensor in quartz tube furnace.

Several experiments were performed, including the influence of variable flow rate (100-500 sccm), NO and NO_2 individually (0, 25, 50, and 100 ppm), O_2 (4-19%), and temperature (600-700°C). All experiments were performed at 650°C in 500 sccm of 10% O_2 unless otherwise noted. The balance of the gas flow consisted of N_2 or N_2 and NO_x. Frequency sweeps between 1 MHz and 1 Hz were performed at 25 mV excitation amplitude. The impedance response was recorded using a Solartron Analytical SI 1260 impedance/gain-phase analyzer in combination with a Solartron Analytical SI 1287 electrochemical interface controlled by ZPlot data acquisition software (Scribner Associates, Inc.). The use of a reference electrode in a conventional three electrode cell is difficult for systems with solid electrolytes on account of the cell geometry, so a two electrode configuration was employed.[316] Ten measurements per decade were recorded. Two sweeps were performed for each sensor at each flow rate, gas composition, and temperature. Overlap of the two resulting impedance spectra confirmed repeatable measurements under steady state conditions.

Phase angles were calculated at a specific frequency (10 Hz) and subtracted from the base case of 0 ppm NO_x in order to obtain the phase angle difference. This difference was related to species concentration. The phase angle difference was the primary metric used to evaluate sensor performance.

Sensitivity to flow rate was investigated by performing EIS on a gas stream comprised of 10% O_2 with 100 ppm NO at different flow rates from 100 to 500 sccm. The sensing responses to NO and NO_2 were investigated by varying concentrations from 0 to 100 ppm in 10% O_2 and balance N_2. Bottles of 1000 ppm NO_x in N_2 were diluted with air and N_2 to obtain the desired concentrations. Sensor responses due to various concentrations of O_2 from 4-18.9% in balance N_2 were recorded. After changing the test gas concentration, at least 3 minutes elapsed in order to ensure steady state process gas conditions. A study was undertaken to determine if one sensor can simultaneously detect both O_2 and NO_x by examining phase angles at different frequencies (10 Hz and 1 kHz). The effect of temperature was also examined between 600-700°C. Equivalent circuit models were examined using LEVM software.[317] All parameters were allowed to vary in order to account for the effects of microstructural aging.

5.3 Results and Discussion

Data obtained by recording the impedance response of each sensor to various influences was analyzed by making Nyquist plots, by calculating phase angle differences at 10 Hz, and by performing equivalent circuit analysis. A discussion of each variable factor follows.

---

[316] Barsoukov, 518.

[317] James Ross Macdonald, LEVM/LEVMW Version 8.09 Complex Nonlinear Least Squares Fitting Program, (accessed on Dec. 16, 2009), available from http://www.jrossmacdonald.com/levminfo.html.

5.3.1 Flow Rate

In order to determine if diffusion through the boundary layer would be affected by normal variation of exhaust flow, the effect of flow rate on sensor output was examined. A mixture of
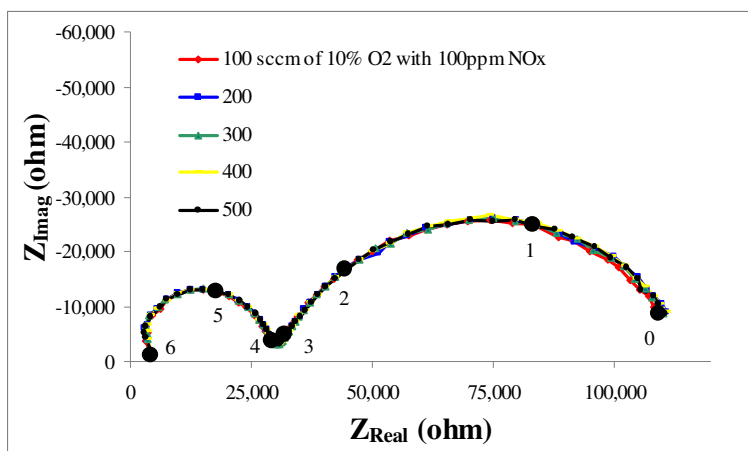
Figure 39. Impedance response is independent of flow rate.

10% O_2 with 100 ppm NO evoked the same impedance response from 100 to 500 sccm as shown in Figure 39. Numerals in the figure indicate the logarithm of the measurement frequency. Frequencies at each decade are indicated by filled circles on the plot. The diameter of each semicircular arc reflects the resistance of each process associated with each arc. Whereas the high frequency arcs overlap regardless of gas mixture, here the electrode-sensitive low frequency arcs (f < 1 kHz) overlap as well. Impedance measurements are independent of flow rate; they depend only on the composition of the mixture. Nakatou and Miura found similar results for an impedance-based sensor for a different analyte gas.[318]

5.3.2 NO$_x$ Sensing

Sensors were exposed to NO and NO_2 at 0, 25, 50, and 100 ppm. Additional concentrations of NO (30, 40, and 75 ppm) were examined in order to examine in detail the relationship between phase angle difference and NO concentration. The Nyquist plots for NO and NO_2 are shown in Figure 40 and Figure 41, respectively. Arabic numerals indicate the log of the interrogation frequency. For reference, each decade of frequency is indicated for the base case (10% O_2/N_2) by filled circles. The Nyquist plots exhibit two arcs: a small high frequency arc and a larger low frequency arc. Consistent with previous findings, NO$_x$ affects the low frequency measurements (f < 1 kHz).[319, 320, 321, 322, 323, 324, 325, 326, 327] In specific, NO$_x$ reduces the impedance response of the sensor at low frequencies.

---

[318] Nakatou, (2006) 57-62.

[319] Miura, (2002), 286.

[320] Miura, (2003), 224.

[321] Miura, (2004), 1138.

[322] Martin, J Electrochem Soc, (2007), J97-J104.

[323] Woo, J Electrochem Soc, (2007), J130.

[324] Woo, (2008), J35.

[325] Stranzenbach, Sensor Actuator B Chem, (2007), 226.

The high frequency arcs (10^4-10^6 Hz) are nearly perfect semicircles, indicating that the impedance can be attributed to a single activation-energy controlled relaxation process.[328]

Both NO and NO_2 evoke an inward shift of the low frequency arc. NO_2 evokes a larger shift than an equivalent concentration of NO when evaluated at 650°C. Miura *et al.* reported nearly identical responses to NO and to NO_2 at 700°C allowing total NO_x detection regardless of their relative concentrations.[329, 330] This finding may result from thermodynamic equilibrium that establishes itself at increasing temperatures above 600°C in which NO_2 dissociates to NO.[331, 332]
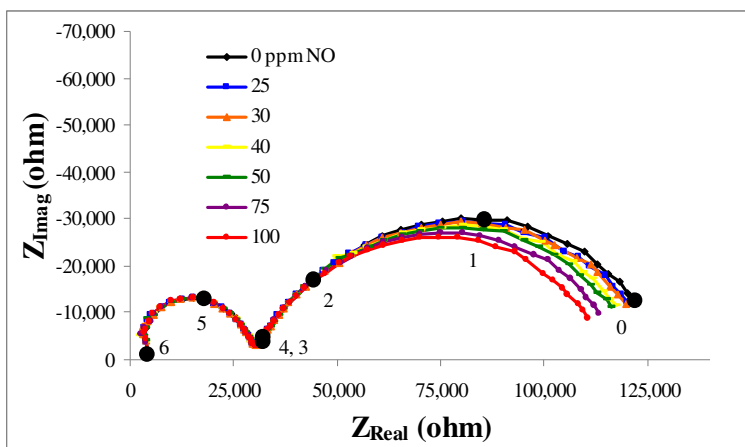
Figure 40. Sensor impedance response decreases with increasing NO content.
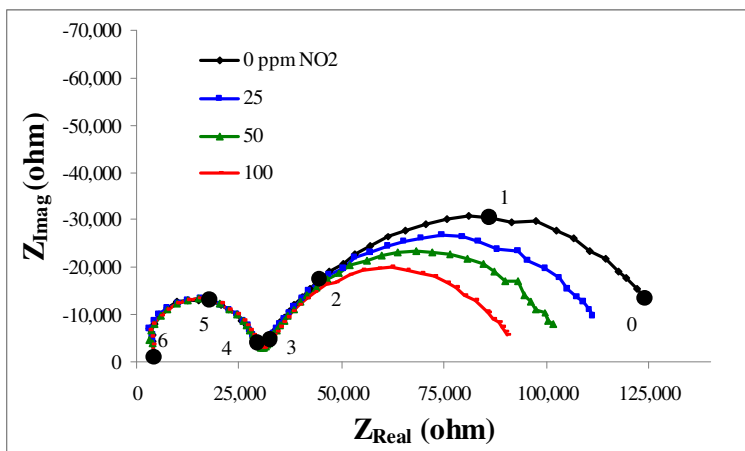
Figure 41. Sensor impedance response decreases with increasing NO_2 content.

A linear relationship exists between the change in phase angle and NO concentration from 25-100 ppm, as demonstrated in Figure 42. The experimental setup for this study limited NO_x concentration to a minimum of 25 ppm. A linear regression of the experimental data had a high

[326] Murray, 57.

[327] Stranzenbach, (2009), 156.

[328] Orazem, 313.

[329] Miura, (2002), 284–287.

[330] Miura, (2003), 221–228.

[331] Zhuiykov, (2008), 215.

[332] Woo, J Electrochem Soc, (2007), J133.

R^2 value of 0.9923, indicating a good fit. This fitted line, however, does not pass through the origin. The intercept with the abscissa is at 13.7 ppm; at this concentration, the sensor would have a phase angle shift of zero in the presence of NO, meaning the sensor does not respond to NO. It is preferable that the linear relationship between NO_x concentration and phase angle shift include the origin in order to detect at low concentrations. When the origin is included in the regression data, the R^2 deteriorates to 0.9398. Martin *et al.* reported linear relationships between phase angle shift and NO_x concentration in the range of 8-50 ppm over a wide range of O_2 concentrations. These lines generally passed through the origin.[333]
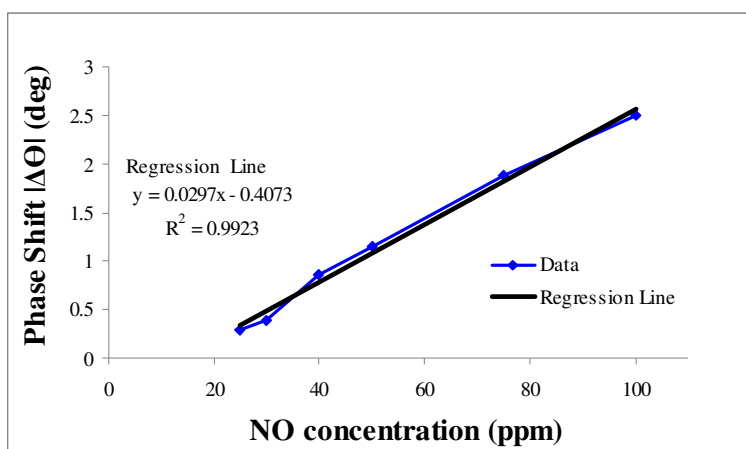
Figure 42. Phase angle difference varies linearly with NO content.
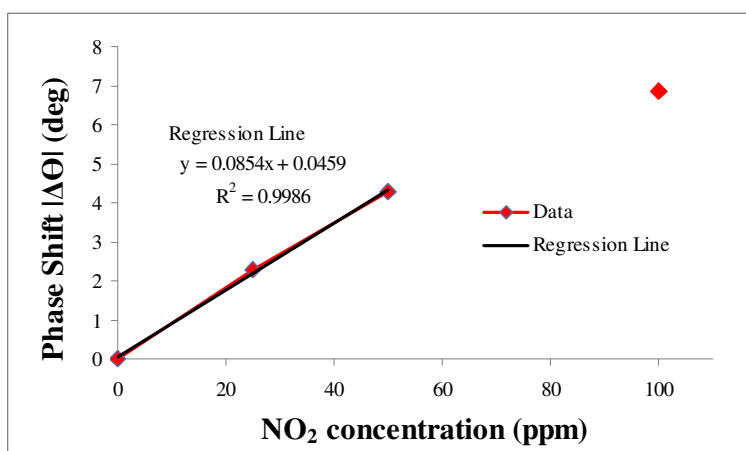
Figure 43. Phase angle difference varies linearly with NO$_2$ content.

For NO_2 (Figure 43), the data analysis yielded a linear relationship but over a smaller range of concentration. From 0-50 ppm, a regression line fits the data between very well ($R^2 = 0.9986$), however, only three data points were recorded in this range, including zero NO$_2$. The data point at 100 ppm is also shown for reference. When this point is included in the regression, the fit is still very good ($R^2 = 0.9797$), but the regression line no longer passes through the origin. Although these results show promise for a low concentration sensor, additional data points are necessary to be conclusive.

---

[333] Martin, <u>J Electrochem Soc</u>, (2007), J97-J104.

A phenomenon was observed in which the sensor required a protracted time to recover from the exposure to NO_2. The low frequency arc of the impedance spectrum shifted inwards (smaller Z_{Real}) due to NO_2 as seen in Figure 41, but after the NO_2 supply was shut off, the spectrum did not return to the same position as before exposure to NO_2. Rather, flowing the base case gases (10% O_2 in N_2, 0 ppm NO_x) caused the low frequency arc to shift outwards to larger impedances in comparison to before flowing NO_2. This effect was transient and repeatable. Figure 44 shows the recovery of the impedance spectrum. Over time, the low frequency arc shifted back inwards. Eventually the entire spectrum overlapped the pre-exposure case. Recovery of the impedance spectrum occurred after 2½ hours. This effect may be caused by species that reversibly adsorb on sites of electrochemical reactions and impede reactions with O_2. In a later experiment, increasing the temperature to 800°C following NO_2 exposure was attempted to assist with the recovery of the low frequency arc. The thermal treatment did not bring about an immediate recovery. This temporary poisoning effect might be circumvented by shifting NO_2 to NO at increased temperature using a rhodium catalyst before sensing, however, no investigation thereof is made here.
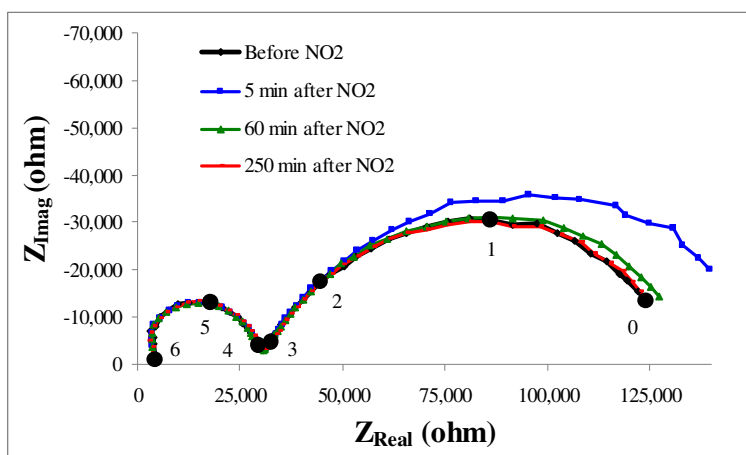
Figure 44. Nyquist plot detailing recovery of sensor to NO_2.

West *et al.* reported that recovery time was required after exposure to NO. The time decreased with increasing temperature.[334]

5.3.3 Cross Sensitivity

In addition to NO_x species, the sensor responds to the excess O_2 that is likely to be found in diesel exhaust. It might also be sensitive to HCs, but its location downstream of an oxidation catalyst may mitigate this concern. This section explores the effect of the excess oxygen, compares the response of the sensor to O_2 and NO_x species, and examines a compensation strategy for the O_2.

---

[334] David L. West, Fred C. Montgomery, Timothy R. Armstrong, "NO-selective" NO_x sensing elements for combustion exhausts", <u>Sensor Actuator B Chem</u>, 111–112, (2005), 84–90.

Effect of O_2

Figure 45 depicts the effect that changing the oxygen concentration has on the response signal. Filled circles indicate decades of frequency shown on the spectra for the highest and lowest concentrations of O_2.
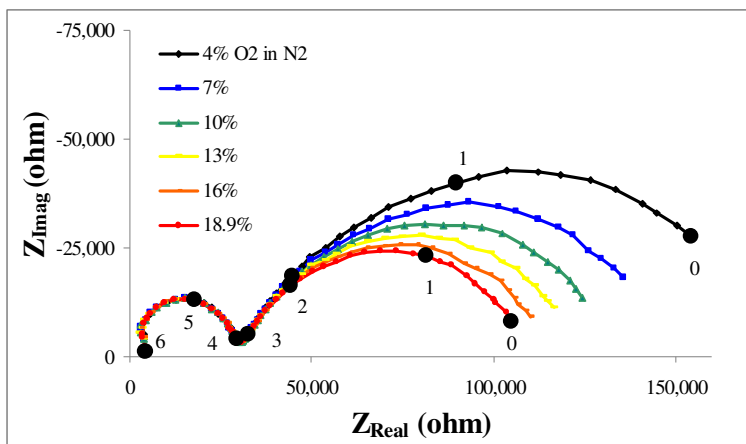
Figure 45. Increasing O_2 concentration shifts the low frequency arcs inward.

Figure 46 shows the results under the same conditions but with 100 ppm NO added. In both Figure 45 and Figure 46, the low frequency arcs shift inwards with increasing O_2 concentration. The addition of NO shifts the low frequency arcs even further inward, decreasing the magnitude of the phase angle.
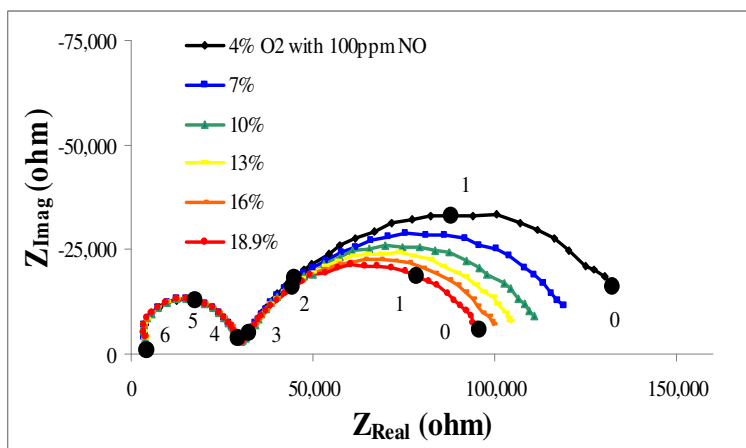
Figure 46. Adding NO to increasing O_2 shifts the low frequency arcs inwards.

The high frequency arcs in Figure 45 and Figure 46 are the same regardless of gas concentration, as expected. A high frequency arc may represent ion transport within the bulk of the electrolyte[335] or within the electrode.[336]

The locus of points specified by the phase angles at 10 Hz in Figure 45 and Figure 46 are shown in Figure 47. The variation in phase angle at 10 Hz over a wide range of O_2 concentration

---

[335] Wu, 51.
[336] Miura, (2003), 226.

is approximately linear. The 100 ppm NO has the effect of shifting the measured phase angle a constant amount over the entire range of O_2 measurement.

In the literature, significant cross sensitivity to O_2 has been reported. The O_2 changes the modulus, |Z|, which can be linearly correlated with the logarithm of O_2 concentration.[337]

The phase angles at 1 kHz are also shown in Figure 47. At this frequency, the phase angles vary only slightly to the presence of NO. This result suggests that 1 kHz is not the best frequency for the detection of NO.
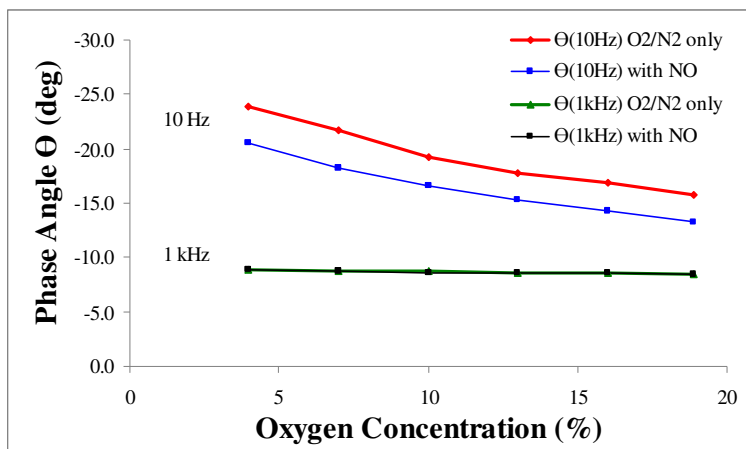
Figure 47. Phase angles at 10 Hz and 1 kHz over various Po$_2$ with and without NO.
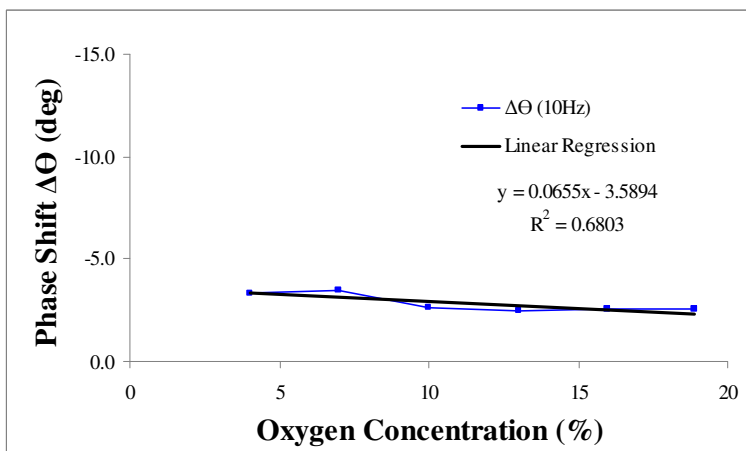
Figure 48. Phase angle changes due to 100 ppm NO at various [O$_2$].

By subtracting one 10 Hz line from another in Figure 47, the resulting subtrahends represent the change in phase angle at 10 Hz due to 100 ppm NO. Figure 48 shows that a plot of the phase angle shift versus O_2 concentration is roughly linear ($R^2 = 0.68$). The lower R^2 value compared to the NO data in Figure 42 may be due to the much larger range of concentration. The plot is not flat; at lower O_2 concentrations, the phase angle shift due to 100 ppm NO is larger. This observation suggests that NO and O_2 compete for reaction sites. As a result, when there is less O_2, the phase angle shift due to NO is larger.

---

[337] Zhuiykov, (2005), 330.

Relative Effects of NO, NO₂, and O₂

In Figure 49, the overlapping low frequency arcs show a similar impedance response of differing amounts of O$_2$, NO, and NO$_2$ at 650°C. Adding 25 ppm NO$_2$ or 100 ppm NO to a 10% O$_2$ gas mixture has approximately the same effect as adding an additional 4% O$_2$. The oxides of nitrogen evoke a response that is several orders of magnitude larger than an equivalent amount of oxygen, confirming results in the literature.[338] Some sources report that an impedancemetric NO$_x$ sensor has nearly an identical response to NO as to NO$_2$ regardless of their relative concentrations at a specific temperature, allowing total NO$_x$ sensing.[339, 340, 341, 342] It is unclear whether the equivalent sensitivity is due to the detection capability of the sensor or due to the natural thermal equilibrium shift of NO$_2$ to NO. At T > 600°C, NO$_x$ in exhaust gases equilibrates so that the mixture consists primarily of NO (>90%).[343] Alternately, to address the different responses of NO and NO$_2$, a catalyst might be used to shift all NO$_x$ to one species.
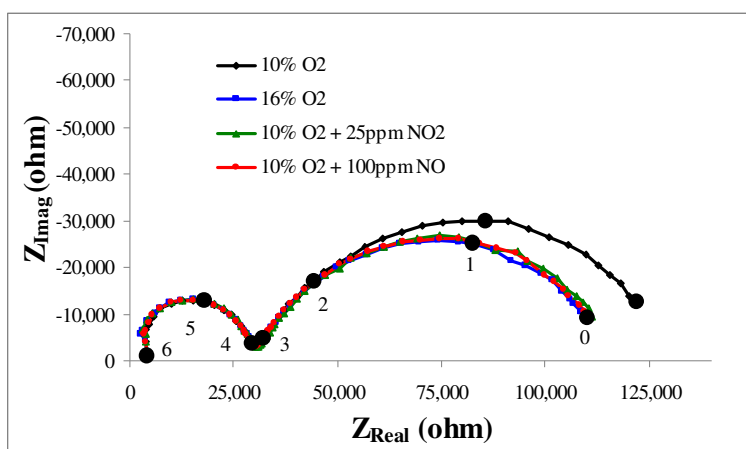
Figure 49. Equivalent impedance response for different amounts of O₂, NO, and NO₂.

Simultaneous Sensing of NO$_x$ and O₂

In principle, compensation for O$_2$ is possible if O$_2$ evokes a response at a frequency at which NO$_x$ does not. Martin *et al.* reported sensing of O$_2$ regardless of NO$_x$ at 1 kHz and proposed a method of compensation.[344] However, the system required several minutes to equilibrate, and Martin questioned the practicality of O$_2$ compensation in this fashion. Nevertheless, this method was investigated for its applicability to the experimental data acquired. The following steps were performed:

1. Calibrate sensor for O$_2$

   a. Measure phase angle at 10 Hz and 1 kHz for a range of O$_2$ concentration with and without known quantities of NO$_x$.

---

[338] Woo, <u>J Electrochem Soc</u>, (2007), J132.
[339] Miura, (2002), 284–287.
[340] Woo, <u>J Electrochem Soc</u>, (2007), J133.
[341] Miura, (2003), 221–228.
[342] Miura, (2009), 201.
[343] Zhuiykov, (2008), 215.
[344] Martin, <u>J Electrochem Soc</u>, (2007), J97-J104.

b. Plot the data without NO_x (10 Hz vs. 1 kHz).

c. Relate phase angle at 10 Hz as a function of phase angle at 1 kHz by linear regression, as shown in Figure 50.
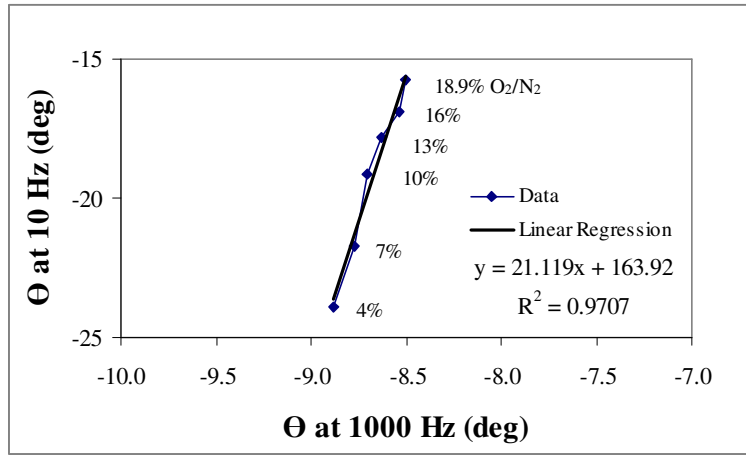
Figure 50. Calibration for O_2 compensation.

2. Calibrate sensor for NO_x

   a. From the phase angle data of gases with NO_x at 10 HZ, subtract the contribution of O_2 to obtain the phase angle due to known quantities of NO_x.

   b. Plot this data (phase angle vs O_2 concentration at 10 Hz). Figure 48 shows the phase angle due to 100 ppm NO.

   c. Relate phase angle at 10 Hz as a function of phase angle at 1 kHz by linear regression.

3. Perform compensation

   a. Measure phase angle at 10 Hz and 1 kHz of a mixture of gases that include O_2 and unknown quantities of NO_x

   b. From the 1 kHz phase angle data that depends solely on O_2, calculate the corresponding phase angle at 10 Hz.

   c. Subtract the contribution of O_2 to phase angle at 10 Hz to obtain the phase angle due solely to NO_x.

   d. Calculate the corresponding NO_x concentration using the regression equation in step 2.

This compensation method was carried out in full. The sensors under investigation were still affected by O_2 at 1 kHz, however, the sensitivity was small. The phase angle changed only 0.38° for a 14.9% change in O_2 concentration. Figure 51 shows the actual phase angle measurements and the calculated phase angle values using the method described in step 1 above over a wide range of O_2 concentration. These curves do not overlap; some error exists in the O_2-compensation process. The relative error ranged from 2 to 8%.
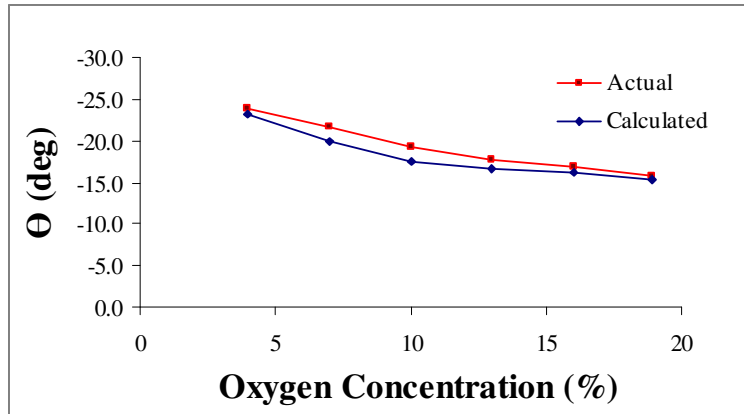
Figure 51. Actual and calculated phase angles due to various O$_2$ concentrations.

The error in calculating the O$_2$ concentration propagated to the calculation of NO$_x$ quantity. The phase angle shift due to 100 ppm NO only is shown in Figure 52. Relative error ranged from 15 to 59%. Martin *et al.* reported that their compensation method yielded inaccurate results at low O$_2$ concentration on account of slow sensor response.[345] In this study, the error over the entire range of O$_2$ by this method is unacceptably high. Using these sensors, the simultaneous detection of NO$_x$ and O$_2$ is impractical.
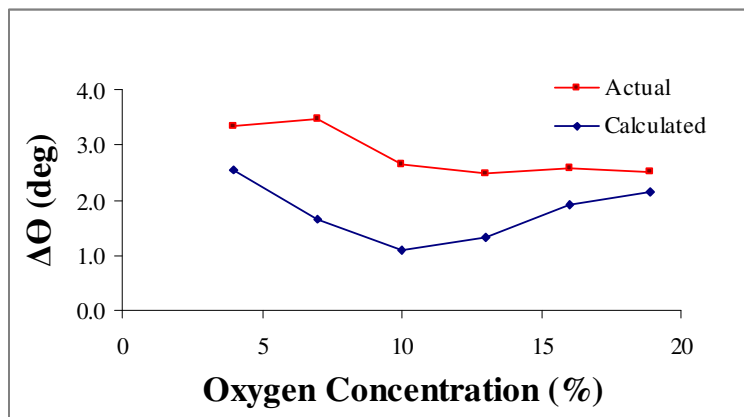
Figure 52. Actual and calculated phase angles due to 100 ppm NO.

A further investigation into the large error during simultaneous compensation for cross sensitivity to O$_2$ was undertaken. The premise of the correction for O$_2$ is that the sensor detects only O$_2$ and not NO$_x$ at 1 kHz frequency. This premise was further explored. In Figure 47 above, the plot of phase angles at 1 kHz over a range of concentrations of O$_2$ with and without 100 ppm NO appear. Whereas at 10 Hz, the presence of NO noticeably affected the phase angle, no change in phase angle is readily visible at 1 kHz. Rather, the phase angle remained relatively constant regardless of NO concentration at 1 kHz. Upon closer inspection, the phase angle at 1 kHz changed for both cases (10% O$_2$/N$_2$ alone and with 100 pm NO), as shown in Figure 53. This plot represents the same data as presented previously in Figure 47 but with a scale that allows more detailed examination of the data. The introduction of 100 ppm NO induces the same change in phase angle as a change in O$_2$ of several percent. The sensitivity to both O$_2$ and NO at

---

[345] Ibid., J100-J102.

1 kHz disallows the simultaneous determination of both O_2 and NO_x concentrations using the sensors under investigation. It is conceivable that at a higher frequency, the sensitivity to NO_x might diminish to naught, however, sensitivity to O_2 would decrease as well, as seen in Figure 45.
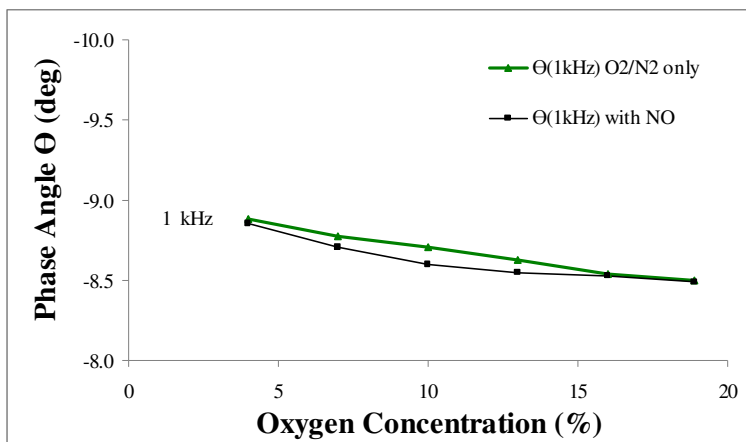
Figure 53. Phase angles at 1kHz change with of O_2 and with 100 ppm.

The practicality of this method of cross sensitivity compensation was questioned by its authors. They reported that the response of their sensor to O_2 took several minutes to equilibrate, which they stated may be too slow to be useful. In addition, the compensation method was not accurate across the entire range of O_2, especially at low O_2 concentration (2%). Furthermore, the sensor signal drifted over time.[346] As a result, compensation for O_2 would potentially require periodic recalibration over the life of the device.

The inaccuracy at low O_2 concentration is particularly problematic. A high rate of NO_x formation is possible during low O_2 conditions in a diesel engine in which high fuel consumption and the attendant high heat release rate promote thermal (Zeldovich) NO_x formation. Under high load conditions, the low quantity of excess O_2 results in less heat absorption by O_2 since intake air in diesel engines is not throttled (i.e. approximately the same quantity of intake air enters regardless of the accelerator position and the fuel injection rate).

In summary, the procedure to compensate a NO_x measurement for variable O_2 content is lengthy, complicated, and only accurate under certain conditions. The simultaneous detection of NO and O_2 at 1 kHz phase angle was not possible with the sensors under investigation.

5.3.4 Effect of Temperature

For gas-sensing, the sensor output must be calibrated to known gas concentrations at specific temperatures. When temperature varies, it is difficult to determine the concentration of gaseous species from a low frequency impedance measurement because impedance depends on temperature. An examination of the effects of temperature under controlled conditions yields useful information.

---

[346] Martin, <u>Mater Res Soc Symp Proc</u>, (2007).

Low Frequency Arc

Sensitivity tends to increase as temperature decreases. This statement is true both when sensitivity is measured by phase angle shift (Figure 54) and by change in modulus (Figure 55). Both graphs present impedance data measured at 10 Hz. Parameter changes resulted from the introduction of 100 ppm NO.
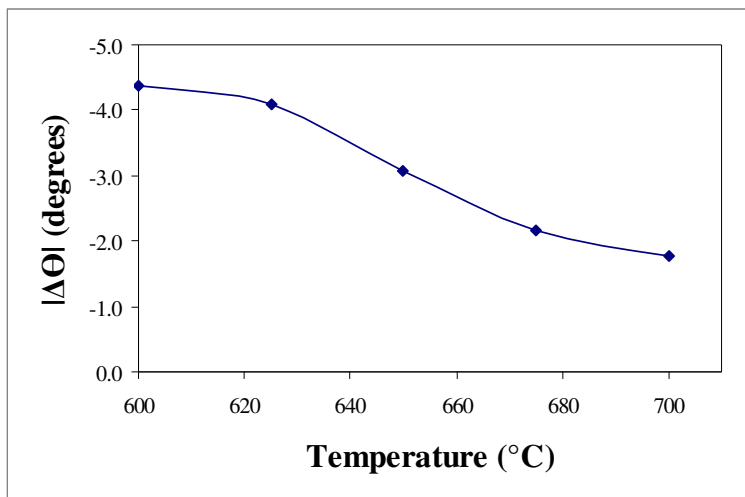
Figure 54. Phase angle shift due to 100 ppm NO increases as temperature decreases.

The largest phase angle shift due to 100 ppm NO was observed at the lowest temperature examined. This finding may be due to slow kinetics of oxygen reactions (reduction and incorporation in to lattice) at temperatures below 600°C. As a result, the effects of NO and NO_2 are more readily detected.[111][347]

Unfortunately, the signal becomes noisy at lower temperatures. Sometimes the arcs depart from smooth, continuous curves (not shown) as the effects of heterogeneities become more pronounced. The selection of a 650°C temperature for most measurements represents a balance of sensitivity and noise.

For the modulus, the largest changes due to 100 ppm NO occurred at lower temperatures, as seen in Figure 55. The largest difference occurred at 625°C. As temperature increases, the change in magnitude of the impedance steadily decreased until the upper end of the temperature range investigated. A smaller shift in modulus was also seen as temperature decreased. The reason for this is not clear.

---

[347] Zhuiykov, (2008), 99.
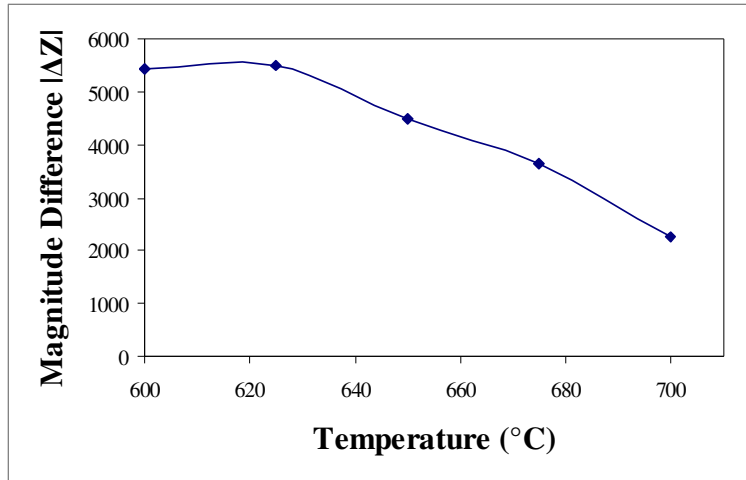
Figure 55. Modulus shift resulting from 100 ppm NO is larger at lower temperatures.

High Frequency Arc

In contrast to low frequency arcs, high frequency arcs are not affected by gaseous species. Figure 56 portrays high frequency arcs with and without NO_x concentrations at specific temperatures. These arcs consist of measurements from approximately 10^4 to 10^6 Hz in 10% O_2. The impedance spectra are identical for both cases; they exhibit perfect overlap.
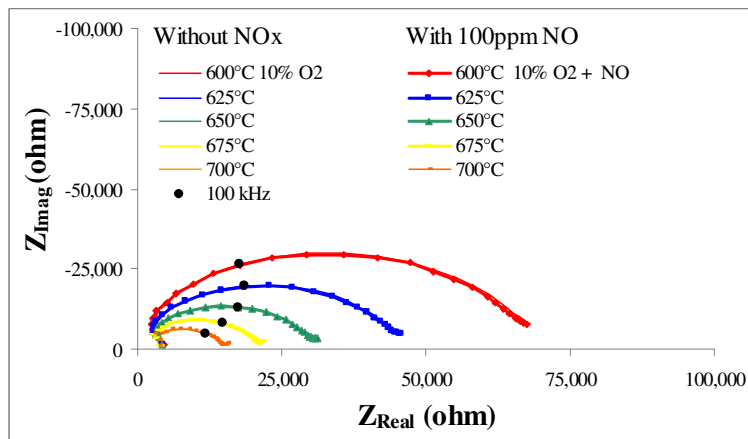
Figure 56. High frequency arcs at various temperatures for 10% O_2/N_2.

An analysis of the effect of temperature on the high frequency arcs suggests that a high frequency measurement may be used to determine temperature. The phase angle at 10^5 Hz for each temperature shown in Figure 56 was calculated and plotted in Figure 57, which shows that the phase angle at 10^5 Hz was directly proportional to temperature regardless of gas species. A line was fit to the data with a very high R^2 value of 0.9955. This finding suggests that the high frequency arcs were dependent on a temperature-dependent mechanism such as ionic conductivity.
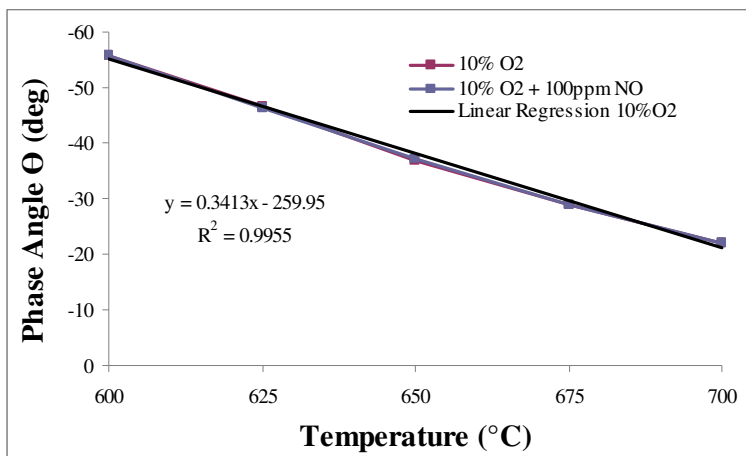
Figure 57. Phase angles at 10^5 Hz vary linearly with temperature for all gases.

As a result, a stable NO_x sensor may be calibrated for use as a thermometer, as long as the high frequency arc does not change significantly due to aging. Protracted heat treatment may cause microstructural changes in the sensor.[348] These changes alter the high frequency arc of the impedance spectrum. Such changes were observed with the sensors used for these measurements. Aging effects were noticed over the course of days.

Murray *et al.* noticed significant change in impedance after 11 days of testing. The drift in the phase response was attributed to material instability. The temperature dependence and signal drift must be overcome for a viable NO_x sensor.[349]

5.3.5 Equivalent Circuit Analysis

The Nyquist plots provided guidance for the fitting of impedance data with an equivalent circuit. Typically, two arcs offset from the origin appeared. Each arc represents a reaction step with a unique time constant.[350] The offset can be modeled by a resistor, whereas the arcs are reproduced by a series combination of Voigt elements (RC) and/or Cole elements (RQ). A Voigt circuit[351] consisting of a resistor with two Voigt elements was initially evaluated, however, replacing one Voigt element with a Cole element better replicated the low frequency impedance data that represents processes taking place at the sensing electrode. The equivalent circuit model thus consisted of a resistor, a Voigt element, and a Cole element in series, R_0-(R_1C_1)-(R_2Q_2), as depicted in Figure 58. This model provided the best fit as determined by the lowest sum of squares of residuals.

In the equivalent circuit analysis, the contributions of measurement leads to capacitance and resistance were assumed to be negligible.

---

[348] Junya Kondoh,Tsuyoshi Kawashima,Shiomi Kikuchi,Yoichi Tomii,and Yasuhiko Ito, "Effect of Aging on Yttria-Stabilized Zirconia I. A Study of Its Electrochemical Properties", <u>J. Electrochem. Soc.</u>, 145:5, May 1998, 1527-1536.

[349] Murray, 60-62.

[350] H. Fukunaga, M. Koyama, N. Takahashi, C. Wen, K. Yamada, "Reaction model of dense $Sm_{0.5}Sr_{0.5}CoO_3$ as SOFC cathode", <u>Sol. Stat. Ion.</u>, 132, (2000), 281.

[351] Agarwal, 1918.
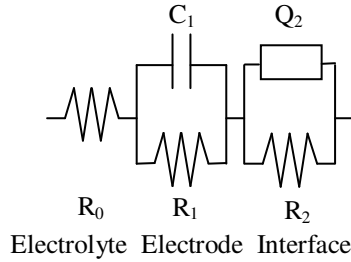
Figure 58. Equivalent circuit for NO_x sensor with gold wire sensing electrode.

Figure 59 shows both the empirical data points for the base case (10% O_2 in N_2, 650°C) and the equivalent circuit model results. The output of the equivalent circuit agrees very well with the discrete data points with nearly perfect superposition. In addition to the base case, the same equivalent circuit model was also used to fit the data obtained with various gas compositions and at different temperatures. Once again, this model provided an excellent fit for all scenarios.
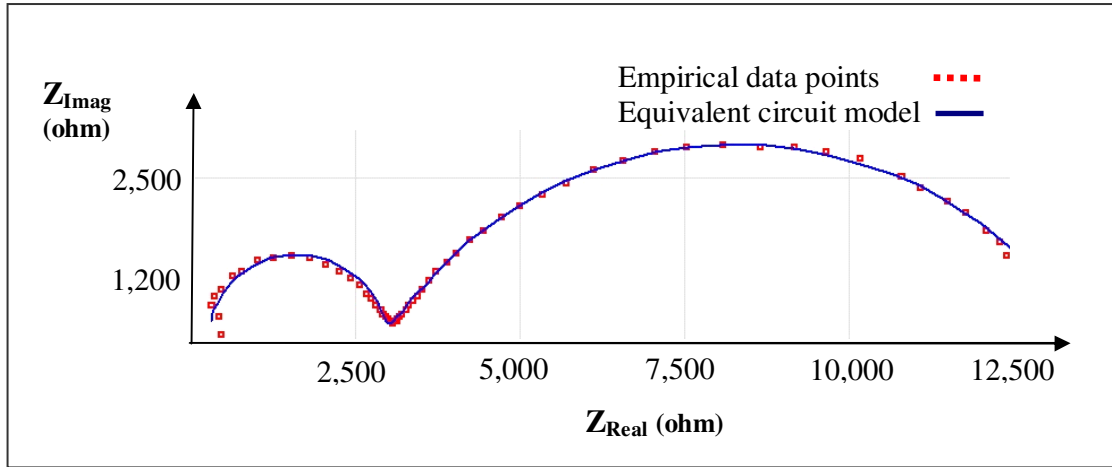
Figure 59. Impedance data points fitted by equivalent circuit model.

Interpretations for the equivalent circuit elements from the literature are summarized in Table 10. For systems with oxide electrodes, the resistor R_0 usually represents the YSZ bulk resistance.[352, 353] The high frequency arc, whose impedance is replicated by (R_1C_1), has been attributed to the bulk of the electrode.[353] In contrast, Wu *et al.* modeled a system with noble metal electrodes; they attributed R_0 to contact resistance and the high frequency arc (R_1C_1) to the YSZ bulk.[354] Yoon *et al.* also attributed the high frequency arc to the YSZ electrolyte bulk.[355]

The Cole element (R_2Q_2) models the response to low frequency stimulus. Exposure to analyte gases evokes changes in the parameter values associated with the interface. Only this arc changed in the presence of sample gases. As a result, the values of R_2 and the parameter values for Q_2 change accordingly. This Cole element represents processes that occur at the interface of

[352] Miura, (2002), 285-286.
[353] Miura, (2003), 221–228.
[354] Wu, 49–53.
[355] J. W. Yoon, (2001), 486.

the electrode and electrolyte for all systems regardless of electrolyte materal.[354, 355, 356, 357, 358, 359] The discussion focuses on this arc and its parameters.

Nyquist Plot Feature	Circuit Element	Physical Interpretation
Offset from Z_{imag}	R_0	- resistance to ion transport in bulk electrolyte (YSZ) - contact resistance
High Frequency Arc	Voigt (R_1C_1)	- electrode bulk (gold) - electrolyte bulk (YSZ)
Low Frequency Arc	Cole (R_2Q_2)	Interfacial processes (adsorption, surface diffusion, electrochemical reactions)

Table 10. Physical interpretations of equivalent circuit models.

In the Cole element, R_2 represents the resistance of charge-transfer at the interface of the electrode and electrolyte due to processes such as adsorption and electrode reactions.[352, 353, 354, 357, 358, 359, 360] R_2 has been called "reaction-resistance" for adsorption, dissociation, and electrochemical reactions at the electrode. Since the resistance value of the Cole element that represents low frequency behavior depends on the exchange of O^{2-} ions, it indicates the oxygen sensitivity of the sensor.[361]

The CPE parameter, Q_2, accounts for the non-ideal behavior of the double layer. If the phase angle exponent, φ, takes on a value close to one, then the CPE parameter is an approximate measure of capacitance of charges at the interface.[362]

The impedance of a CPE is typically $Z = 1/[(j\omega)^{\varphi}Q]$, where Q is a CPE parameter related to double layer capacitance.[363] In this equivalent circuit modeling effort, the impedance of the CPE is defined as $Z = 1/[(j\omega Q)^{\varphi}]$. This relationship resulted in a better fit. This CPE differs only slightly from the more conventional definition because the phase angle exponent, φ, took on a value close to 1 (actually 0.988 or higher) over the entire range of NO_x concentrations.

Despite prior investigations, the precise sensing mechanism is poorly understood.[364] A detailed sensing mechanism is not readily available in the literature. The following sections attempt to cast light on the effects of various parameters on sensing ability by discussing the results from the equivalent circuit modeling effort.

Effect of NO_x

NOx causes reversible changes in low frequency arcs. In specific, R_2 and the CPE parameter, Q, of the Cole element change. These parameters are associated with the working electrode. For NO, the values for R_2 show a linear trend with respect to NO concentration as shown in Figure 60. The linear relationship between R_2 and NO concentration departs somewhat at 25 and 30 ppm due to limitations of experimental setup. A long gas delivery tube was used which

---

[356] Woo, <u>Mater Res Soc Symp Proc</u>, (2007).

[357] Nakatou, (2004), 995–998.

[358] Nakatou, (2005), 2411–2415.

[359] Nakatou, (2006), 57–62.

[360] Wama, 2774.

[361] Stranzenbach, (2009), 154–163.

[362] Woo, <u>J Electrochem Soc</u>, (2007), J131.

[363] Barsoukov, 495.

[364] Zhuiykov, (2008), 128.

resulted in a large pressure drop under the low flow conditions at low NO concentration. Nevertheless, the regression line shows a high R^2 value.
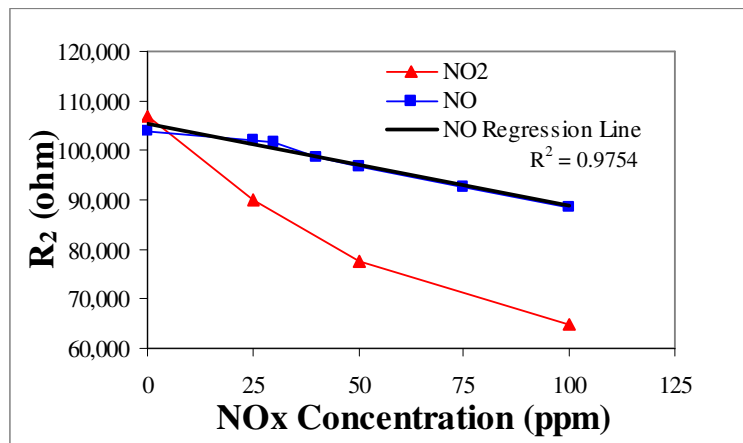
Figure 60. R_2 varies approximately linearly with NO concentration.

For NO_2, the R_2 values changed dramatically, even more than for NO. The data points, however, did not follow a linear trend. Only 4 data points were recorded, though. Additional study is necessary to further define the relationship between R_2 and NO_2.

Yoon *et al.* showed that NO_2 decreases the resistance at the electrode/electrolyte interface. This finding confirms the interpretation of the equivalent circuit in Figure 58. They offered that the active groups from the dissociation of NO_2 migrate easily at the electrode interface and react with vacancies in the solid electrolyte, which decreases the overvoltage, thereby increasing current and decreasing impedance.[365]

Since NO and NO_2 evoked responses of different magnitude in the same sensor, total NO_x sensing is not possible with this sensor at 650°C. At a different temperature, total NO_x sensing might be possible. The data points for 0 ppm were similar for both NO_x gases but not identical.
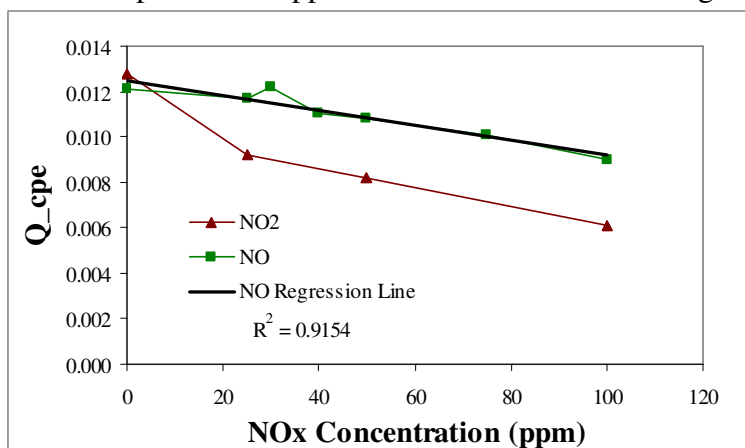
Figure 61. The CPE parameter, Q, varies approximately linearly with NO concentration.

---

[365] J. W. Yoon, (2001), 486.

The CPE parameter, Q, also varied nearly linearly over the range of measured NO concentrations, as seen in Figure 61. Since the phase angle exponent, φ, typically took on a value close to 1, Q represents capacitance. Once again, experimental error can be seen in the measurement at 30 ppm, and the zero points are similar but not identical.

The CPE parameter, Q, changed more in the presence of NO_2 than NO. As was the case for R_2, the Q values were not linear over the entire range of NO_2 concentration, although excluding 0 ppm leaves the rest of the data points appear to follow a linear pattern. Once again, further investigation is necessary to define this relationship.

Miura *et al.* made a similar equivalent circuit model for their sensor with a $ZnCr_2O_4$ sensing electrode. Their circuit consisted of a Voigt circuit with two Voigt elements.[366] Only their R_2 changed with NO_x exposure; in contrast, here the CPE parameter, Q, which represents capacitance, also varies. The nature of the relationship of R_2 with concentration was not stated by Miura *et al.*

Effect of O_2

Oxygen evokes a concentration-dependent low frequency relaxation in the sensors. As was the case with NO_x, O_2 affects the parameters of the Cole element in the equivalent circuit. Both R_2 and the CPE parameter, Q, change dramatically due to the exposure to O_2 over a wide range of concentrations. However, the nature of these relationships was not linear as with NO, rather parameter values for R_2 and Q varied according to a power law as shown in Figure 62 and Figure 63, respectively. The reason for this differing relationship may be due to the larger range of concentrations for O_2 in comparison to the 100 ppm for NO. Over a larger range of NO concentration, it is possible that parameter values would also follow a power law. Conversely, over a sufficiently narrow range of O_2 concentration, the parameter values may vary according to a linear relationship. The powers according to which R_2 and Q vary are not the same as can be seen in the figures.

The chart shows R_2 (ohm) on the y-axis versus O_2 Concentration (%) on the x-axis, with:
$$y = 276850x^{-0.4118}$$
$$R^2 = 0.9996$$
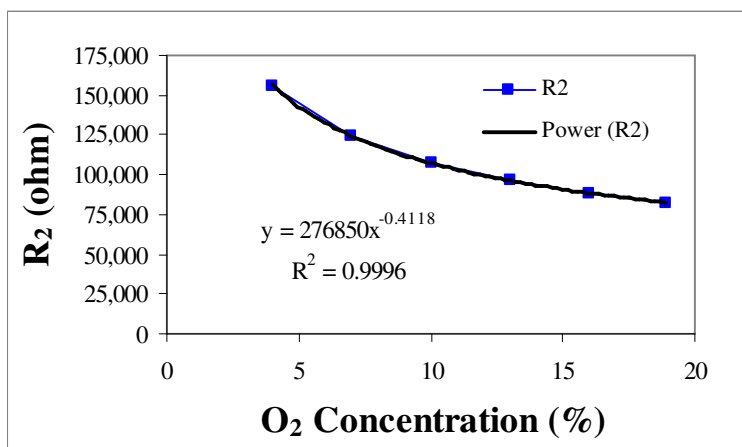
Figure 62. R_2 varies according to a power law over a wide range of O_2 concentration.

[366] Norio Miura, (2003), 221–228.
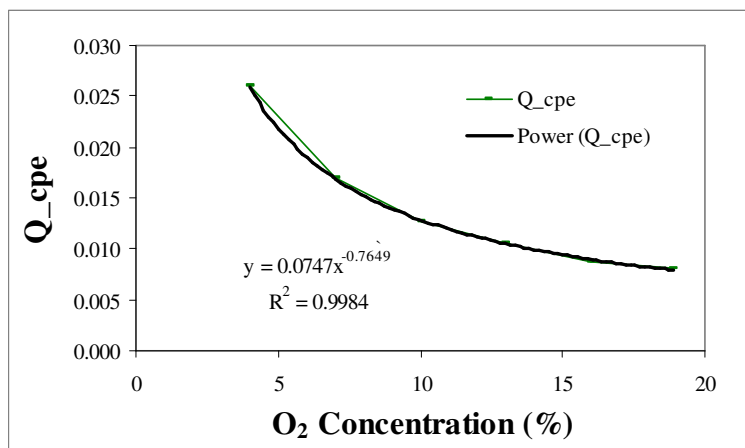
Figure 63. Q varies according to a power law over a wide range of O_2 concentration.

An examination of the resistance in the Cole element of the equivalent circuit can shed light on the rate-limiting step of the sensing mechanism. In particular, if the inverse of resistance is proportional to O_2 concentration raised to a power, i.e. $\sigma_2 = 1/R_2 \, \alpha \, (Po_2)^n$, where σ is the conductivity, then the value of the exponent, n, suggests the rate-limiting step. Yamamoto *et al.* compiled a summary of values of the exponent, n, and reaction steps to which they correspond (Table 11).[367]

n	Physical interpretation of rate limiting step
1	-Molecular O_2 processes (adsorption, surface diffusion, or dissociation)
½	-Atomic O_2 processes (dissociation or surface diffusion)
+¼	-Langmuir type oxygen atom adsorption with low surface coverage and charge transfer (high temperature, low Po_2)
-¼	-Langmuir type oxygen atom adsorption with high surface coverage and charge transfer (low temperature, high Po_2)

Table 11. Rate-limiting steps correlated to n in $1/R \, \alpha \, (Po_2)^n$.

In the cases when the exponent equals ±¼, Langmuir adsorption assumes a homogeneous surface, monolayer coverage, and no inter-atomic or inter-molecular forces.[368]

Figure 64 shows the variation of conductivity with the partial pressure of O_2 at an interrogation frequency of 10 Hz for all of the resistors in the equivalent circuit. Each locus of data points was fit by a line that follows a power law relationship. The exponent for each conductivity (i.e. n in $\sigma_2 \, \alpha \, (Po_2)^n$) is listed in Table 12 below. Only R_2 depended strongly on Po_2.

---

[367] Y. Takeda, R. Kanno, M. Noda, Y. Tomida, and O. Yamamoto, "Cathodic Polarization Phenomena of Perovskite Oxide Electrodes with Stabilized Zirconia", J. Electrochem. Soc.: Electrochemical Science and Technology, 134:11, (Nov. 1987), 2659.

[368] Irving Langmuir, "The Constitution and Fundamental Properties of Solids and Liquids. II. Liquids", J. Am. Chem. Soc., 39:9, 1917, 1848-1906.
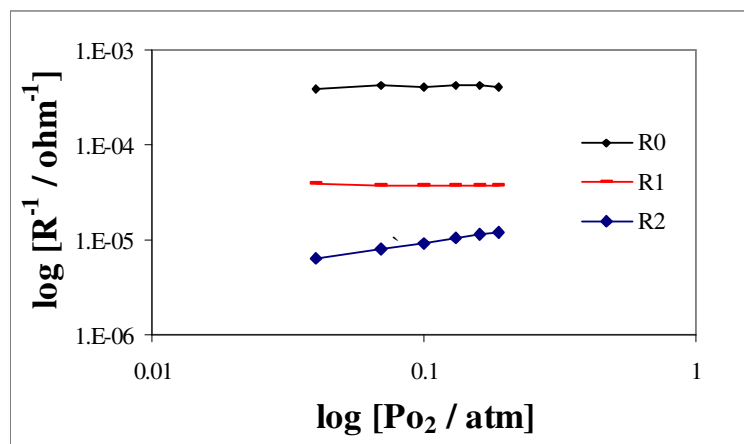
Figure 64. Log plot of variation of $1/R_i$ with O_2 concentration at 10 Hz.

In Figure 64, neither R_0 nor R_1 depended on P_{O_2}. The conductivity remained approximately constant over the entire range of O_2. In both cases, the exponent associated with the power fit approximated zero. Independence from P_{O_2} is consistent with a conductivity relaxation.[369, 370]

Conductivity	n	Physical Process
$1/R_0$	0.025	Contact resistance
$1/R_1$	-0.009	Charge transport in electrolyte (conductivity)
$1/R_2$	0.412	Adsorption and dissociation of O_2

Table 12. Dependence of $1/R$ on $(P_{O_2})^n$ and the physical significance.

R_2 depended on P_{O_2}. Its exponent is 0.412. This value was approximately ½, which suggests that atomic O_2 processes such as dissociation or surface diffusion serve as the rate-limiting step (Table 11).[367] Woo *et al.* found a similar exponent (0.42) using a sensor that also had a dense gold sensing electrode and YSZ electrolyte.[371]

Effect of Temperature

Figure 65 depicts the changes in parameter values induced by changes in temperature in a mixture of gases consisting of $10\%O_2$ in N_2. The changes are normalized to the value taken at the lowest temperature examined (600°). Temperature causes the parameters in the Voigt and Cole elements to change. Typically, as temperature increased, parameter values for resistance and capacitance decreased according to a power law with a negative exponent. For the CPE, since the phase angle exponent, φ, was approximately 1 (actually 0.97 or higher) with little change over the entire range of temperatures, the value of Q approximated capacitance. It too varied strongly with temperature.

Surprisingly, R_0 did not vary much relative to the other parameters. This result suggests that the ionic conductivity is not greatly affected by changes in temperature from 600-700°C, however, one would expect resistance to increase markedly at lower temperature.

---

[369] M. J. Jørgensen and M. Mogensen, "Impedance of Solid Oxide Fuel Cell LSM/YSZ Composite Cathodes", J. Electrochem. Soc., 148:5, (2001), A433-A442.

[370] Barsoukov, 259.

[371] Woo, (2008), J39.
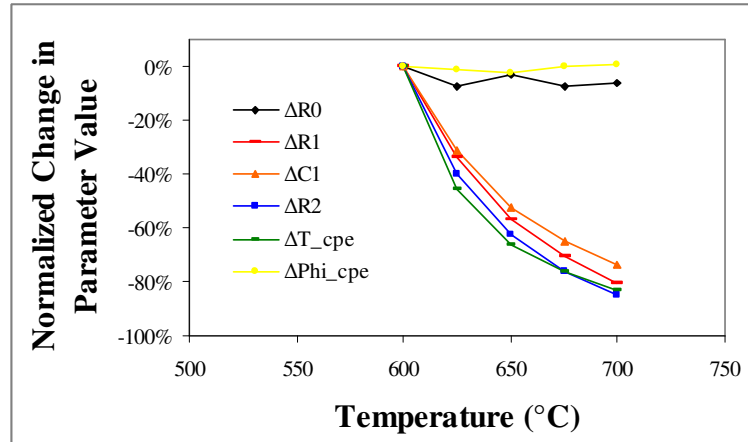
Figure 65. Normalized variation of parameter values with temperature.

An Arrhenius plot of resistance data sheds light on the activation energies of various processes. Figure 66 shows that the Arrhenius plots of the resistances are linear over the temperature range examined. R_0 has little or no dependence on temperature in the temperature range, as confirmed in Figure 65. This finding supports the interpretation of Wu *et al.* that R_0 represents contact resistance and not bulk electrolytic resistance.[354]

Conversely, R_1 and R_2 were both temperature-dependent. They both had a similar slope, and thus similar activation energy. A similar thermally activated process such as charge transfer may have been responsible for the resistance at the interface and electrodes.
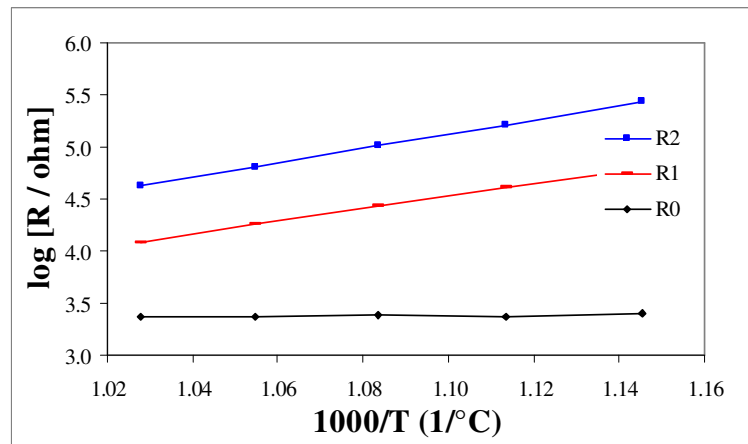
Figure 66. Arrhenius plot of R_i in P_{O_2} of 0.1 and at 10 Hz.

5.3.6 Alternative NO_x-Determination Methods

This section discusses the determination of NO_x concentration by three methods: direct DC measurement, total real component of impedance at low frequency, and real component of low frequency arc (R_2) at low frequency.

Sensing NO_x is possible by applying a DC current and recording the change in resistance due to the exposure to NO_x. Resistance consists solely of the real component of impedance. Ho *et al.* noticed changes in conductivity in sensors upon exposure to NO_x. The resistance increased due

to NO, but it decreased with NO_2 in air at 400°C. The changes were related to concentration; they were also greatly affected by O_2.[372] Miura *et al.* also observed a change in the DC resistance that varied with the concentration of both NO and NO_2.[373] Although this change was small, a DC measurement is easier to perform than an impedance measurement. This method, however, may be affected by microstructural changes in the electrolyte (aging), requiring recalibration, which is difficult to perform in-situ.

As an alternative to a direct DC measurement, Miura *et al.* offered that the DC resistance (i.e. real component of total impedance) could be extracted from total impedance data.[374,375] The real component $(R_0 + R_1 + R_2)$ determined at low frequency may be used to indicate NO concentration. At sufficiently low frequency, this measurement converges with the DC measurement discussed above. It is merely the modulus of the impedance consisting entirely of resistance. At 10 Hz, the real component of total impedance correlates to NO concentration linearly (Figure 67). The R^2 value is somewhat low (0.9186) due to the limitations of the experimental setup at low NO concentrations, as discussed earlier. At 1 Hz, the real component of overall impedance correlates to NO concentration linearly even better ($R^2 = 0.9862$). Using this method over the direct DC measurement may result in a faster response. However, a direct measurement of DC resistance represents a simpler, less costly method. Miura *et al.* reported a small change in DC resistance upon exposure to NO or to NO_2 gas diluted with air.[373, 375]
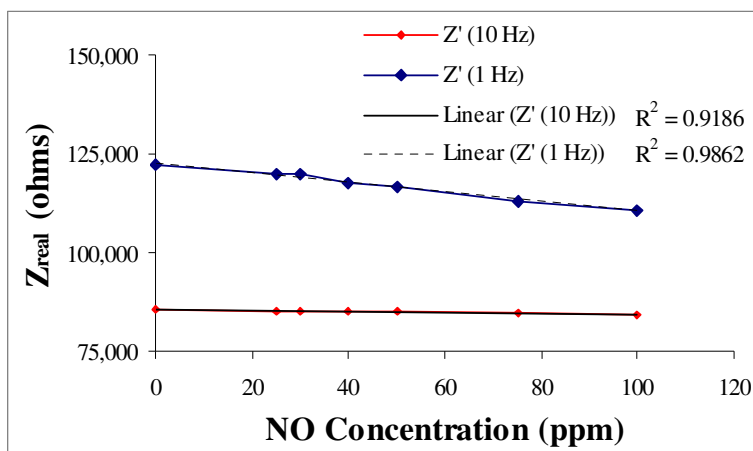
Figure 67. Z_{real} varies approximately linearly with NO concentration at 10 Hz.

Last of all, the interfacial resistance R_2 may be a better indication of NO concentration than phase angle. Figure 60 shows that the R_2 values were linear over wider range of NO (0-100 ppm) than the change in phase angle (25-100 ppm, Figure 42). In addition, the measurement of R_2 was not affected by aging of electrolyte, as are the phase angle and modulus. It is more complicated, however, to determine R_2 because electronic equipment and software are necessary to interrogate a range of frequencies in order to determine the width of the low frequency arc that corresponds to R_2. In addition, the effect of NO_2 on R_2 was nonlinear. Last of all, as is the case with phase

---

[372] Kwun-Yao Ho, Masaru Miyayama, Hiroaki Yanagida, "NO_x gas responding properties of Nd_2CuO_{4-y} thick film", Mater Chem Phys, 49, (1997), 9-10.
[373] Miura, (2002), 285
[374] Ibid., 286.
[375] Miura, (2003), 225.

angle and modulus, the R_2 parameter values must be calibrated to known NO_x concentrations in order to make a functioning sensor.

5.5 Conclusions

Sensors with gold wire working electrodes have been fabricated and evaluated using impedance methods and equivalent circuit analysis. The invariability of the impedance response to flow rate has been demonstrated. The linear relationship between low NO concentration and phase angle has been confirmed between (25-100 ppm). For NO_2, a linear relationship was observed over a narrower range (0-50 ppm). The sensors were more sensitive to NO and to NO_2 than to O_2 by several orders of magnitude by examination of the difference in phase angle obtained at 10 Hz. Among the NO_x species, NO_2 evoked a larger response than an equivalent amount of NO at 650°C. At a frequency of 1 kHz, the sensors exhibited sensitivity to both O_2 and NO thereby precluding the use of these sensors to self compensate for O_2 by simultaneously determining O_2 and NO_x concentrations. Experimental results suggested that NO and O_2 compete for reaction sites. The sensors were most sensitive to NO_x at the low end of the investigated temperature range. The phase angle at 10^5 Hz was linearly related to temperature, independent of gas species.

In the equivalent circuit modeling analysis, NO induced a linear change in parameters of the Cole element that represent the electrode-electrolyte interface. In specific, R_2 and the CPE parameter, Q, that represents capacitance, varied directly with NO concentration over the entire range of NO investigated (0-100 ppm). This result suggests R_2 as an alternative metric instead of phase angle and modulus. The Cole element parameters also varied in the presence of O_2 but according to a power law over a wider range of concentration (4-18.9%). Temperature affected the Voigt and Cole element parameters exclusively. The rate-limiting step associated with R_2 was most likely dissociation or surface diffusion. Both R_1 and R_2 showed a similar temperature dependence that suggests a similar process is responsible for the rate determining step.

The performance of gold sensing electrodes is promising, however, noble metals are costly, and the coefficient of thermal expansion of gold differs from both the zirconia electrolyte and the alumina substrate. The melting temperature of gold prevents the cofiring of the electrodes with the electrolyte in one step. In the following chapter, a metal oxide electrode material with a coefficient of thermal expansion that approximates that of zirconia is investigated.

CHAPTER 6: NO$_x$ Sensor with Gelcast Lanthanum Strontium Manganate Electrodes

Electrochemical NO$_x$ sensors with partially stabilized zirconia electrolyte were fabricated with electrodes of lanthanum strontium manganate (LSM, La$_{0.85}$Sr$_{0.15}$MnO$_3$) on substrates of alumina or partially stabilized zirconia. The sensors were examined in simulated lean exhaust using impedance spectroscopy techniques and equivalent circuit analysis. The performance metric, phase angle shift, was invariant to flow rate. Phase angle shifts varied linearly with NO$_x$ concentration from 25-100 ppm. The shifts were generally smaller than those obtained with gold wire electrodes in the preceding chapter (less than 1° of phase angle shift versus several degrees for gold wire). An equivalent circuit model consisting of R$_0$-(R$_1$C$_1$)-(R$_2$Q$_2$)-(R$_3$Q$_3$) revealed that NO$_x$ significantly affected only the CPE parameter for interfacial capacitance. An analysis of the power law relationship between conductivities of equivalent circuit parameter elements and the partial pressure of oxygen provided insights into physical processes. Microstructural aging caused signal drift over time.

In this model, the lone resistor, R$_0$, represents YSZ bulk resistance; the first Voigt element (R$_1$C$_1$) represents the electrode bulk properties, and the Cole element (R$_2$Q$_2$) represents the electrode-electrolyte interface. Exposure to NO$_x$ affects the parameters of the Cole element. R$_2$ varied linearly with NO content from 1-100 ppm. R$_2$ is suggested as an indicator of NO$_x$ species.

6.1 Introduction

Diesel engines utilize fuel more efficiently than stoichiometric engines due to their higher compression ratios. The attendant emissions of both particulate matter and nitrogen oxides (NO$_x$) are deleterious to health[376] and to the natural environment.[377] A particulate trap can be used to address particulate emissions, as discussed in Section 2.3.2 Diesel Emissions Mitigation Strategies. Particulate traps require periodic regeneration by pulses of rich gases.[378]

NO$_x$ emissions from combustion processes consist overwhelmingly of NO in the concentration of several hundred parts per million (ppm) to several thousand ppm. NO$_2$ is also present in the range of tens of ppm.[379] Other forms of NO$_x$ are also present, but at much lower concentration than NO and NO$_2$. To abate NO$_x$ emissions, either a NO$_x$ trap or selective catalytic reduction (SCR) is possible. The NO$_x$ trap regeneration penalizes fuel economy whereas SCR requires a supply of ammonia or urea.[380] Regardless of which NO$_x$ mitigation technology is used, future on board diagnostic (OBD) requirements mandate that its performance be monitored in

---

[376] G. M. Solomon, T. R. Campbell, T. Carmichael, G. Ruderman Feuer, J. S. Hathaway, "Exhausted By Diesel: How America's Dependence on Diesel Engines Threatens Our Health", (Natural Resources Defense Council, New York, 1998), 5-10.

[377] A. C. Lloyd and T. A. Cackette, "Diesel Engines: Environmental Impact and Control", J. Air & Waste Manage. Assoc., 51, (2001), 809-847.

[378] G. Saracco, N. Russo, M. Ambrogio, C. Badini, V. Specchia, "Diesel particulate abatement via catalytic traps", Catal Today, 60, (2000), 33-41.

[379] Borman, 125.

[380] Johnson, (2008), 23-37.

heavy duty vehicles. For this to occur, a more accurate NO_x sensor is needed than the current amperometric technology.[381]

NO_x sensors that function on the basis of an impedance measurement have been investigated by several groups.[382,383,384,385,386,387,388,389,390,391,392,393,394,395] Impedancemetric sensors have also been developed to detect water vapor, [396] CO, [397] and hydrocarbons[398,399] One sensor detected propene at very low concentrations: 0.05 – 0.8 ppm.[400]

Impedancemetric sensors function on the basis of a low frequency process associated with a time-constant relaxation that alters impedance. Measurements of impedance are obtained from an electrochemical cell by applying an alternating voltage at a specific frequency. The current that results is recorded. Then impedance is calculated as the ratio of small signal voltage over current. Exposure to a gas that reacts electrochemically causes a change in the modulus (magnitude) of the impedance; this change can be calibrated to correspond to low concentrations of NO_x. The phase angle that characterizes lag or lead between the signals can also be calibrated to yield NO_x concentration at low frequencies (f < 100Hz). In addition, the impedance measurements obtained over a range of frequencies reveal information about the sensor. The capacitive arcs that result yield information about physicochemical processes.

For NO_x sensors, detection on the order of single parts per million has been reported using the phase angle shift ($\Delta\Theta = \Theta_2 - \Theta_1$), which is more sensitive to NO_x concentration than the change in modulus.[386,401] The phase angle shift is linearly proportional to NO_x concentration between 8-50 ppm.

In addition to sensitivity, impedance-based NO_x sensors have an advantage over mixed potential sensors: both NO and NO_2 evoke a shift in the signal in the same direction. In contrast, the output EMF of mixed potential sensors is negative with NO and positive with NO_2.[402] As a

[381] California Air Resources Board, "Technical Status and Revisions to Malfunction and Diagnostic System Requirements for 2010 and Subsequent Model Year Heavy Duty Engines (HD OBD)", (Sep. 11, 2008), 16.

[382] Miura, (2002), 284–287.

[383] Miura, (2003), 221–228.

[384] Miura, (2006), 979–986.

[385] Martin, Mater Res Soc Symp Proc, (2007).

[386] Martin, J Electrochem Soc, (2007), J97-J104.

[387] Murray, (2008), 43-62.

[388] Woo, Mater Res Soc Symp Proc, (2007).

[389] Woo, J Electrochem Soc, (2007), J129-J135.

[390] Woo, (2008), J32-J40.

[391] Woo, (2009).

[392] Stranzenbach, Gramckow, Saruhan, (2007), 224–230.

[393] Stranzenbach and Saruhan, (2007), 983-986.

[394] Stranzenbach, (2009), 154–163.

[395] Shimizu, 479-482.

[396] Nakatou, (2004), 995–998.

[397] Wu, 49–53.

[398] Nakatou, (2005), 2411–2415.

[399] Nakatou, (2006), 57–62.

[400] Wama, (2007), 2774–2777.

[401] Orazem, 315-6.

[402] Norio Miura, Perumal Elumalai, Vladimir Plashnitsa, Taro Ueda, Ryotaro Wama, and Masahiro Utiyama, "Solid-State Eectrochemical Gas Sensing", in Solid State Gas Sensing, eds. E. Comini, G. Faglia, G. Sberveglieri, (Springer, New York, 2009), 201.

result, the responses interfere with one another and make accurate NO_x detection difficult when using mixed potential sensors.

Impedance-based sensors face some obstacles such as selectivity, long term stability, and complexity. They are still more expensive than potentiometric ones, especially their supporting electronics and the attendant signal processing equipment. The relationship between impedance and the sensing mechanism is poorly understood.[403] In general, impedancemetric gas sensors for NO_x detection are less developed than the other types (amperometric and mixed potential).[404]

The perovskite lanthanum strontium manganate (LSM) is a possible material for NO_x sensor working electrodes. It is known to be an electrode material for the oxygen reduction reaction in solid oxide electrolyzer anodes[405] and solid oxide fuel cell cathodes.[406,407,408,409,410,411] LSM is a n-type semiconducting metal oxide.[412]

The coefficient of thermal expansion (CTE) of LSM closely matches that of the yttria-stabilized zirconia (YSZ) electrolyte commonly used in SOFCs, which is beneficial for the mitigation of internal stresses. Long sensor life depends on resistance to thermal and mechanical shock.[413] Thermally induced stresses arise between materials with different CTEs, for example, at the interface of the alumina substrate and zirconia electrolyte. Alumina is a desirable substrate material due to its ubiquity and low cost. In addition, alumina is stable with the electrolyte stabilized zirconia.[414] In fact, thermal barrier coatings for turbines are engineered so that the zirconia coat contacts a dense oxide of alumina.[415] Alumina has a lower CTE than zirconia, though.[416] The average CTE of alumina over the temperature range is 10 µm/°C; for ZrO_2, the CTE is 13 µm/°C.[417] Despite this difference, the CTE of alumina better matches that of zirconia than other common insulator materials such as aluminous porcelain and mullite. Strategies exist to deal with the CTE mismatch between ZrO_2 and Al_2O_3: reduce material thickness, use partially stabilized zirconia (PSZ) electrolyte with a CTE closer to that of Al_2O_3, and blend ZrO_2 and

[403] Zhuiykov, (2008), 127-8.

[404] Fergus, (2007), 659.

[405] Wensheng Wang, Yingyi Huang, Sukwon Jung, John M. Vohs, and Raymond J. Gorte , "A Comparison of LSM, LSF, and LSCo for Solid Oxide Electrolyzer Anodes", J. Electrochem. Soc., 153:11, (2006), A2066-A2070.

[406] O. Yamamoto, Y. Takeda, R. Kanno, and M. Noda, "Perovskite-Type Oxides as Oxygen Electrodes for High Temperature Oxide Fuel Cells", Sol. Stat. Ion., 22, (1987), 241-246.

[407] Y. Takeda, R. Kanno, M. Noda, Y. Tomida, and O. Yamamoto, "Cathodic Polarization Phenomena of Perovskite Oxide Electrodes with Stabilized Zirconia", J. Electrochem. Soc.: Electrochemical Science and Technology, 134:11, (Nov. 1987), 2656-2661,

[408] Fred van Heuveln, "Characterisation of Porous Cathodes for Application in Solid Oxide Fuel Cells", (Doctoral Dissertation, Technische Universiteit Twente, 1997).

[409] M. J. Jørgensen and M. Mogensen, "Impedance of Solid Oxide Fuel Cell LSM/YSZ Composite Cathodes", J. Electrochem. Soc., 148:5, (2001), A433-A442.

[410] San Ping Jiang, "Cathode materials of solid oxide fuel cells: a review", J Mater Sci, 43, (2008), 6799–6833.

[411] Rose-Marie Belardi, Jonathan Deseure, Márcia Caldeira Brant, Tulio Matencio, Rosana Zacarias Domingues, "Electrical study of cathodic activation and relaxation of $La_{0.80}Sr_{0.20}MnO_3$", Ionics, (2009), 15:227–232.

[412] Eric Wachsman and Subhash Singhal, "Solid Oxide Fuel Cell Commercialization, Research, and Challenges", Interface, (New Jersey: The Electrochemical Society, 18:3, Fall 2009), 39.

[413] Zhuiykov, (2008), 201.

[414] Zhuiykov, (2008), 137.

[415] D.R. Clarke and C.G. Levi, Materials Design for the Next Generation Thermal Barrier Coatings, Annu. Rev. Mater. Res., 33, (2003), 388.

[416] Zhuiykov, (2008), 137.

[417] Zhuiykov, (2008), 198.

Al$_2$O$_3$ at interface (50-50 weight ratio). The blending method is used in commercial gas sensors and molten metal sensors made of zirconia.[418]

A popular way of applying LSM electrodes is by sputtering.[406,407] This technique, however, requires a clean room environment. Electrodes of LSM have also been applied to SOFCs by gelcasting, a near net shape technique that does not require a clean room at the expense of feature size.[419] Researchers at Oak Ridge National Laboratory pioneered gelcasting techniques, a near net shape process that involves forming ceramic particles using polymerization techniques.[420,421,422,423,424,425,426,427,428,429] Another group also made an early contribution to the art.[430]

Gelcasting is an additive technique that can be used to make sensor electrodes from metal oxide powders. The gelcasting process consists of multiple steps, as illustrated in Figure 68. First, ceramic powder particulates and polymer precursors are mixed together to form a slurry. The addition of an initiator sets polymerization in motion. The slurry is then cast into the desired form and allowed to solidify. The polymers hold the particulates in place. Upon demolding and drying, the "green" material can be machined.[424,427,431] Subsequent heat treatment drives off the polymers during binder burn out and sintering. Depending on the sintering treatment, a pore

[418] Zhuiykov, (2008), 199.

[419] Lan Zhang, Yujun Zhang, Y. D. Zhen and San Ping Jiang. "Lanthanum Strontium Manganite Powders Synthesized by Gel-Casting for Solid Oxide Fuel Cell Cathode Materials", J. Am. Ceram. Soc., 90:5, (2007), 1406–1411.

[420] O. O. Omatete, A. Bleier, C. G. Westmoreland, and A. C. Young, "Gelcast Zirconia-Alumina Composites", 15th Annual Conference on Composites and Advanced Ceramics, (Cocoa Beach, FL, Jan. 1991).

[421] O. O. Omatete, M. A. Janney, and R. A. Strehlow, "Gelcasting—A New Ceramic Forming Process," Am. Ceram. Soc. Bull., 70:10, (1991), 1641-1649.

[422] A. C. Young, O. O. Omatete, M. A. Janney, and P. A. Menchhofer, ''Gelcasting of Alumina,'' J. Am. Ceram. Soc., 74:3, (1991), 612–618.

[423] S. D. Nunn, O. O. Omatete, C. A. Walls, and D. L. Barker, "Tensile Strength of Dried Gelcast Green Bodies," Ceram. Eng. Sci. Proc., 15:4, (1994), 493-498.

[424] S. D. Nunn and G. H. Kirby, "Green Machining Of Gelcast Ceramic Materials," Cer. Engg. Sci. Proc., 17:3, (1996), 209–213.

[425] Ogbemi O. Omatete, Mark A. Janney and Stephen D. Nunn, "Gelcasting: From Laboratory Development Toward Industrial Production", J. Eur. Ceram. Soc., 17, (1997), 407-413.

[426] Mark A. Janney, Ogbemi O. Omatete, Claudia A. Walls, Steven D. Nunn, Randy J. Ogle, and Gary Westmoreland, "Development of Low-Toxicity Gelcasting Systems," J. Am. Ceram. Soc., 81:3, (1998), 581-591.

[427] Mark A. Janney, Stephen D. Nunn, Claudia A. Walls, Ogbemi O. Omatete, Randy B. Ogle, Glen H. Kirby, and April D. McMillan, "Gelcasting", Chapter in The Handbook of Ceramic Engineering, Mohamed N. Rahaman, (ed.), (Marcel Dekker Inc., New York, 1998).

[428] M.A. Janney, "Attaining High Solids in Ceramic Slurries", Chapter in Advances in Process Measurements for the Ceramic Industry, A. Jillavenkatesa, G.Y. Onoda (eds.), (The American Ceramic Society, Ohio, 1999), 179–203.

[429] M.A. Janney, W.J. Ren, G.H. Kirby, S.D. Nunn, S. Viswanathan, "Gelcast tooling: net shape casting and green machining", Mater. Manuf. Process.,13, (1998), 340–389.

[430] Gideon S. Grader and Limor Zuri, "Tape Casting Slip Preparation by in Situ Polymerization", J. Am. Ceram. Soc. 76:7, (1993), 1809-1814.

[431] R.K. Kamboj, S. Dhara, P. Bhargava, "Machining behaviour of green gelcast ceramics", J. Eur. Ceram. Soc., 23 (2003), 1005–1011.

network may be left behind. Sintering conditions dramatically affect sensing ability.[432] Total shrinkage depends on several factors including solids loading and sintering temperature.
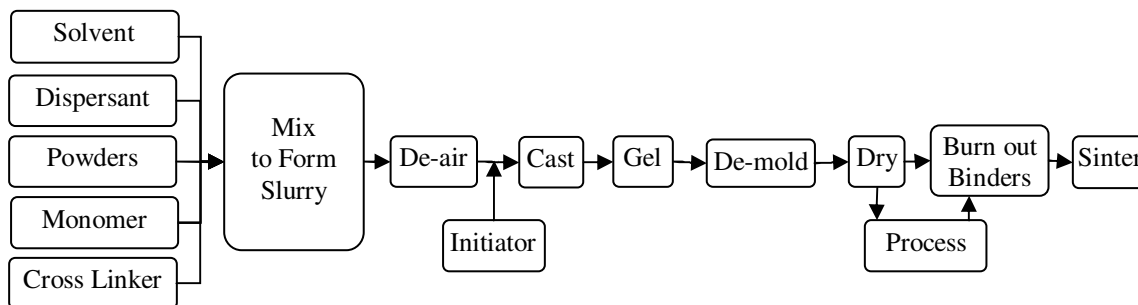
Figure 68. Gelcasting process.

Polymerization lies at the heart of gelcasting. Figure 69 shows the various steps of the polymerization process.
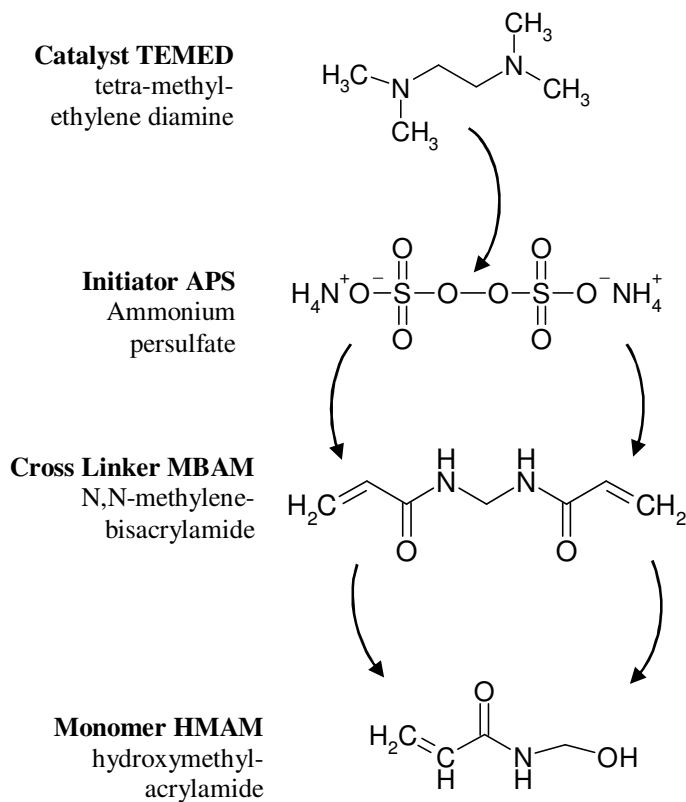
Figure 69. Chemistry of gelcasting.

In this investigation, the catalyst TEMED causes the initiator APS to cleave into two radicals that attack the double covalent bonds of the cross linker MBAM. This causes polymerization of

---

[432] Zhuiykov, (2008), 107.

the monomer HMAM which entraps and binds powder, effectively gluing it together in a desired shape or form. The polymerization process takes some time, which permits the casting of the slurry into a desired form.

The pH of the slurry can be controlled to maximize the solid content. Strongly acidic and strongly basic slurries generally result in higher solids loading on account of the attendant charged particles that stabilize the slurry and reduce sedimentation.[433]

During polymerization, a vacuum may be applied to prevent O_2 from interfering with the gelation process.[434]

Following polymerization, the green bodies are heated slowly in order to burn out binders and then sintered to 1500-1600°C in order to increase the density of the ceramic mass.[435] Generally, some shrinkage occurs during these processes.[436]

The NO_x sensors in this investigation have working and counter electrodes of gelcast LSM pre-fired to 1500ºC. A topcoat of porous electrolyte material (PSZ) covers the electrodes and provides an ion conduction path between them (Figure 70). These elements are arranged on a dense (pre-fired) tile of either alumina or PSZ.
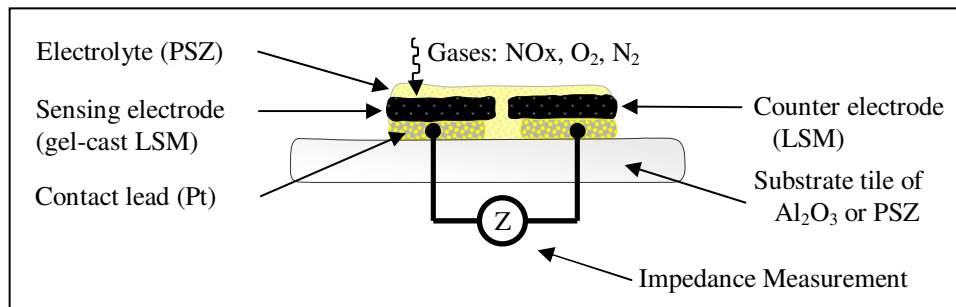
Figure 70. Schematic cross section of NO_x sensor with LSM electrodes (not to scale).

During sensor operation, gaseous species such as NO, NO_2, and O_2 diffuse through the topcoat of the porous electrolyte. The purpose of this layer is to increase the interface between the electrode and electrolyte, thereby enhancing the detection of NO_x species. Some gaseous species participate in redox reactions. Transfer of electrons changes the conductivity between the leads, which is characterized by an impedance measurement. Changes in the impedance characteristics can be calibrated to NO_x concentration.

This work relates the results of the first application of gelcasting to LSM for a NO_x sensor application. Both partially stabilized zirconia (PSZ) and alumina (Al_2O_3) were investigated as substrate materials for dense LSM electrodes. The main goal of this investigation is to evaluate the capability of LSM electrodes on alumina and PSZ substrates to sense NO_x. In addition, further objectives include exploring the performance of these sensors including:

- determine the effect of flow rate on sensor output

- establish the relationship between NO_x concentration and phase angle below 100 ppm

[433] Omatete, (Jan. 2009), 8.
[434] Janney. The Handbook of Ceramic Engineering, (1998), 8.
[435] Young, (1991), 613.
[436] Janney, The Handbook of Ceramic Engineering, (1998), p. 3.

- investigate the relative effects of O_2, NO, and NO_2

- evaluate the detection of O_2 and NO_x simultaneously

- examine the effect of temperature over time on device performance

- perform equivalent circuit modeling

- evaluate equivalent circuit for physical insights into the sensing mechanism

In the following pages, the results of the explorations into these areas are reported.

6.2 Experimental

NO_x sensors were constructed on 1 cm^2 square dense substrates of alumina and PSZ. Figure 90 depicts overhead view of a typical sensor. First, leads of platinum ink (Engelhard 6082) were painted in parallel stripes 1 mm wide and 3 mm apart and fired at 1200°C for 2 hours in ambient air inside a Thermolyne muffle furnace. In order to accommodate the burnout of organic species, a low thermal ramp rate was used early in the thermal treatment.

Presintered LSM electrodes were fabricated according to a gelcasting process in which LSM particles ($La_{0.85}Sr_{0.15}MnO_3$, d_{50} 2.6 µm, Praxair) were mixed with N-(hydroxymethyl) acrylamide monomer (HMAM, 48 wt% in water, Sigma-Aldrich) and deionized water (Millipore) using a magnetic stir. To this solution, N,N'-methylenebisacrylamide crosslinker (MBAM, Sigma-Aldrich) and polyacrylic acid dispersant (PAA, average MW ca. 1,800, Sigma-Aldrich) were added and mixed in, creating a thick slurry. Then ammonium persulfate initiator (APS, 98+%, A.C.S. reagent, Sigma-Aldrich) and N,N,N',N'-tetramethylethylenediamine catalyst (TEMED, Sigma-Aldrich) set the gelcasting processes in motion. The slurry was quickly poured into forms and allowed to dry overnight. Then the green bodies were placed in a furnace and the temperature was slowly ramped to 1000°C for binder burnout. After firing at this temperature for 2 hours, they were subsequently fired to 1500°C for 2 hours for sintering.

Working and counter electrodes of pre-sintered, gelcast LSM were attached to the leads using additional platinum ink. An electrolyte slurry containing PSZ was applied on top of and between the electrodes and allowed to dry. The sensors were placed in an oven and fired to 1200°C for 2 hours. Then the gold wire leads were electrically attached using a noble metal paste (Engelhard A3770) as a means to export the signal. These leads were anchored to the alumina tile using alumina cement (Aremco Resbond 920). The sensors were once again fired for 2 hours but at 1000°C as to avoid melting the gold wire leads.
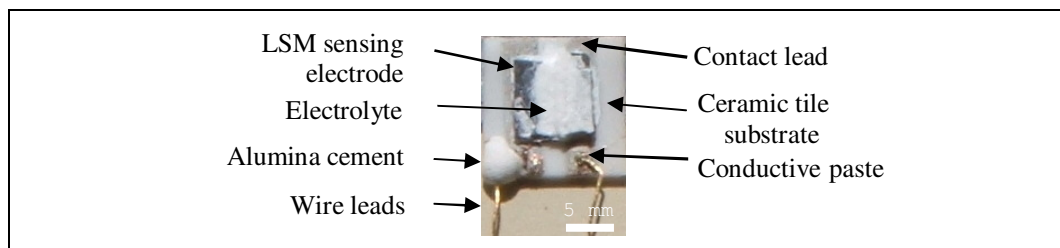
Figure 71. Top view NO_x sensor with gelcast LSM electrodes.

In order to interrogate the sensors using electrochemical impedance spectroscopy (EIS), the gold wire leads were attached to an analysis apparatus and the entire sensors were loaded into a quartz tube furnace.

The following factors were investigated: influence of variable flow rate (100-500 sccm); effect of NO and NO_2 individually (0, 25, 50, and 100 ppm); analysis of O_2 cross sensitivity (4-19%); and role of temperature on output over time. Unless otherwise stated, all experiments were carried out at 650°C in 500 sccm of 10% O_2 with the balance of the gas flow consisting of N_2 or N_2 with minute quantities of NO_x (<100 ppm).

Using a Solartron Analytical SI 1260 impedance/gain-phase analyzer with a Solartron Analytical SI 1287 electrochemical interface controlled by ZPlot data acquisition software (Scribner Associates, Inc.), EIS measurements were performed. Frequency sweeps between made from 1 MHz to 1 Hz at 25 mV excitation amplitude and ten impedance measurements per decade. A two electrode cell configuration was used. Two sweeps were performed for each sensor at each flow rate and gas composition. When the replicated impedance spectra showed overlap, the conclusion was drawn that steady state conditions had been reached.

From the impedance measurements, phase angles were calculated as the arctangent of the ratio of the capacitive contribution of the impedance to the resistive contribution for the frequency 10 Hz. By subtracting the phase angle of a specific gas composition from that of the base case (0 ppm NO_x), the shift in phase angle was calculated. This shift was evaluated for its relationship to species concentration. The shift in phase angle was the primary metric for sensor performance evaluation.

The first examination investigated whether sensor output changed with flow rate. EIS was carried out on a gas stream comprised of 10% O_2 with 100 ppm NO at different flow rates from 100 to 500 sccm. Sensitivity to NO and NO_2 was investigated by varying NO_x concentration from 0 to 100 ppm in 10% O_2 with balance N_2. Gas bottles containing 1000 ppm NO_x in N_2 were diluted with air and N_2 in order to obtain the desired concentrations. Next, the responses of sensors exposed to concentrations of O_2 from 4-18.9% in balance N_2 were recorded and evaluated. After changing the concentration of the analyte gas, at least 3 minutes time was passed with flowing gases in order to reach steady state. Furthermore, a study was carried out in order to determine the possibility of simultaneous detection of both O_2 and NO_x by examining shifts in phase angles at different frequencies (10 Hz and 1 kHz). Lastly, the effect of temperature on phase angle was also examined over several hundred hours. Using the experimental data, equivalent circuit modeling was performed using LEVM software.[437] In the modeling work, all model parameters were permitted to vary in order to identify any possible effects of changes in microstructure (aging).

6.3 Results and Discussion

During the fabrication of LSM electrodes, the LSM attained a density of 5.45 g/cm^3 as determined by the Archimedes method. Total linear shrinkage approximated 30%. Final electrode dimensions measured approximately 2 mm by 5 mm.

---

[437] James Ross Macdonald, LEVM/LEVMW Version 8.09 Complex Nonlinear Least Squares Fitting Program, (accessed on Dec. 16, 2009), available from http://www.jrossmacdonald.com/levminfo.html.

Impedance data from the various experiments was analyzed by making Nyquist plots, by calculating shifts in phase angle at 10 Hz, and by carrying out equivalent circuit modeling. A discussion of each variable factor follows.

6.3.1 Flow Rate

Flow experiments were carried out to see if a wide range of exhaust gases flow rates would affect diffusion through the boundary layer. Sensors with LSM electrodes recorded very similar impedance responses to mixtures of 10% O_2 with 50 ppm NO flowing from 100 to 500 sccm regardless of the substrate, as shown in Figure 72. Arabic numerals in the figures label the logarithm of the measurement frequency. Each decade of frequency is indicated by filled circles.

For the LSM sensors on Al_2O_3 substrates (LSM/Al_2O_3), the first impedance measurement at 1 MHz for all measurements was not located on the capacitive side of the Nyquist plot; rather it indicated inductance. Often a startup transient occurs during the measurement taken at the first frequency in a series of measurements.[438] This inductance is ascribed primarily to the leads.[439,440] It is difficult to eliminate inductance from measurements that result from lead length and positioning.[441] Other investigations of impedance-based sensors have exhibited such startup transients.[442] This inductance can be corrected.[443] For the purpose of this investigation, the inductance is identified and recognized but not corrected.

The high frequency arcs usually overlap regardless of gas mixture. In these experiments, the low frequency arcs (f < 10 kHz) that are sensitive to gases show good overlap as well, however, the overlap is not perfect. This may be attributed to the smaller impedance values of the PSZ substrate that make the error appear larger. The sensors with the PSZ substrate had both real and imaginary components of impedance an order of magnitude smaller than for Al_2O_3.

Al₂O₃ substrate   PSZ substrate
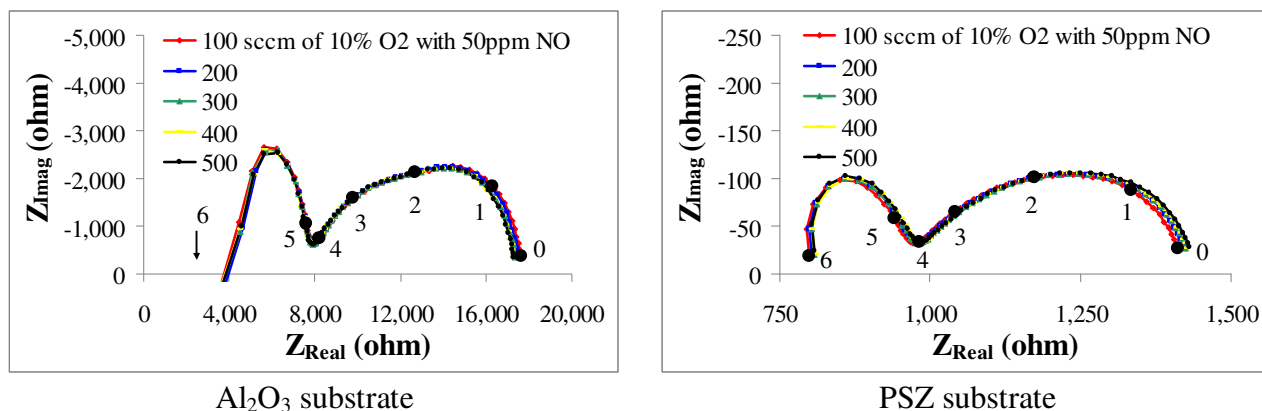
Figure 72. Impedance spectra are independent of flow rate for LSM/Al_2O_3 and LSM/PSZ.

---

[438] Orazem, 149.

[439] S. PrimdahI and M. Mogensen, "Oxidation of Hydrogen on Ni/Yttria-Stabilized Zirconia Cermet Anodes", J. Electrochem. Soc., 144:10, (Oct. 1997), 3411.

[440] Joshua L. Hertz, Anja Bieberle, and Harry L. Tuller, "Characterization of the Electrochemical Performance of YSZ Thin Films with Nanometer-Sized Grain Structure", MIT-Tohoku '21COE' Joint Workshop on Nano-Science in Energy Technology, (Cambridge, MA, Sept.27-28, 2004).

[441] Barsoukov, 232.

[442] Woo, (2008), J38.

[443] Barsoukov, 233.

In fact, the sensor with the PSZ substrate has less deviation over the examined flow range when the phase angle at 10 Hz is used as the metric, as indicated in Table 13. Measurements for sensors of both substrates have low standard deviations over the entire gas flow rate.

In Figure 72, both impedance spectra are offset from the ordinate. The sensor with the PSZ substrate has a very small offset, possibly due to a low contact resistance. Similarly, the width of its high frequency arc is much smaller than that of Al_2O_3, signaling a smaller ion transfer resistance through the bulk electrolyte. The pre-sintered PSZ substrates are expected to have a lower resistance.

Total Gas Flow Rate	LSM/Al_2O_3 Θ(10Hz)	LSM/PSZ Θ(10Hz)
100	-6.47	-3.77
200	-6.33	-3.78
300	-6.27	-3.80
400	-6.24	-3.80
500	-6.22	-3.84
St Dev:	0.10	0.03

Table 13. Phase angles at 10 Hz for LSM sensors over a range of flow rates.

In summary, the output of both types of LSM sensors are independent of flow rate, allowing them to be used to detect the composition of the mixture over a range of exhaust flow rates. Nakatou and Miura also found similar results for an impedance-based sensor.[444]

6.3.2 NO$_x$ Sensing

All sensors were exposed to NO and NO_2 at 0, 25, 50, and 100 ppm. Nyquist plots were made from the collected impedance data. They are shown in Figure 73 and Figure 74, for NO and NO_2, respectively. The Arabic numerals label the logarithm of each decade of frequency in the base case (10% O_2/N_2, no NO$_x$). The Nyquist plots exhibit two arcs with a cusp at approximately 10 kHz. Consistent with previous findings in the literature, the presence of NO$_x$ affects the low frequency arcs (f < 10 kHz) of the impedance spectra by decreasing the magnitude of the impedance response.[445, 446, 447, 448, 449, 450, 451, 452, 453] Some variation in the high frequency arcs due to microstructural transformation is visible in the figures.

Both NO$_x$ species evoke an inward shift of the low frequency arc. NO evokes a larger shift than NO_2, however, at all concentrations, the shifts are small. This finding is contrary to the previous chapter in which sensors with gold wire electrodes had a larger response for NO_2 than for NO.

---

[444] Nakatou, (2006), 57-62.
[445] Miura, (2002), 286.
[446] Miura, (2003), 224.
[447] Miura, (2004), 1138.
[448] Martin, J Electrochem Soc, (2007), J97-J104.
[449] Woo, J Electrochem Soc, (2007), J130.
[450] Woo, (2008), J35.
[451] Stranzenbach, Sensor Actuator B Chem, (2007), 226.
[452] Murray, 57.
[453] Stranzenbach, (2009), 156.

Al$_2$O$_3$ substrate   PSZ substrate
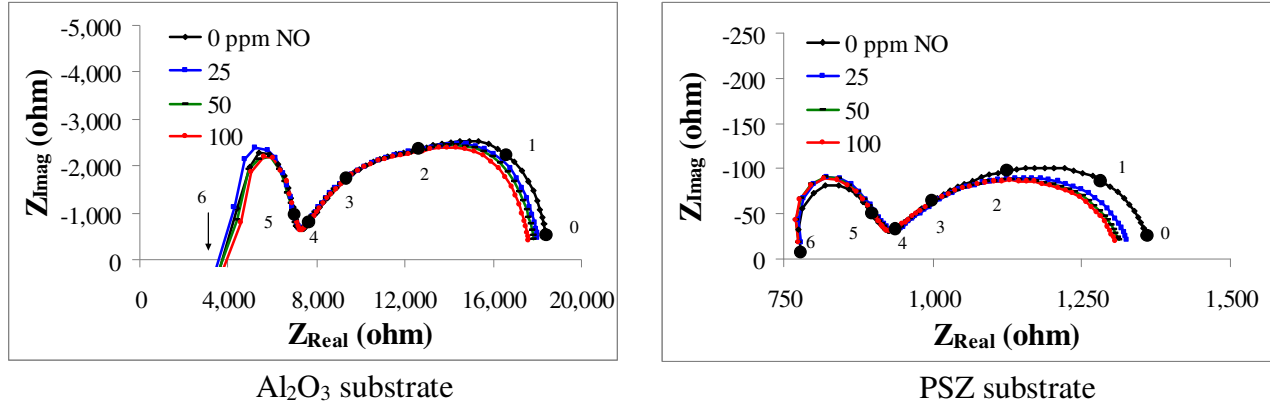
Figure 73. Sensor impedance response decreases with increasing NO content.

Miura *et al.* found that by manipulating the temperature, nearly identical responses to NO and to NO$_2$ could be obtained. This finding permitted total NO$_x$ detection at 700°C.[454, 455, 456, 457] This result may be due to thermodynamic equilibrium that occurs at temperatures above 600°C that involves the dissociation of NO$_2$ to NO.[458, 459]

Al$_2$O$_3$ substrate   PSZ substrate
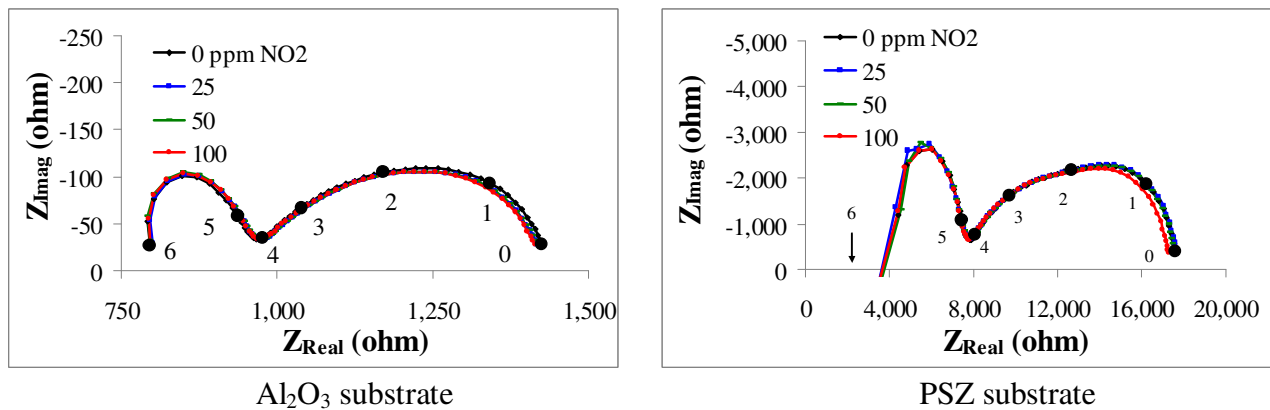
Figure 74. Sensor impedance response decreases with increasing NO$_2$ content.

The shifts of the low frequency arcs for NO$_2$ were small and inconsistent for the LSM sensors on both substrates. Figure 75 shows a close up view of the low frequency arcs for both types of sensors. In the case of the Al$_2$O$_3$ substrate, the arc did not always shift inwards due to the presence of NO$_2$. This finding has unfavorable implications for these sensors.

---

[454] Miura, (2002), 284–287.
[455] Miura, (2003), 221–228.
[456] Woo, <u>J Electrochem Soc</u>, (2007), J133.
[457] Miura, (2009), 201.
[458] Zhuiykov, (2008), 215.
[459] Woo, <u>J Electrochem Soc</u>, (2007), J133.
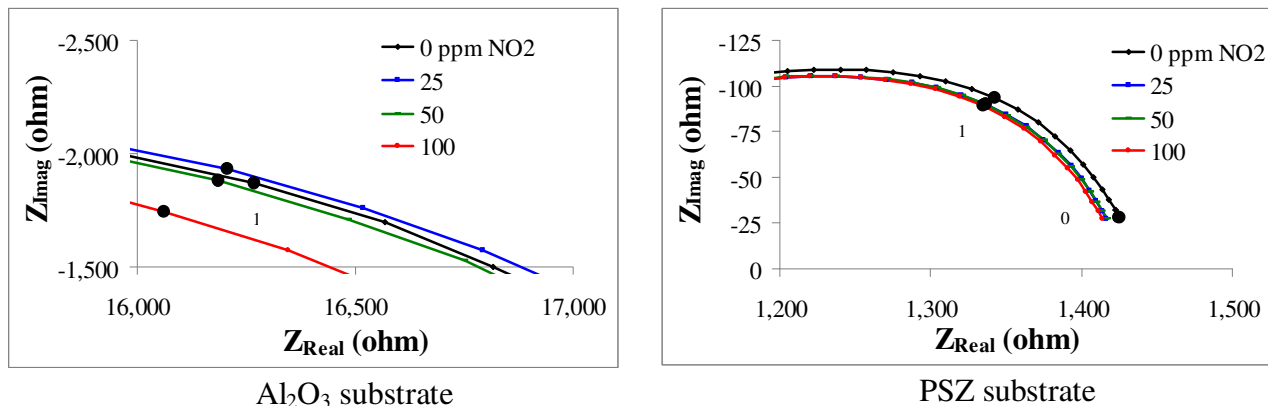
Figure 75. Enlarged low frequency arcs of LSM sensors show low sensitivity to NO₂.

Using a small number of data points, a linear relationship was shown to exist between the change in phase angle and NO concentration from 25-100 ppm for both substrates (Figure 76). The limitations of the experimental setup did not permit investigation of NO_x concentration less than 25 ppm. Linear regression lines of the experimental data had high R^2 values, however, upon extrapolation they do not pass through the origin. While it may be possible to calibrate such a sensor to known concentrations of NO, the empirical data suggests that a NO concentration of zero evokes a non-zero change in phase angle. Martin *et al.* discovered linear relationships between the shift in phase angle and NO_x concentration from 8-50 ppm that generally passed through the origin.[460]
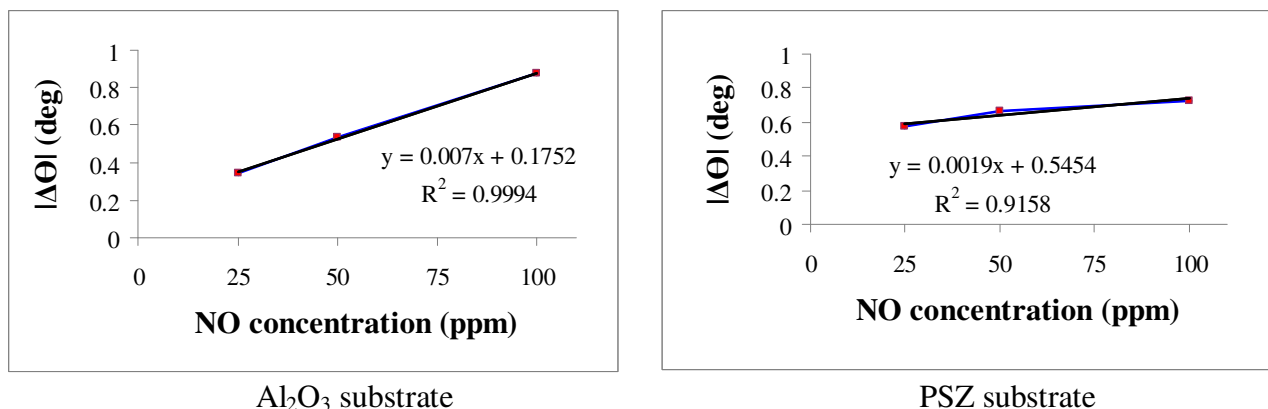
Figure 76. Phase angle difference varies linearly with NO content.

For NO₂, the data analysis also yielded linear relationships Once again, only three points were included in the regression, and the regression did not include the origin (Figure 77). For NO₂, a different metric was used; the phase angle shift was examined in lieu of the absolute value thereof. This metric is useful for the Al₂O₃ substrate whose linear relationship crosses the abscissa. From the graph, there is no phase angle shift at approximately 55 ppm for the LSM sensors on the Al₂O₃ substrate, and some concentrations of NO₂ evoke responses in different directions. This result is inauspicious for the future prospects of this type of sensor. For the PSZ substrate, the response is very small – perhaps too small to be useful. These characteristics suggest that the gelcast LSM sensors are not adequate for NO_x detection.

---

[460] Martin, J Electrochem Soc, (2007), J97-J104.

Al$_2$O$_3$ substrate   PSZ substrate
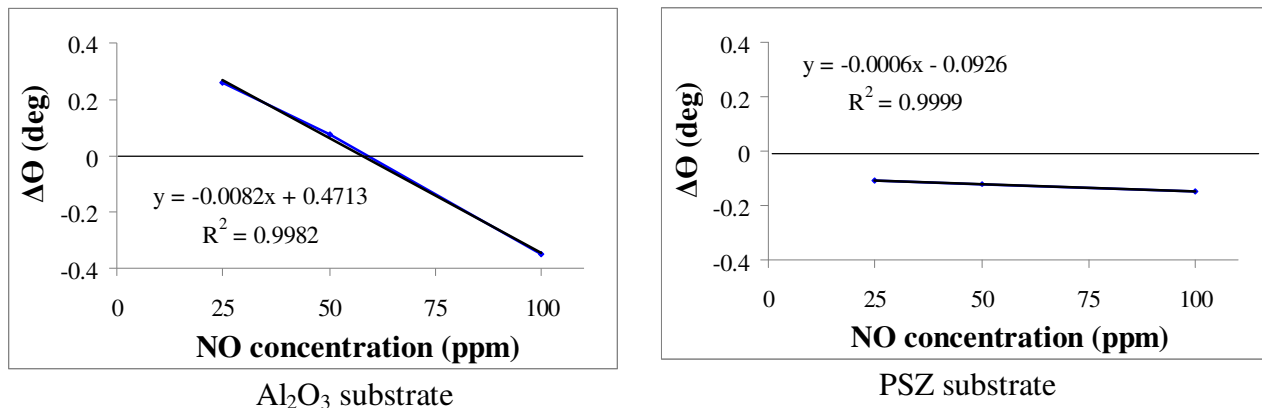
Figure 77. Phase angle difference varies linearly with NO$_2$ content.

6.3.3 Cross Sensitivity

The sensors respond to O$_2$ content found in diesel exhaust in addition to NO$_x$ species. The sensors might be affected by HCs, but the oxidation catalyst upstream may address this concern. This section examines the effect of the excess O$_2$ compared to NO$_x$ species.

Effect of O$_2$

Changing the O$_2$ concentration alters the impedance spectra (Figure 78). Filled circles on the spectra for the highest and lowest concentrations of O$_2$ are associated with decades of frequency indicated by Arabic numerals.

Al$_2$O$_3$ substrate   PSZ substrate
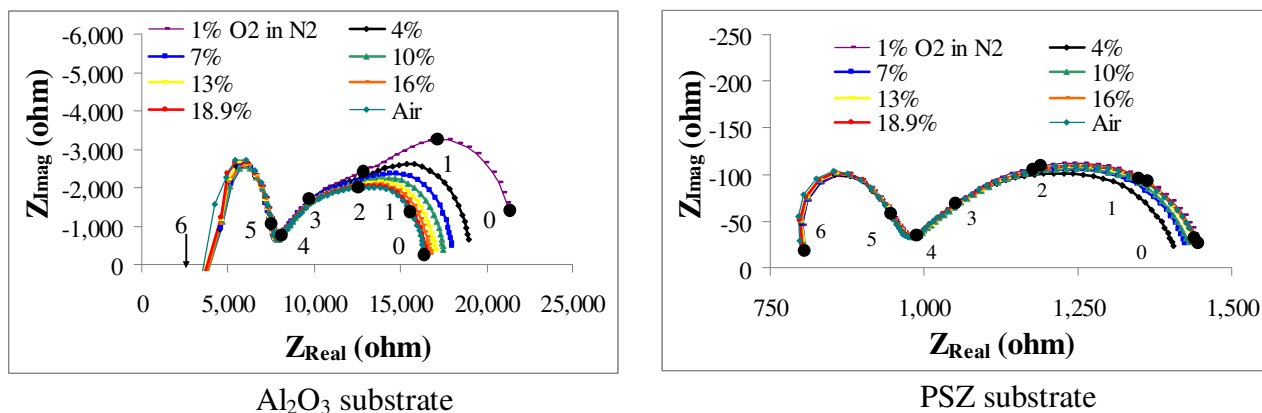
Figure 78. The effect of O$_2$ on impedance spectra.

In Figure 78, the high frequency arcs stay more or less the same regardless of gas concentration, as expected. Minor variations in the high frequency arcs from one measurement to another are attributed to sensor microstructural transformation (aging) of the bulk of the electrolyte[461] or within the electrode itself.[462]

For the Al$_2$O$_3$ substrate, the low frequency arcs shift inwards with increasing O$_2$ concentration, decreasing the magnitude of the phase angle. For the PSZ substrate, however,

---

[461] Wu, 51.

[462] Miura, (2003), 226.

opposite behavior was observed: increasing O_2 shifted the arcs outwards. This result is shown in enlarged detail in Figure 79. In this plot, the filled circles represent the measurements of the highest and lowest O_2 concentrations at 10 Hz. The measurement with 1% O_2 acts as expected (highest impedance), but the 4% O_2 arc for the second smallest O_2 concentration had the largest shift inwards. The changes in impedance are very small for this sensor; for all intents and purposes, these curves can be considered to be the same, and the sensor with the PSZ substrate is not very sensitive to O_2. Unfortunately, this type of sensor is not very sensitive to NO_x either.
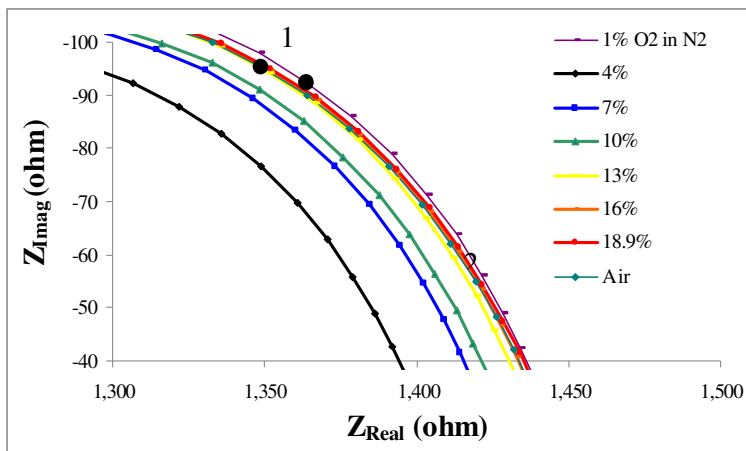
Figure 79. Increasing O_2 concentration shifts the low frequency arcs outward for LSM/PSZ.

Plots of phase angles over a wide range of O_2 concentration for several frequencies in the low frequency arc are shown in Figure 80. For the PSZ substrate, the curves are flat which indicates a lack of sensitivity to O_2, as discussed above. Woo *et al.* found that sensors that can detect NO have large impedance values that suggest few electrochemical reaction sites. Sensors with low impedance such as the LSM sensors on PSZ substrates were not sensitive. PSZ may have furnished too many reaction sites, making it a poor sensor. A rate-limiting process is necessary for detection.[463]
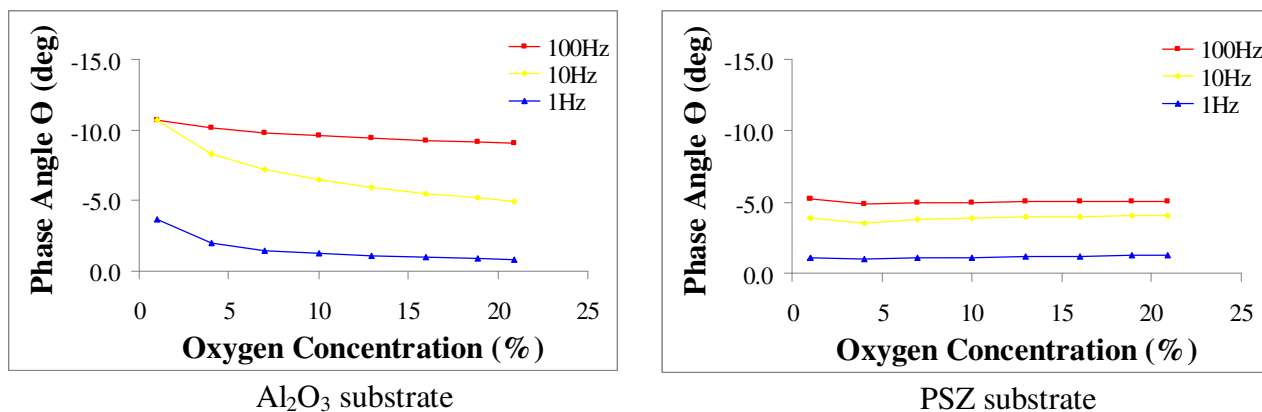
Figure 80. Phase angles at low frequencies over a range of P_{O_2}.

For the substrate Al_2O_3, the curves are approximately linear at concentrations above 7%, but some curvature occurs at concentrations below this value. This curvature makes it difficult to

---

[463] Woo, (2008), J39.

create an algorithm to compensate for excess O_2 typically found in diesel exhaust. In the literature, O_2 cross sensitivity has been recorded.[464]

Simultaneous Sensing of NO_x and O_2

For sensors that detect both NO_x and O_2, Martin *et al.* reported a method of compensation for excess O_2.[465] It involved detecting O_2 at a higher frequency that is insensitive to NO_x. With their electrochemical system, several minutes were required for equilibration, and the authors questioned the practicality of this method of compensation.

The sensitivity of gelcast LSM sensors to O_2 at higher frequencies (1 kHz and above) was investigated. Figure 81 shows the phase angles over a range of O_2 concentrations for both sensor types. In general, the curves are flat, indicating very little sensitivity to O_2. In the case of the Al_2O_3 substrate, the curve for 1 kHz shows a non-zero slope, however, the change is only a fraction of a degree of phase angle over the entire range of O_2 concentration. At this frequency, the experimental impedance data did not vary due to NO_x concentration.

| Al_2O_3 substrate | PSZ substrate |
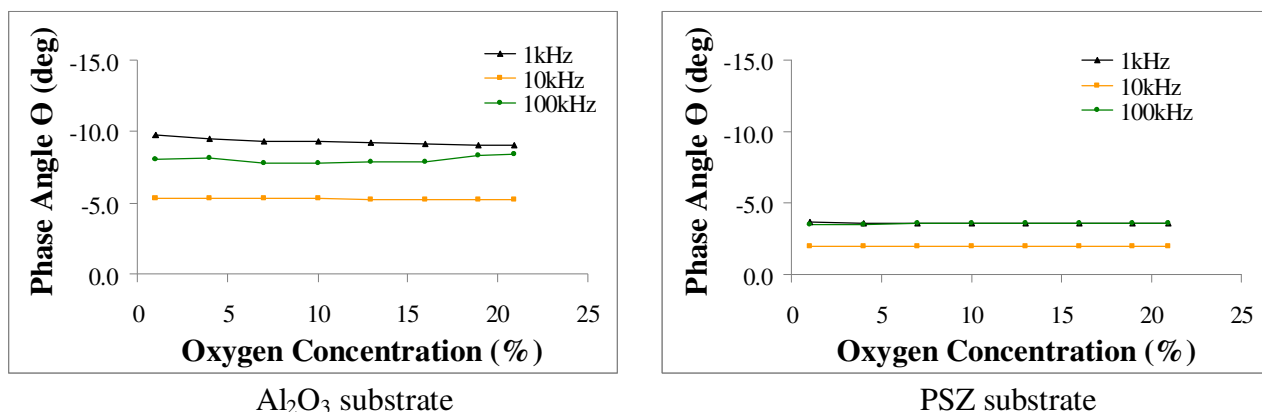
Figure 81. Phase angles at high frequencies over a range of Po_2 show little sensitivity to O_2.

A calibration curve was constructed for the LSM sensor with the Al_2O_3 substrate (Figure 83). It relates the phase angle at 1 kHz to that at 10 Hz. Empirical data points were fit by a trend line with a high R^2 value. Such a calibration graph might provide a correction for O_2 cross sensitivity at 10 Hz by sensing O_2 at 1 kHz, thereby enabling simultaneous sensing of NO_x and NO_2 according to the method of Martin *et al.*[465]

---

[464] Zhuiykov, (2005), 330.
[465] Martin, J Electrochem Soc, (2007), J97-J104.
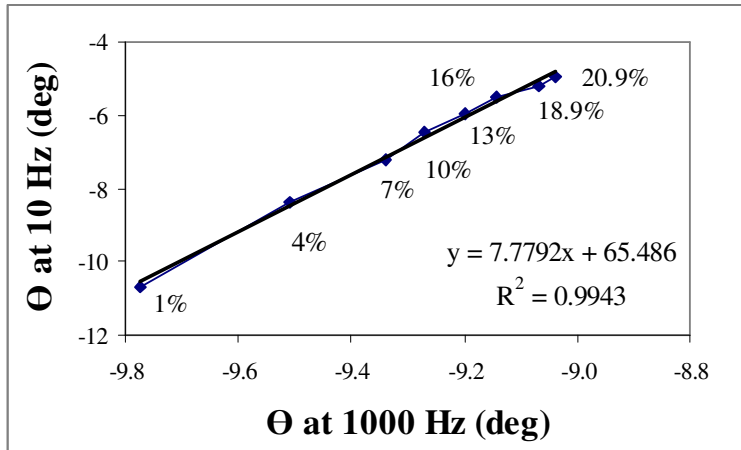
Figure 82. Calibration curve for O_2 compensation of LSM sensor with Al_2O_3 substrate.

Figure 83 shows that the change in phase angle at 1 kHz is small – less than 1°. As a result, a small error in this measurement could result in a large error in the compensation of O_2. These measurements were taken at intervals of several minutes; the time to equilibrate is unrealistic for real time correction. Last of all, this calibration curve might change over time due to microstructural aging. Due to these drawbacks, the simultaneous sensing of NO_x and O_2 by interrogation of the sensors at different frequencies is impractical using these gelcast LSM sensors on Al_2O_3 substrates.

6.3.4 Effect of Temperature

For gas-sensing, the sensor output must be calibrated to known gas concentrations at specific temperature. Nevertheless, even at a known temperature, the impedance spectrum drifted over time when exposed to air at 650°C.
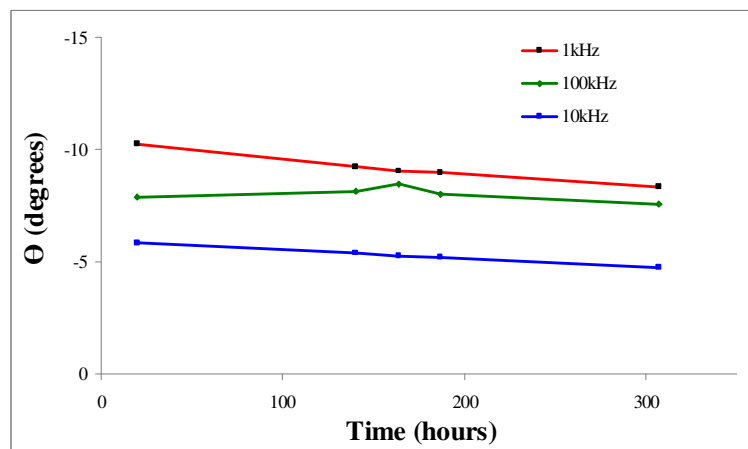
Figure 83. Aging of LSM sensor with Al_2O_3 substrate in air at 650°C.

Figure 83 shows the changes in phase angle at higher frequencies that occurred over hundreds of hours in the sensors with Al_2O_3 substrates. These frequencies are associated with the PSZ electrolyte. The output at lower frequencies also changes as a result. Microstructural transformation of the electrolyte alters the conductivity of the sensors. It is not possible to heat

109

treat the sensors at high temperature (1500°C) in order to complete the microstructural transformation because of the formation of zirconates at (1300°C) that retard conductivity.[466]

Murray *et al.* also reported changes in impedance after 11 days of evaluation. The drift in the phase angle was attributed to material instability. In order for these types of NO_x sensor to be viable signal drift must be overcome.[467]

6.3.5 Equivalent Circuit Analysis

Equivalent circuit modeling was carried out for the base case (10% O_2 in N_2, 650°C) for both types of sensors. In addition, modeling of exposure to NO_x gases was performed on the sensors with the Al_2O_3 substrates. In this equivalent circuit analysis, the contributions of measurement leads to capacitance and resistance were assumed to be negligible. In addition, the inductive transient upon start up exhibited by the sensors with the Al_2O_3 substrate was not included in the model.

The impedance spectra provided insights into fitting the impedance data with an equivalent circuit. The offset from the ordinate can be modeled by a resistor, whereas the arcs are reproduced by a combination of a Voigt element (RC) and Cole elements (RQ) in series. A Voigt circuit[468] consisting of a resistor with three Voigt elements was initially evaluated, however, replacing some Voigt elements with Cole elements more closely replicated the impedance data at low frequencies that represents the sensing electrode processes. The Cole elements represent non-ideal Voigt elements that feature a distribution of relaxation times due to inhomogeneities in the electrode-material system or due to nonuniform diffusion.[469]

For both types of sensors, the equivalent circuit model consisted of a resistor, a Voigt element, and two Cole elements in series, R_0-(R_1C_1)-(R_2Q_2)-(R_3Q_3), as shown in Figure 84. This combination of circuit elements provided the best fit with the lowest sum of squares of residuals.

Woo *et al.* also used 2 Cole elements to model one low frequency arc, implying that two physicochemical processes with similar time constants were taking place. Woo suggested that the rate-determining step for NO-sensing may depend on O_2 reactions that take place away from the triple-phase boundary. Although the exact mechanism was not determined, adsorption and diffusion of O_2 were offered as possible rate-limiting steps for the detection of NO.[390]
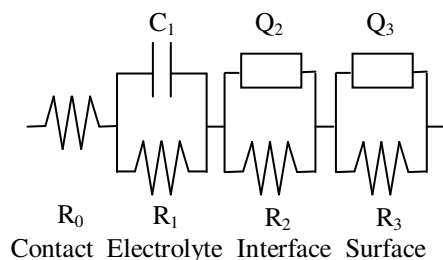
Figure 84. Equivalent circuit for NO_x sensor with gold wire sensing electrode.

[466] Claudia Alicia Cortés-Escobedo, Juan Muñoz-Saldaña, Ana María Boların-Miró, Félix Sánchez-de Jesús, "Determination of strontium and lanthanum zirconates in YPSZ–LSM mixtures for SOFC", J Power Sourc, 180, (2008), 209–214.
[467] Murray, 60-62.
[468] Agarwal, 1918.
[469] Barsoukov, 87.

Figure 85 shows the match between the modeling and the experimental data. Discrete empirical data points for the base case (10% O_2 in N_2, 650°C) align well with the impedance response of the equivalent circuit for both sensor types. The two CPEs have similar time constants; as a result, their arcs overlap into one larger, low frequency arc. Similar modeling was also performed on the data obtained with the LSM sensor on the Al_2O_3 substrate for various gas compositions; the model fit equally well.

The low frequency arcs associated with gas-sensing generally had excellent fit with the model. The high frequency arcs contained a few points that exhibited a transient effect at the beginning of the sweep from high to low frequencies. The high frequency arcs were approximately semicircular in shape, suggesting that the impedance resulted from a single activation-energy controlled relaxation process.[470]
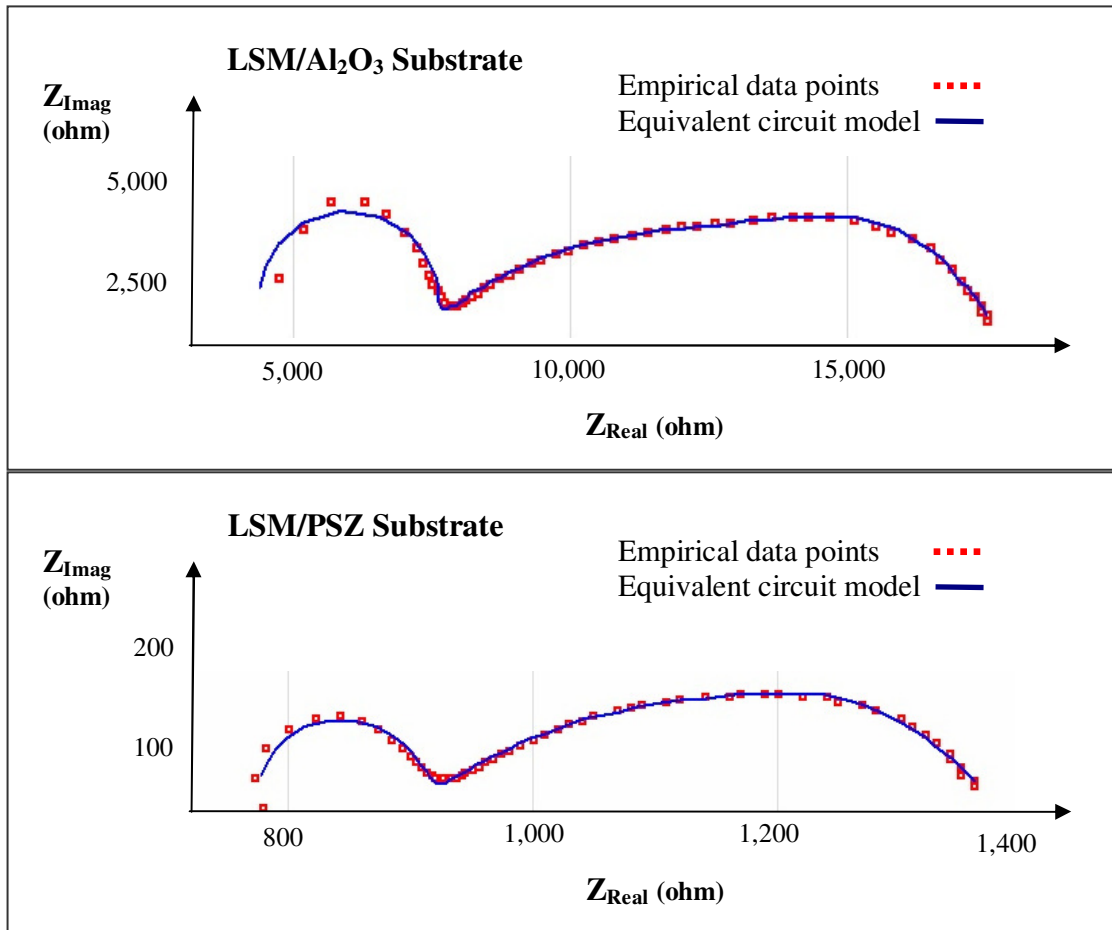
Figure 85. Impedance data points fitted by equivalent circuit model.

The impedance of the high frequency arc is replicated by (R_1C_1); it has been attributed to the bulk of the electrolyte.[455,471,472] In the previous section, as the electrolyte aged, the data points associated with the high frequency arc also changed. This observation confirms that the high frequency arc represents the electrolyte.

---

[470] Orazem, 313.

[471] Wu, 49–53.

[472] Yoon, (2001), 486.

The Cole elements (R_2Q_2 and R_3Q_3) model the response to low frequency stimulus. Each element represents a different process. The discussion focuses on this arc and its parameters.

In the literature, a detailed sensing mechanism is not readily available because the mechanism is still poorly understood.[473] The sections below associate the effects of various gases on parameters in equivalent circuit model which are related to physical processes.

Effect of NO_x

Exposure to NO_x caused reversible changes in CPE parameter of one of the Cole elements, Q_2, associated with the low frequency arc. Only this arc changed significantly in the presence of sample gases. Figure 86 shows that this parameter changes more than one hundredfold compared to the base case without NO_x. Other parameters did not vary as drastically upon the addition of NO_x.
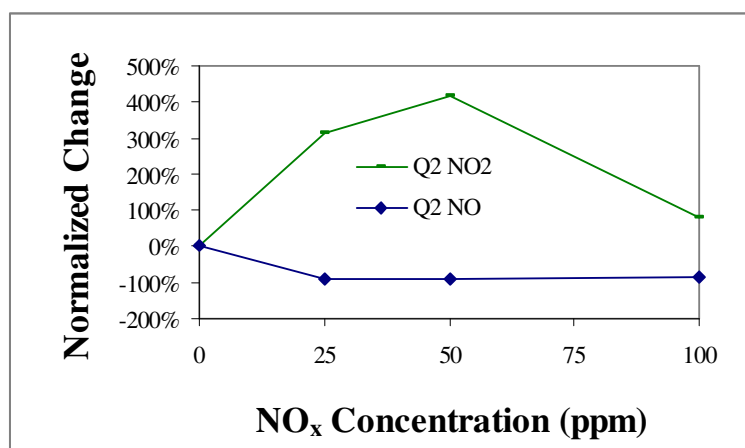
Figure 86. Q_2 changes due to NO_x in LSM sensor on Al_2O_3 substrate.

The impedance of a CPE is usually given by $Z = 1/[(j\omega)^{\varphi}Q]$, where Q is a CPE parameter related to double layer capacitance.[474] Here, the impedance of the CPE is defined as $Z = 1/[(j\omega Q)^{\varphi}]$, which yielded a better fit. This definition of CPE differs slightly from the more traditional one because the phase angle exponent, φ, took on a value close to 1 over the entire range of or all NO_x concentrations.

The CPE parameter, Q_2, accounts for the non-ideal behavior of a double layer. Since the value of the constant phase element exponent, φ, took on values close to 1, the CPE represented a non-ideal capacitor; the CPE parameter, Q_2, was an approximate measure of capacitance. This double layer represented an interface between the sensing electrode and the electrolyte.[471, 472, 475, 476, 477, 478, 479]

---

[473] Zhuiykov, (2008), 128.
[474] Barsoukov, 495.
[475] Woo, <u>Mater Res Soc Symp Proc</u>, (2007).
[476] Nakatou, (2004), 995–998.
[477] Nakatou, (2005), 2411–2415.
[478] Nakatou, (2006), 57–62.
[479] Woo, <u>J Electrochem Soc</u>, (2007), J131.

The parameter, Q_2, changes for both NO and NO_2. The changes were larger for NO_2 than NO. In the case of NO_2, the capacitance increased, whereas it decreased for NO. These results may be due to the different electrochemical reactions that these different gases underwent. The changes in capacitance did not follow a trend with NO_x concentration.

Yoon *et al.* reported that NO_2 dissociates and migrates easily at the electrode interface. This may explain the increase in capacitance.[480]

The resistor in the first Cole element, R_2, did not change with NO_x exposure. This parameter represents the interfacial charge-transfer from the electrode to the electrolyte. It is associated with processes such as adsorption, dissociation, and electrochemical reactions at the electrode.[454,455,471,476,477,478,481] This resistance depends on O^{2-} ion exchange.[482] In the gelcast LSM on Al_2O_3, NO_x did not change the value of this parameter. NO_x only changed the parameter Q_2 significantly. However, the precise mechanism remains unclear.

Effect of O_2

Oxygen evokes concentration-dependent relaxations in the gelcast LSM sensors on Al_2O_3 substrates. Figure 90 shows the parameters that changed the most with respect to the case with 1% O_2: R_1, C_1, Q_2, R_3, and Q_3. Surprisingly, the parameters associated with the Voigt element that represent the bulk of the electrolyte (R_1 and C_1) changed in the presence of O_2, especially at lower concentrations. As concentration increased, the curve flattened out. These parameters are associated with the high frequency arc. Restricting the amount of oxygen appears to decrease the conductivity of the electrolyte, as well as provide fewer species for a double layer.

As was the case with NO_x, Q_2 changed, but very erratically. The interface is important for O_2. Once again R_2 did not change.

R_3 and Q_3 both altered considerably in the presence of increasing O_2. Q_3 showed the largest change of all. Since these parameters did not change due to NO_x concentration (above), they are associated with a process containing O_2 such as adsorption or dissociation.
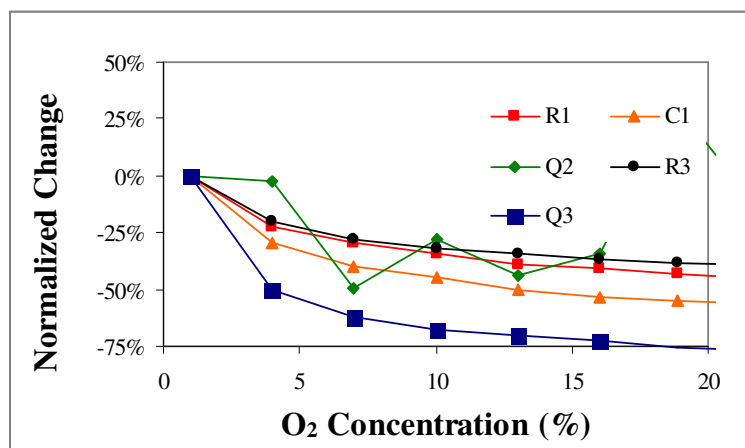
Figure 87. Q_2 changes due to NO_x in LSM sensor on Al_2O_3 substrate.

---

[480] J. W. Yoon, (2001), 486.
[481] Wama, 2774.
[482] Stranzenbach, (2009), 154–163.

More in depth consideration of the resistance elements of the equivalent circuit offers clues on the rate-limiting step for the sensing mechanism. In specific, if the inverse of resistance is proportional to O_2 concentration raised to a power, i.e. $1/R_2 \alpha (Po_2)^n$, then the exponent, n, offers indication of the rate-limiting step. Yamamoto *et al.* summarized exponent values and corresponding reaction steps. (Table 11).[483]

Figure 88 shows the change in conductivity over a range of partial pressure of O_2 for an interrogation frequency of 10 Hz for each resistor in the equivalent circuit. Each curve was fit by a power law relationship. The exponent for each conductivity (i.e. "n" in $\sigma_2 \alpha (Po_2)^n$) is listed in Table 14. Only R_2 depended strongly on Po_2.
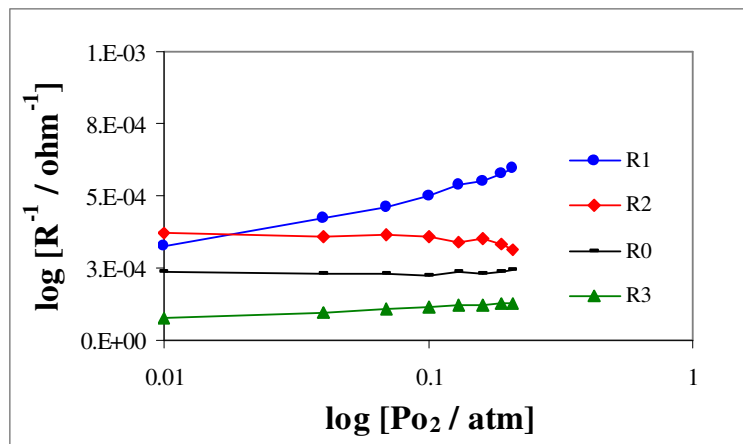
Figure 88. Log plot of variation of $1/R_i$ with O_2 concentration at 10 Hz.

In Figure 88, neither R_0 nor R_2 depended on Po_2. The bulk electrolyte conductivity, $1/R_2$, remained approximately constant with minor variation over the entire range of O_2. In both cases, the exponent associated with the power fit approximated zero. Independence from Po_2 is consistent with a conductivity relaxation,[484, 485] however, a contact resistance should also be independent of Po_2.

Conductivity	n	Physical Process
$1/R_0$	0.0068	Conductivity of contact
$1/R_1$	0.1953	Charge transfer through electrolyte bulk
$1/R_2$	-0.0374	Conductivity through electrode or interfacial conductivity
$1/R_3$	0.1651	Adsorption of O_2

Table 14. Dependence of $1/R$ on $(Po_2)^n$ and the physical significance.

The resistance R_3 changed with Po_2, so an O_2-related process such as adsorption is responsible.

[483] Y. Takeda, R. Kanno, M. Noda, Y. Tomida, and O. Yamamoto, "Cathodic Polarization Phenomena of Perovskite Oxide Electrodes with Stabilized Zirconia", J. Electrochem. Soc.: Electrochemical Science and Technology, 134:11, (Nov. 1987), 2659.

[484] M. J. Jørgensen and M. Mogensen, "Impedance of Solid Oxide Fuel Cell LSM/YSZ Composite Cathodes", J. Electrochem. Soc., 148:5, (2001), A433-A442.

[485] Barsoukov, 259.

R_3 depended on Po_2. This value was approximately ¼, which suggests that atomic oxygen processes such as atom adsorption with low surface coverage serve as the rate-limiting step (Table 11).[367]

Microstructural Transformation (Aging)

EIS was performed on LSM sensors on Al_2O_3 substrates in the presence of air over approximately 300 hours. Equivalent circuit modeling was performed. Over time, the resistance values of the equivalent circuit changed. The change in the resistance values appear in Table 15.

Resistor	Change	Physical Representation
R_0	+13 %	Resistance of contact
R_1	-16 %	Charge transfer resistance through electrolyte bulk
R_2	+ 9 %	Resistance through electrode or interfacial resistance
R_3	-22 %	Adsorption of O_2

Table 15. Change in resistance values over approximately 300 hours.

As time progressed, the contact resistance (R_0) grew larger, suggesting that the connection degraded as the microstructure of the PSZ changed. R_1 characterized the change in PSZ. It declined over time as the PSZ sintered and the resistance to ion flow through the PSZ decreased. The resistance associated with the electrodes, R_2, increased, suggesting that the contact between LSM and PSZ degraded. The resistance associated with O_2 adsorption, R_3, decreased, indicating that a physical feature such as surface area or crystal grain orientation became more favorable for adsorption. Further experimentation is necessary to confirm these findings.

6.4 Conclusions

Gelcast LSM was examined as an electrode material for a NO_x sensor. Sensors with LSM working electrodes were fabricated and evaluated using impedance spectroscopy and equivalent circuit analysis. Variation in the flow rate of the simulated lean exhaust did not change the sensor response appreciably. Both sensors exhibited a linear relationship between phase angle and NO_x concentration from 25-100 ppm, however, limited data points were examined, and the trend lines did not include the zero NO_x case. Sensors with LSM on PSZ substrates did not show cross sensitivity to O_2. In contrast, those on Al_2O_3 did. At a frequency of 1 kHz, the sensors on Al_2O_3 exhibited sensitivity to O_2 but not to NO, however the sensitivity was small. Compensation for O_2 that affects the NO measurement at 10 Hz may be possible, however the long equilibration time and low sensitivity suggested that it was impractical.

The equivalent circuit model that represented the LSM sensors consisted of a series combination of a resistor, a Voigt element, and two Cole elements. The modeling results of sensors with the Al_2O_3 substrates revealed that NO_x affects only the CPE parameter Q_2 significantly. The physical representation of this parameter is capacitance. For NO, the capacitance decreased by two orders of magnitude, whereas for NO_2 it increased by over two orders of magnitude. Variation of O_2 altered more parameters. In particular, the changes in resistance values provided insights into physical processes. An analysis of the change of resistances over time helped to confirm the physical processes suggested by the analysis of Po_2.

In summary, the model yielded fruitful results that allow better understanding of the physicochemical processes at work in the sensor.

The performance of sensing electrodes of LSM is not as promising as gold. In addition, LSM presents other challenges. LSM it is stable in contact with PSZ until approximately 1300°C beyond which insulating zirconate phases form.[84] This temperature is below the usual firing temperature of 1500°C of conventional high temperature cofired ceramic (HTCC) techniques.[486] Consequentially, the sintering temperature of the sensors in this study did not complete the microstructural aging process. As a result, signal drift occurred. A different manufacturing method for sensors with LSM electrodes is necessary to provide a viable sensor.

---

[486] Wayne S. Young, Sarah H. Knickerbocker, "Chapter 9 Multilayer Ceramic Technology", Relva C. Buchanan (ed), <u>Ceramic Materials for Electronics – Processing, Properties, and Applications</u>, 2nd edn., (Marcel Dekker Inc., New York, 1992), 511.

CHAPTER 7: Statistical Optimization of a NO$_x$ Sensor with Gold Electrodes

Four single cell impedancemetric NO$_x$ sensors were fabricated in the context of a two level, half fractional factorial experimental design (2_{III}^{3-1}) to determine the effect of design features on sensitivity to NO or NO$_2$. Three design factors were varied: number of working electrode sensing wires, electrolyte thickness, and the spacing between sensing wires. Sensing ability was measured by performing electrochemical impedance spectroscopy and calculating the phase angle difference at 10 Hz for 50 ppm NO or NO$_2$ with 10% oxygen and balance nitrogen. As determined by ANOVA, the number of electrodes did not affect detection of NO, however, fewer electrodes and the attendant smaller electrode surface area did affect NO$_2$-sensing. Electrolyte thickness was statistically significant for sensing both NO and NO$_2$. Sensors with thicker layers of porous YSZ electrolyte showed larger sensitivity as measured by the shift in phase angle due to NO$_x$. Equivalent circuit modeling showed that a thicker porous electrolyte layer lowered bulk electrolyte resistance instead of increasing it. The rate-limiting step for NO$_x$ sensitivity depended on the surface area of the porous electrolyte, however, the exact mechanism was unclear. Although the bulk YSZ resistance did not change with gas species, this resistance was important for sensing ability. The third factor, electrode spacing, did not affect gas-sensing.

7.1 Introduction

Government regulations have stipulated the continuous monitoring of NO$_x$ cleanup units in heavy duty diesel vehicles.[487] This on board diagnostics requirement has spurred development of NO$_x$ sensors, including amperometric, [121, 122] mixed potential, [103-108] and impedancemetric varieties.[213-239] Of these, the impedance-based sensors have shown promise for detection on the scale of single parts per million and lower. [7, 239]

In the preceding chapters, sensors with gold wire electrodes have demonstrated larger sensitivity to NO$_x$ exposure than sensors with lanthanum strontium manganate (LSM) electrodes. Sensitivity was measured as the change in impedance characterized by phase angle shift at 10 Hz on a Nyquist plot. In this investigation, gold wire sensors were examined with the goal of increasing the sensitivity to NO$_x$ gases by using design of experiment techniques.

Fractional factorial experiments allow one to change several variables (factors), to perform fewer experiments, and to quantify the influence (effects) of each factor on performance. A 2_{III}^{3-1} fractional factorial experimental design was used. It has a resolution of III, which refers to the number of main factors in the generating relation; three factors were investigated, and 4 experiments (2^{3-1}) were performed. [488] A 2^{3-1} experimental design requires half as many experiments as a full factorial design (2^3 experiments). The price that one pays for fewer experiments is aliasing, which is when main effects are confounded with interactions between effects. To address aliasing, one chooses factors that are not likely to interact with one another.

---

[487] US Environmental Protection Agency Regulatory Announcement, "EPA Finalizes Regulations Requiring Onboard Diagnostic Systems on 2010 and Later Heavy-Duty Engines Used in Highway Applications Over 14,000 Pounds; Revisions to Onboard Diagnostic Requirements for Diesel Highway Heavy-duty Applications Under 14,000 Pounds", EPA-420-F-08-032, (Dec. 2008).

[488] G. E. P. Box, J. S. Hunter, W. G. Hunter, Statistics for Experimenters: Design, Innovation, and Discovery, (Wiley-Interscience, Hoboken, NJ, 2005), 242.

The three factors were (A) the number of dense gold working electrode sensing wires, (B) electrolyte thickness, and (C) the spacing between sensing wires. High (+) and low (-) levels of each factor were identified.

The experimental design can be portrayed as a cube (Figure 89). Each side corresponds to a factor either at a high or low level. The corners represent all the unique combinations of high and low levels of each different factor. In a fractional factorial experimental design, one does not perform an experiment at every corner as one would for a full factorial, rather, experiments are selectively performed as represented by specific corners (designated here in red). In the experiments performed, each factor appears at both the high and low levels the same number of times. Two corners on each face of the cube represent the experiments that were performed. The experiments can be projected on planes representing each factor. Each square on the planes represents a 2^2 full design.[489] The four corners of each square are influenced by the experiments performed. Ideally the factors do not interact with one another, and the main effects due to the individual factors can be isolated (cube faces). Nevertheless, when interactions between factors exist, the interaction can be represented physically as diagonal planes that do not align with edges.[490]
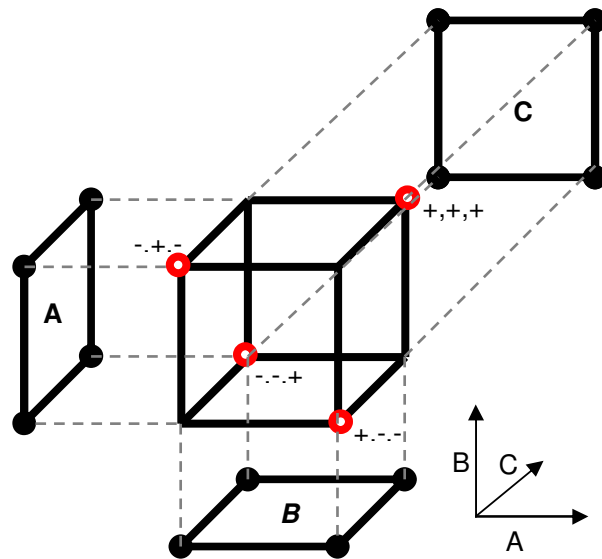
Figure 89. Design space fractional factorial experiment with three factors.[491]

This investigation has the objective to determine the effect and significance of the three controlled factors on sensor performance.

7.2 Experimental

Design of experiments techniques were used to investigate various design aspects of single cell, impedancemetric NO_x sensors. Four sensors were fabricated by varying three factors according to a half fractional factorial experiment of resolution three (2_{III}^{3-1}) as shown in Table 16. One sample of each particular design was fabricated in order capture the 1st order response;

---

[489] Ibid., 243.

[490] Ibid., 245

[491] Ibid., 244.

variation between identical samples was not investigated. Electrolyte thickness (factor B) was measured with an Alpha Step IQ profilometer.

Factor	Description	Low level (-)	High level (+)
A	Number of sensing wires	2 mm	4 mm
B	Thickness of electrolyte (number of coats)	6 mm	10 mm
C	Spacing between sensing electrode wires	1 mm	2 mm

Table 16. Factors and their values at two levels.

The experimental design matrix in Table 17 shows that the design is balanced with the same number of observations for all treatments. All factors occur at low and high levels the same number of times, which is also true for interactions. The columns are orthogonal. The alias structure has factor C confounded with the interaction of A and B. The defining relation is I=ABC. Since this relation has 3 letters, the resolution is III. Resolution addresses ability to separate main effects from low order interactions. For resolution III, the main effects are aliased with 2-order interactions. Both NO and NO_2 were investigated separately at 50 ppm. Two replicate impedance sweeps were recorded for each gas.

Sensor	A (no. wires)	B (thickness)	C (spacing)
I	+	+	+
II	+	-	-
III	-	+	-
IV	-	-	+

Table 17. Experimental design matrix.

Sensor fabrication was described previously (p. 70). Figure 90 depicts the sensors prior to wire-bonding and topcoat slurry application. All experiments were performed at 650°C in 500sccm of 10% O_2/N_2 unless otherwise noted.
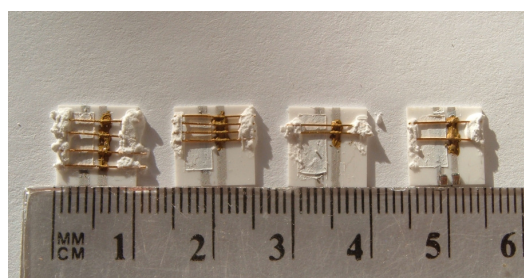
Figure 90. NO_x sensors displaying factors at various levels.

The calculated shift in phase angle, $\Delta\Theta = |\Theta_{NOx} - \Theta_{no\_NOx}|$, at 10 Hz due to exposure of 50 ppm NO_x served as the primary performance metric in the statistical analysis. Tests with NO and NO_2 were considered separately. Plots of the main effects were made for both gases. Analysis of Variance (ANOVA) was performed to determine the significance of each main effect. The predicting equations were derived from the estimates.

7.3 Results and Discussion

In order to perform the statistical analysis, data was obtained by recording the impedance response of each sensor to both NO and NO_2. The data was analyzed by making Nyquist plots and by calculating phase angle shifts at 10 Hz.

Table 18 shows the design matrix with replicated responses in the form of the absolute value of phase angle differences for both NO and NO_2 evaluated at 50 ppm and 10 Hz. All sensors exhibited larger phase angle shifts for NO_2 than for NO, confirming the findings in Chapter 5. The largest phase angle shifts occur in sensors I and III, which both have the larger electrolyte thickness (factor B).

Factors:	A (no. wires)	B (thickness)	C (spacing)	NO 50 ppm		NO_2 50 ppm	
Aliases:	bc	ac	ab	$|\Delta\Theta|$	$|\Delta\Theta|$	$|\Delta\Theta|$	$|\Delta\Theta|$
Sensor							
I	+	+	+	1.0	1.1	3.8	4.2
II	+	-	-	0.1	0.3	3.0	2.9
III	-	+	-	1.2	1.1	5.2	5.3
IV	-	-	+	0.2	0.1	3.9	4.3

Table 18. Design matrix with replicated responses.

From the responses, main effects for each factor were calculated by subtracting the average of the responses at the high (+1) level from that of the low (-1) level.[492]

$$X_i = \bar{y}_+ - \bar{y}_-$$

Main effect plots for each factor appear in Figure 91. Next to the legend of both graphics, the main effects are indicated. In this study, main effects are the absolute value of the amount of shift in the phase angle caused by changing a factor from a low level (-) to the high level (+). For example, the effect of increasing the electrolyte thickness (B) from the low level to the high level in the presence of NO_2 is to increase the phase angle shift $|\Delta\Theta|$ by +1.1 degrees. Thus a thicker electrolyte appears to be beneficial for sensing. The plots show that for any given factor, the trend is the same for NO and NO_2, i.e. the slope is either positive or negative for both gases. In general, the phase angle shifts due were larger for NO_2 than for NO as indicated on the ordinates of the plots. The slopes of the plots indicate the magnitude of the effects. The plots with the largest slopes have the largest effects. The main effects for NO_2 were consistently larger than those for NO. This finding is consistent with observations in the previous chapters in which phase angle shifts were larger in the presence of NO_2. The number of wires (A) had a large main effect only with NO_2, whereas the effect due to electrolyte thickness (B) was large for both gases. Wire spacing (C), did not matter; it did not affect the phase angle for either NO or NO_2.

The main effect plots suggest that a sensor with the attributes "-+·" with (A) low, (B) high, and (C) any level would have the best performance. One such sensor was fabricated, sensor III, with attributes "-+-". Indeed this sensor demonstrated the highest phase angle shifts due to both NO and NO_2 exposure.

---

[492] Ibid., 237.
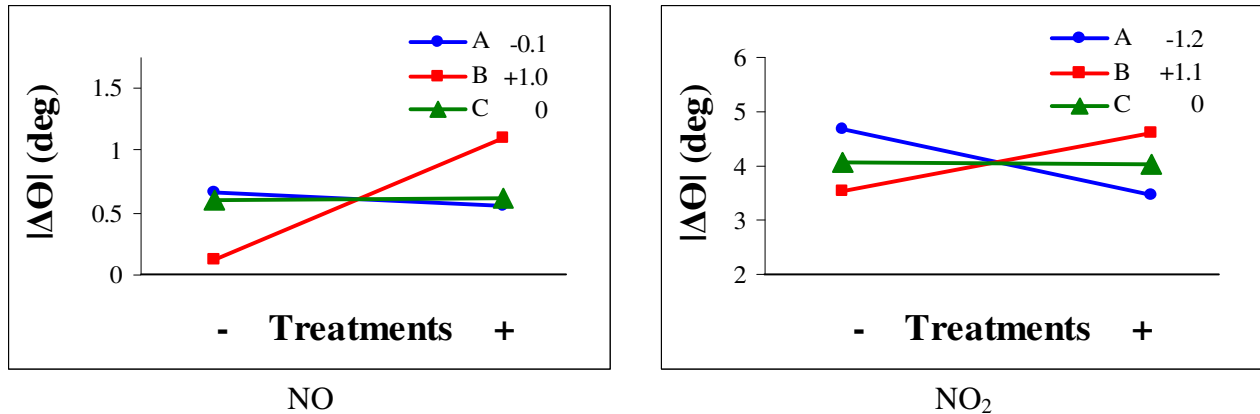
Figure 91. Main effect plots for (A) no. of wires, (B) electrolyte thickness, and (C) spacing.

Variance was analyzed in order to determine the statistical significance of these effects. Tables of analysis of variance (ANOVA) were constructed for NO and NO_2 sensing (Table 19 and Table 20, respectively).[493] No statistical analysis program was used.

Sources of Variation	Sum of Squares SS	DOF	Mean Square MS	Calculated F Value
Mean	2.99	1	2.988	579
A (no. wires)	0.02	1	0.020	4
B (thickness)	1.93	1	1.931	374
C (spacing)	0.001	1	0.001	0.12
Pure Error	0.02	4	0.005	-
Total	4.96	8	-	-

Table 19. ANOVA table for NO.

Sources of Variation	Sum of Squares SS	DOF	Mean Square MS	Calculated F Value
Mean	132.46	1	132.462	3451
A (no. wires)	2.98	1	2.981	78
B (thickness)	2.38	1	2.382	62
C (spacing)	0.002	1	0.002	0.06
Pure Error	0.15	4	0.038	-
Total	137.98	8	-	-

Table 20. ANOVA table for NO_2.

To test for significance, the calculated F values for each factor in the ANOVA tables were compared with critical F values for the appropriate number of degrees of freedom (DOF) and the desired significance level from statistical tables of the F distribution.[494] Effects are deemed

---

[493] R. E. DeVor, T. H. Chang, J. W. Sutherland, Statistical Quality Design and Control: Contemporary Concepts and Methods, (Prentice Hall, Upper Saddle River, NJ, 1992), 650.

[494] Ibid., 795-797.

significant at each confidence level for $F_{ANOVA} > F_{critical}$. A tabulation of the critical F values appears in Table 21 for several confidence levels and with degrees of freedom $\nu_1 = 1$ and $\nu_2 = 4$.

Confidence level	95%	99%	99.9%
Critical F value	$F_{crit(1,4,0.95)} = 7.71$	$F_{crit(1,4,0.99)} = 21.20$	$F_{crit(1,4,0.999)} = 74.14$

Table 21. Table of critical F values.

The number of wires (A) did not matter for NO-sensing, however, for NO_2 it did matter. With 99.9% confidence, fewer wires appeared to enhance sensing. Decreasing the electrode surface area has been shown to be beneficial for NO-sensing capability;[495] perhaps it promotes NO-detection as well. A decrease in the surface area of gold electrodes has been shown to enhance the detection of NO;[496] here it enhances NO_2-sensing. From practical experience, though, sensors with fewer wires tended to result in less reliable signals. They were often noisier due to inhomogeneities in the conduction path. Since the NO concentration in diesel exhaust typically exceeds NO_2 concentration by an order of magnitude, sensor design should favor the sensing of NO, and a larger sensing area (more wires) is desirable.

The null hypothesis was rejected for factor B, the electrolyte thickness (number of slurry coats). This factor was significant for both NO and NO_2-sensing at the 99% level. For NO, the electrolyte thickness affected sensing to the 99.9% confidence level. The porous electrolyte thicknesses measured approximately 27µm and 63µm for the low and high levels, respectively.

For wire spacing (C), the null hypothesis was rejected at all confidence levels. It was determined to be statistically insignificant. The spacing of the electrode wires had no effect whatsoever on sensing ability for NO or NO_2.

The effect of factor B, electrolyte thickness, on sensing ability comes as a surprise. Electrolyte thickness was thought to be responsible for the ionic charge transport resistance. Typically bulk ionic conduction does not change with gas species, however, in this case it appears to affect sensing performance. Using electrochemical impedance spectroscopy, bulk ionic conduction can be resolved at high frequencies ($f > 10^6$ Hz), whereas gas-sensitive phenomena such as adsorption and diffusion are resolved at much low frequencies ($f < 100$ Hz). These processes are typically not related to one another. The role of the porous electrolyte thickness on the sensing mechanism is not clear. Several possible reasons exist:

- larger surface area for adsorption, dissociation, equilibration of NO_2 to NO, and/or charge transfer reactions

- increased triple phase boundary length

- relative rate of surface diffusion versus gaseous diffusion

Woo *et al.* reduced the electrode surface area and thus the triple phase boundary length in a similar sensor that also had a dense gold electrode and a YSZ electrolyte. They claimed that the triple phase boundary length was not the rate-limiting step responsible for NO-sensing.[497] While certainly conceivable, it is also possible that the design space was too limited to demonstrate an effect, i.e. the triple phase boundary length may have not been altered enough to affect NO-sensing.

---

[495] Woo, (2008), J39.

[496] Ibid.

[497] Ibid.

Equivalent circuit modeling was performed for all sensors using the model presented in Chapter 5 (page 85) and the NO data. Table 22 presents the resistance vales of the circuit model. For a sensor with noble metal electrodes, Wu *et al.* proposed that R_0 represents contact resistance; R_1 accounts for bulk YSZ resistance, and R_2 is due to interfacial resistance.[219] All resistances were average values of the replicates. Because R_2 is sensitive to gas species, average values for R_2 are presented separately for the cases with and without NO.

Sensor	A (no. wires)	B (thickness)	C (spacing)	R_0 (Ω) (average)	R_1 (Ω) (average)	R_2 (Ω) (no NO)	R_2 (Ω) (with NO)
I	+	+	+	2,510	26, 465	103,990	96,876
II	+	-	-	2,834	144,163	135,355	143,675
III	-	+	-	2,424	10,200	26,049	23,218
IV	-	-	+	4,006	145,718	281,610	278,775

Table 22. Equivalent circuit model resistances for NO data.

Contrary to expectations, thicker electrolytes (factor B) did not result in higher bulk YSZ resistance (R_1); rather these values were lower for the sensors with thick electrolytes. This finding suggests that the geometric length of the ion migration path through the electrolyte is not the primary determinant of resistance in the porous electrolyte. The large changes in R_1 due to the change in electrolyte thickness reaffirm the equivalent circuit interpretation of Wu *et al.* that R_1 represents bulk YSZ resistance.[219]

The number of electrode wires (factor A) did not affect contact resistance (R_0). No pattern was evident.

The best sensor as measured by the phase angle shifts in Table 18 was sensor III. It had the lowest resistance values for every category. However, the worst sensor (II) did not have the highest resistance values in each category. Resistance alone does not enable sensing ability, as suggested in the literature.[498]

Woo *et al.* examined the effect of porous YSZ electrolyte thickness (150 μm vs. 75 μm) on sensors with gold electrodes. The larger thickness enhanced sensitivity to NO_2 but not to NO. The thinner porous electrolyte layer was preferred because it evinced an equivalent response to both NO and NO_2 and thus facilitated total NO_x sensing.[499]

The fabrication of one sample of each sensor resulted in an analysis of the 1st order response. Ceramic electrochemical system performance is often beset by issues of reproducibility due to variation from one sensor to another and due to changes in microstructure over time. More extensive tests might reveal the effects of variation in individual sensors.

Predicting equations were calculated from the measured phase angle shifts according to standard procedure:[500]

$$\hat{y}_{NO} = + 0.61 + (-0.05)*x_A + (0.49)*x_B + (0.01)*x_C$$

$$\hat{y}_{NO2} = + 4.07 + (-0.61)*x_A + (0.55)*x_B + (-0.02)*x_C$$

---

[498] Ibid.
[499] Woo, Glass, Novak, Visser, (2009).
[500] DeVor, 651.

where x_i is either +1 or -1 according to the factor level for each sensor. The terms for factor C can be excluded because they were not statistically significant. These equations can be used to predict the output of a sensor with a specific combination of design features. For example, the phase angle shift of sensor III when exposed to 50 ppm NO is calculated below. From Table 18, sensor III has the design attributes "-+-".

$$\hat{y}_{NO2} = + 4.07 + (-0.61)*(-1) + (0.55)*(+1) + (-0.02)*(-1) + 0 = 5.24°$$

The calculated value compares favorably with the experimental observations. The average of the replicated measurements for sensor III was 5.23° (Table 18). The value calculated from the prediction equation showed good agreement (error of 0.3%). These predicting equations are valid for sensors consisting of any combination of high and low levels (+ or -) of factors, i.e. any corner of the cube in Figure 89.

Although elimination of sources of variation in the fabrication and testing of the sensors was attempted, some variation was present. In particular, difficulty existed in controlling one fabrication parameter: electrolyte slurry consistency. Ethanol, the primary solvent in the slurry, evaporated during the application of the slurry. This change in composition introduced variation between sensors.

In addition, sensor III was fabricated three times due to poor performance. The sensors initially made according to the design specifications of sensor III exhibited open circuit defects and would not reliably resolve the low frequency arc necessary to detect gaseous species. The electrolyte slurries were made anew each time. On the third version of sensor III, the electrolyte slurry topcoat appeared thicker than other sensors most likely due to the volatility of the ethanol solvent. The thickness of the topcoat thus served as a source of variation. Later during testing, sensor III showed itself to be the best sensor for NO, as indicated by the largest difference in phase angles for NO sensing. In the future, this variation may be addressed by using a solvent with a low vapor pressure such as terpineol. Further experimentation is required in order to pinpoint the contribution of the topcoat. As shown above, the factor with the most significant effect for NO sensing is the electrolyte thickness, which in the case of sensor III may have provided a source of variation.

7.4 Conclusions

A 2_{III}^{3-1} half fractional factorial experimental design was performed by fabricating four NO_x sensors in which three design elements were varied: number of working electrode sensing wires, electrolyte thickness, and the spacing between sensing wires. Electrochemical impedance spectroscopy was performed, and the phase angle differences were calculated at 10 Hz between 50 ppm NO or NO_2 and 10% oxygen with balance N_2. The difference in phase angles characterized the sensing ability of each sensor for which two replicated measurements were made. Variation between sensors with identical design features was not examined.

Within the design space investigated, decreasing the number of sensing wires and thus the surface area was beneficial for NO_2-sensing, but not for NO. This finding suggests that electrode surface area affects the sensing mechanisms for NO and NO_2 differently.

Electrolyte thickness was statistically significant for both NO and NO_2-sensing. Increasing it augmented the phase angle shift due to NO. Equivalent circuit modeling showed that a thicker porous electrolyte layer lowered bulk electrolyte resistance instead of increasing it. The exact

mechanism is not clear, but it suggests that the increased surface area of the thicker layer of porous YSZ electrolyte plays a role. Although the bulk YSZ resistance does not change with gas species, this resistance is important for sensing ability.

The third factor, electrode spacing, did not affect gas-sensing.

Since NO_x in diesel exhaust consists predominantly of NO, this work suggests that the thick electrolyte coatings that have been shown to enhance NO_x sensitivity should be applied to the design of future impedancemetric sensors. Due to variation in reproducibility of results from identical sensors, further work might examine higher order responses.

CHAPTER 8: Analysis, Summary and Conclusions

In general, sensors with gold working electrodes perform better (i.e. larger phase angle shift) than those with LSM electrodes. None of the sensors investigated can be manufactured by conventional HTCC manufacturing methods. Possible development paths towards a viable sensor are discussed.

8.1 Comparison of Sensors

Three sensor types were analyzed for their ability to detect NO, NO_2, and O_2. The three types of sensors are (1) gold wire electrode on Al_2O_3 substrate, (2) LSM electrode on Al_2O_3 substrate, and (3) LSM electrode on Al_2O_3 substrate. The change in phase angle shift across a range of concentration served as the metric for sensitivity. The results appear in the figures below.
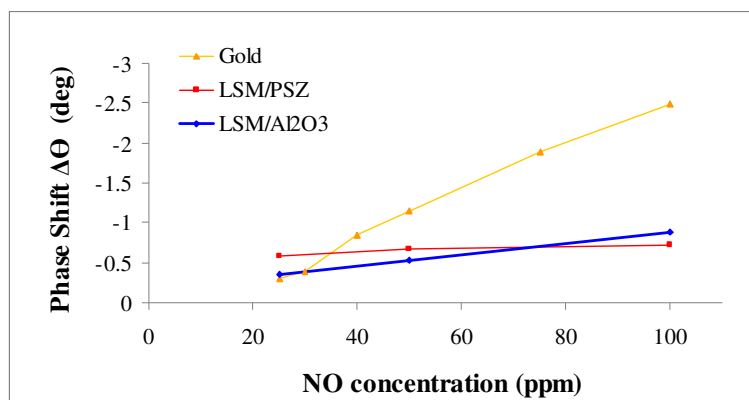
Figure 92. Comparison of sensitivity to NO.

For NO-sensing, gold wire electrodes were the most sensitive to NO. Figure 92 shows that the slope of the line associated with gold was the largest and thus gold was the most sensitive.

Similarly, gold had the largest sensitivity to NO2 (Figure 93). Neither of the sensors with LSM electrodes showed much sensitivity to NO_2.
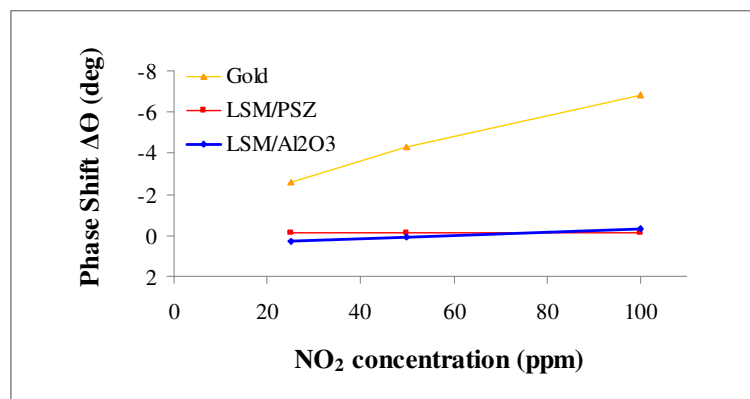

Figure 93. Comparison of sensitivity to NO_2.

Cross sensitivity to O_2 was also evaluated. The data was normalized to 10% O_2 concentration. Once again, gold exhibited the largest phase angle shift over the range of concentration investigated. The sensor with LSM electrodes on PSZ substrate showed the least cross sensitivity to O_2, however, it showed low sensitivity to NO_x.
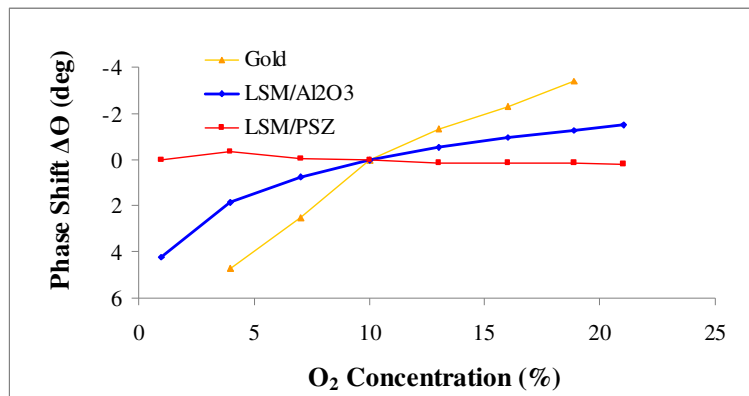
Figure 94. Comparison of sensitivity to O_2.

In summary, sensors with gold wire electrodes were more sensitive than ones with LSM electrodes for all analyte gases at all concentrations.

8.2 Technological Challenges

Designing sensors is a challenging process. They must be inexpensive to produce, operate over a wide range of changing conditions (pressure, temperature, oxygen partial pressure), and endure a harsh environment with constant vibration. Several technological obstacles question the viability of this technology as discussed below.

8.2.1. Manufacturability

Standard high temperature cofired ceramic (HTCC) methods involve screen printing inks on unfired sheets of ceramic material, stacking the sheets, laminating them, singulating (cutting) them to size, and cofiring them to 1500C.[501] HTCC processes are not compatible with the sensor materials investigated in this effort. In specific, the sensing electrode materials cannot be cofired to such a high temperature. Gold melts at 1064°C; its melting temperature is lower than the 1500°C required for densification in standard HTCC processes. The other electrode material investigated, LSM, starts to form insulating zirconate phases that degrade sensor performance at approximately 1300°C when in contact with zirconia.[84] The inability to fire the sensors to 1500°C resulted in an unstable signal over time, as discussed below. Alternative electrode materials or a different manufacturing method is necessary to make a viable impedance-based sensor. Recent patent applications did not address the manufacturing issues and the associated signal drift of impedance-based gas sensors.[502,503]

---

[501] Young, 489-526.
[502] Louis P. Martin, "Multiple frequency method for operating electrochemical sensors", US Patent Application 20080067080, (filed Aug. 16, 2007).

As an alternative to HTCC methods, the deposition of thin films of electrodes and electrolytes may also be possible by microfabrication techniques such as sputtering or PLD. Nevertheless, heat treatment would likely be necessary for in order to avoid *in-situ* aging resulting in signal drift.

8.2.2 Stability

For long term durability, stability considerations such as long term mechanical performance, resistance to chemical attack, and microstructural aging must be met.[504] For mechanical stability, a minimum of 5,000 hours (100,000 miles) of signal stability is required in an environment of thermal cycling, mechanical shock, and constant vibration. Diesel exhaust contains primarily N_2, CO_2, water vapor, and excess O_2; however, it can also contain chemicals such as ammonia and incompletely burned hydrocarbons that might foul the sensor. LSM degrades in reducing gases (HCs and CO); rich transients may degrade sensors.[505] For long term signal stability, sensor output must not be affected by these species.

Microstructural stability of the electrodes and the electrolyte is the resistance to chemical attack and to morphology changes due to grain boundary growth. Other researchers have reported such aging effects as signal instability due to electrochemical or microstructural aging.[506,507] In the present work, the signal from the sensors signal were not stable over time due to aging of the zirconia microstructure. Aging involves the phase transition of electrolyte material from tetragonal to monoclinic microstructure thereby affecting conductivity and thus impedance.[508] The electrolyte was deposited as a slurry and subsequently fired to only 1000°C; the phase transformation was not complete; and the electrolyte was not stable. In addition, grain boundary growth can affect conductivity in polycrystalline solid electrolytes over time.

Stability can be attained in a polyphase ceramic by protracted heat treatment.[509] In specific, the aging process could be accelerated by exposure to high temperature (1400-1500°C for several hours), [510,511] but the melting point of gold (1064°C) and the zirconate formation temperature of LSM and PSZ (1300°C) must be taken into account. The electrode materials used in these studies are incompatible with low cost HTCC manufacturing.

To address aging, a single crystal electrolyte might be used to avoid grain boundary growth, however, HTCC techniques would not be applicable because tape-casting generally does not form a monocrystal.

In summary, stability remains as a large challenge for sensors in this study due to the limitations on sintering temperature imposed by material properties of the electrodes.

---

[503] Leta Yar-li Woo, Robert S. Glass, Robert F. Novak, Jacobus Hendrick Visser, Erica Perry Murray, Louis Peter Martin, "Frequency Technique for Electrochemical Sensors", US Patent Application 20090223836, (filed Apr. 21, 2009).

[504] David C. Hill and Harry L. Tuller, "Chapter 5 Ceramic Sensors: Theory and Practice", Relva C. Buchanan (ed), <u>Ceramic Materials for Electronics – Processing, Properties, and Applications</u>, 2nd edn., (Marcel Dekker Inc., New York, 1992), 286.

[505] Meilin Liu, "Oxygen sensor and emission control system", US Patent 6440283, (filed Aug. 27, 2002).

[506] Martin, <u>J Electrochem Soc</u>, (2007), J103-J104.

[507] Murray, 60-62.

[508] Barsoukov, 254.

[509] <u>Ibid.</u>, 255.

[510] <u>Ibid.</u>,

[511] Hill, 286.

8.2.3 Reliability

Reliability testing is the single most important evaluation test to enable manufacturing.[512] "Despite a significant number of published research works so far, there is a lack of reliable zirconia-based gas sensors available on the market at present."[513] The long term stability of impedance sensors has not been established.[514] A minimum of 10,000 hours of testing is required operation at temperature in order to ascertain long term stability. Few if any gas sensors are tested this long.[515]

The sensors tested in this treatise suffered from microstructural aging. They did not pass the Scotch Tape test in which a film coated with adhesive (tape) was attached to the structural features of the sensors and subsequently removed. The electrodes stuck to the tape, thereby failing the test. For reliable sensors, both the mechanical and aging issues must be solved. In addition, the strong temperature dependence must be resolved.

8.2.4 Additional Challenges

The main obstacles to commercialization are the interrelated challenges of poor manufacturability, a lack of stability, and low reliability. An additional challenge is cross talk from other devices; for example, the high current flowing through the sensor's resistance heater might influence the output.

Operating temperature is yet another related technological challenge. An impedance-based NO_x sensor will likely require continuous heating in order to operate at a temperature of 600°C or higher. Continuous Joule heating will introduce a parasitic load on the electrical system. For example, SCR catalysts operate at 300°C or lower,[516] but the impedance-based NO_x sensor located downstream of it operates several hundred degrees hotter. Maintaining the temperature will be a challenge. As a result, research and development efforts should focus on sensor designs that will function at lower temperature. Such designs would suffer from less thermal aging. Thin films of YSZ exhibit ion conduction at lower temperatures.[517]

Another open question is the speed of the sensor. The investigations in this treatise examined steady state conditions that established over several minutes. An interrogation frequency of 10 Hz may be sufficiently fast, but a higher frequency with a lower phase angle shift may be necessary.

Selectivity is an ongoing issue. The demonstrated cross sensitivity to O_2 likely also occurs with water vapor and ammonia. The effects of cross sensitive reducing gases such as hydrocarbons and CO may be mitigated by an oxidation catalyst.

Commercialization requires cross sensitivity, impact of humidity on output signal and device life at various temperatures, vibration test, thermal shock test, and other extreme condition tests (reducing environment). Product verification testing of at least one year using the final sensor design is common practice in industry in order to evaluate long term stability. Academics usually

---

[512] Zhuiykov, (2008), 267.
[513] Ibid.
[514] Ibid., 128.
[515] Ibid., 221.
[516] Johnson, (2009), 280.
[517] Selmar de Souza, Steven J. Visco, and Lutgard C. De Jonghe, "Reduced-Temperature Solid Oxide Fuel Cell Based on YSZ Thin-Film Electrolyte", J Electrochem Soc, 144:3, (March 1997), L35-L37.

do not perform tests for so long. Well designed and well made sensors show long term stability over 3-10 years of operation.[518]

8.3 Future Work

This line of technological inquiry involving impedance-based NO_x sensors with gold wire or gelcast LSM electrodes faces gargantuan technological challenges. As a result, the investigation of other sensors with different electrode deposition methods is encouraged.

The operating temperature of these sensors must be significantly reduced from above 600°C to 300°C for these sensors to operate without a heater. Lower temperature operation is possible using thin films (50nm). At temperatures below 600°C, electrolyte performance suffers due to low ionic conductivity and slow charge transfer reactions at the interfaces of electrodes and electrolyte.[519] Low ionic conductivity is acceptable if the distance is extremely short and/or if no grain boundaries are present. Atomic layer deposition (ALD) is a process that results in an extremely thin nanocrystalline layer of electrolyte material.[520,521] Electrode materials can be applied by ALD on dense tiles of alumina followed by the application of electrode material. Sputtering and pulsed laser deposition (PLD) are alternatives.

ALD is not a standard HTCC process. It requires dense (prefered) substrates and a clean room environment. ALD would introduce significant cost into the manufacturing process. The electrolyte film may not work as well; it would be free of pinholes,[522] whereas the porous electrolyte of the sensors made for these investigations provided a large surface area for redox reactions to take place. In addition, an ALD nanofilm may have too good ionic conductivity; in the preceding work, the sensors on PSZ substrate had very good ionic conductivity but very low sensing capability.

In the study of sensors with gold wire, as the temperature decreased, phase angle shifts due to NO_x increased. This observation held true within the window of temperature investigated (from 700°C down to 600°C). Whether a sensor can operate acceptably at an even lower temperature remains to be seen. Yoon *et al.* examined a mixed potential NO_2 sensor at 400°C.[523]

One key to development of impedance-based sensors lies in eliminating the drift caused by the microstructural transformation (aging) process. While thin films of electrolyte put down by physical deposition methods may allow the lower temperature operation required in diesel exhaust, the long term stability of the electrolyte is not clear. Some thermal treatment may be necessary.

Ultra low temp operation may require noble metal electrodes. These electrode materials may be screen-printed using the conventional HTCC manufacturing process. Alternately, physical

---

[518] Zhuiykov, (2008), 266-7.

[519] Barsoukov, 292.

[520] Cécile Bernay, Armelle Ringuedé, Philippe Colomban, Daniel Lincot, Michel Cassir, "Yttria-doped zirconia thin films deposited by atomic layer deposition ALD: a structural, morphological and electrical characterisation", J Phys Chem Solid, 64, (2003), 1761–1770.

[521] Cynthia N. Ginestra, Raghavasimhan Sreenivasan, Annamalai Karthikeyan, Shriram Ramanathan, and Paul C. McIntyre, "Atomic Layer Deposition of Y_2O_3/ZrO_2 Nanolaminates A Route to Ultrathin Solid-State Electrolyte Membranes", Electrochem Solid State Lett, 10:10, 2007, B161-B165.

[522] Ginestra, B161.

[523] Yoon, 483-488.

vapor deposition methods can be used: gold and silver electrodes can be easily applied by vacuum evaporation on account of their high vapor pressures, whereas metals that have lower vapor pressure such as platinum and palladium can be deposited by RF sputtering (100 nm film).[524] An alloy of Pt-Ag in thin film form has been tested with YSZ at a temperature as low as 300°C.[525] An alloy of Pt-Rh may be an interesting electrode material because rhodium is a well known NO_x reduction catalyst.[526] Composite electrodes that have some of the gold contained in Au/YSZ thick film electrode substituted by the metals Pt and Rh have shown to decrease the cross sensitivity to oxygen and simultaneously improve the NO-sensitivity."[527] Platinum and gold electrodes are blocking to oxygen at T<600°C.[528] Silver has been used as an electrocatalyst in alkaline fuel cells for oxygen reduction.[529] Alkaline fuel cells operate at 80°C. This electrode material or alloys thereof may be worthy of investigation for a low temperature NO_x gas sensor application.[530]

Electrodes consisting of other electrode materials such as metal oxides may be worthy of investigation, but they may require an operating temperature higher than 300°C.[531] Recently WO_3 has been the source of many inquiries for NO_x sensors.[532,533,534] WO_3 increases selectivity to NO_x.[535] It might be applied as a thin film by sputtering tungsten metal (W) and then oxidizing it to WO_3. Sputtering is not a standard HTCC process.

Last of all, alternatives to direct NO_x sensing may be worthy of investigation for the monitoring of the NO_x mitigation system required by HD OBD regulations. For example, engine-mapping techniques in conjunction with oxygen sensors have obviated the need for an exhaust gas NO_x sensor for US Tier 2 Bin 5 diesel passenger vehicles such as the 2009 Volkswagen 2.0 L common rail TDI engine,[536], but this technology suggests when to regenerate the NO_x trap; it does not indicate whether the NO_x trap is functioning within specification or not.

[524] Barsoukov, 234.

[525] N. Matsui, "Complex-Impedance Analysis for the Development of Zirconia Oxygen Sensors", Solid State Ionics, 3:4, (1981), 525–529.

[526] D.C. Skelton, R.G. Tobin, D.K. Lambert, C.L. DiMaggio and G.B. Fisher, "A surface-science-based model for the selectivity of platinum–gold alloy electrodes in zirconia-based NO_x sensors", Sensor Actuator B Chem, 96, (2003), 46–52.

[527] Peter Schmidt-Zhang, "Untersuchungen zur Entwicklung amperometrischer Hochtemperatur-NO-Gassensoren auf der Basis von Zirconiumdioxid", (TU-Berlin Doctoral Dissertation, 2008).

[528] Barsoukov, 234.

[529] Ibid., 510.

[530] Ibid., 498.

[531] Elisabetta Di Bartolomeo, Maria Luisa Grilli, Jong Won Yoon, and Enrico Traversa, "Zirconia-Based Electrochemical NO_x Sensors with Semiconducting Oxide Electrodes", J. Am. Ceram. Soc., 87:10, (2004), 1884.

[532] Ibid., 1883–1889.

[533] Jiho Yoo, Dongjo Oh, Eric D. Wachsman, "Investigation of WO_3-based potentiometric sensor performance (M/YSZ/WO_3,M= Au, Pd, and TiO_2) with varying counter electrode", Solid State Ionics, 179, (2008), 2090–2100.

[534] Jiun-Chan Yang, Prabir K. Dutta, "Solution-based synthesis of efficient WO_3 sensing electrodes for high temperature potentiometric NO_x sensors", Sensor Actuator B Chem, 136, (2009), 523–529.

[535] Fergus, (2007), 658.

[536] Hadler, (June 2008), 535.

8.4 Summary of Findings and Conclusions

Solid state electrochemical sensors that measure nitrogen oxides (NO_x) in lean exhaust have been investigated in order to help meet future on-board diagnostic (OBD) regulations for diesel vehicles. The sensors consisted of a planar, single cell design with yttria-stabilized zirconia (YSZ) electrolyte and various working electrode materials. No reference to ambient air was required. An impedance analysis method yielded a signal that is proportional to the analyte gas concentration at a specific frequency. These sensors functioned by detecting the change in impedance caused by electron exchange in the redox reactions of NO_x gases at the sensing electrodes. From the impedance data, the resulting shift in phase angle ($\Delta\Theta$) was calculated, which was calibrated to yield to the NO_x concentration at parts per million (ppm) levels (< 100 ppm).

This research presented in this dissertation is novel in several respects. For the first time, a study of surface micromachining techniques applied to unfired sheets of ceramic material is made publicly available. Never before has an optimization study of impedance-type NO_x sensors with gold wire electrodes been performed using design of experiments techniques. In addition, for the first time gelcast LSM electrodes were fabricated in a NO_x sensor and analyzed.

Surface micromachining techniques applied to unfired ceramic sheets were evaluated for the potential to reduce the size and mass of sensors. Both wet and dry etching were investigated. These techniques, however, were not effective at micromachining unfired ceramic sheets of partially stabilized zirconia.

Three varieties of NO_x sensors were fabricated manually, tested with both NO and NO_2 gases at concentrations typical of diesel exhaust, and analyzed under various conditions. Sensors consisted of either (1) gold wire on a dense alumina substrate, (2) prefired, gelcast lanthanum strontium manganate (LSM, $La_{0.85}Sr_{0.15}MnO_3$) on a dense alumina substrate, or (3) LSM sensors on a partially stabilized zirconia (PSZ, ZrO_2 with Y_2O_3) substrate. Electrochemical impedance spectroscopy (EIS) techniques were used to interrogate the sensors. At low frequency (10 Hz), a signal was obtained proportional to low analyte gas concentration. The effects of temperature, total gas flow rate, and cross sensitivity to oxygen were examined for all sensors. Gold wire electrodes showed higher sensitivity to NO_x than gelcast LSM ones. No sensors showed dependence on total gas flow rate. They did exhibit, however, cross sensitivity to both O_2 and dependence on temperature, requiring these variables to be known in order to evaluate NO_x concentration. The phase angles at 10^5 Hz were linearly proportional to temperature for the sensors with gold wire electrodes allowing them to be used as thermometers (with appropriate calibration). In addition, for the gold wire sensors, phase angle shifts generally increased in magnitude as temperature decreased; the best results were obtained at the lowest temperature investigated (600°C).

Equivalent circuit modeling was performed for all three sensor types in order to better understand the processes underlying sensor operation. Excellent agreement with gold sensor data was obtained with a R_0-(R_1C_1)-(R_2Q_2) circuit. The presence of NO_x affected only the Cole element (R_2Q_2) which is responsible for non ideal behavior at low frequencies. Both interfacial resistance, R_2, and the constant phase element parameter representing interfacial capacitance, Q_2, were found to vary linearly with NO concentration. The real component of impedance was also found to correlate linearly with NO at low frequency. A DC measurement may be a less expensive way to determine NO_x concentration.

Design of Experiments techniques were applied to the NO_x sensors with gold wire electrodes. The optimum sensor design had a thicker electrolyte and any spacing between sensing electrodes. Smaller electrode surface area favored NO_2-sensing. Equivalent circuit modeling revealed that a thicker layer of porous electrolyte had lower resistance, implying that surface area played a role in the rate-determining step of the sensing mechanism.

This technology faces several challenges prior to commercialization including the interrelated problems of signal drift and poor manufacturability. Signal drift resulted from microstructural changes (aging) in the electrolyte during exposure to high temperature gases. Elevating the sintering temperature to 1500°C according to the standard practice in the manufacturing of oxygen sensors using high temperature cofired ceramic (HTCC) methods would mitigate aging by completing the microstructural phase transformation, however, this temperature would degrade the electrodes of gold or LSM. Typically the electrodes and electrolyte are cofired in order to achieve good contact, but at 1500°C the gold electrodes would melt and the LSM electrodes would form nonconductive zirconate phases. Microfabrication methods that physically deposit the electrolyte might address the aging issue, but they would increase cost.

Most studies of NO_x sensors involved temperatures that are much higher than the exhaust gas temperature downstream of the NO_x conversion device in a diesel engine. Future work should investigate sensors that operate at lower temperatures in order to avoid parasitic losses and to preclude thermal aging.

Bibliography

Agarwal, Pankaj, and Mark E. Orazem, Luis H. Garcia-Rubio, "Measurement Models for Electrochemical Impedance Spectroscopy I. Demonstration of Applicability", J. Electrochem. Soc., 139:7, 1992, 1917-1927.

Akbar, Sheikh, Prabir Dutta, and Chonghoon Lee, "High-Temperature Ceramic Gas Sensors: A Review", Int. J. Appl. Ceram. Technol., 3:4, 2006, 302–311.

Anderson, H.U., W. Huebner, I.Kosacki, Z. Byars and B. Gorman, "Thin Film Structures and Low Temperature Electrodes for SOFC's", EPRI /GRI / DOE Fuel Cells Review Meeting, Chicago, IL, Aug. 1999, 16. Accessed July 22, 2007, available from http://www.netl.doe.gov/publications/proceedings/99/99fuelcell/fc4-1.pdf.

Association for Emissions Control by Catalyst Newsletter, "Progress on Light-Duty Euro 5 Regulation", International Regulatory Developments, Brussels, July-Aug 2006. Accessed Oct. 16, 2009, available from http://www.aecc.eu/en/content/pdf/AECC%20Newsletter%20July-August%202006.pdf

Bard, A. J., L. R. Faulkner, Electrochemical Methods Fundamentals and Applications, John Wiley & Sons, Inc., New York, 1980.

Barfod, R., A. Hagen, S. Ramousse, P. V. Hendriksen, and M. Mogensen, "Break Down of Losses in Thin Electrolyte SOFCs", Fuel Cells 06, 2, 2006, 141–145.

Barsoukov, Evgenij, J. Ross Macdonald (eds.), Impedance Spectroscopy: Theory, Experiment, and Applications, 2nd edn., John Wiley & Sons, Inc., New Jersey, 2005.

Di Bartolomeo, Elisabetta , Maria Luisa Grilli, Jong Won Yoon, and Enrico Traversa, "Zirconia-Based Electrochemical NO_x Sensors with Semiconducting Oxide Electrodes", J. Am. Ceram. Soc., 87:10, 2004, 1883–1889.

Bauerle, James, "Study of solid electrolyte polarization by a complex admittance method", J Phys Chem Solid, 30, 1969, 2657-2670.

Belardi, Rose-Marie, Jonathan Deseure, Márcia Caldeira Brant, Tulio Matencio, Rosana Zacarias Domingues, "Electrical study of cathodic activation and relaxation of $La_{0.80}Sr_{0.20}MnO_3$", Ionics, 2009, 15:227–232.

Bernay, Cécile, Armelle Ringuedé, Philippe Colomban, Daniel Lincot, Michel Cassir, "Yttria-doped zirconia thin films deposited by atomic layer deposition ALD: a structural, morphological and electrical characterisation", J Phys Chem Solid, 64, 2003, 1761–1770.

Borman, Gary L., and Kenneth W. Ragland, <u>Combustion Engineering</u>, McGraw-Hill: Boston, 1998.

Boukamp, B.A., "Electrochemical impedance spectroscopy in solid state ionics: recent advances", <u>Sol. Stat. Ion.</u>, 169, 2004, 65-73.

Boukamp B.A. and H.J.M. Bouwmeester, "Interpretation of the Gerischer impedance in solid state ionics", <u>Sol. Stat. Ion.</u>, 157, 2003, 29-33.

Bundesministerium fuer Verkehr, Bau, und Stadtentwicklung, "German proposal Regulation [EC] 692/2008 Annex XVI, Section 6", European Commission Motor Vehicle Emissions Group, 99th Meeting, Feb. 23, 2009.

Burch, R., J.P. Breen, F.C. Meunier, "A review of the selective reduction of NO_x with hydrocarbons under lean-burn conditions with non-zeolitic oxide and platinum group metal catalysts", <u>Appl Catal B Environ</u>, 39, 2002, 283–303.

California Air Resources Board, "Diesel Engine Major Monitors", Oct. 16, 2003. Accessed Nov. 21, 2009, available from http://www.arb.ca.gov/msprog/obdprog/hdobd_workshop2.pdf

California Air Resources Board, "On-Board Diagnostic II (OBD II) Systems - Fact Sheet / FAQs", Sep. 28, 2009. Accessed Oct. 28, 2009, available from http://www.arb.ca.gov/msprog/obdprog/obdfaq.htm .

California Air Resources Board, "Staff Report: Initial Statement of Reasons for Proposed Rulemaking -- Technical Status and Revisions to Malfunction and Diagnostic System Requirements for Heavy-Duty Engines (HD OBD) and Passenger Cars, Light-Duty Trucks, and Medium-Duty Vehicles and Engines (OBD II)", Apr. 10, 2009. Accessed Oct. 28, 2009, available from http://www.arb.ca.gov/regact/2009/hdobd09/obdisor.pdf .

California Air Resources Board, "Technical Status and Revisions to Malfunction and Diagnostic System Requirements for 2010 and Subsequent Model Year Heavy Duty Engines (HD OBD)", Sep. 11, 2008. Accessed Nov. 12, 2009, available from www.arb.ca.gov/msprog/obdprog/hdobd_wsreport.doc .

California Air Resources Board Advanced Engineering Section Mobile Source Control Division, "Workshop for 2009 Biennial Heavy-Duty OBD Changes", CARB Workshop, El Monte, CA, Oct. 15, 2008. Accessed Oct. 26, 2009, available from http://www.arb.ca.gov/msprog/obdprog/hdobd_wspresentation.pdf .

Chen, X.J., K.A. Khor, S.H. Chan, L.G. Yu, "Influence of microstructure on the ionic conductivity of yttria-stabilized zirconia electrolyte", <u>Mater Sci Eng</u>, A335, 2002, 246–252.

Clark Jr, L C., R. Wolf, D. Granger and Z. Taylor, "Continuous recording of blood oxygen tensions by polarography", <u>Journal of. Applied Physiology</u>, 6:3 1953, 189-193.

Clarke, D.R. and C.G. Levi, "Materials Design for the Next Generation Thermal Barrier Coatings", <u>Annu. Rev. Mater. Res</u>., 33, 2003, 383–417.

Cooper, B. J., "Challenges in Emission Control Catalysis for the Next Decade", <u>Platinum Metals Rev</u>., 1994, 38:l, 2-10.

Cortés-Escobedo, Claudia Alicia; Juan Muñoz-Saldaña, Ana María Boların-Miró, Félix Sánchez-de Jesús, "Determination of strontium and lanthanum zirconates in YPSZ–LSM mixtures for SOFC", <u>Journal of Power Sources</u>, 180, 2008, 209–214.

DeVor, R. E., T. H. Chang, J. W. Sutherland, <u>Statistical Quality Design and Control: Contemporary Concepts and Methods</u>, Prentice Hall, Upper Saddle River, NJ, 1992.

Docquier, N. and S. Candel, "Combustion control and sensors: a review", <u>Progress in Energy and Combustion Science</u>, 28:2, 2002, 107-150.

Dupont product literature, "DuPont™ Riston® Special FX900 Series Data Sheet and Processing Information". Accessed on Dec. 9, 2009, available from http://www2.dupont.com/Imaging_Materials/en_US/assets/downloads/datasheets/fx900series.pdf.

Dutta, Atanu, and Ishihara, Tatsumi, "Amperometric NO_x sensor based on oxygen pumping current by using $LaGaO_3$-based solid electrolyte for monitoring exhaust gas", <u>Sensor Actuator B Chem Proceedings of the Tenth International Meeting on Chemical Sensors</u>, 108:1-2 Japan, July 22, 2005, 309-313.

Ernst, S. , R. Herber, E. Slavcheva, I. Vogel, and H. Baltruschat, "Continuous Detection of Volatile Aromatic, Unsaturated or Halogenated Hydrocarbons in Air by Adsorption on Pt-Electrodes and Subsequent Oxidative Desorption", <u>Electroanalysis</u>, 13:14, 2001, 1191-1197.

Fergus, Jeffrey W. "Materials for high temperature electrochemical NO_x gas sensors", <u>Sensor Actuator B Chem</u>, 121, 2007, 652–663.

Espinoza-Vallejos, Patricio and Jorge Santiago-Avilés, "Photolithographic Feature Fabrication in LTCC", <u>The International Journal of Microcircuits and Electronic Packaging</u>, 23:3, 2000, 287-292.

Etsell, T. H., S. N. Flengas, "The Electrical Properties of Solid Oxide Electrolytes", <u>Chem. Rev</u>., 70, 1970, 339-376.

European Union, "Regulation (EC) No 715/2007 of the European Parliament and of the Council", June 20, 2007.

Fukunaga, H., M. Koyama, N. Takahashi, C. Wen, K. Yamada, "Reaction model of dense $Sm_{0.5}Sr_{0.5}CoO_3$ as SOFC cathode", Sol. Stat. Ion., 132, 2000, 279–285.

Ginestra, Cynthia N., Raghavasimhan Sreenivasan, Annamalai Karthikeyan, Shriram Ramanathan, and Paul C. McIntyre, "Atomic Layer Deposition of Y_2O_3/ZrO_2 Nanolaminates A Route to Ultrathin Solid-State Electrolyte Membranes", Electrochem Solid State Lett, 10:10, 2007, B161-B165.

Gongora-Rubio, M.R., P. Espinoza-Vallejos, L. Sola-Laguna, J.J. Santiago-Avilés, "Overview of low temperature co-fired ceramics tape technology for meso-system technology (MsST)", Sensor Actuator Phys, 89, 2001, 222-241.

Grader, Gideon S. and Limor Zuri, "Tape Casting Slip Preparation by in Situ Polymerization", J. Am. Ceram. Soc. 76:7, 1993, 1809-1814.

Gutiérrez, J., L. Arés, M.C. Horillo, I. Sayago, J. Agapito, L. López, "Use of Complex Impedance Spectroscopy in Chemical Sensor Characterization", Sensor Actuator B Chem, 4, 1991, 359-363.

Hadler, Jens, Falko Rudolph, Richard Dorenkamp, Hartmut Stehr, Jürgen Hilzendeger, Sebastian Kranzusch, "Der neue 2,0-l-TDI-Motor von Volkswagen für niedrigste Abgasgrenzwerte – Teil 1", Motortechnische Zeitschrift, 69, May, 2008, 386-395.

Hadler, Jens, Falko Rudolph, Richard Dorenkamp, Martina Kösters; Dieter Mannigel; Burkhard Veldten, "Der neue 2,0-l-TDI-Motor von Volkswagen für niedrigste Abgasgrenzwerte – Teil 2", Motortechnische Zeitschrift, 69, June 2008, 536-539.

Harrington, Winston, "The Design of Effective Regulations of Transport", International Transport Forum, 2008-2, Washington, DC, Jan. 2008.

Hertz, J. L., A. Rothschild and H. L. Tuller, "Highly Enhanced Electrochemical Performance of Silicon-Free Platinum – Yttria Stabilized Zirconia Interfaces", J. Electroceramics, 22, 2009, 428-435.

van Hassel, B.A., B.A. Boukamp and A.J. Burggraaf, "Electrode polarization at the Au, $O_{2(g)}$/yttria stabilized zirconia interface. Part I: Theoretical considerations of reaction model", Solid State Ionics, 48, 1991, 139-154.

van Hassel, B.A., B.A. Boukamp and A.J. Burggraaf, "Electrode polarization at the Au, O2(g)/yttria stabilized zirconia interface. Part II: Electrochemical measurements and analysis", Solid State Ionics, 48, 1991, 155-171.

Hertz, Joshua L., Anja Bieberle, and Harry L. Tuller, "Characterization of the Electrochemical Performance of YSZ Thin Films with Nanometer-Sized Grain Structure", MIT-Tohoku '21COE' Joint Workshop on Nano-Science in Energy Technology, Cambridge, MA, Sept.27-28, 2004.

van Heuveln, Fred ,"Characterisation of Porous Cathodes for Application in Solid Oxide Fuel Cells", (Doctoral Dissertation, Technische Universiteit Twente), 23.

Hill, David C. and Harry L. Tuller, "Chapter 5 Ceramic Sensors: Theory and Practice", Relva C. Buchanan, (ed.), Ceramic Materials for Electronics – Processing, Properties, and Applications, 2nd edn., (Marcel Dekker Inc., New York, 1992), 249-348.

Ho, Kwun-Yao, Masaru Miyayama, Hiroaki Yanagida, "NO$_x$ gas responding properties of Nd2Cu04-y thick film", Mater Chem Phys, 49, 1997, 7-11.

Hong, KS, "Synthesis of Particle Dispersion", in Somasundaran, P (ed.), Encyclopedia of Surface and Colloid Science vol. 8, 2nd edn., CRC Press, Boca Raton, 6208-6220.

van Hoy, Charles, Andrew Barda, and Michelle Griffith, and John W Halloran, "Microfabrication of Ceramics by Co-extrusion", J. Am. Ceram. Soc., 81:1, 1998, 152–58.

Hughes, Daniel C., Steven E. Ernster, "Screen Printed Feature Size Capabilities", Ceramic interconnect technology: the next generation, IMAPS conference on ceramic interconnect technology, Denver, CO, Apr. 7-9 2003, 58-62.

Imen, Kamran and Susan D. Allen, "Pulse CO Laser Drilling of Green Alumina Ceramic", IEEE Transactions on Advanced Packaging, 20:4, Nov 1999.

Ivers-Tiffée, E. , K.H. Härdtl, W. Menesklou, J. Riegel, "Principles of solid state oxygen sensors for lean combustion gas control", Electrochim. Acta, 47, 2001, 807–814.

Jaeger, Richard C, Introduction to Microelectronic Fabrication, 2nd edn., Prentice Hall, Upper Saddle River, NJ, 2002.

Janney, M.A., "Attaining High Solids in Ceramic Slurries", Chapter in Advances in Process Measurements for the Ceramic Industry, A. Jillavenkatesa, G.Y. Onoda (eds.), The American Ceramic Society, Ohio, 1999, 179–203.

Janney, Mark A., Ogbemi O. Omatete, Claudia A. Walls, Steven D. Nunn, Randy J. Ogle, and Gary Westmoreland, "Development of Low-Toxicity Gelcasting Systems," J. Am. Ceram. Soc., 81:3, 1998, 581-591.

Janney, Mark A., Stephen D. Nunn, Claudia A. Walls, Ogbemi O. Omatete, Randy B. Ogle, Glen H. Kirby, and April D. McMillan, "Gelcasting", in The Handbook of Ceramic Engineering, Mohamed N. Rahaman, (ed.), Marcel Dekker, Inc., New York, 1998.

Janney, M.A., W.J. Ren, G.H. Kirby, S.D. Nunn, S. Viswanathan, "Gelcast tooling: net shape casting and green machining", Mater. Manuf. Process.,13, 1998, 340–389.

Jiang, San Ping, "Cathode materials of solid oxide fuel cells: a review", <u>J Mater Sci</u>, 43, 2008, 6799–6833.

Johnson, Tim, "Diesel Engine Emissions and Their Control", <u>Platinum Metals Rev</u>., 52:1, 2008, 23-37.

Johnson, Tim, "Review of diesel emissions and control", <u>Int. J. Engine Res</u>., 2009, 275-285.

Jørgensen, M. J. and M. Mogensen, "Impedance of Solid Oxide Fuel Cell LSM/YSZ Composite Cathodes", <u>J. Electrochem. Soc.</u>, 148:5, 2001, A433-A442.

Käding, S., S. Jakobs, and U. Guth, "YSZ-Cells for Potentiometric Nitric Oxide Sensors", <u>Ionics</u>, 9, 2003, 151-154.

Kamboj, R.K., S. Dhara, P. Bhargava, "Machining behaviour of green gelcast ceramics", <u>J. Eur. Ceram. Soc.</u>, 23, 2003, 1005–1011.

Karjalainen, Heidi, Ulla Lassi, Katariina Rahkamaa-Tolonen, Virpi Kroeger, Riitta L. Keiski, Thermodynamic equilibrium calculations of sulfur poisoning in Ce–O–S and La–O–S systems, <u>Catal Today</u>, 100, 2005, 291–295.

Kharton, V.V., F.M.B. Marques, A. Atkinson, "Transport properties of solid oxide electrolyte ceramics: a brief review", <u>Sol. Stat. Ion.</u>, 174, 2004, 135– 149.

Knitter, R, E Günther, C Odemer, and U Maciejewski, "Ceramic microstructures and potential applications", <u>Microsystem Technologies 2</u>, Springer, New York, 1996, 135-138.

Kobayashi, Shoji, Atsushi Yamasaki and Takeo Fujiwara, "Electronic Structure and Dielectric Properties of Cubic Zirconia" <u>Jpn. J. Appl. Phys</u>. 42, Japan: Japan Society of Applied Physics, 2003, 6946-6950.

Kondoh, Junya,Tsuyoshi Kawashima,Shiomi Kikuchi,Yoichi Tomii,and Yasuhiko Ito, "Effect of Aging on Yttria-Stabilized Zirconia I. A Study of Its Electrochemical Properties", <u>J. Electrochem. Soc.</u>, 145:5, May 1998, 1527-1536.

Kumar, R.V., "Some Innovative Technologies using Solid Electrolytes in Measuring Gas Compositions", <u>Ionics</u>, 3, 1997, 161-169.

Langmuir, Irving, "The Constitution and Fundamental Properties of Solids and Liquids. II. Liquids", <u>J. Am. Chem. Soc.</u>, 39:9, 1917, 1848-1906.

Lee, H D, R L Pober, P D Calvert, and H K Bowen, "Photopolymerizable binders for ceramics", <u>Journal of Materials Science Letters</u>, 5, Chapman and Hall Ltd, 1986, 81-83.

Lee, Jong-Heun, "Review on zirconia air-fuel ratio sensors for automotive applications", <u>Journal of Materials Science</u>, 38, 2003, 4247 – 4257.

Levinson, Harry J, <u>Principles of Lithography</u>, 2nd edn., SPIE Press, 2005.

Liu, Meilin, "Oxygen sensor and emission control system", US Patent 6440283, filed Aug. 27, 2002.

Logothetis, Eleftherios, Richard Soltis, "Method for determining relative amount of oxygen containing gas in a gas mixture", U.S. Patent 5145566, 1992.

Macdonald, James Ross, LEVM/LEVMW Version 8.09 Complex Nonlinear Least Squares Fitting Program. Accessed on Dec. 16, 2009. Available from http://www.jrossmacdonald.com/levminfo.html.

Madou, Marc J., <u>Fundamentals of Microfabrication: The Science of Miniaturization</u>, 2nd edn., CRC Press, Boca Raton, 2002.

Marek, J., Y. Suzuki, <u>Sensors for Automotive Applications</u>, John Wiley and Sons, 2003, 502-504.

Louis P. Martin, "Multiple frequency method for operating electrochemical sensors", US Patent Application 20080067080, filed Aug. 16, 2007.

Martin, L. P., L. Y. Woo, R. S. Glass, "Impedancemetric NO_x sensing using YSZ electrolyte and YSZ/Cr_2O_3 composite electrodes", <u>J. Electrochemical Soc.</u>, 154:3, 2007, J97-J104.

Martin, L. Peter, Leta Y. Woo, and Robert S. Glass, "Impedancemetric Technique for NO_x Sensing Using a YSZ-Based Electrochemical Cell", Materials Research Society Symposium Proceedings, 972, 2007.

Maskell, William C., "Progress in the development of zirconia gas sensors", <u>Sol. Stat. Ion.</u>, 134, Amsterdam: Elsevier Science B.V., 2000, 43–50.

Matsui, N., "Complex-Impedance Analysis for the Development of Zirconia Oxygen Sensors", <u>Solid State Ionics</u>, 3:4, 1981, 525–529.

Menil, Francis, Veronique Coillard, Claude Lucat, "Critical review of nitrogen monoxide sensors for exhaust gases of lean burn engines", <u>Sensor Actuator B Chem</u>, 67, 2000, 1–23.

Meulenbelt, Jan, "Nitrogen and Nitrogen Oxides", <u>Medicine</u>, 31:10, Oct. 2003, 64.

Miura, N., Y. Yan, G. Lu and N. Yamazoe, "Sensing characteristics and mechanism of hydrogen sulfide sensor using stabilized zirconia and oxide electrode", <u>Sensor Actuator B Chem</u>, 34, 1996, 367–372.

Miura, Norio, Geyu Lu, Noboru Yamazoe, "High-temperature potentiometric / amperometric NO_x sensors combining stabilized zirconia with mixed-metal oxide electrode", <u>Sensor Actuator B Chem</u>, 52, 1998, 169–178.

Miura, N., M. Nakatou, S. Zhuiykov, "Impedance-based total-NO_x sensor using stabilized zirconia and $ZnCr_2O_4$ sensing electrode operating at high temperature", <u>Electrochem Comm</u>, 4, 2002, 284–287.

Miura, Norio, Mitsunobu Nakatou, Serge Zhuiykov, "Impedancemetric gas sensor based on zirconia solid electrolyte and oxide sensing electrode for detecting total NO_x at high temperature", <u>Sensor Actuator B Chem</u>, 93, 2003, 221–228.

Miura, N., M. Nakatou, S. Zhuiykov, "Development of NO_x sensing devices based on YSZ and oxide electrode aiming for monitoring car exhausts", <u>Ceramics International</u>, 30, 2004, 1135–1139.

Miura, Norio, Tatsuya Koga, Mitsunobu Nakatou, Perumal Elumalai, Masaharu Hasei, "Electrochemical NO_x sensors based on stabilized zirconia: comparison of sensing performances of mixed-potential-type and impedancemetric NO_x sensors", <u>J Electroceram</u>, 17, 2006, 979–986.

Miura, Norio, Perumal Elumalai, Vladimir Plashnitsa, Taro Ueda, Ryotaro Wama, and Masahiro Utiyama, "Solid State Eectrochemical Gas Sensing", Chapter 5 in <u>Solid State Gas Sensing</u>, E. Comini, G. Faglia, G. Sberveglieri (eds.) Springer, New York, 2009.

Moore, Gordon, "Cramming More Components onto Integrated Circuits", <u>Proc. of IEEE</u>, 86:1, Jan 1998.

Moos, Ralf, "A Brief Overview on Automotive Exhaust Gas Sensors Based on Electroceramics", <u>Int. J. Appl. Ceram. Technology</u>, 2:5, 2005, 401–413.

Murray, E. Perry, R.F. Novak, D.J. Kubinski, R.E. Soltis, J.H. Visser, L.Y. Woo, L.P. Martin, and R.S. Glass, "Investigating The Stability And Accuracy Of The Phase Response For NO_x Sensing 5% Mg-Modified $LaCrO_3$ Electrodes", <u>ECS Transactions</u>, 6:20, The Electrochemical Society, 2008, 43-62.

Nahass, Paul, Richard L. Pober, Wendell E. Rhine, William L. Robbins, and H. Kent Bowen, "Prediction and Explanation of Aging Shrinkage in Tape-Cast Ceramic Green Sheets", <u>J Am Ceram Soc</u>, 75:9, 1992, 2373-78.

Nakao, Masato, Harunobu Sato, Kiichi Kamimura, and Yoshiharu Onuma, "Preparation and Property of Tetragonal Zirconia Thin Films for Oxygen Sensor", <u>Proceedings of the IEEE/CPMT International Electronics Manufacturing Technology (IEMT) Symposium 1995</u>, Japan: IEMT Symposium, 1995, 162-165.

Nakatou, Mitsunobu, Norio Miura, "Detection of combustible hydrogen-containing gases by using impedancemetric zirconia-based water-vapor sensor", <u>Sol. Stat. Ion.</u>, 176, 2005, 2411–2415.

Nakatou, Mitsunobu, Norio Miura, "Detection of propene by using new-type impedancemetric zirconia-based sensor attached with oxide sensing-electrode", <u>Sensor Actuator B Chem</u>, 120, 2006, 57–62.

Nakatou, Mitsunobu, Norio Miura, "Impedancemetric sensor based on YSZ and In_2O_3 for detection of low concentrations of water vapor at high temperature", <u>Electrochem Comm</u>, 6, 2004, 995–998.

Nernst, Walther , „Über die Elektrolytische Leitung Fester Körper bei Sehr Hohen Temperaturen", <u>Zeitschrift für Elektrochemie</u>, 6, 1899, 41-43.

NGK Insulators, Ltd, "Bringing the world's first high-precision NO_x sensor to market", Press Release, June 11, 2008. Accessed Oct. 26, 2009, available from http://www.ngk.co.jp/english/news/2008/0611.html .

Noda, Makoto, Nobuhide Kato, Hiroshi Kurachi, "Electrochemical NO_x sensor", U.S. Patent 4,770,760, 1988.

Nowotny, J., T. Bak, M. K. Nowotny and C. C. Sorrell, "Charge transfer at oxygen/zirconia interface at elevated temperatures Part 1: Basic properties and terms", <u>Adv. App. Cer.</u>, 104:4, 2005, 147-153.

Noyce, Robert N., "Semiconductor device-and-lead structure", US Patent 2981877, 1961.

Nunn, S. D., O. O. Omatete, C. A. Walls, and D. L. Barker, "Tensile Strength of Dried Gelcast Green Bodies," <u>Ceram. Eng. Sci. Proc.</u>, 15:4, 1994, 493-498.

Nunn S. D., and G. H. Kirby, "Green Machining Of Gelcast Ceramic Materials," <u>Cer. Engg. Sci. Proc.</u>, 17:3, 1996, 209–213.

Oelgeklaus, R. , H. Baltruschat, "Detection of hydrocarbons in air by adsorption on Pt-electrodes using continuous impedance measurements", <u>Sensor Actuator B Chem</u>, 42, 1997 31-37.

Oliver, Michael R, <u>Chemical-Mechanical Planarization of Semiconductor Materials</u>, Springer, New York, 2004.

Omatete, O. O., A. Bleier, C. G. Westmoreland, and A. C. Young, "Gelcast Zirconia-Alumina Composites", 15th Annual Conference on Composites and Advanced Ceramics, Cocoa Beach, FL, Jan. 1991.

Omatete, O. O. M. A. Janney, and R. A. Strehlow, "Gelcasting—A New Ceramic Forming Process," <u>Am. Ceram. Soc. Bull</u>., 70:10, 1991, 1641-1649.

Omatete, Ogbemi O., Mark A. Janney and Stephen D. Nunn, "Gelcasting: From Laboratory Development Toward Industrial Production", <u>J. Eur. Ceram. Soc.</u>, 17, 1997, 407-413.

Ono, Takashi, Masaharu Hasei, Akira Kunimoto, Toshiro Yamamoto, Akira Noda, "Performance of the NO_x sensor based on mixed potential for automobiles in exhaust gases", <u>JSAE Review</u>, 22, 2001, 49-55.

Orazem, Mark, Bernard Tribollet, <u>Electrochemical Impedance Spectroscopy</u>, John Wiley & Sons, Inc., New Jersey, 2008.

Park, , C.O., J.W. Fergus, N. Miura, Jinsu Park, Angi Choi, "Solid-state electrochemical gas sensors", <u>Ionics</u>, 15, 2009, 261-284.

Park, Jr, J. L. "Manufacture of Ceramics", U.S. Patent 2,966,719, 1961.

Park, Jinsu, B.Y. Yoon, C.O. Park, Won-Jun Lee, C.B. Lee, "Sensing behavior and mechanism of mixed potential NO_x sensors using NiO, NiO(+YSZ) and CuO oxide electrodes", <u>Sensor Actuator B Chem</u>, 135, 2009, 516.

Petronis, S, K L Eckert, J Gold, and E Wintermantel, "Microstructuring ceramic scaffolds for hepatocyte cell culture", <u>Journal of Materials Science: Materials in Medicine</u>, 12, 2001, 523-528.

Piotter, Volker, Thomas Gietzelt, and Lothar Merz, "Micro powder-injection moulding of metals and ceramics", <u>Sadhana</u>, 28:1&2, Feb/Apr 2003, 299–306.

Preidel, W., I. von Lucadou, W. Lager, L. Ruprecht, S. Saeger, "Glucose Measurements by Electrocatalytic Sensor in the Extracorporeal Blood Circulation of a Sheep", <u>Sensor Actuator B Chem</u>, 2, 1990, 257-263.

Prestat, Michel,, Jean-François Koenig, and Ludwig J. Gauckler, "Oxygen reduction at thin dense $La_{0.52}Sr_{0.48}Co_{0.18}Fe_{0.82}O_{3-\delta}$ electrodes Part I: Reaction model and faradaic impedance", <u>Journal of Electroceramics</u>, Springer Netherlands, Mar. 14, 2007, 87-101.

PrimdahI S., and M. Mogensen, "Oxidation of Hydrogen on Ni/Yttria-Stabilized Zirconia Cermet Anodes<u>", J. Electrochem. Soc.</u>, 144:10, Oct. 1997, 3409-3419.

Rajaram, Raj Rao, and Stephen Poulston, "NO_x-trap", US Patent 7287370, filed Sep. 17, 2001.

Ramamoorthy, R., P. K. Dutta, S. A. Akbar, "Oxygen sensors: Materials, methods, designs and applications", <u>J. Mats. Sci.</u>, 2003, 4271 – 4282.

Rangachary, Mukundan, and Fernando Garzon, "Electrochemical Sensors for Energy and Transportation", Interface, <u>The Electrochemical Society</u>, Summer 2004, 30-35.

Ren, Lu-quan, Shu-jie Wang, Xi-mei Tian, Zhi-wu Han, Lin-na Yan, Zhao-mei Qiu, "Non-Smooth Morphologies of -pica1 Plant Leaf Surfaces and Their Anti-Adhesion Effects", <u>Journal of Bionic Engineering</u>, 4, 2007, 33-40.

Rheaume, Jonathan "Simulation of In Situ Solid State Electrochemical Sensor for Improved Diagnostics and Control of Lean Engines", Masters Thesis, University of California at Berkeley, 2008.

Riegel, J., H. Neumann, H.-M. Wiedenmann, "Exhaust gas sensors for automotive emission control", Sol. Stat. Ion., 152–153, 2002, 783– 800.

Rimini, E, Ion Implantation: Basics to Device Fabrication, Springer, New York, 1995.

Robert Bosch GmbH, Diesel Engine Management, United Kingdom: John Wiley & Sons, 2007.

Rodgers, Robert, "The Constant Phase Element (CPE)". Accessed Oct. 30, 2000, available from http://www.consultrsr.com/resources/eis/cpe1.htm

Saracco, G., N. Russo, M. Ambrogio, C. Badini, V. Specchia, "Diesel particulate abatement via catalytic traps", Catal Today, 60, 2000, 33-41.

Schmidt-Zhang, Peter, "Untersuchungen zur Entwicklung amperometrischer Hochtemperatur-NO-Gassensoren auf der Basis von Zirconiumdioxid", (TU-Berlin Doctoral Dissertation, 2008).

Schneider, Philip, W. Beall Fowler, "Band Structure and Optical Properties of Silicon Dioxide", Phys Rev Lett, 36:8, New York: American Physical Society, Feb. 23, 1976, 425-428.

Shan, Xuechuan, S H Ling, H P Maw, C W Lu and Y C Lam, "Micro Embossing of Ceramic Green Substrates for Micro Devices", DTIP'08 Proceedings Symposium on Design, Test, Integration and Packaging of MEMS/MOEMS, Nice, France, 2008.

Shan, Xuechuan, H. P. Maw, R. T. Tjeung, S. H. Ling, C. W. Lu, R. Jachowicz, "Microstructure formation on low temperature co-fired ceramic green substrates using micro embossing", Microsystem Technologies, 14, 2008, 1405–1409.

Shimizu, Youichi, Satoko Takase, Daisuke Koba,"A NO_x Sensor Based on Solid-Electrolyte Impedance Transducer", Adv Mater Res, 47-50, 2008, 479-482.

Shukla, Pavan K., Mark E. Orazem, Oscar D. Crisalle, "Validation of the measurement model concept for error structure identification", Electrochim. Acta, 49, 2004, 2881–2889.

Skelton, D.C., R.G. Tobin, D.K. Lambert, C.L. DiMaggio and G.B. Fisher, "A surface-science-based model for the selectivity of platinum–gold alloy electrodes in zirconia-based NO_x sensors", Sensor Actuator B Chem, 96, 2003, 46–52.

Solomon, G. M., T. R. Campbell, T. Carmichael, G. Ruderman Feuer, J. S. Hathaway, "Exhausted By Diesel: How America's Dependence on Diesel Engines Threatens Our Health", Natural Resources Defense Council, New York, 1998.

Song, Qingwen, George Zhu, "Model-Based, Closed-Loop Control of Urea SCR Exhaust Aftertreatment System for Diesel Engine", SAE 2002-01-0287, March 2002.

Smith, Donald Leonard, Thin-film Deposition: Principles and Practice, McGraw-Hill Professional, New York, 1995.

de Souza, Selmar , Steven J. Visco, and Lutgard C. De Jonghe, "Reduced-Temperature Solid Oxide Fuel Cell Based on YSZ Thin-Film Electrolyte", J. Electrochem. Soc., 144:3, March 1997, L35-L37.

Stanford Materials, "Applications and Preparations of Zirconia and Stabilized Zirconia Powders". Accessed Dec. 11, 2006, available from http://www.stanfordmaterials.com/zr.html.

Stranzenbach, M., E. Gramckow, B. Saruhan, "Planar, impedance-metric NO_x-sensor with spinel-type SE for high temperature applications, Sensor Actuator B Chem, 127, 2007, 224–230.

Stranzenbach, M., B. Saruhan, "Equivalent circuit analysis on NO_x impedance-metric gas sensors", Sensor Actuator B Chem, 137, 2009, 154–163.

Stranzenbach M. and B. Saruhan, "Planar, impedance-metric NO_x-sensor with NiO SE for high temperature applications", Transducers and Eurosensors '07, The 14th International Conference on Solid-State Sensors, Actuators and Microsystems, Lyon, France, June 10-14, 2007, 983-986.

Takeda, Y., R. Kanno, M. Noda, Y. Tomida, and O. Yamamoto, "Cathodic Polarization Phenomena of Perovskite Oxide Electrodes with Stabilized Zirconia", J. Electrochem. Soc.: Electrochemical Science and Technology, 134:11, Nov. 1987, 2656-2661.

Taguchi, N. "Gas-Detecting Device", U.S. Patent 3,631,436, 1971.

Uedaa Taro, Takayuki Naganoa, Hajime Okawaa and Seiji Takahashi, "Zirconia-based amperometric sensor using La–Sr-based perovskite-type oxide sensing electrode for detection of NO_2", Electrochem Comm, 11, 2009 1654–1656.

US Environmental Protection Agency, "Nonroad Diesel Equipment Regulations and Standards". Accessed Oct. 22, 2009, available from http://www.epa.gov/nonroad-diesel/regulations.htm

US Environmental Protection Agency, "Rules and Regulations", Federal Register, 65:28, Feb 10, 2000.

US Environmental Protection Agency Regulatory Announcement, "EPA Finalizes Regulations Requiring Onboard Diagnostic Systems on 2010 and Later Heavy-Duty Engines Used in Highway Applications Over 14,000 Pounds; Revisions to Onboard Diagnostic Requirements for Diesel Highway Heavy-duty Applications Under 14,000 Pounds", EPA-420-F-08-032, Dec. 2008.

US Environmental Protection Agency Office of Transportation and Air Quality, "On-Board Diagnostics". Accessed May 5, 2010, available from http://www.epa.gov/obd/basic.htm.

Vestreng, V., Ntziachristos, L., Semb, A.,Reis, S., Isaksen, I. S. A. and Tarrason, L., "Evolution of NO_x emissions in Europe with focus on road transport control measures", <u>Atmos. Chem. Phys.</u>, 9, 2009, 1503–1520.

Vladikova, D., G. Raikova, Z. Stoynov, J. A. Kilner and S. J. Skinner, Electrical "Properties in Yttria Stabilized Zirconia Investigated by Impedance Spectroscopy", <u>Recent Progress and Future Perspectives in Infrared Microscopy and Spectroscopy with Advanced Light Sources</u>, Triest, Italy, Oct. 28-30, 2004, 1-3. Accessed on Nov. 7, 2007, available from http://www.elettra.trieste.it/events/2004/imas/docs/P10.pdf.

Wachsman, Eric and Singhal, Subhash, "Solid Oxide Fuel Cell Commercialization, Research, and Challenges", <u>Interface</u>, New Jersey: The Electrochemical Society, 18:3, Fall 2009,38-43.

Wama, Ryotaro, Masahiro Utiyama, Vladimir V. Plashnitsa, Norio Miura, "Highly sensitive impedance-based propene sensor using stabilized zirconia and zinc oxide sensing-electrode", <u>Electrochem Comm</u>, 9, 2007, 2774–2777.

West, David L., Fred C. Montgomery, Timothy R. Armstrong, "NO-selective" NO_x sensing elements for combustion exhausts", <u>Sensor Actuator B Chem</u>, 111–112, 2005, 84–90.

Wilcox, David L. Sr., Jeremy W. Burdon, Rajnish Changrani, Chia-Fu Chou, Steve Dai, Ramesh Koripella, Manny Oliver, Daniel Sadler, Paul von Allmen, and Frederic Zenhausern, "Add Ceramic 'MEMS' to the Pallet of MicroSystems Technologies", <u>Materials Research Society Symposium Proceedings</u>, 687, 2002.

Wilcox, David L., Jeremy W. Burdon, "Methods for manufacturing patterned ceramic green-sheets and multilayered ceramic packages", US Patent 20020174935, 2002.

Williams, KR Muller, RS, "Etch rates for micromachining processing", <u>J. Microelectromechanical Systems</u>, Dec. 1996, 5:4, 256-269.

Woo, Leta Y., L. Peter Martin, Robert S. Glass, and Raymond J. Gorte, "Impedance Analysis of Electrochemical NO_x Sensor Using a Au/Yttria-Stabilized Zirconia (YSZ)/Au cell", <u>Materials Research Society Symposium Proceedings</u>, 972, 2007.

Woo, L. Y., L. P., Martin, R. S. Glass and R. J. Gorte, "Impedance Characterization of a Model Au/Yttria-Stabilized Zirconia/Au Electrochemical Cell in Varying Oxygen and NO_x Concentrations", J Electrochem Soc, 154:4, 2007, J129-J135.

Woo, Leta Y. , L. Peter Martin, Robert S. Glass, Wensheng Wang, Sukwon Jung, Raymond J. Gorte, Erica P. Murray, Robert F. Novak, and Jaco H. Visser, "Effect of Electrode

Composition and Microstructure on Impedancemetric Nitric Oxide Sensors Based on YSZ Electrolyte", J Electrochem Soc, 155:1, 2008, J32-J40.

Woo, L. Y., R. S. Glass, R. F. Novak, and J. H. Visser, "Impedancemetric NO_x Sensing Based On Porous Yttria-Stabilized Zirconia (YSZ) Electrolyte: Effect of Electrode Materials on Total-NO_x Sensing and Stability", 215th ECS Meeting, Abstract 1503, 2009.

Woo, Leta Yar-Li, Robert S. Glass, Robert F. Novak, Jacobus Hendrick Visser, Erica Perry Murray, Louis Peter Martin, "Frequency Technique for Electrochemical Sensors", US Patent Application 20090223836, filed Apr. 21, 2009.

Wu, Nianqiang, Zheng Chen, Jianhui Xu, Minking Chyu, Scott X. Maob, "Impedance-metric Pt/YSZ/Au–Ga2O3 sensor", Sensor Actuator B Chem, 110, 2005, 49–53.

Yang, Jiun-Chan, Prabir K. Dutta, "Solution-based synthesis of efficient WO_3 sensing electrodes for high temperature potentiometric NO_x sensors", Sensor Actuator B Chem, 136, 2009, 523–529.

Yamamoto, O., Y. Takeda, R. Kanno, and M. Noda, "Perovskite-Type Oxides as Oxygen Electrodes for High Temperature Oxide Fuel Cells", Sol. Stat. Ion., 22, 1987, 241-246.

Yau, You-Wen, Michael A Booke, and Nirmal S Sandhu, Joseph J Fulton, "Microelectronics Packaging Processing Using Focused High Power Electron Beams", Electronic Components and Technology Conference, 1991, Proceedings, 41st, 1991, 636-638.

Yoo, Jiho, Suman Chatterjee, and Eric D. Wachsman, "Sensing properties and selectivities of a WO_3/YSZ/Pt potentiometric NO_x sensor", Sensor Actuator B Chem, 122:2, 2007, 644-652.

Yoo, J. , F. M. Van Assche, and E. D. Wachsman, J. Electrochem. Soc., 153, 2006, H117.

Yoo, Jiho, Dongjo Oh, Eric D. Wachsman, "Investigation ofWO3-based potentiometric sensor performance (M/YSZ/WO_3,M= Au, Pd, and TiO_2) with varying counter electrode", Solid State Ionics, 179, 2008, 2090–2100.

Yoon, J.W., M.L. Grilli, E. Di Bartolomeo, R. Polini, E. Traversa, "The NO_2 response of solid electrolyte sensors made using nano-sized $LaFeO_3$ electrodes," Sens. Actuators B, 76, 2001, 483–488.

Young, A. C., O. O. Omatete, M. A. Janney, and P. A. Menchhofer, ''Gelcasting of Alumina,'' J. Am. Ceram. Soc., 74:3, 1991, 612–618.

Young, Wayne S., Sarah H. Knickerbocker, "Chapter 9 Multilayer Ceramic Technology", Relva C. Buchanan (ed.), Ceramic Materials for Electronics – Processing, Properties, and Applications, 2nd ed., Marcel Dekker Inc.: New York, 1992, 489-526.

Yttria Stabilized Zirconia graphic. Accessed on Dec. 11, 2006, availiable from http://www.jaist.ac.jp/ms/labs/handoutai/horita-lab/YSZ/YSZ.files/image004.gif.

Yu, Tai-Chiang, Henry Shaw, "The effect of sulfur poisoning on methane oxidation over palladium supported on g-alumina catalysts", Appl Catal B Environ, 18, 1998, 105-114.

Zeldovich, Y. B., "The Oxidation of Nitrogen in Combustion Explosions", Acta Physicochimica U.S.S.R., 21, 1946, 577-628.

Zhang, Lan, Yujun Zhang, Y. D. Zhen and San Ping Jiang, "Lanthanum Strontium Manganite Powders Synthesized by Gel-Casting for Solid Oxide Fuel Cell Cathode Materials", J. Am. Ceram. Soc., 90:5, 2007, 1406–1411.

Zhang, X, X N Jiang, and C Sun, "Micro-stereolithography of polymeric and ceramic microstructures", Sensor Actuator Phys, 77, 1999, 149–156.

Zhuiykov, Serge, Takashi Nakano, Akira Kunimoto, Noboru Yamazoe, Norio Miura, "Potentiometric NO_x sensor based on stabilized zirconia and $NiCr_2O_4$ sensing electrode operating at high temperatures", Electrochem Comm, 3, 2001, 97-101.

Zhuiykov, S. and Miura, N., "Solid-state electrochemical gas sensors for emission control", in Materials for Energy Conversion Devices, C. C. Sorrell, J. Nowotny, and S. Sugihara (eds), Cambridge: Woodhead Publishing, 2005, 303-335.

Zhuiykov, Serge, Electrochemistry of Zirconia Gas Sensors, New York: CRC Press, 2008.